



Sakai, Satoru (2011) *The effect of Shapiro delay on pulsar timing*.
PhD thesis.

<http://theses.gla.ac.uk/3020/>

Copyright and moral rights for this thesis are retained by the author

A copy can be downloaded for personal non-commercial research or study, without prior permission or charge

This thesis cannot be reproduced or quoted extensively from without first obtaining permission in writing from the Author

The content must not be changed in any way or sold commercially in any format or medium without the formal permission of the Author

When referring to this work, full bibliographic details including the author, title, awarding institution and date of the thesis must be given

The Effect of Shapiro Delay on Pulsar Timing

A thesis submitted to The University of Glasgow for the degree of
Doctor of Philosophy
in the Faculty of Physical Sciences

2011

**Satoru Sakai
Astronomy & Astrophysics Group
Department of Physics & Astronomy**

Contents

List of Figures	9
List of Tables	17
Abstract	19
Declaration	21
Copyright Statement	22
Dedication	24
Acknowledgements	25
The Author	26
Abbreviations	27
Common symbol index	29
I Introduction	31
1 Introduction	33
1.1 Shapiro delay and Gravitational lensing	44
1.2 Thesis outline	47
II Background	49
2 Gravitational Lensing	51
2.1 History and General Relativity	51

CONTENTS

2.2	Basic lens equation	54
2.3	Multiple images and Fermat's principle	57
2.4	Time delay equation	58
2.5	Comparison of geometric and gravitational time delay	60
2.6	Shapiro time delay	62
2.7	Complete equation for Shapiro delay	64
2.7.1	Sensitivity of the Shapiro delay to ξ and ρ	65
2.8	Probability of observing a 'Shapiro event'	66
2.8.1	Detection radius	67
2.9	Change in Shapiro delay	69
2.10	Pulsar light curves	71
III	Globular Cluster Simulation	83
3	Globular Cluster Simulation	85
3.1	Analytical approach	86
3.2	Numerical approach	89
3.3	Comparison of simulation results with analytical expression	93
3.3.1	1D model	94
3.3.2	2D model	99
3.3.3	3D model	103
3.3.4	PDF overview	110
3.4	Determining $\langle(\Delta t_{\text{sh}})^2\rangle$	111
3.4.1	Number of dimensions	111
3.4.2	Number of stars	112
3.4.3	Prediction for Δt for 10^8 stars	113
3.5	Summary	114

IV Timing Residuals	115
4 Pulsar timing residuals	117
4.1 Timing residual	117
4.2 Determining f_0 and \dot{f}_0	120
4.3 Maximum-likelihood method for the TOA	122
4.3.1 Log-likelihood function	123
4.3.2 Eigenvalues and eigenvectors	124
4.3.3 Determining eigenvalues and eigenvectors	125
4.3.4 Application to MC simulation	127
4.3.5 Note on χ^2 -fitting	129
4.4 Polynomial fitting	130
4.4.1 Polynomial fitting for Δt_{Sh}	131
4.5 Summary	139
5 Determining timing residuals from MC simulation	141
5.1 Sample realisations	145
5.1.1 Simulation A1	145
5.1.2 Simulation A2	147
5.1.3 Simulation A3	149
5.1.4 Summary of realisations	151
5.2 Optimizing the MC Simulation	154
5.2.1 Cumulative Distribution Function	155
5.2.2 Cylinder approximation	157
5.2.3 Comparison of the cut-off distance derived from the cylindrical approximation with the simulation prediction	159
5.2.4 Comparison of the timing residual of the optimised simulation with the MC simulation	161
5.3 Summary	162

CONTENTS

6 Stellar distribution	163
6.1 Timing residuals	167
6.1.1 Simulation B1	168
6.1.2 Simulation B2	170
6.1.3 Simulation B3	172
6.2 Determining $\langle t_{\text{RMS}} \rangle$ and summary	174
7 Full globular cluster simulation	177
7.1 Simulated timing residual map	179
7.2 Observed timing residuals	181
7.3 Overplotting the simulated and observed timing residuals for the J-pulsar	190
7.4 $\langle t_{\text{RMS}} \rangle$ and pulsar position	191
7.5 Summary	199
8 Gravitational Acceleration	201
8.1 Simulations: Initial Conditions	203
8.2 Determining the change in pulsar time of arrival	204
8.3 Simulation 1: No initial velocity	207
8.4 Simulation 2: With initial velocity	209
8.5 Combining with Shapiro noise	211
8.6 Summary	213
V Stellar Mass Density	215
9 Stellar Mass Density	217

VI Conclusion	225
VII Appendices	231
A	233
A.1 Change in Römer delay	233
A.2 Small angle approximation	234
References	237

CONTENTS

List of Figures

1.1	Variation in pulse arrival time due to the Earth's orbit around the Sun. Image from Lorimer and Kramer (2004).	38
1.2	Figure showing the various types of evolutions that produce neutron stars (pulsars). Image taken from Lorimer (2005).	40
2.1	Simple gravitational lensing diagram. The thick solid line indicates the lensed trajectory of the light ray.	54
2.2	Geometry of Fermat's principle. Image taken from SEF.	57
2.3	Comparison between the geometric and gravitational components of the time delay as a function of impact parameter, when a lens is situated halfway between observer and source (pulsar) positioned 5130 pc away. Note this plot is a log-log plot.	61
2.4	Shapiro time delay. This figure is a re-arranged version of Figure 2.1 where the lens moves instead of the source.	62
2.5	Shapiro time delay. This figure is a re-arrangement of Figure 2.4 where the lens is behind the source.	64
2.6	The Shapiro delay as a function of ξ , the impact parameter. The function has been truncated at $\xi = 0$ since the function becomes infinite at this point.	66

LIST OF FIGURES

2.7	The Shapiro delay as a function of ρ , the distance along the LOS. At all values of ρ , $\xi = 1$ pc. $\rho < 0$ indicates that the star is behind the pulsar; $\rho = 0$ is when the pulsar and the star have the same distance along the LOS; $\rho > 0$ indicates that the star is between the pulsar and the observer.	67
2.8	Configuration to determine the detection radius, r_{det} for a globular cluster.	68
2.9	Change in Shapiro delay.	70
2.10	How time delay affects pulse profiles. In the above, $\xi = 5 \times 10^{-6}$ pc.	76
2.11	How time delay affects pulse profiles. In the above, $\xi = -2 \times 10^{-5}$ pc (top left), $\xi = -7.5 \times 10^{-6}$ pc (top right), $\xi = 7.5 \times 10^{-6}$ pc (bottom left), $\xi = 1.5 \times 10^{-5}$ pc (bottom right).	78
2.12	How time delay affects pulse profiles. In the above, $\xi = 5 \times 10^{-6}$ pc and $\sigma = 5 \times 10^{-5}$ s.	80
2.13	How time delay affects pulse profiles. In the above, $\xi = -2 \times 10^{-5}$ pc (top left), $\xi = -7.5 \times 10^{-6}$ pc (top right), $\xi = 7.5 \times 10^{-6}$ pc (bottom left), $\xi = 1.5 \times 10^{-5}$ pc (bottom right). For all light curves, $\sigma = 5 \times 10^{-5}$ s.	81
3.1	The relationship between the Cartesian co-ordinate system (x , y , z) and cylindrical polar co-ordinate system (ρ , ξ , θ). The centre of the globular cluster (and pulsar position) is at the origin. The LOS is along the x-axis.	87
3.2	Shapiro noise for a mini globular cluster containing 6 pulsars in the core and 10^5 stars, over an observing period of 3600 days. The pulsars are randomly distributed near the center of the globular cluster, and the stars are distributed within the dimensions of the globular cluster. Note that in the simulation 1 month = 30 days. .	92

3.3	Comparison of the analytical and numerical results for the normalized 1D probability distribution function (PDF).	98
3.4	The PDF shown in Figure 3.3 in \log_{10} scale. The figure shows that that the correlation between the analytical results (red line) and the numerical results (blue line) is very good.	98
3.5	The relationship between the two-dimensional Cartesian co-ordinate system (y,z) and polar co-ordinate system (ξ,θ). The centre of the globular cluster is at the origin, and the LOS to the observer (the x direction) is out of the page.	99
3.6	Comparison of the analytical and numerical results for the normalized two dimensional probability distribution function (PDF). . .	102
3.7	The PDF shown in Figure 3.6 in \log_{10} scale, showing good correlation between the analytical and numerical results.	102
3.8	Comparison of the analytical and numerical results for the normalized 3D probability distribution function (PDF).	108
3.9	The PDF shown in Figure 3.8 in \log_{10} scale. The analytical and numerical results also correlate very well in the 3D case.	108
3.10	Comparisons of the normalized PDF for each dimension.	110
4.1	The arrival pulse number as a function of arrival time for the case of no change in spin frequency (blue line), and for the case where the change in spin frequency, \dot{f}_0 , is set to 1×10^{-7} Hz s $^{-1}$ (red line). The red line is the plus-sign solution in Equation 4.4.	119
4.2	The change in time of arrival when a change in spin frequency is introduced. The red and cyan curves are solutions to Equation 4.4.	120
4.3	χ^2 -fit to determine the best fit values for f_0 and \dot{f}_0	128

LIST OF FIGURES

4.4	Comparison between the analytical estimation (eigenvectors, blue) and the contour lines from the χ^2 -fit obtained from the numerical simulation. The eigenvectors are perpendicular to one another, the cross hairs at the same location as the minimum of the χ^2 contour levels.	128
4.5	Logarithm of Shapiro noise as a function of observation time.	132
4.6	<i>Top</i> : Timing residual after first order subtracted. <i>Bottom</i> : Timing residual after first and second order subtracted.	134
4.7	<i>Top</i> : Timing residual after first order subtracted. <i>Bottom</i> : Timing residual after first and second order subtracted.	136
4.8	<i>Top</i> : Timing residual after first order subtracted. <i>Bottom</i> : Timing residual after first and second order subtracted. Note the scale, the fluctuations in the bottom figure are very small compared to the other figures – this would be a straight line when plotted over Figures 4.6 and 4.7.	138
5.1	RA and DEC of each pulsar. The RA and DEC values are given in http://www.naic.edu/~pfreire//47Tuc/ and the units have been converted into parsecs.	144
5.2	DEC and the distance along the LOS for each pulsar. See Freire et al. (2003) and Table 5.1 for errors in pulsar position along the LOS (not drawn in figure). The red line shows the distance from the observer to the centre of 47 Tucanae (5130 pc).	144
5.3	Simulation A1: Timing residuals from a sample run of a globular cluster containing 10^6 stars.	146
5.4	Simulation A2: Timing residuals from a sample run of a globular cluster containing 10^6 stars.	148
5.5	Simulation A3: Timing residuals from a sample run of a globular cluster containing 10^6 stars.	150

5.6	Histogram of the RMS timing residuals for 100 realisations for the I-pulsar.	153
5.7	Comparison of the cumulative distribution function (CDF) for different number of stars in a globular cluster.	156
5.8	Comparison of the cumulative distribution function (CDF) for different number of stars in a globular cluster.	156
5.9	The cylinder approximation for a Gaussian distribution.	158
5.10	Comparison of ξ_0 as a function of the number of stars for varying total number of stars in a globular cluster.	160
5.11	Comparison of ξ_0 as a function of the number of stars for varying total number of stars in a globular cluster.	161
6.1	Distribution of r , θ , and ϕ to change the distances from spherical to Cartesian (x,y,z) co-ordinates.	165
6.2	Comparison with the three dimensional position distribution in the simulation and the double king profile.	166
6.3	Comparison with the two dimensional position distribution in the simulation and the double king profile.	167
6.4	Simulation B1: Timing residuals from a sample run of a globular cluster containing 10^6 stars using a double King profile to generate the stars within the globular cluster.	169
6.5	Simulation B2: Timing residuals from a sample run of a globular cluster containing 10^6 stars using a double King profile to generate the stars within the globular cluster.	171
6.6	Simulation B3: Timing residuals from a sample run of a globular cluster containing 10^6 stars using a double King profile to generate the stars within the globular cluster.	173
7.1	Timing residuals from a sample run of a globular cluster containing 10^8 stars.	180

LIST OF FIGURES

7.2	Timing residuals for the C-pulsar. From the simulations, the average RMS timing residual, $\langle t_{\text{RMS}} \rangle = 0.38 \pm 0.45 \mu\text{s}$	182
7.3	Timing residuals for the D-pulsar. From the simulations, the average RMS timing residual, $\langle t_{\text{RMS}} \rangle = 5.90 \pm 16.10 \mu\text{s}$	182
7.4	Timing residuals for the E-pulsar. From the simulations, the average RMS timing residual, $\langle t_{\text{RMS}} \rangle = 0.11 \pm 0.83 \mu\text{s}$	183
7.5	Timing residuals for the F-pulsar. From the simulations, the average RMS timing residual, $\langle t_{\text{RMS}} \rangle = 17.37 \pm 70.09 \mu\text{s}$	183
7.6	Timing residuals for the G-pulsar. From the simulations, the average RMS timing residual, $\langle t_{\text{RMS}} \rangle = 18.27 \pm 95.11 \mu\text{s}$	184
7.7	Timing residuals for the H-pulsar. From the simulations, the average RMS timing residual, $\langle t_{\text{RMS}} \rangle = 1.14 \pm 4.91 \mu\text{s}$	184
7.8	Timing residuals for the I-pulsar. From the simulations, the average RMS timing residual, $\langle t_{\text{RMS}} \rangle = 22.10 \pm 24.35 \mu\text{s}$	185
7.9	Timing residuals for the J-pulsar. From the simulations, the average RMS timing residual, $\langle t_{\text{RMS}} \rangle = 2.91 \pm 15.67 \mu\text{s}$	185
7.10	Timing residuals for the M-pulsar. From the simulations, the average RMS timing residual, $\langle t_{\text{RMS}} \rangle = 1.43 \pm 11.26 \mu\text{s}$	186
7.11	Timing residuals for the N-pulsar. From the simulations, the average RMS timing residual, $\langle t_{\text{RMS}} \rangle = 15.05 \pm 51.95 \mu\text{s}$	186
7.12	Timing residuals for the O-pulsar. From the simulations, the average RMS timing residual, $\langle t_{\text{RMS}} \rangle = 33.33 \pm 127.94 \mu\text{s}$	187
7.13	Timing residuals for the Q-pulsar. From the simulations, the average RMS timing residual, $\langle t_{\text{RMS}} \rangle = 2.76 \pm 13.93 \mu\text{s}$	187
7.14	Timing residuals for the S-pulsar. From the simulations, the average RMS timing residual, $\langle t_{\text{RMS}} \rangle = 29.08 \pm 58.76 \mu\text{s}$	188
7.15	Timing residuals for the T-pulsar. From the simulations, the average RMS timing residual, $\langle t_{\text{RMS}} \rangle = 9.68 \pm 37.07 \mu\text{s}$	188

7.16 Timing residuals for the U-pulsar. From the simulations, the average RMS timing residual, $\langle t_{\text{RMS}} \rangle = 0.15 \pm 0.17 \mu\text{s}$	189
7.17 Comparison of observed and predicted timing residual for the J-pulsar.	190
7.18 $\langle t_{\text{RMS}} \rangle$ as a function of r , the distance from the centre of the globular cluster. Error bars obtained from Freire et al. (2003) are shown in red. The blue error bars, showing the error in simulated timing residual, has been reduced by a factor of 10.	192
7.19 $\langle t_{\text{RMS}} \rangle$ as a function of ξ , the perpendicular distance between the pulsar and the globular cluster centre, along the LOS. Error bars obtained from Freire et al. (2003) are shown in red. The blue error bars, showing the error in simulated timing residual, has been reduced by a factor of 10.	193
7.20 Comparison of the stellar distributions functions.	195
8.1 The effect of gravitational acceleration between one pulsar and one star. The acceleration a and velocity v are both along the distance r for both timesteps.	204
8.2 Variations in timing residual as a function of D , the core box width, for a 10^6 star globular cluster.	208
8.3 Variations in timing residual as a function of stellar density in the core ρ , for a 10^6 star globular cluster. The red line denotes the core stellar density of 47 Tucanae as described in Pryor and Meylan (1993).	209
8.4 Variations in timing residual as a function of D , the core box width, for a 10^6 star globular cluster.	210
8.5 Variations in timing residual as a function of ρ , the stellar density, for a 10^6 star globular cluster. The red line denotes the core stellar density of 47 Tucanae as described in Pryor and Meylan (1993). . .	211

LIST OF FIGURES

9.1	LOS to a pulsar in the spiral arms of a galaxy.	218
9.2	<i>Left:</i> The thin stellar disk along the LOS between pulsar and Earth. <i>Right:</i> The ‘window’ of stellar distribution around the LOS to the pulsar.	218
9.3	The average RMS timing residual as a function of stellar surface density in a thin disk at varying distances along the LOS.	219
9.4	The Average RMS timing residual as a function of stellar density around the pulsar.	221
9.5	The distribution of core stellar density for 22 globular clusters containing MSPs. The red line is ρ_{\min} , the minimum core stellar density.	222
9.6	The distribution of pulsars according to the core stellar density of the globular cluster containing the pulsar. The red line is ρ_{\min} , the minimum core stellar density.	222

List of Tables

3.1	Initial conditions for MC simulation	91
3.2	Comparison of the root-mean-square (RMS) value for the change in Shapiro delay, Δt_{Sh} for one star and one pulsar, observed for a period of 3600 days.	112
3.3	The change in Shapiro delay, $\langle(\Delta t_{\text{Sh}})\rangle$ for different number of stars in a globular cluster, observed over a period of 3600 days.	113
5.1	The position and velocity of each pulsar in 47 Tucanae.	143
5.2	The average and variance RMS value for the timing residual for each pulsar in a 10^6 star 47 Tucanae.	151
5.3	Comparison of $\langle t_{\text{RMS}} \rangle$ values of the optimised simulation with the full simulation, for a different number of total stars in the globular cluster.	162
6.1	The average and variance of the RMS value for the timing residual for each pulsar in a 10^6 star 47 Tucanae. The stellar distribution of this globular cluster was modelled using a double King profile. .	174
7.1	Comparison between the observational and simulated RMS timing residual values.	177
7.2	Comparison of the stellar distribution ratio of a Gaussian distri- bution (with varying values of σ) and the double King profile. .	198

LIST OF TABLES

8.1 Comparison of the timing residual with and without gravitational acceleration for a 10^6 star globular cluster.	212
9.1 Comparison of the core stellar density of globular clusters containing milli-second pulsars (MSPs).	224

The University of Glasgow

ABSTRACT OF THESIS submitted by Satoru Sakai
for the Degree of Doctor of Philosophy and entitled
The Effect of Shapiro Delay on Pulsar Timing, June 2011

Light passing near a massive object (star) will take longer to arrive at the Earth than it would if the object was not present. This additional time is called the Shapiro delay. In globular clusters, where there are millions of stars, the cumulative effect of the Shapiro delay from these stars will affect pulsar timings by introducing an additional noise term. This effect has been previously assumed to be small, yet no definite investigation has been done to determine its magnitude.

In this thesis a model of the globular cluster 47 Tucanae was created in order to determine the effect of the change in Shapiro delay (called the Shapiro noise) for an observed duration of 3600 days – the current longest observation period for pulsar timing. This noise was then added to the pulsar time of arrival (TOA) as the only noise source in pulsar timing. A polynomial fit was then used to subtract the first two orders from the pulse arrival time (the f and \dot{f} terms) to determine the timing residuals. This model was then realised 100 times to obtain the average root mean square (RMS) timing residual for every pulsar. The model showed that the Shapiro noise has a significant, and observable effect on pulsar timing, especially for pulsars situated close to the core of the globular cluster. From the model the average RMS timing residuals were of the order of 10^{-5} to 10^{-7} seconds and the variance of the RMS timing residuals were significantly larger in magnitude, ranging from 10^{-4} to 10^{-7} seconds for every pulsar. The importance of this result motivated further investigation of the stellar distribution of the globular cluster.

In addition an investigation on how the effect of gravitational acceleration

(produced by stars situated close to the pulsar) affects pulsar timing residual was also done. While the acceleration has an effect, the effect is smaller than that of the Shapiro noise.

From the timing residuals produced by the Shapiro noise, it was then discussed whether any star close to the LOS would have an affect on the pulsar timing residuals. From additional simulations it was determined that stars anywhere along the LOS will have an affect on pulsar timing, however the stellar density of such a region would have to be greater than $\rho_{\min} > 10^5 M_\odot pc^{-3}$. The implications of this result for other pulsars in (other) globular clusters is discussed.

Declaration

I declare that no portion of the work referred to in the thesis has been submitted in support of an application for another degree or qualification of this or any other university or other institute of learning.

Copyright Statement

- (i) Copyright in text of this thesis rests with the Author. Copies (by any process) either in full, or of extracts, may be made only in accordance with instructions given by the Author. This page must form part of any such copies made. Further copies (by any process) of copies made in accordance with such instructions may not be made without the permission (in writing) of the Author.
- (ii) The ownership of any intellectual property rights which may be described in this thesis is vested in The University of Glasgow, subject to any prior agreement to the contrary, and may not be made available for use by third parties without the written permission of the University, which will prescribe the terms and conditions of any such agreement.
- (iii) Further information on the conditions under which disclosures and exploitation may take place is available from the Head of Department of Physics and Astronomy.

Anyone who doesn't take truth seriously in small matters cannot be trusted in large ones either.

Albert Einstein

Dedication

To my parents.

Acknowledgements

I wish to thank my supervisor Professor Graham Woan and Dr Martin Hendry for their round the clock support (quite literally) during my studies. Even when they were both away for months at a time (occasionally without telling me), they would always give me ideas and methods to try. I would like to thank the staff at the University of Glasgow for allowing me to (ab)use the computing facilities for my monstrous MATLAB simulations. Many thanks to Dr Iain Sim for keeping ~~sothis~~ up and running for me to use and process my simulated data, and MATLAB for making my life easier.

I would like to thank the postgraduates (Hazel Bain, Euan Bennet, Christina Burge, Ewan Dickson, Hoda Ghodsi, Colin Gill, Jingnan Guo, David Graham, Natasha Jeffrey, Craig Lawrie, Procheta Mallik, Robert McKay, Craig McLachlan, Heather Ratcliffe, Fatima Rubio da Costa, Ignacio Santiago, Bethmini Senevirathne, Fiona Speirits, Craig Stark, Edward Thomson, Fraser Watson) and the postdocs (Matthew Pitkin, Hugh Potts) and many others for their help, support and the occasional sanity check.

I would like to thank my football teammates (Carnage Colin, Cancellation Cowie, Inter Milan Craig, Crazy OG Craig, Depressingly skillful Derek, Dangerous Deepak, Ecstatic Eric, Fingertip-save Fraser, Goal-minded Grant, Injury-plagued Nacho, Juan Bonnets, Killer Keith, Side-defenseman Matt, Watford Matt, Germany Paul, Pete, Sedated Siong) and other random players they've managed to drag to the Stevenson building in order to keep my fitness levels up (from zero) and also as a means of stress relief.

I would also like to thank STFC for funding my studentship and subsidising for my research travels.

Finally I would like to thank my family for their endless support.

This thesis was typeset with L^AT_EX.

The Author

The author was born in Akita, Japan but has lived most of his life in Eindhoven, the Netherlands, where he completed his high school education in 2001. He completed his undergraduate degree, an MPhys in Astrophysics (hons), at the University of Edinburgh in 2006, and a MPhil postgraduate degree in radio astronomy at The University of Manchester

He is currently studying for a PhD at the University of Glasgow, the result of which are presented in this thesis.

Abbreviations

Throughout this thesis the following conventions and abbreviations have been used:

AU: Astronomical Unit

CDF: Cumulative Distribution Function

DEC: Declination

DM: Dispersion measure

EPL: Extra path length

FWHM: Full width at half maximum

GL: Gravitational Lensing

GR: General Relativity

GW: Gravitational wave

ISM: Interstellar matter

KS91: Krauss and Small (1991)

LIGO: Laser Interferometer Gravitational-wave Observatory

LISA: Laser Interferometer Space Antenna

LK: Lorimer and Kramer (2004)

LOS: Line of sight

MC: Monte-Carlo (simulation)

MSP: Milli-second pulsar

PDF: Probability distribution function

PPTA: Parkes Pulsar Timing Array

PTA: Pulsar Timing Array

RA: Right Ascension

RMS: Root mean square

SEF: Schneider et al. (1992)

SE07: Siegel et al. (2007)

SE08: Siegel (2008)

SSB: Solar System Barycenter

SKA: Square Kilometer Array

SNR: Signal-to-noise ratio

TOA: Time of arrival

Common symbol index

Throughout this thesis the following symbols have been used:

c : Speed of light

f : Spin frequency

\dot{f} : Rate of change of spin frequency

f_0 : Best-fit spin frequency

\dot{f}_0 : Best-fit rate of change of spin frequency

G : Newton's constant of gravity

M_\odot : Solar mass

N : Number of stars in a globular cluster

N_0 : Total number of stars in a globular cluster

r : Distance between star and pulsar

ρ : (i) Distance along the LOS (Chapter 2, 3) (ii) Stellar density (Chapter 5 – 9)

ξ : Impact parameter in the plane perpendicular to the line of sight

Part I

Introduction

1

Introduction

Baade and Zwicky (1934) predicted the existence of rapidly rotating neutron stars as a result of core collapse of massive (few orders of solar masses) stars in supernovae. The neutron stars were predicted to be very compact (~ 10 km radii), with masses of the order of the Chandrasekhar mass ($\sim 1.4 M_{\odot}$), and rapidly spinning due to conservation of angular momentum of the parent stellar core. Neutron stars also possess high magnetic fields due to conservation of magnetic flux. Since charged particles moving along the magnetic field can cause beams of radiation to be emitted, when the neutron star rotates this beam sweeps across space. When such a beam is directed towards Earth a pulse may be observed using radio telescopes. As the pulsar radiates energy and angular momentum (predominantly through magnetic dipole radiation at the spin frequency) its rate of spin slows down and we detect a decrease in the observed pulse frequency. The time period between pulses is the time it takes for the neutron star to complete one revolution on its axis.

The rotation periods of pulsars can be timed by monitoring their rotation and tracking the time of arrival (TOA) of radio pulses over long periods of time – spanning years if not decades – and because pulsar rotation is highly stable it is possible to use it as a test bed for physics (Lyne et al. 2004), including theories of gravity.

To perform accurate pulsar timing measurements, the time series from the pulsar is “folded” – individual pulses are combined together to form a single integrated pulse profile. Although individual pulses may vary in shape, the combined pulse profile is very stable. This integrated pulse profile has a high signal-to-noise ratio that can be used (in models) to determine parameters such as phase offset. When multiplying the phase offset with the pulse period P , it is possible to determine a time offset that can be added to a reference point, e.g. at the beginning of the pulse/leading edge of the pulse profile, to create a TOA measured on the Earth.

In the inertial frame of the Solar System Barycentre (SSB), the period of pulsar rotation is nearly constant, and the phase $\phi(t_{\text{SSB}})$ can be usefully approximated by a Taylor expansion,

$$\phi(t_{\text{SSB}}) = \phi(t_0) + f \cdot (t_{\text{SSB}} - t_0) + \frac{1}{2} \dot{f} \cdot (t_{\text{SSB}} - t_0)^2 + \dots, \quad (1.1)$$

where t_0 is an arbitrary reference time and t_{SSB} is the time measured in the frame of the Solar System Barycentre. The remaining terms on the right hand side are the pulse frequency f and the change in pulse frequency, \dot{f} . These two terms affect the phase of the pulse period by taking the pulsar rotational evolution into account. The \ddot{f} term is included as pulsars spin down (see above), resulting in a quadratic variation in phase over time.

Pulse time of arrival (TOA)

In order to infer $\phi(t_{\text{SSB}})$, some correction terms are applied to the observed TOAs. The pulses are observed on Earth at a topocentric (i.e. measured from a fixed point on Earth’s surface) time, t_{topo} , and it is possible to project this to the time in the SSB frame, t_{SSB} , and also correct for interstellar dispersion. t_{SSB} can then be described by

$$t_{\text{SSB}} = t_{\text{topo}} + t_{\text{corr}} - \Delta D/f^2 + \Delta_{R\odot} + \Delta_{E\odot} + \Delta_{S\odot}, \quad (1.2)$$

where t_{corr} is a clock correction made to the observatory time to bring it into line with the Terrestrial Time (see Backer and Hellings 1986 for details).

Correction factors

The $\Delta D/f^2$ term is the (systematic frequency-dependent) delay of an electromagnetic signal by electrons whose density varies along the line of sight (LOS) to the pulsar from the Earth (the ΔD term is defined in Lorimer and Kramer 2004). This delay is relative to the propagation time of the signal in a vacuum. Electromagnetic waves vary as $E = E_0 \exp(-i\omega t)$, where ω is the angular frequency. Electrons oscillate around protons at distance x as $x = x_0 \exp(-i\omega t)$. This charge separation appears as a bulk polarization P^1 that defines the relative permittivity of the plasma ϵ_r ,

$$P = n_e p = (\epsilon_r - 1) \epsilon_0 E , \quad (1.3)$$

where $p = xe$ is the dipole moment for one electron/proton pair. The equation of motion for the electron oscillation is given by,

$$eE = m_e \ddot{x} = -m_e \omega^2 x , \quad (1.4)$$

and by combining the above equations, ϵ_r can then be re-written as,

$$\epsilon_r = 1 - \frac{n_e e^2}{\epsilon_0 m_e \omega^2} . \quad (1.5)$$

The refractive index η of the plasma is,

$$\eta = \epsilon_r^{1/2} = \left(1 - \frac{f_p^2}{f^2} \right)^{1/2} \quad (1.6)$$

where f_p is the plasma frequency (the natural oscillation frequency of the plasma) given by,

$$f_p = \frac{1}{2\pi} \left(\frac{n_e e^2}{\epsilon_0 m_e} \right)^{1/2} . \quad (1.7)$$

¹This P stands for polarization, not pulse period.

1: INTRODUCTION

From above it can be seen that the refractive index η is frequency dependent, so the signal travel time is also dependent on frequency,

$$t = \int_0^d \frac{dl}{\eta(l) c}, \quad (1.8)$$

where d is the distance from the source to the telescope, along l . If this frequency is well above the plasma frequency of the cold unmagnetized plasma that the signal is propagating through, i.e. $f \gg f_p$, the ‘extra’ time the signal has to travel – the time delay due to the plasma – is given by,

$$\Delta t = \frac{e^2}{2\pi m_e c} \frac{1}{f^2} \int_0^d n_e(l) dl \quad (1.9)$$

$$\propto \frac{\int_0^d n_e dl}{f^2} \quad (1.10)$$

where n_e is the electron density in the interstellar matter (ISM) and $\int_0^d n_e dl$ is the volume density of electrons integrated along the LOS l from Earth at 0 to the pulsar at distance d . This integral is defined as the **Dispersion Measure** (DM) to the source (see Section 5). Since telescopes accept radio waves within a certain bandwidth at a particular frequency, for example 100 MHz bandwidth around a central frequency of 1.4GHz, the arrival times of different frequency components are spread out in time, or *dispersed*. This also means that observations at multiple frequencies allow the dispersion to be characterized and overcome by *de-dispersion* (see Lorimer and Kramer 2004, pg. 106-120 for details).

The **Römer delay**, $\Delta_{R\odot}$, is the classical light travel time across Earth’s orbit. This delay is expressed as

$$\Delta_{R\odot} = -\frac{1}{c} \vec{r} \cdot \hat{s}, \quad (1.11)$$

where \hat{s} is the unit vector pointing from the SSB to the pulsar and \vec{r} is the vector from the SSB to the observatory. The maximum Römer delay obtainable is when Earth is positioned at the extrema as shown in Fig 1.1. The extra path length l

that the light from the pulsar has to travel is given by,

$$l = r_{\text{SSB}} \cos \beta , \quad (1.12)$$

which results in a delay of,

$$\Delta_{R\odot} = \frac{r_{\text{SSB}}}{c} \cos \beta \quad (1.13)$$

$$\sim 500 \cos \beta \text{ s} , \quad (1.14)$$

as the Earth-Sun distance is 1 AU $\sim 150 \times 10^9$ m and therefore $\frac{1\text{AU}}{c} \sim 500$ s. β is the ecliptic latitude of the pulsar. The ecliptic is the path that the Sun appears to follow across the sky over the course of a year, and also the projection of the Earth's orbital plane onto the celestial sphere. The ecliptic co-ordinate system uses the ecliptic for its fundamental plane. The ecliptic latitude (β) is measured positive towards Earth, and the ecliptic longitude angle λ is measured eastwards from 0 to 360 degrees, where 0 points towards the Sun from Earth at Northern hemisphere vernal equinox.

The change in the Römer delay is produced by the change in the position (longitude and latitude) of the Earth (see Section A.1 for full details).

The **Einstein delay**, $\Delta_{E\odot}$, accounts for the change in arrival time due to the effects of gravitational redshift, itself changing due to the motion of the Sun and planets other than the Earth at the observer end, as well as the motion of any binary companion at the pulsar end. This effect accounts for the deviation in atomic clocks on Earth due to the change in gravitational potential as the Earth orbits around the Sun. The delay is expressed in Backer and Hellings (1986) as

$$\frac{d\Delta_{E\odot}}{dt} = \frac{GM}{c^2 r_E} + \frac{v_E^2}{2c^2} - \text{constant} , \quad (1.15)$$

where the gravitational potential is the sum of all the bodies in the Solar System (excluding Earth), r_E is the distance between the body and the Earth, and v_E is the velocity of the Earth relative to the Sun. The second term is the velocity of the geocentre relative to the SSB (Edwards et al. 2006). The constant is chosen such that the terms on the right hand side becomes zero over long time intervals.

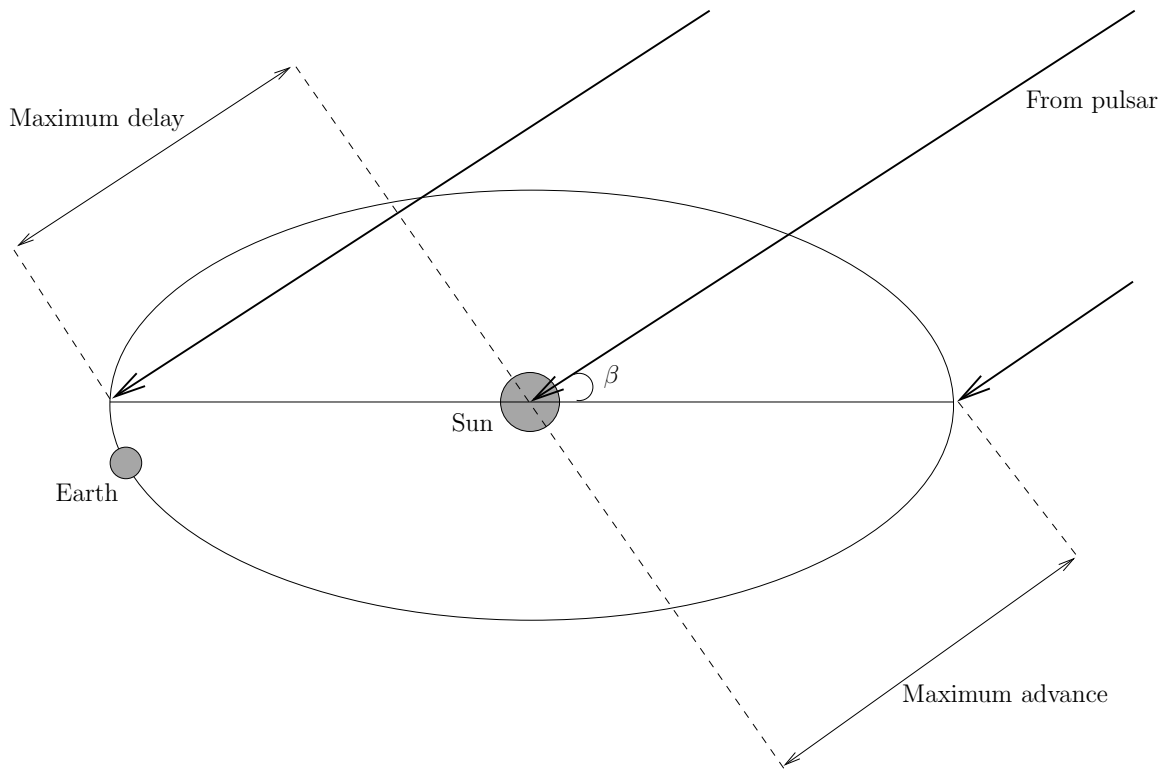


Figure 1.1: Variation in pulse arrival time due to the Earth's orbit around the Sun. Image from Lorimer and Kramer (2004).

Let us estimate the Einstein delay by only including the Sun, the most massive body in our Solar System ($> 99\%$ of total mass of Solar System). The mass M is then one solar mass, r_E is one astronomical unit (AU) as it is the Earth-Sun distance, and $v_E \sim 30 \text{ km s}^{-1}$. The (rate of change of) Einstein delay is then given by,

$$\begin{aligned}\frac{d\Delta_{E\odot}}{dt} &= \frac{GM_\odot}{c^2 r_E} + \frac{v_E^2}{2c^2} - \text{constant} \\ &\sim 9.871 \times 10^{-9} + 5.007 \times 10^{-9} \\ &\sim 1.488 \times 10^{-8} \text{ s s}^{-1} \quad (1.16)\end{aligned}$$

$$\sim 0.470 \text{ s yr}^{-1}. \quad (1.17)$$

The **Shapiro delay**, $\Delta_{S\odot}$, is the correction term for delays due to the space-time curvature caused by the presence of massive bodies in the Solar System

(Shapiro 1964). This delay term is the sum over all bodies in the Solar System (see Backer and Hellings 1986),

$$\Delta_{S\odot} = -2 \sum_i \frac{GM_i}{c^3} \ln [\hat{s} \cdot \vec{r}_i + |r_i|] + \Delta_{S\odot 2}, \quad (1.18)$$

where G is Newton's gravitational constant, M_i is the mass of body i , \hat{s} is the unit vector pointing to the pulsar, \vec{r}_i is the vector from body i to the telescope, and $\Delta_{S\odot 2}$ is a second-order correction term. As with the Einstein delay, it is common to consider only the effects of the Sun. However there are cases where Jupiter is also included (Backer and Hellings 1986). When only considering the Sun, the above equation approximates to,

$$\begin{aligned} \Delta_{S\odot} &= -\frac{2GM_\odot}{c^3} \ln [r_\odot \cos \theta + r_\odot] \\ &= -\frac{2GM_\odot}{c^3} \ln [r_\odot (1 + \cos \theta)] \\ &= \frac{2GM_\odot}{c^3} \ln [|r_\odot| (1 + \cos \theta)], \end{aligned} \quad (1.19)$$

where θ is the pulsar-Sun-Earth angle at the time of observation, and r_\odot is the telescope position relative to the Sun. The largest possible time delay is when $\cos \theta \rightarrow 1$, which results in a Shapiro delay of

$$\Delta_{S\odot} = 6.829 \mu\text{s}. \quad (1.20)$$

However, there is also a Shapiro delay produced by massive bodies around the LOS to pulsars. This delay may have a large effect for pulsars situated within high stellar population regions, such as inside globular clusters. As will be discussed later, the observations are not sensitive to the magnitude of this Shapiro delay, but they are sensitive to the change in the magnitude of the Shapiro delay.

Globular clusters and millisecond pulsars

Figure 1.2 shows, in simple terms, the currently accepted model (see Bisnovatyi-Kogan and Komberg 1974 and references therein) that explains how various systems of neutron stars form. Starting with a binary system (Figure 1.2, top left)

1: INTRODUCTION

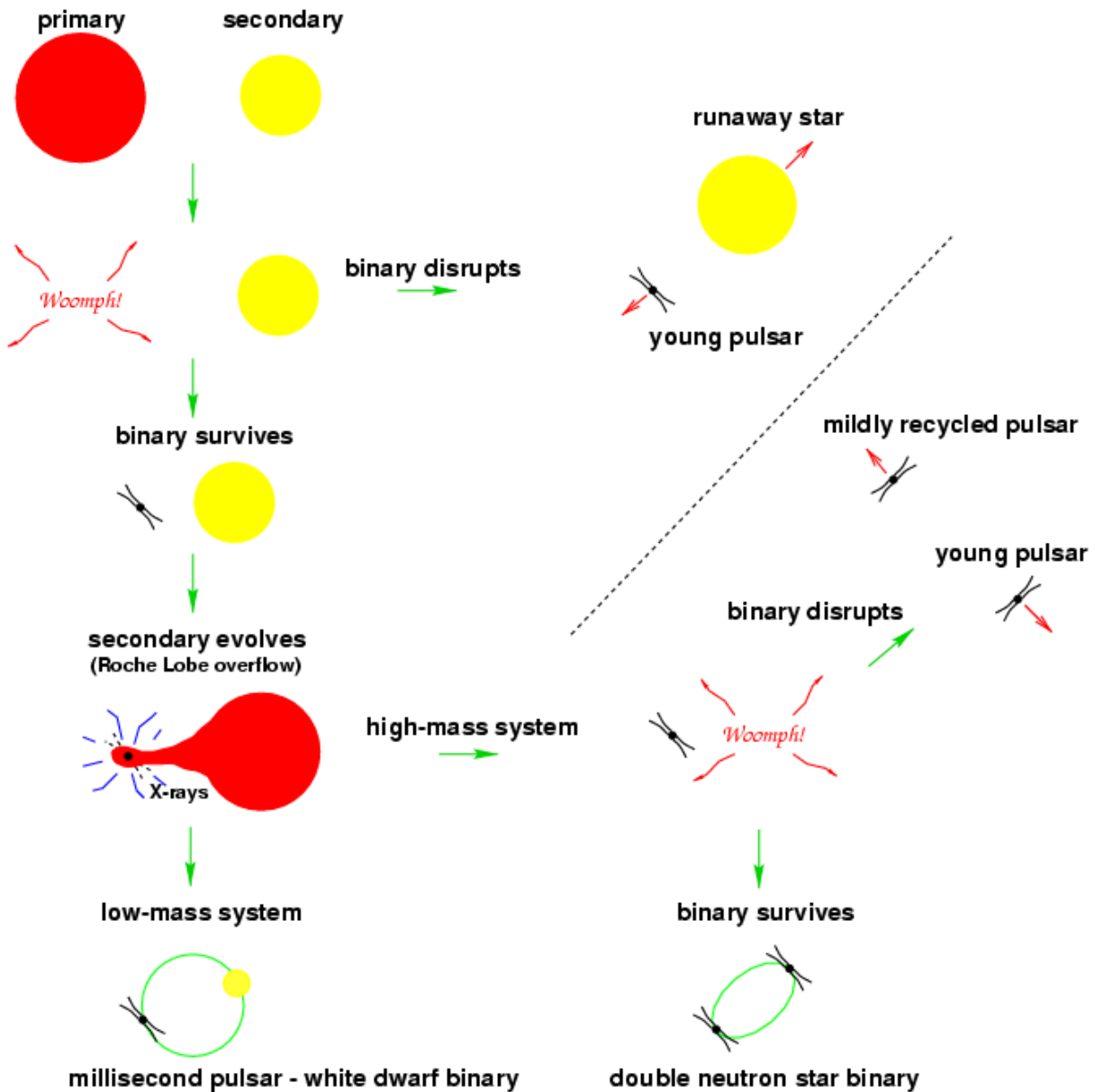


Figure 1.2: Figure showing the various types of evolutions that produce neutron stars (pulsars). Image taken from Lorimer (2005).

a neutron star is formed after the larger of the two stars undergoes a supernova. During the explosion, depending on the quantity of total mass prior to the supernova, the binary system either survives or gets disrupted. The latter will occur if either (i) more than a half of the total pre-supernova mass is ejected (from

the virial theorem), or (ii) the random kick velocity of the neutron star, which originates from the asymmetric explosion, is sufficiently large to disrupt the binary system (Hills 1983). This kick velocity results in a high velocity neutron star and an OB “run-away” star (Blaauw 1961). After the supernova the angular momentum of the neutron star may decrease through emission of relativistic particles and magnetic dipole radiation (a radio pulsar), and may either increase or decrease (i.e. spin up or spin down) through accreting matter from the companion star (x-ray pulsar in a binary system). If the companion star is sufficiently massive to evolve into a giant star and overflow its Roche lobe, it is possible for the neutron star to be spun-up into a pulsar once more by accreting matter at the expense of the orbital angular momentum of the binary system. In a high-mass binary system the companion star will also explode as a supernova, resulting in a second neutron star. Depending on this second supernova the neutron stars may stay as a binary system or become a disrupted system. In a low-mass binary system the mass from the companion star is transferred to the pulsar (which will be spun up), and the remaining companion star becomes a white dwarf star – a pulsar-white dwarf binary system.

After the discovery of the first millisecond pulsar (Backer et al. 1982), there was an interest in observing globular clusters for millisecond pulsars. This was because the pulsars inside the clusters were believed to be old neutron stars that had been ‘spun up’ to short rotation periods by the accretion of matter from a companion star. This process results in a change of the cluster’s angular momentum (Alpar et al. 1982). The large populations of stars in the cores of globular clusters were then postulated to increase the possibility of a neutron star capturing an ordinary star to form an X-ray binary (Fabian et al. 1975). Lyne et al. (1987) discovered the first pulsar observed in such clusters, a 3 ms period pulsar in M27, and many more pulsars have since been discovered in globular clusters (see Lyne 1992, Manchester 1993 for details).

Globular clusters are collections of stars that orbit around a galactic core and

1: INTRODUCTION

are usually found in the galactic halo. The number of stars contained within a globular cluster is higher, and the stars are much older, than for open (and other types of) clusters found in the galactic disk. About a third of the known globular cluster pulsars are within the globular cluster 47 Tucanae (de Lacaille 1757). As 47 Tucanae is nearby, massive and dense, this cluster has been a good candidate for the detection of spun-up pulsars (Manchester et al. 1990, Manchester et al. 1991). The pulsars in 47 Tucanae are labeled B0021-72C to B0021-72M.

Even though the stars in globular clusters are low-mass stars (of the order of $1 M_{\odot}$), the large number of stars (around 10^8) in 47 Tucanae means that many will be close to our LOS to each pulsar, and hence will contribute to the Shapiro delay in pulsar timing. This dense stellar population, therefore, has a dual effect; (i) it increases the likelihood for the generation and observation of spun-up pulsars and, (ii) it infers a gravitational (Shapiro) delay to the pulsar timing.

While the first effect has been investigated thoroughly (as described above) the second effect has been largely ignored. The lack of knowledge of how stars affect pulsar timing will, to a degree, limit the precision at which millisecond pulsars in globular clusters can be timed. Analysis of high precision pulsar timing observations may result in the detection of gravitational waves (GW), and therefore how much effect this Shapiro delay has on pulsar timing needs to be investigated.

Gravitational waves

General Relativity (GR) predicts that when there is an acceleration in a non-axially symmetric pulsar (i.e. a pulsar with a small ‘bump’ on its surface at the Equator), it will lose energy in the form of quadrupolar gravitational radiation (and higher multipoles). The radiation propagates outwards from the pulsar in the form of gravitational waves (GWs), which are distortions (ripples) of space-time and separable from (familiar) non-propagating gravitational fields in regions where the static field is weak (Roos 2003, Thorne 1987). This radiation has not

yet been directly observed, and will require sensitive measuring instruments, such as GEO600, LIGO (Laser Interferometer Gravitational-wave Observatory), LISA (Laser Interferometer Space Antenna) and Virgo (the French-Italian interferometric detector), as theory predicts that it is extremely weak.

The metric strain from gravitational waves affects pulsar timing, and as a result pulsars can be used to detect an isotropic, stochastic gravitational wave (GW) background (Detweiler 1979). In such cases, many thousands (or millions) of GW sources are added together producing a spectrum that is dominated by low frequency GWs. However, in the pulsar timing procedure the lowest frequency GWs are subtracted because it is necessary to fit for the period (P) and period derivative (\dot{P}) of the pulsar. The result is called the pulsar timing residual. The strongest signals that are left have periods that are close to our data-span. The stochastic GW background therefore is an effect that may compete with the Shapiro delay in pulsar timing.

Jenet et al. (2005) showed that in order to detect low frequency ($f_g \sim 10^{-9}$ Hz) GW signals, pulsars need to be timed to a precision of $10 \mu\text{s}$ (10^{-5} s) over a time span of ~ 5 years. To date, Pulsar Timing Arrays (PTA), such as the Parkes Pulsar Timing Array (PPTA), have data spanning approximately four years with root-mean-square timing residuals of around 0.1 to $1 \mu\text{s}$ (Zurb Adami et al. 2010). It is expected that timing residuals studies will continually improve with new observing systems and improvements made in signal processing (Hobbs et al. 2009).

The question one can ask is then “To what extent do the stars close to the LOS from the pulsar contribute to the Shapiro delay?” This will be answered in this thesis. In order to determine the effect of Shapiro delay, let us first investigate the Shapiro delay itself.

1.1 Shapiro delay and Gravitational lensing

The magnitude of the Shapiro delay produced by the stars surrounding pulsars should be considered in the context of gravitational lensing. Here follows a brief introduction to gravitational lensing.

Gravitational lensing (Einstein 1936) occurs when a massive body passes between a source and an observer. The gravity of the intervening mass distorts the space-time around it resulting in a deflection of light from the source. Zwicky (1937) proposed that massive objects, such as a cluster of galaxies, could act as gravitational lenses. This was confirmed by Walsh et al. (1979) by the discovery of the twin quasar Q0957+561. The two quasars have identical spectra, implying that these are actually two images of the same source.

Gravitational lensing can be separated into three categories: strong-, weak- and micro-lensing. Strong lensing is where the gravity of a very large mass object ($\sim 10^{10} M_{\odot}$ and larger), such as a galaxy, produce an effect large enough to form multiple images (arcs and Einstein rings) that are clearly visible. Weak lensing occurs when the gravitational effect is a lot smaller and it is necessary to analyze a large number of sources to find any signs of distortion. From these distortions it is possible to reconstruct the mass distribution, especially that of dark matter in the universe, and so this type of lensing is used to test cosmological parameters (e.g. Λ -CDM models). Micro-lensing is lensing where there is no resolved distortion but a change in the amount of light received from a source. When an object passes across the LOS of a bright object, such as a quasar, the bending of light due to the gravitational field results in several distorted and unresolved images combining to give the observed magnification. This allows for the detection of fainter objects, and so micro-lensing is used to study the galactic population of objects such as brown dwarfs, neutron stars, and also detecting extrasolar planets. Gravitational lensing as a whole is not frequency dependent.

This thesis will use ideas of gravitational lensing to obtain the gravitational

time delay, known as the Shapiro delay. Each star ($\sim 1 M_{\odot}$) has its own gravitational potential and will impart a time delay in the pulse TOA. The potentials of every star combine together to form a ‘total’ potential both along and across the LOS. From this total potential the Shapiro delay can be obtained. It is important to note that, for lensing by a large number of very small masses ($\sim 1 M_{\odot}$), the light signals may encounter scattering and scintillation effects (For a good review of electromagnetic scintillation see Rickett 1977 or Deguchi and Watson 1986 and references therein), in addition to being simply bent by gravitational lensing.

Gravitational lensing by low mass ($\sim 1 M_{\odot}$) objects is not a new concept (see Wex et al. 1996, Walker 1996 and references therein), neither is the application of gravitational time delays to pulsars and pulsar timing (Krauss and Small 1991 (hereafter KS91), Larchenkova and Doroshenko 1995, Larchenkova and Kopeikin 2006, Larchenkova and Lutovinov 2007, and Hosokawa et al. 1999). While previous works have concentrated on determining the value of the Shapiro delay, this thesis will focus more on determining the rate of change of Shapiro delay. This is because the Shapiro delay itself cannot be observed directly, whereas it *is* possible to observe some changes in the Shapiro delay. The change in the Shapiro delay arises from stellar motion within the globular cluster. Previous works indicated that the Shapiro delay does not change much over time, however they do not give the magnitude of this change. This value will be determined in this thesis. Determining how much effect this change in Shapiro delay will have on pulsar timing allows for the introduction of another correction term in Equation 1.2, allowing for the possibility of reducing timing noise, as well as improving the chances for detecting gravitational waves.

KS91 and Larchenkova and Doroshenko (1995) both investigated the *relative*² time delay between two images, as this is easier to model (the constraints are observable) compared with the *absolute*² time delay. KS91 assumes that even if lensed images cannot be resolved spatially, the light pulses of the lensed images

²See Section 2.10 for detailed description of these terms.

1: INTRODUCTION

may be resolved in time. The primary application of micro-lensing in KS91 is the determination of mass distribution in galaxies. Larchenkova and Doroshenko (1995) claimed that there was a lensing event in the timing residuals of one pulsar, PSR B0525+21, caused by a $330 M_{\odot}$ black hole. The observed timing residuals were obtained by fitting the Shapiro delay parameters onto a model (least-square fit of the pulsar spin and astrometric parameters, as well as the parameters that describe the time delay in a gravitational mass field). The observed residuals and the predicted delay curve do not fit very well (Larchenkova and Doroshenko 1995, Figure 1), suggesting that this interpretation of results may be unrealistic.

Walker (1996) was the first to comment that, if pulsars were gravitationally lensed, the lens had to be very close to the LOS between the Earth and the pulsar. Additionally, Walker (1996) also concluded that even though the gravitational (Shapiro) time delay might be large, it would not change much in time (termed “stochastic Shapiro delay”) (see Hosokawa et al. 1999). These results had been confirmed by Siegel et al. (2007) and Siegel (2008) (hereafter SE07 and SE08, respectively), and Wex et al. (1996) as follows: Wex et al. (1996) uses lensing events in pulsar timing to detect supermassive black holes (SMBH) in the centres of galaxies. Such a lensing event will not be detected unless the lens mass crosses the LOS (Pulsar-Earth axis). In addition, Wex et al. (1996) also suggest that lensing events (in pulsar timing) could be used to determine the mass distributions of galaxies. The interstellar medium however has an effect on the observed pulsar properties (such as dispersion, scattering) resulting in large timing uncertainties. Both SE07 and SE08 tried to determine the dark matter substructure in globular clusters, as lensing events in pulsar timing should be able to probe masses less than $10^6 M_{\odot}$. The two papers state that the probability of observing such a “transit” is very small, however, as (i) there is a large sample size of millisecond pulsars both in the near (within 1 kpc) field, (ii) instrument sensitivity is constantly improving, and (iii) the gravitational effects are able to be separated from other effects, it might be possible to observe a transit event.

Since the lens has to be close to the LOS, the lensing optical depth (i.e. the probability of detecting such a lensing event) is very low, between 0.1 and 1 event per year (Jetzer et al. 1998), which is not surprising. This has resulted in searches elsewhere, mostly in globular clusters (Wex et al. 1996, Larchenkova and Lutovinov 2007), as globular clusters have a very high stellar density in their cores, meaning that there is more stellar mass that could act as lenses.

1.2 Thesis outline

In this thesis, the equations for the Shapiro delay and the change in Shapiro delay for the stars in the globular cluster will be derived in Chapter 2, as they are new concepts and are not present in past literature. In Chapter 3 a globular cluster, with properties similar to that of 47 Tucanae, is simulated using a Monte-Carlo (MC) method to determine the change in Shapiro delay. This change in the Shapiro delay will be called the **Shapiro noise** throughout this thesis. The Shapiro noise will have the following definition: Shapiro noise is the Shapiro delay variation from one or an ensemble of stars over the whole observed period as a continuous function of time. In Chapter 4 this term will be added to the pulsar time of arrival as the only noise term, and then subtracted from the TOA (not using least-squares fitting) to determine the magnitude of the timing residuals. In Chapter 5 the MC simulation will then be modified to include actual pulsar positions and velocities in 47 Tucanae. In Chapter 6 a more realistic model of the observed stellar distribution is presented. In Chapter 7 the total star count of the cluster will be increased to 10^8 stars, to reflect a more realistic model for the globular cluster 47 Tucanae. Finally, Chapter 8, the effect of gravitational acceleration will be introduced to the simulation in order to determine how both this, and the Shapiro delay, affect timing residuals.

1: INTRODUCTION

Part II

Background and Theory

2

Gravitational Lensing

In this section the basics of gravitational lensing are discussed. For a more in-depth review of gravitational lensing, see Schneider et al. (1992) (hereafter SEF) and Schneider (2006).

Using gravitational lensing, the time delay inferred by an intervening mass is derived from first principles. The components of the time delay – geometric and gravitational – are then investigated separately and a comparison made between them. This is done to determine if one component is more dominant than the other, indicating that the time delay equation can be simplified to using just one of the components. As it will be shown in Section 2.5 the time delay can indeed be simplified to only investigating the gravitational (Shapiro) time delay, as the geometric term is sufficiently small that it can be neglected. Finally a short analysis on how both the geometric and gravitational time delay components affect light curves from a pulsar is given.

2.1 History and General Relativity

Michell (1784), and later Soldner (1801), used Newtonian gravitational theory to calculate that light propagating around a spherically symmetric mass M would be deflected by an angle $\hat{\alpha}_N = 2GM/(c^2\xi)$, where G is Newton's constant of

gravity, and ξ is the impact parameter (perpendicular distance between the light path and the centre of the spherically symmetric mass) of the incoming light ray. General Relativity predicts a similar result, but a factor of 2 larger (Einstein 1915),

$$\hat{\alpha} = \frac{4GM}{c^2\xi} = \frac{2R_S}{\xi}, \quad (2.1)$$

where $R_S = \frac{2GM}{c^2}$ is the Schwarzschild radius of the mass.

The term ‘lens’ was first used by Lodge (Lodge 1919). Lodge also commented that the gravitational field does not “act as a lens, for it has no focal length”. Lodge then discussed the similar relationship between refractive index and radial distance (from the centre of a lens) for the deflection of light by gravity. Eddington (1920) was the first person to suggest that multiple images would occur if there was good alignment between two stars.

Einstein (1936) calculated how a foreground star affected the deflection of light from the background star, and also determined that the flux density of the images would change with different configurations of the source, lens and observer. An image could be highly magnified if the three were well aligned, although Einstein stated that “there is no great chance of observing this phenomenon”, based on the fact that the image separation would be too small to be resolved by the optical telescopes at that time.

Zwicky however published two papers (Zwicky 1937a and Zwicky 1937b) where he considered “extragalactic nebulae” (galaxies) as lenses and images would be resolvable with telescopes. In Zwicky (1937a) it was shown that “extragalactic *nebulae* offer a much better chance than *stars* for the observation of gravitational lens effects”. Zwicky estimated the deflection angle of a nebula and investigated the formation of ring-shaped images, and also calculated the total flux (and magnification) and then went further and claimed that,

“the discovery of images of nebulae which are formed through the gravitational fields of nearby nebulae would be of considerable interest

for a number of reasons.

1. It would furnish an additional test for the general theory of relativity.
2. It would enable us to see nebulae at distances greater than those ordinarily reached by even the greatest telescopes. Any such *extension* of the known parts of the universe promises to throw very welcome new light on a number of cosmological problems.
3. The problem of determining nebulae masses at present has arrived at a stalemate ... Observations on the deflection of light around nebulae may provide the most direct determination of nebular masses.”

In Zwicky (1937b) it was estimated that “provided that our present estimates of the masses of *cluster nebulae* are correct, the probability that nebulae which act as gravitational lenses will be found becomes practically a *certainty*.” Zwicky investigated photographic plates and estimated that around 1/400 of the total area on the plates were covered by nebula, and when he included the effect of gravitational focusing he concluded that in “around one in about one hundred nebulae the ring-like image of a distant nebula should be expected, *provided* that the chosen nebula has an apparent angular radius smaller than the angles through which light is deflected on grazing the surface of this nebula.”

In these two papers Zwicky proved the importance of gravitational lensing, however it took nearly four decades for the discovery of a multiply imaged quasar (QSO 0957+561) by a massive foreground lensing galaxy (Walsh et al. 1979).

Radio astronomy allowed for more theoretical work on gravitational lensing, notably by Refsdal (1964). Refsdal gives a full description of how a point mass produces a gravitational lens, and the concept of time delay between two images, due to the different light travel times for each image. In particular, Refsdal showed

that it was possible to use geometrical optics (see “thin lens approximation” later on) when considering gravitational lensing (Schneider et al. 1992, Nakamura and Deguchi 1999).

2.2 Basic lens equation

In this section the fundamental relationships of gravitational lensing – the (linear and radial) distance relationships between the observer, lens and source – will be determined. Figure 2.1 shows how the configurations of the observer, lens and source can produce images (one above of the source and another below – not shown).

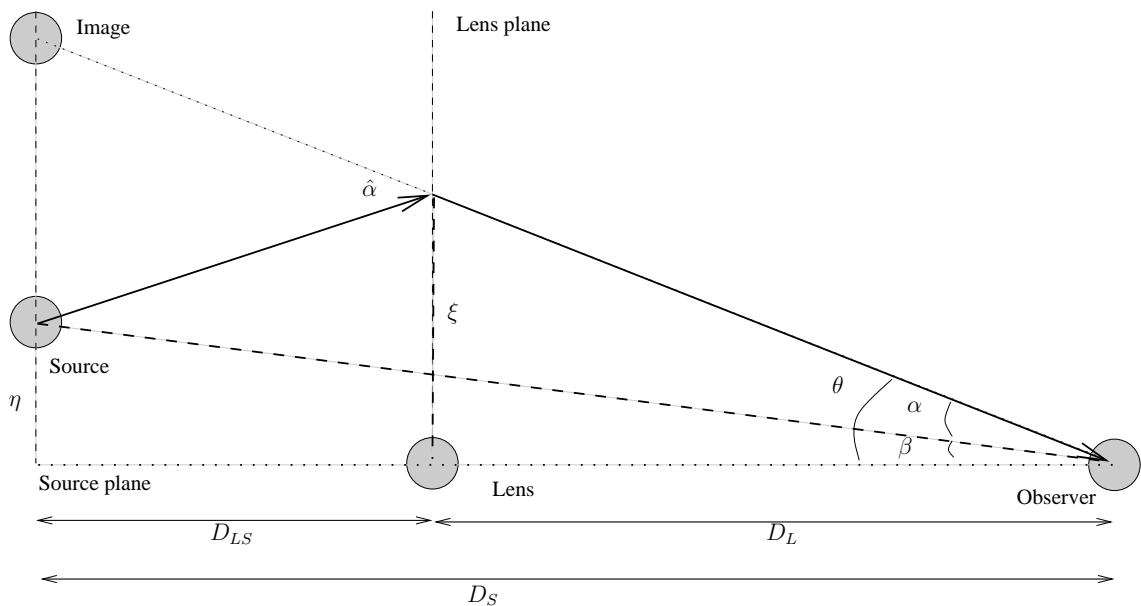


Figure 2.1: Simple gravitational lensing diagram. The thick solid line indicates the lensed trajectory of the light ray.

If there was no lens at distance D_L , the path the light ray would follow is the dashed line. In Figure 2.1 this dashed line subtends the optical axis (the dotted line) at an angle β .

Introducing a mass at a distance D_L results in the deviation of the light path

of the source at a distance $D_S \cos \beta$. Assuming that there are no other masses close to the LOS and if the size of the lens is far smaller than the distances D_L and D_S , the light rays coming from the source can then be approximated as two straight light rays with a ‘kink’ near the lens, even though the actual light rays are smoothly curved around it. This is the “thin-lens” approximation. The magnitude and direction of this ‘kink’ is determined by the deflection angle $\hat{\alpha}$ as described in Equation 2.1,

$$\hat{\alpha} = \frac{4GM}{c^2} \frac{1}{\xi}, \quad (2.2)$$

where ξ is the impact parameter, which is the minimum distance between the lensed trajectory of light and the distance to the lens in the lens plane. This value is assumed to be much greater than the Schwarzschild radius, i.e. $\xi \gg R_S \equiv 2GMc^{-2}$ (Weinberg 1972).

The lens equation relates the actual position of the source to its observed position on the sky. As shown in Figure 2.1, the source- and lens planes are defined as planes perpendicular to the LOS at a distance of the source and the lens, respectively. Let η be the distance between the source and the optical axis on the source plane. The source plane is perpendicular to the optical axis. Using the small angle approximation (such that $\sin \hat{\alpha} \approx \hat{\alpha} \approx \tan \hat{\alpha}$) η^1 is given by,

$$\eta = \xi' - D_{LS}\hat{\alpha}, \quad (2.3)$$

where ξ' is the projection of the impact parameter ξ on the source plane, so $\xi' = \frac{D_S}{D_L}\xi$. Furthermore, from the small angle approximation ξ and η can be approximated to

$$\eta = D_S\beta \quad \text{and} \quad \xi = D_L\theta, \quad (2.4)$$

where θ is the angle between the light from the image to the optical axis, and β is the angle between the light ray from the source and the optical axis. Substituting

¹This is a different η from that used in Chapter 1 to describe refractive index.

into the above equation:

$$D_S\beta = \frac{D_S}{D_L}D_L\theta - D_{LS}\hat{\alpha}, \quad (2.5)$$

$$\Rightarrow \beta = \theta - \frac{D_{LS}}{D_S}\hat{\alpha}. \quad (2.6)$$

The relationship between the angles can also be determined from Figure 2.1,

$$\beta = \theta - \alpha(\theta) \quad (2.7)$$

$$\Rightarrow \alpha(\theta) = \frac{D_{LS}}{D_S}\hat{\alpha}. \quad (2.8)$$

Using this relation, along with Equation 2.1 and $\xi = \theta D_L$, means that β can be re-written as

$$\beta = \theta - \frac{D_{LS}}{D_S D_L} \frac{4GM}{c^2 \theta}.$$

For the special case of $\beta = 0$, θ is then given by,

$$\theta = \sqrt{\frac{4GM}{c^2} \frac{D_{LS}}{D_S D_L}}. \quad (2.9)$$

This equation is a special case when the source, lens and observer are exactly aligned ($\beta = 0$). This is defined as the Einstein radius θ_E . Rearranging and substituting for θ_E in Equation 2.7,

$$\beta = \theta - \frac{\theta_E^2}{\theta}, \quad (2.10)$$

which has two solutions (θ_1 and θ_2) relating to the image positions on the source plane

$$\theta_{1,2} = \frac{1}{2} \left(\beta \pm \sqrt{\beta^2 + 4\theta_E^2} \right). \quad (2.11)$$

The equation above shows that there are two solutions of θ and they have the opposite sign. Physically, this means that the images are on opposite sides of the unlensed image (the image of the source that would be observed, had it not been lensed).

2.3 Multiple images and Fermat's principle

Let us now characterize the light ray passing from the pulsar to the observer using Fermat's principle (Schneider 1985, Kovner 1990, Perlick 1990). Fermat's principle states that a light ray travelling between two points takes the path that can be crossed in the shortest amount of time. From Figure 2.2, let S be an event and l a (time like) world line. The light ray will travel from S and arrives at l at time τ . The light ray will travel along γ such that

$$\delta\tau = 0. \quad (2.12)$$

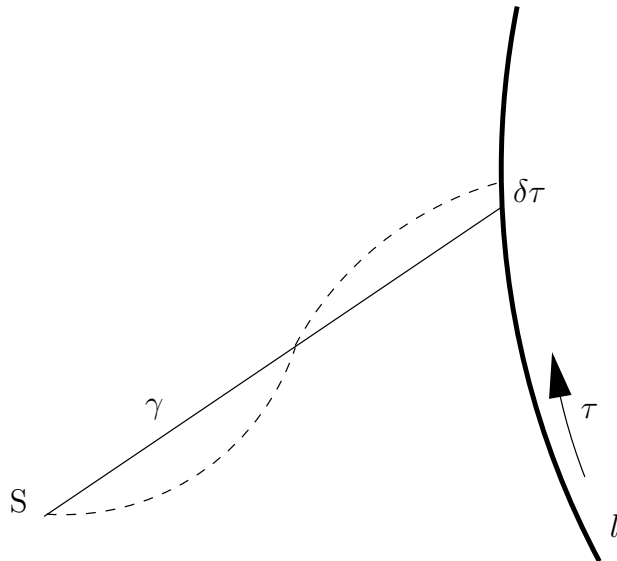


Figure 2.2: Geometry of Fermat's principle. Image taken from SEF.

The arrival time τ of a light ray γ is not only a stationary value but also a minimum (Perlick 1990). In other words Fermat's principle states that light rays travel the shortest path possible (through the gravitational potential). See Kovner (1990) and Perlick (1990) for details.

Let us now define the Fermat potential $\tau(\theta, \beta)$ (see SEF) as

$$\tau(\theta, \beta) = \frac{1}{2}(\theta - \beta)^2 - \psi(\theta), \quad (2.13)$$

where ψ is the (effective) gravitational potential of the intervening mass/lens. This is a function of the lens plane position θ , the source position β , and

$$\nabla \tau(\theta, \beta) = 0 \quad (2.14)$$

is equivalent to Equation 2.7. As it has been shown in SEF, $\tau(\theta, \beta)$ is the travel time of a light ray starting at source position β on the source plane, passing through the lens plane at angular position θ and arriving at the observer. As a result the Fermat potential describes the additional time taken for a light ray to travel ‘around’ a matter distribution, compared to the light travel time directly from a source. This is synonymous with the time delay resulting from the presence of an intervening mass. Let us therefore use the Fermat potential to determine the time delay.

Burke (1981) proved a theorem on the number of images produced by a gravitational lens: for a gravitational lens with a smooth surface mass density that decreases faster than $\frac{1}{|\theta|}$ for $|\theta| \rightarrow \infty$, the number of images corresponding to an extrema will be the number of saddle points plus 1, provided the source is not at a caustic. This means that there will always be an odd number of images, and at least one of the images will correspond to a minimum value of τ . The odd image will likely be very faint. For the simple system of one source (pulsar) and one point mass lens (star) that will be used in this thesis, this means there will be three images predicted by Burke’s theorem - two observable images and one very faint image. The positions and the magnifications of the two observable images will be used in this thesis; the third faint image will be ignored.

2.4 Time delay equation

Substituting Equation 2.13 into Equation 2.14, Fermat’s principle can be re-written as (Schneider 1985)

$$\nabla \left(\frac{1}{2}(\theta - \beta)^2 - \psi(\theta) \right) = 0. \quad (2.15)$$

The time delay between the perturbed and unperturbed light path is then given by (see Schneider 1985)

$$\Delta t = \tau_{\text{geom}} + \tau_{\text{grav}} = \frac{1}{c} \frac{D_L D_S}{D_{LS}} \left(\frac{1}{2} (\theta - \beta)^2 - \psi(\theta) \right), \quad (2.16)$$

where the first part inside the brackets is the geometric component (time delay induced by the extra path length (EPL) of the light ray due to the presence of a lens), and the second part is the gravitational component (time delay induced by the lens mass). For a point mass lens (an assumption valid for a small lens mass) the gravitational potential term ψ is given below, as well as the deflection angle (see Narayan and Bartelmann 1996 for derivations of both terms)

$$\psi(\theta) = \frac{D_{LS}}{D_L D_S} \frac{4GM}{c^2} \ln |\theta| \quad (2.17)$$

$$\alpha = \nabla \psi \quad (2.18)$$

$$\alpha = \frac{D_{LS}}{D_L D_S} \frac{4GM}{c^2} \frac{1}{|\theta|}. \quad (2.19)$$

Substituting $\theta - \beta$ with the deflection angle α and separating the geometric and gravitational components, the time delay equation can be modified to

$$\Delta t = \frac{1}{c} \frac{D_L D_S}{2D_{LS}} (\alpha(\theta))^2 - \frac{1}{c} \frac{4GM}{c^2} \ln |\theta| \quad (2.20)$$

for each image. For the relative time delay, this is the time difference between two images (labeled + and -). Using the identity $2 \ln |x| \equiv \ln |x^2|$, the relative time delay equation becomes

$$\begin{aligned} \Delta t &= \frac{1}{c} \left(\frac{D_L D_S}{2D_{LS}} \alpha_-^2 - \frac{2GM}{c^2} \ln |\theta_-^2| \right) \\ &\quad - \frac{1}{c} \left(\frac{D_L D_S}{2D_{LS}} \alpha_+^2 - \frac{2GM}{c^2} \ln |\theta_+^2| \right) \end{aligned} \quad (2.21)$$

$$\Rightarrow \Delta t = \frac{1}{c} \left(\frac{D_L D_S}{2D_{LS}} [\alpha_-^2 - \alpha_+^2] + \frac{2GM}{c^2} \ln \left| \frac{\theta_+^2}{\theta_-^2} \right| \right). \quad (2.22)$$

This equation is consistent with KS91 Equation 4, if one assumes the redshift $z_L \rightarrow 0$ and sets $c = 1$.

2.5 Comparison of geometric and gravitational time delay

Let us now investigate how the geometric and gravitational time delay vary with ξ , the impact parameter. This is necessary in order to determine the magnitudes of each term, which may lead to simplifying the time delay to one term - as it may be that the other term is negligibly small.

Substituting for α in Equation 2.2 and using the small angle approximation $\theta = \frac{\xi}{D_L}$ (see Figure 2.2) it is possible to re-write Equation 2.20 as

$$\begin{aligned}\Delta t &= \frac{1}{c} \frac{D_L D_S}{2 D_{LS}} \left[\frac{D_{LS}}{D_L D_S} \left(\frac{4GM}{c^2} \right)^2 \frac{D_L}{\xi} \right]^2 - \frac{1}{c} \left(\frac{4GM}{c^2} \right) \ln \left| \frac{\xi}{D_L} \right| \\ &= \left(\frac{4GM}{c^2} \right)^2 \frac{D_{LS} D_L}{2c D_S} \frac{1}{\xi^2} + \frac{4GM}{c^3} \ln \left| \frac{D_L}{\xi} \right|\end{aligned}\quad (2.23)$$

Let us now simulate a star ($1 M_\odot$) situated on the plane halfway between the source ($D_S = 5130$ pc), and the observer (so $D_L = D_{LS} = \frac{1}{2}D_L$). Figure 2.3 shows how the time delay varies as a function of the impact parameter of such a star.

The geometric term dominates very close to the LOS and decreases rapidly with increasing ξ . The gravitational term varies less sharply. At $\sim 8 \times 10^{-6}$ pc the two terms become identical. It is also the turning point where the gravitational term starts to dominate over the geometric term. In most cases the star has a larger impact parameter ($> 10^{-6}$ pc, see Section 2.8) such that the approximation that the gravitational term is *always larger* than the geometric term can be made. Also, since the geometric term is so small this means that the light ray does not deviate significantly from the optical axis, and so the light path can be approximated as being straight (i.e. a straight line approximation) along the optical axis. From here onwards, the geometric term is ignored when calculating the time delay – only the gravitational (Shapiro) delay is included.

It needs to be stressed that the above is true only for low-mass ($1 M_\odot$) stars in

2.5: COMPARISON OF GEOMETRIC AND GRAVITATIONAL TIME DELAY

globular clusters. For larger masses, the geometric term will be more likely to be dominant in the Shapiro delay, as the geometric term is a function of M^2 and the gravitational term is a function of M . de Marchi and Paresce (1995) had shown from observations that the mass function (derived from the luminosity function) of the stars in 47 Tucanae has a power-law slope of gradient $\alpha \simeq 1.5$ in the range $0.3 M_{\odot}$ to $0.55 M_{\odot}$. McClure et al. (1986) determined the slope of the mass function in the range $0.5 M_{\odot}$ to $0.8 M_{\odot}$. Because of this, and for mathematical convenience, it seems reasonable to set the mass of all the stars in the simulated 47 Tucanae to M_{\odot} .

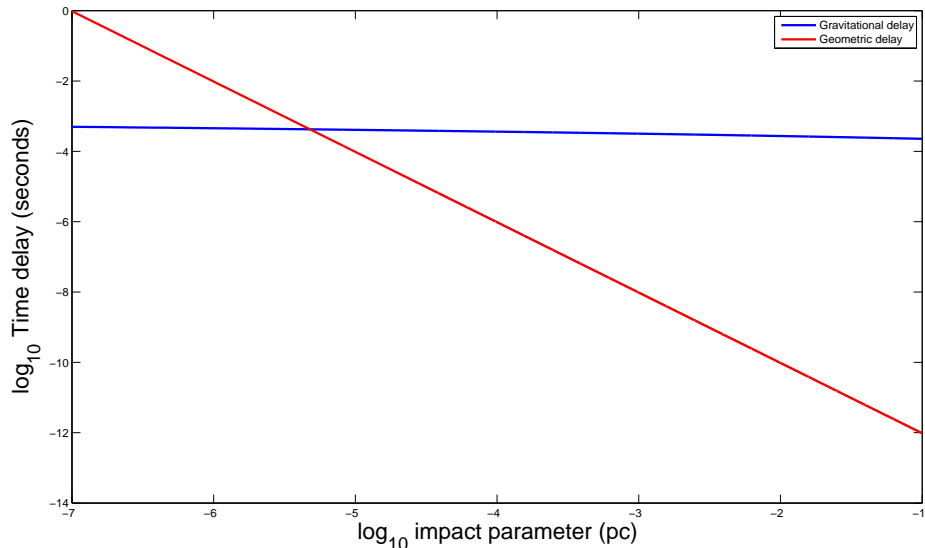


Figure 2.3: Comparison between the geometric and gravitational components of the time delay as a function of impact parameter, when a lens is situated halfway between observer and source (pulsar) positioned 5130 pc away. Note this plot is a log-log plot.

2.6 Shapiro time delay

Section 2.5 showed that the geometric term can be ignored for a low-mass star when determining the time delay. Let us now derive the full expression for the Shapiro delay equation (the second term in Equation 2.20).

Figure 2.1 depicts the configuration when the source is moving along the source plane. In this thesis, the source (pulsar) is initially assumed to be stationary – pulsar velocities will be added later on – with the lens transiting across the LOS. This means that the configuration has to be modified, as shown in Figure 2.4.

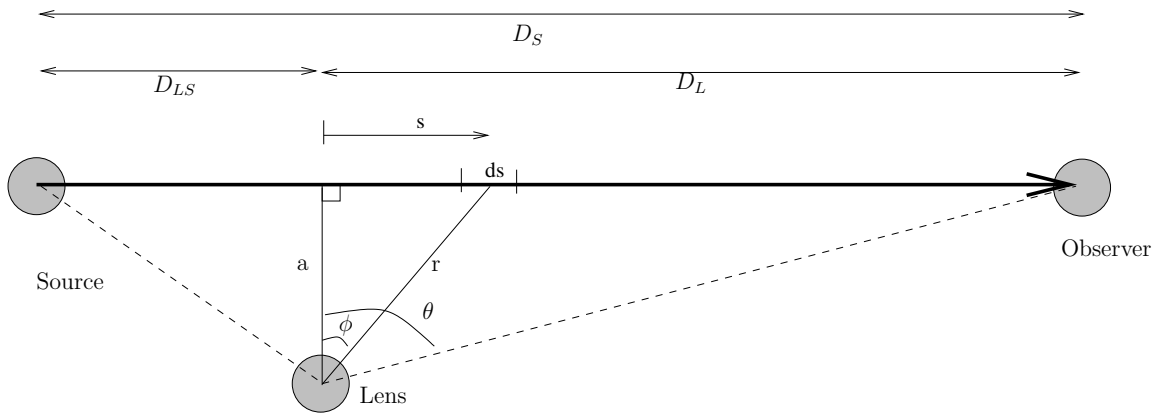


Figure 2.4: Shapiro time delay. This figure is a re-arranged version of Figure 2.1 where the lens moves instead of the source.

Assuming that the light travels straight along the LOS in Figure 2.4 (See Section 2.5), this means that we can define two trigonometric identities,

$$\tan \phi = \frac{s}{a}, \quad \cos \phi = \frac{a}{r}. \quad (2.24)$$

The gravitational time delay for gravitational lensing (the Shapiro time delay) is defined as (Reasenberg et al. 1979)

$$t_{\text{Sh}} = -\frac{2}{c^3} \int_0^{D_S} \varphi \, ds, \quad (2.25)$$

where $\varphi = -\frac{GM}{|r|}$ is the Newtonian gravitational potential. Substituting for φ the Shapiro delay becomes

$$t_{\text{Sh}} = \frac{2GM}{c^3} \left(\int_{s=0}^{s=D_L} \frac{1}{|r|} ds + \int_{D_L}^{D_S} \frac{1}{|r|} ds \right), \quad (2.26)$$

where the two integrals correspond to the path before and after the lens along the LOS. From Figure 2.4 the first term can be written

$$\int_0^{D_L} \frac{ds}{r} = \int_\theta^0 \frac{d\phi}{\cos \phi}$$

which integrates to

$$\begin{aligned} \int_\theta^0 \frac{d\phi}{\cos \phi} &= \left[\ln |\sec \phi + \tan \phi| \right]_\theta^0 \\ &= \ln \left| \frac{\sqrt{D_L^2 + a^2}}{a} + \frac{D_L}{a} \right|. \end{aligned} \quad (2.27)$$

The second integral integrates to

$$\int_{D_L}^{D_S} \frac{ds}{r} = \ln \left| \frac{\sqrt{a^2 + D_{LS}^2}}{a} + \frac{D_{LS}}{a} \right|. \quad (2.28)$$

The total Shapiro delay is the sum of these two logarithms. Using the small angle approximation, the terms in the logarithms become the same, and so the Shapiro time delay can be re-written as

$$t_{\text{Sh}} = \frac{2GM}{c^3} \ln \left| \frac{4D_L(D_S - D_L)}{\xi^2} \right|, \quad (2.29)$$

where the substitutions $a = \xi$ and $D_{LS} = D_S - D_L$ have been made. This equation is consistent with the equations in SE07 and SE08 and is similar to Equation 2.23 since $D_S - D_L = D_{LS} = D_L$ (lens halfway between source and observer) and when using the identity $2 \ln |x| \equiv \ln |x^2|$. The factor of 4 in Equation 2.29 arises due to a slight change in the definition of ξ from Equation 2.23 – in Equation 2.29 ξ represents the distance between the lens and the LOS, in Equation 2.23 ξ is the image location in the lens plane (see Figure 2.1).

2.7 Complete equation for Shapiro delay

Section 2.6 considered the case where the lens is in front of the source. Let us now determine the case where the lens is behind the source, as shown in Figure 2.5.

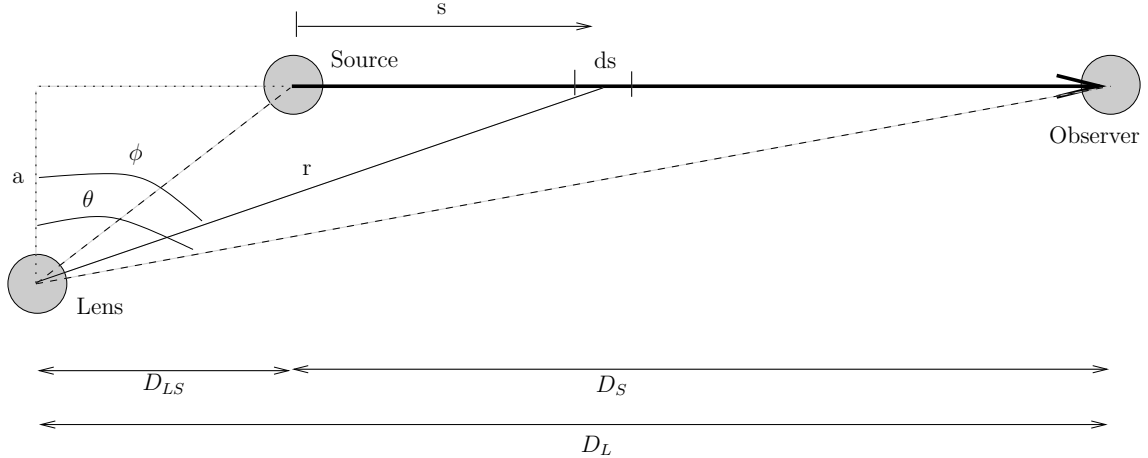


Figure 2.5: Shapiro time delay. This figure is a re-arrangement of Figure 2.4 where the lens is behind the source.

Using Figure 2.5 the two integrals in Equation 2.26 are integrated in a similar manner as shown in Section 2.6. The first term integrates out as,

$$\begin{aligned} \int_0^{D_L} \frac{ds}{r} &= \int_\theta^0 \frac{d\phi}{\cos \phi} \\ &= \left[\ln |\sec \phi + \tan \phi| \right]_\theta^0 \\ &= \ln \left| \frac{\sqrt{D_L^2 + a^2}}{a} + \frac{D_L}{a} \right|, \end{aligned} \quad (2.30)$$

which is the same result as Section 2.6. However the second term integrates to

$$\int_{D_L}^{D_S} \frac{ds}{r} = \ln \left| \frac{\sqrt{a^2 + D_{LS}^2}}{a} - \frac{D_{LS}}{a} \right|. \quad (2.31)$$

The minus sign is due to the change in direction of D_{LS} . As a result, the complete Shapiro delay equation can be written as:

$$t_{Sh} = \frac{2GM}{c^3} \left(\ln \left| \frac{\sqrt{D_L^2 + a^2}}{a} + \frac{D_L}{a} \right| + \kappa \ln \left| \frac{\sqrt{a^2 + D_{LS}^2}}{a} + \kappa \frac{D_{LS}}{a} \right| \right) \quad (2.32)$$

where $\kappa = \frac{D_{LS}}{|D_{LS}|}$. This full expression for the Shapiro delay will be used in the Monte-Carlo (MC) simulation in Chapter 3. From here onwards, D_{LS} will be replaced with ρ , i.e. $\rho = D_{LS}$, and a will be replaced with the impact parameter ξ , such that $\xi = a$.

2.7.1 Sensitivity of the Shapiro delay to ξ and ρ

Figure 2.6 shows the Shapiro delay as a function of impact parameter, ξ . The Shapiro delay is very sensitive to ξ , the distance in the plane perpendicular to the LOS. The function tends to infinity at $\xi = 0$, as at this configuration the star is directly between the pulsar and an observer. Theoretically this also produces an Einstein ring around the star. For very small values of ξ , the geometric term is larger than the gravitational term (see Figure 2.3) so in this region the straight line approximation breaks down. The function decays rapidly as ξ increases from $\xi = 0$ pc to $\xi \sim 10$ pc, but the function resembles a linear decay function at greater impact parameters.

Figure 2.7 shows the Shapiro delay as a function of ρ , the distance between the star and the pulsar along the LOS. A negative value for ρ means that the star is behind the pulsar due to the orientation used when deriving the equation. In the “classical” case this region is unexplored, and so not included in the Shapiro delay. The inclusion of this region results in the changes in sign, and the introduction of a factor κ when deriving the full Shapiro delay equation. As it is shown in Figure 2.7 the negative ρ region has a very small effect. This is due to a smaller portion of the gravitational potential of stars being integrated along the LOS, compared to stars in front of the pulsar. At $\rho = 0$, a theoretical situation when the pulsar and the star are at the same distance from the observer, the magnitude of the Shapiro delay is determined by ξ , the second logarithmic term in Equation 2.32 is zero. The star has a larger effect once it is positioned between the observer and the pulsar (i.e. $\rho > 0$) and has a maximum at halfway between

the observer and the pulsar, namely at $D_L = \frac{1}{2}D_S$.

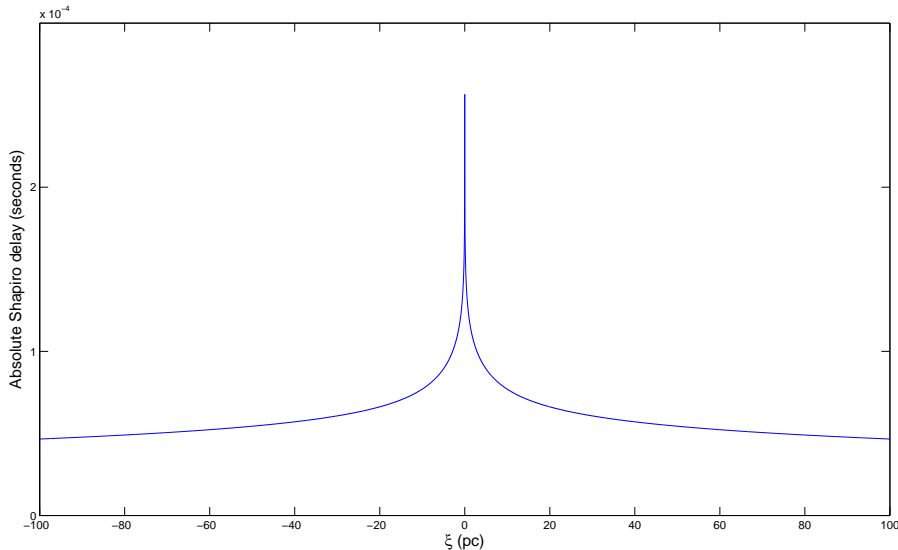


Figure 2.6: The Shapiro delay as a function of ξ , the impact parameter. The function has been truncated at $\xi = 0$ since the function becomes infinite at this point.

2.8 Probability of observing a ‘Shapiro event’

So far, the full expressions for the Shapiro delay equation have been derived. It was also shown that generally the geometric term is negligible and that the straight-line approximation can be made for the light path from the pulsar.

Let us now investigate the probability of detecting a ‘Shapiro event’ – an event where the star is situated close enough to the LOS that it produces a measurable change in time delay over some interval. The closer the star is to the LOS, the larger the Shapiro delay (Figure 2.6). The probability of detecting a lensing event should then be determined by how close a star will be to the LOS. Since the Shapiro delay is symmetric around the LOS (as ξ is measured from the LOS regardless of its orientation) this means that the probability is equivalent to that

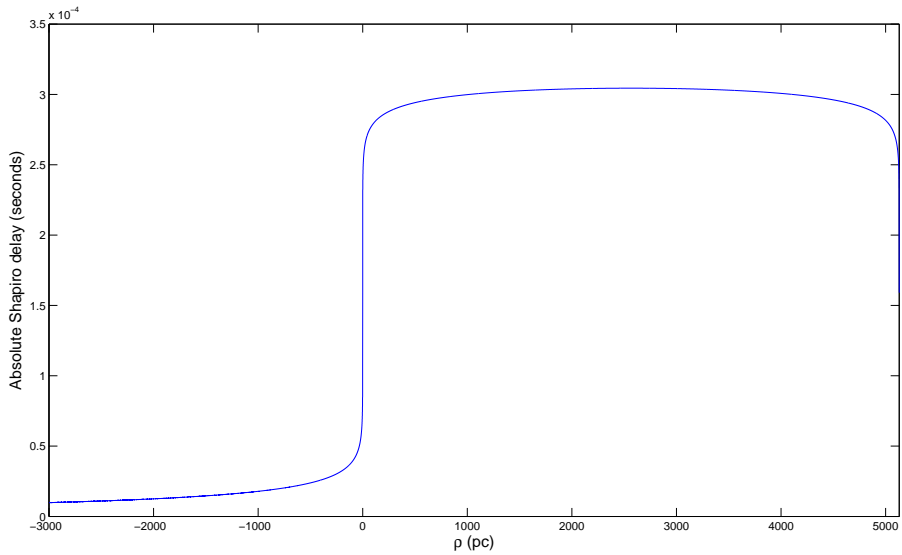


Figure 2.7: The Shapiro delay as a function of ρ , the distance along the LOS. At all values of ρ , $\xi = 1$ pc. $\rho < 0$ indicates that the star is behind the pulsar; $\rho = 0$ is when the pulsar and the star have the same distance along the LOS; $\rho > 0$ indicates that the star is between the pulsar and the observer.

of finding a star in a cylinder around the LOS with a radius r_{det} , where r_{det} is the detection radius (see Figure 2.8).

2.8.1 Detection radius

For simplicity, let us assume the globular cluster is a sphere of uniform (stellar) density with a pulsar situated at the center as shown in Figure 2.8. This globular cluster contains N_0 stars and has a radius r_S . Within this cluster there is a cylinder with cross sectional radius r_{det} containing N stars. When assuming that the cluster and the cylinder have the same stellar density, the fraction of the total

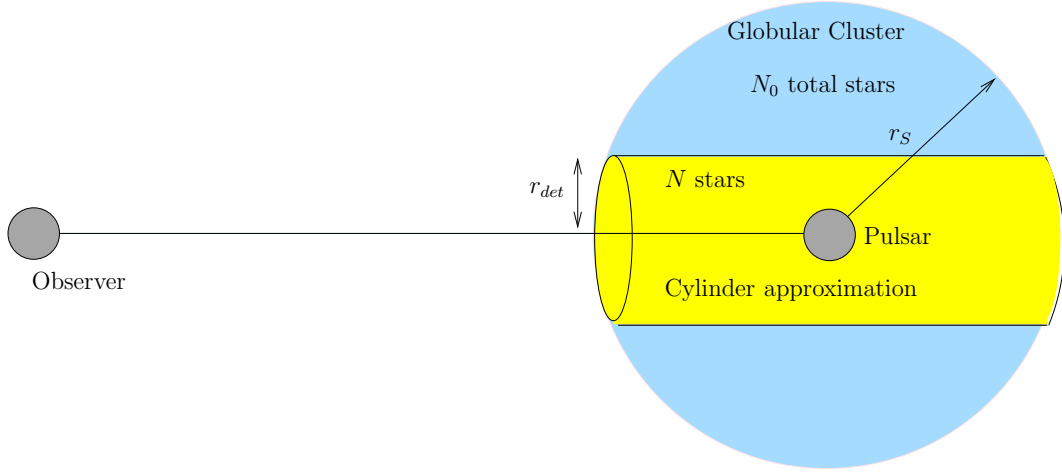


Figure 2.8: Configuration to determine the detection radius, r_{det} for a globular cluster.

number stars contained in this cylinder is then given by

$$\begin{aligned} \frac{N_0}{\frac{4}{3}\pi r_S^3} &= \frac{N}{\pi r_{\text{det}}^2 r_S} \\ \Rightarrow \frac{N}{N_0} &= \frac{\pi r_{\text{det}}^2 r_S}{\frac{4}{3}\pi r_S^3} = \frac{3}{4} \left(\frac{r_{\text{det}}}{r_S} \right)^2 \end{aligned} \quad (2.33)$$

where N is the number of stars detected. For $N_0 \sim 10^8$ (the number of stars in the globular cluster 47 Tucanae) and $r_S = 19$ pc, the radius necessary to find just one star ($N = 1$) is then

$$\begin{aligned} r_{\text{det}} &= \left(\frac{4}{3} \frac{(19 \text{ pc})^2}{10^8} \right)^{1/2} \\ &= 2.1939 \times 10^{-3} \text{ pc}. \end{aligned} \quad (2.34)$$

This is the distance of the closest star to the LOS. At this distance from the LOS the magnitude of Shapiro delay is very large, as this is very close to the “spike” at $\xi = 0$ pc in Figure 2.6. Also, at this distance the gravitational delay dominates (Figure 2.3). If one took a globular cluster that is more concentrated at the core, for example $r_S = 1$ pc, the detection radius is then

$$\begin{aligned} r_{\text{det}} &= \left(\frac{4}{3} \frac{(1 \text{ pc})^2}{10^8} \right)^{1/2} \\ &= 1.1547 \times 10^{-4} \text{ pc}. \end{aligned} \quad (2.35)$$

As a comparison, the distance traveled by a star in one year at a speed of 100 km s⁻¹ is 1.023×10^{-4} pc. Even with such a dense core, the gravitational term is larger than the geometric term at r_{det} .

The values of r_{det} indicate that a Shapiro event is highly likely (if not certain) to occur. This then means that there will be a Shapiro delay, and it will affect pulsar timing. From Figure 2.6 the magnitude of the Shapiro delay from this single star is of the order of 10^{-4} seconds. This would have an effect on pulsar timing precision, as described in Chapter 1. When a Shapiro event occurs, the time of arrival of every pulse will be offset by this amount, and therefore the pulse profile would also be shifted/offset by this amount. Within the model, however, this offset will be subtracted from the pulse TOA as it is a constant effect on all pulsar TOAs and as a result, the pulsar timing residuals will not be influenced by a Shapiro event (or delay), nor is it possible to measure the value of the Shapiro delay.

The above statements is true only for ‘static’ cases, where the star’s position does not change over (observation) time. In some configurations even a small change in stellar position will have a large effect on the magnitude of the Shapiro delay, as shown in Figure 2.6 and Figure 2.7. Such a change in Shapiro delay *is* a measurable quantity.

2.9 Change in Shapiro delay

Section 2.8 showed that the stellar density inside the globular cluster makes it highly likely that a Shapiro event will occur, as there will be stars close ($\sim 10^{-4}$ pc) to the LOS producing a large ($\sim 10^4$ s) Shapiro delay. Such a large Shapiro delay will affect pulsar timing. However, this (static) Shapiro delay is not an observable (and measurable) quantity, as it will affect all the pulses in the same way. On the other hand, stars and pulsars move within globular clusters. Stellar and pulsar velocities change the positions of the stars and pulsars, respectively,

resulting in a *change* in the Shapiro delay. This change in Shapiro delay *is* observable in pulsar timing, as this variable changes over time, and offsets the pulsar time of arrival in different ways for every pulse.

Let us revisit Figure 2.6 to investigate how the Shapiro delay changes with the impact parameter ξ . The change in Shapiro delay is analogous to the difference in time delay between two points on the function in Figure 2.9. Since stellar motion is small (of the order of tens of kilometers per second) the total distance the star moves across the sky is small compared to the distance from the LOS, the fractional change in distance between these two points is very little, and as a result the change in Shapiro delay is also small. This linear change can then be approximated to the tangent of the curve shown in red in Figure 2.9 (linear approximation). This also means that over time the motion of the star can be approximated to linear “cuts” (or slits) across the sky.

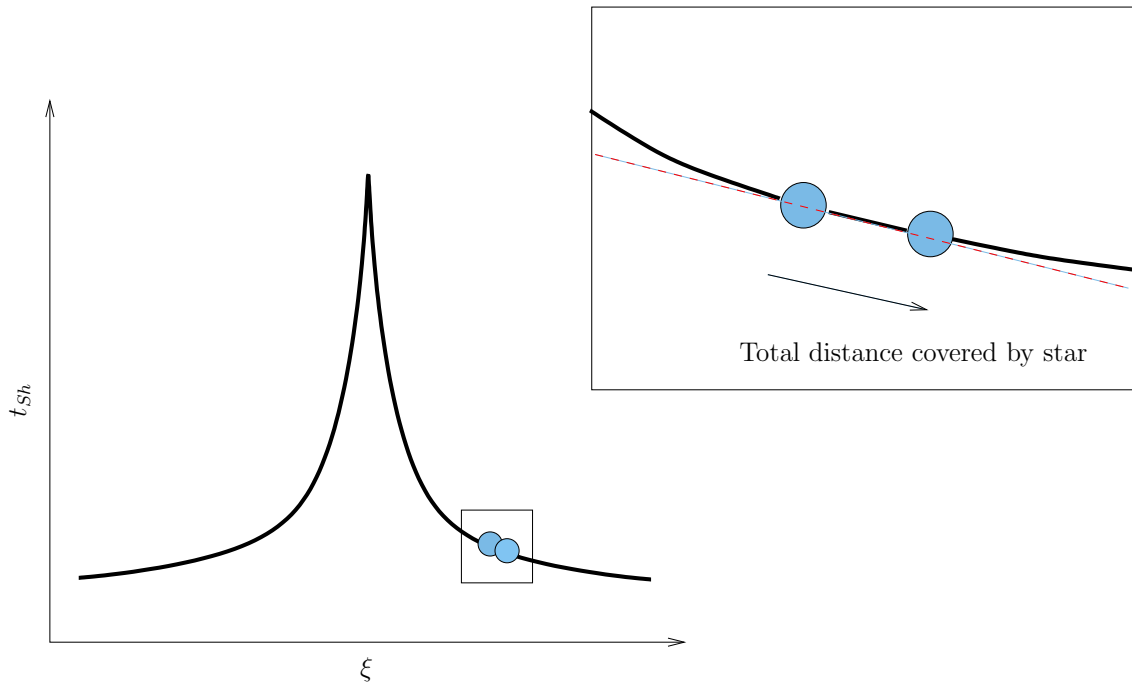


Figure 2.9: Change in Shapiro delay.

Even though the change in Shapiro delay is small for one star, the cumulative

effect of an ensemble of stars may produce a change in Shapiro delay large enough to be observed. This is what will be investigated in the following chapter by simulating a globular cluster.

2.10 Pulsar light curves

Before proceeding to the simulations, let us investigate how the time delay affects pulsar light curves. Since strong lensing produces multiple images there will be many image pulses observed in the pulsar TOA, however they will have different amplitudes, and arrive at different times. This only happens in the region where the geometric term dominates, and the straight line approximation of the light path is no longer valid – the star has to be extremely close to the LOS (order 10^{-9} pc), so the chance of observing this situation is very low.

Even though the probability of observe the geometric time delay of a pulse is very small, what will the pulse profile of a lensed pulsar look like? To answer this question, let us assume the pulse intensity $\mathcal{P}(t)$ is of the form of a Gaussian distribution,

$$\mathcal{P}(t) = \mathcal{P}_0 \exp\left(-\frac{1}{2} \left[\frac{t - t_0}{\sigma}\right]^2\right), \quad (2.36)$$

where \mathcal{P}_0 is the maximum flux of the light pulse (initially set to 1 for the unlensed case), and σ^2 is the variance (the measure of the width of the distribution) of the pulse. The pulses from the lensed images arrived at a delayed time t_0 , where $t_0 = 0$ is taken from the unlensed image.

The \mathcal{P}_0 values for the two images were found by computing the magnification factor of each lensed image. In general, specific intensity is conserved, therefore the (angular) magnification determines the flux. The solid angle magnification is determined by (see SEF)

$$\mu = \frac{\theta}{\beta} \frac{d\theta}{d\beta}. \quad (2.37)$$

In order to solve for $\frac{d\theta}{d\beta}$, it is necessary to use Equation 2.7, and to produce a Jacobian matrix \mathcal{A} that describes the lens mapping at a certain point in the sky as

$$\mathcal{A} = \frac{\partial \beta}{\partial \theta} = \left(\delta_{ij} - \frac{\partial \alpha_i(\theta)}{\partial \theta_j} \right). \quad (2.38)$$

Let us define the potential as (see SEF)

$$\psi_{ij} = \frac{\partial^2 \psi}{\partial \theta_i \partial \theta_j}. \quad (2.39)$$

The dimensionless surface mass density (or the convergence) κ and the external shear $\gamma (\equiv \gamma_1 + i\gamma_2)$ can be defined as

$$\psi_{11} + \psi_{22} = 2\kappa \quad (2.40)$$

$$\gamma_1(\theta) = \frac{1}{2} (\psi_{11} - \psi_{22}) \quad (2.41)$$

$$\gamma_2(\theta) = \psi_{12} = \psi_{21}. \quad (2.42)$$

Therefore the Jacobian matrix can be re-written as

$$\mathcal{A} = \left(\delta_{ij} - \frac{\partial^2 \psi(\theta)}{\partial \theta_i \partial \theta_j} \right) = \begin{pmatrix} 1 - \kappa - \gamma_1 & -\gamma_2 \\ -\gamma_2 & 1 - \kappa + \gamma_1 \end{pmatrix}. \quad (2.43)$$

The determinant of this Jacobian matrix is the inverse of the magnification,

$$\mu = \frac{1}{\det \mathcal{A}} = \frac{1}{(1 - \kappa)^2 - \gamma^2}, \quad (2.44)$$

where the equation has also been written in terms of κ and γ .

Re-writing Equation 2.7

$$x_{\pm} = \frac{1}{2} \left(u \pm \sqrt{u^2 + 4} \right) \quad (2.45)$$

where $x = \frac{\theta}{\theta_E}$ and $u = \frac{\beta}{\theta_E}$.

The magnification μ can now be written as (see Schneider 2006 for details)

$$\mu_{1,2} = \left(1 - \frac{1}{x^4} \right)^{-1} = \frac{u^2 + 2}{2u\sqrt{u^2 + 4}} \pm \frac{1}{2}. \quad (2.46)$$

The magnification of each image and the total magnification is given by

$$\mu_1 = \frac{u^2 + 2}{2u\sqrt{u^2 + 4}} + \frac{1}{2} \quad (2.47)$$

$$\mu_2 = \frac{u^2 + 2}{2u\sqrt{u^2 + 4}} - \frac{1}{2} \quad (2.48)$$

$$\mu_{\text{TOT}} = \mu_1 + |\mu_2| \geq 1. \quad (2.49)$$

Using the magnifications, the amplitudes of the two pulses are

$$\mathcal{P}_1 = |\mu_1| \times f_0 \quad (2.50)$$

$$\mathcal{P}_2 = |\mu_2| \times f_0. \quad (2.51)$$

From the above equations, the amplitude of the two pulses will not be the same as that of the unperturbed light pulse.

Let us now simulate light pulses (pulse $\sigma = 5 \times 10^{-6}$ s) from a pulsar 5130 pc away (distance to globular cluster 47 Tucanae), and a lens halfway between the pulsar and the observer. Figure 2.10 shows how the two light pulses (from the lensed images) compare to that from an unperturbed light pulse (directly from the source) with the presence of a lens at $\xi = 5 \times 10^{-6}$ pc. The unperturbed light pulse is the dashed line at time of arrival equal to zero – this is the light pulse expected from an unlensed source. Adding a lens produces two images (blue and red dotted lines), and the combined light pulse is shown as the solid black line.

From Section 2.2 and Section 2.4 it is possible to determine the magnitude of the time delays. For this particular configuration, $\beta = 9.999 \times 10^{-9}$ radians and the Einstein radius

$$\begin{aligned} \theta_E &= \sqrt{\frac{4GM}{c^2} \frac{D_{LS}}{D_S D_L}} \\ &= \sqrt{\frac{4GM_\odot}{c^2} \frac{2565 \text{ pc}}{5130 \text{ pc} \times 2565 \text{ pc}}} \\ &\sim 6.109 \times 10^{-9} \text{ rad.} \end{aligned} \quad (2.52)$$

From Equation 2.11 the two image positions are

$$\begin{aligned}
 \theta_1 &= \frac{1}{2} \left(\beta + \sqrt{\beta^2 + 4\theta_E^2} \right) \\
 &= \frac{1}{2} \left(9.999 \times 10^{-9} + \sqrt{(9.999 \times 10^{-9})^2 + (4 \times (6.109 \times 10^{-9})^2)} \right) \\
 &= 2.894 \times 10^{-8} \text{ rad}, \\
 \theta_2 &= \frac{1}{2} \left(\beta - \sqrt{\beta^2 + 4\theta_E^2} \right) \\
 &= \frac{1}{2} \left(9.999 \times 10^{-9} - \sqrt{(9.999 \times 10^{-9})^2 + (4 \times (6.109 \times 10^{-9})^2)} \right) \\
 &= -1.289 \times 10^{-8} \text{ rad}.
 \end{aligned}$$

θ_2 is negative because this image is below the optical axis. The absolute time delay of each image is then the sum of the geometric and gravitational time delay

$$\begin{aligned}
 t_{geom,1} &= \frac{1}{2c} \frac{D_{LS}}{D_L D_S} \left(\frac{4GM}{c^3} \right)^2 \frac{1}{\theta_1^2} \\
 &= 4.389 \times 10^{-5} \text{ s}, \\
 t_{grav,1} &= \frac{4GM}{c^3} \ln |\theta_1| \\
 &= 3.874 \times 10^{-4} \text{ s}, \\
 \Delta t_1 &= 4.389 \times 10^{-5} + 3.874 \times 10^{-4} = 3.935 \times 10^{-4} \text{ s}, \\
 t_{geom,2} &= \frac{1}{2c} \frac{D_{LS}}{D_L D_S} \left(\frac{4GM}{c^3} \right)^2 \frac{1}{\theta_2^2} \\
 &= 1.598 \times 10^{-5} \text{ s}, \\
 t_{grav,2} &= \frac{4GM}{c^3} \ln |\theta_2| \\
 &= 3.579 \times 10^{-4} \text{ s}, \\
 \Delta t_2 &= 1.598 \times 10^{-5} + 3.579 \times 10^{-4} = 3.739 \times 10^{-4} \text{ s}.
 \end{aligned}$$

The calculations predict that the second image arrives before the first image, and this is shown in Figure 2.10. The peaks of the images are offset due to the time delay, and the intensity amplitudes are determined by the magnifications (see above). The difference between the image peaks gives the (standard) ‘relative’ time delay investigated in the literature; the difference between the peak of the combined pulse and of the unlensed pulse is the ‘absolute’ time delay. It can be

shown that at this configuration the lensed pulse profile is completely different from the unlensed pulse. If the lens is sufficiently far away from the LOS, the solid and dashed lines will overlap, as this is equivalent to the star not having any effect on the pulse profile.

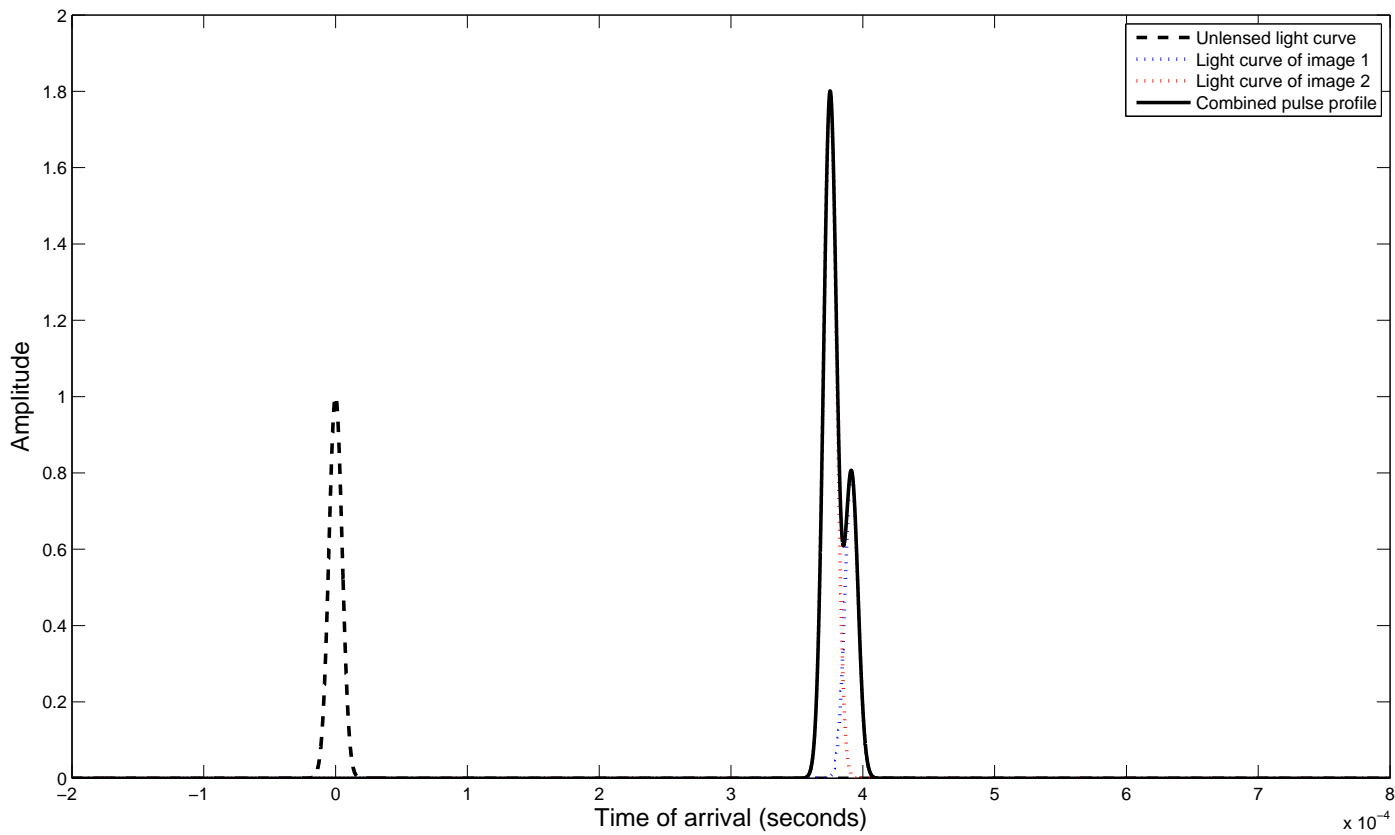


Figure 2.10: How time delay affects pulse profiles. In the above, $\xi = 5 \times 10^{-6}$ pc.

Figure 2.11 shows the pulse profile at different configurations. The top right figure is when the lens is furthest of the four configurations from the LOS. The two lensed images produce two peaks with the image closest to the source (image 1, blue line) producing the higher peak and a shorter time delay. As the lens moves closer to the LOS the relative time delay between the two imaged pulses decreases whilst the absolute time delay increases (Figure 2.11 top right). This continues until the lens is on the LOS, at which point there is infinite magnification (an Einstein ring), and there is no relative time delay but there is, however, an absolute time delay. Once it crosses the LOS the magnification falls (Figure 2.11 bottom left) but now the images are reversed – image 2 (red line) is now the closest. Finally if the lens is further away from the LOS the two image peaks are separated (Figure 2.11 bottom right).

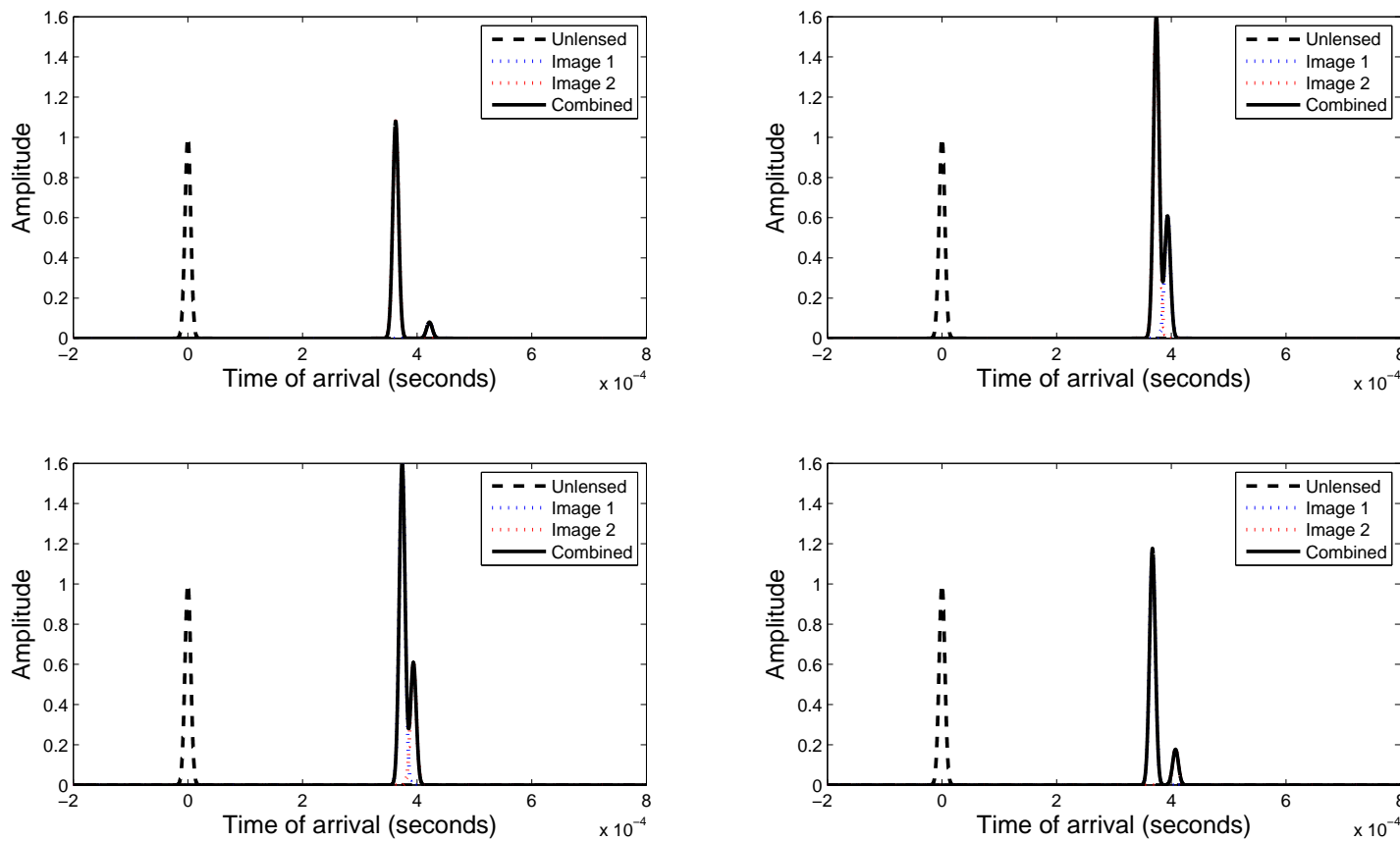


Figure 2.11: How time delay affects pulse profiles. In the above, $\xi = -2 \times 10^{-5}$ pc (top left), $\xi = -7.5 \times 10^{-6}$ pc (top right), $\xi = 7.5 \times 10^{-6}$ pc (bottom left), $\xi = 1.5 \times 10^{-5}$ pc (bottom right).

The peaks of both images will not be separable for a broad pulse profile, i.e. larger pulse σ . For example, Figure 2.12 and Figure 2.13 show the pulse profile for the same lensing configuration as Figure 2.10 but with a σ value that is ten times larger, namely $\sigma = 5 \times 10^{-5}$ s. In such a case, both peaks are ‘buried’ in the pulse profile, and the combined pulse profile looks similar to the unlensed image, albeit slightly larger in amplitude. As a result, Figure 2.13 shows that the geometric lensing event is undetectable for such a broad pulse profile unless careful measurements to detect the change in amplitude of the pulse are made.

The simulations shows how the light pulses change in the presence of a gravitational lens. However, in order to get such an effect the lens has to be positioned very close to the LOS and the probability of this happening is very small.

Let us determine the number of stars necessary in order to observe a geometric time delay. From Figure 2.3 the geometric time delay dominates the gravitational time delay at detection radius $r_{\text{det}} < 10^{-6}$ pc. From Equation 2.33 and using $r_S = 1$ pc, the total number of stars necessary in the globular cluster in order to detect one star that will produce a geometric time delay is $> 1.3 \times 10^{12}$ stars. This equates to a stellar density of approximately $3.1 \times 10^{11} M_\odot \text{ pc}^{-3}$. Both total stellar count and stellar density are far greater than those observed in globular clusters such as 47 Tucanae, and therefore the probability of observing the geometric time delay is very small for a globular cluster such as 47 Tucanae.

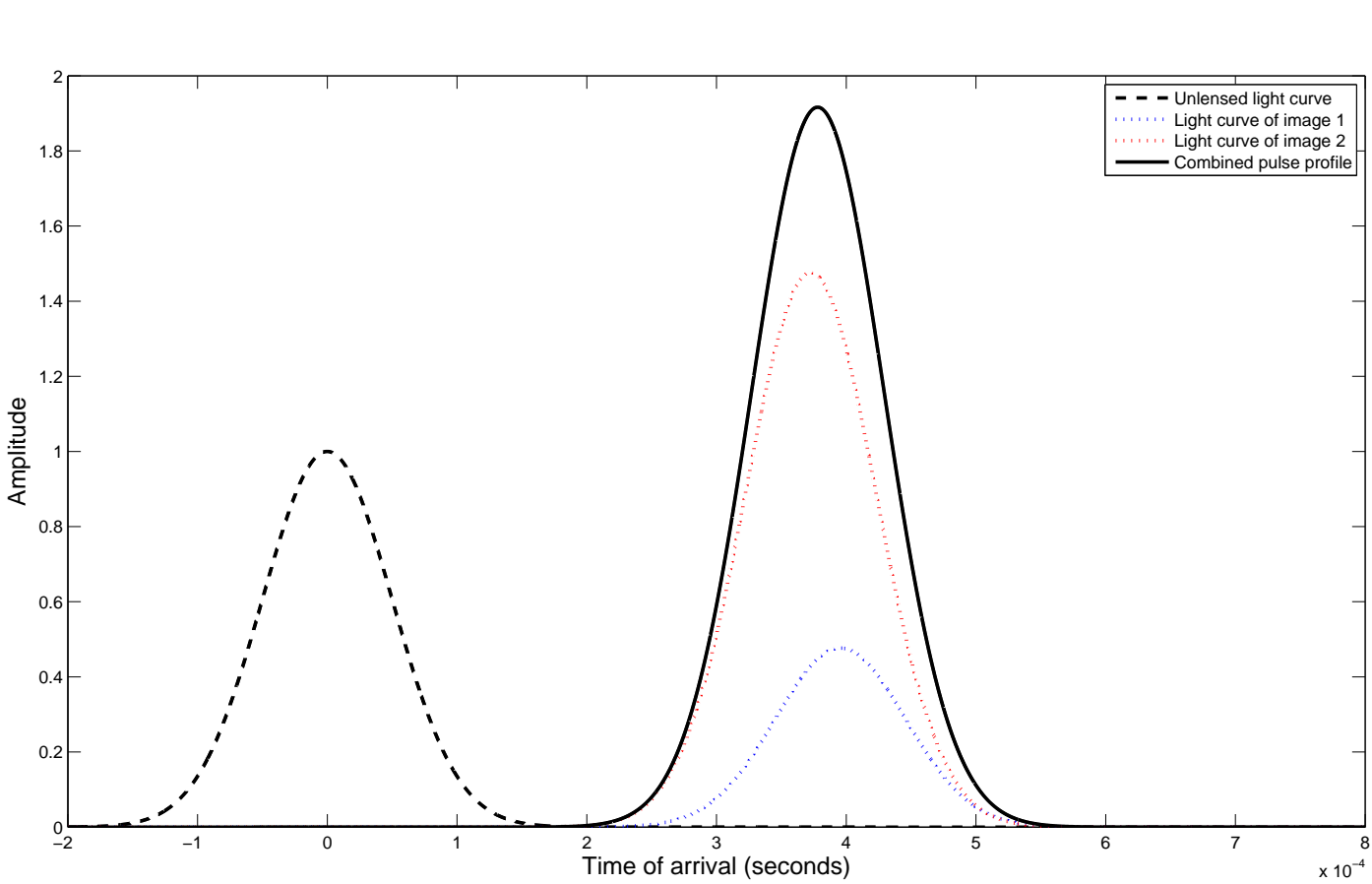


Figure 2.12: How time delay affects pulse profiles. In the above, $\xi = 5 \times 10^{-6}$ pc and $\sigma = 5 \times 10^{-5}$ s.

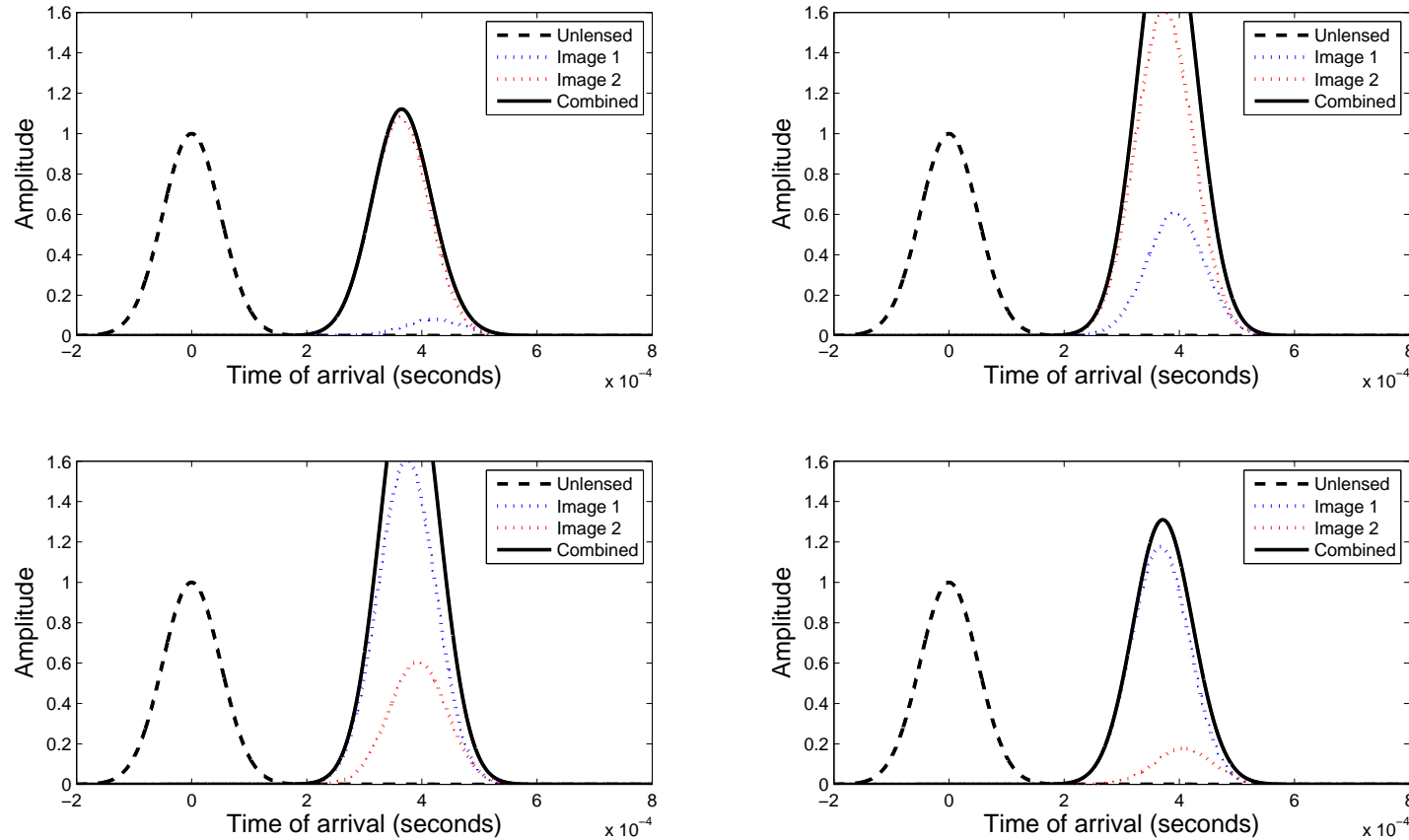


Figure 2.13: How time delay affects pulse profiles. In the above, $\xi = -2 \times 10^{-5}$ pc (top left), $\xi = -7.5 \times 10^{-6}$ pc (top right), $\xi = 7.5 \times 10^{-6}$ pc (bottom left), $\xi = 1.5 \times 10^{-5}$ pc (bottom right). For all light curves, $\sigma = 5 \times 10^{-5}$ s.

Part III

Globular Cluster Simulation

3

Globular Cluster Simulation

In the previous chapter it was shown that it was highly likely that a Shapiro event would have a measurable effect on pulsar timing for pulsars situated inside globular clusters, such as 47 Tucanae. In addition, the Shapiro delay itself is not an observable quantity, while the change in the Shapiro delay is. This section attempts to determine the magnitude of the change in the Shapiro delay over time for a typical globular cluster, as this quantity has not been previously determined.

In order to determine the change in Shapiro delay a simple globular cluster with a pulsar at the centre is constructed. The stellar distribution within the globular cluster used initially is that of a Gaussian sphere – a Gaussian distribution in all three Cartesian co-ordinates. This simple approach was adopted so that it was possible to produce an analytical and numerical prediction for the change in the Shapiro delay, followed by a comparison between the two approaches.

The analytical approach uses probability distribution functions (PDFs) to determine the likelihood of observing a change in the Shapiro delay, Δt_{sh} , from the distribution functions used to determine stellar positions and velocities. From the PDFs it is then possible to analytically deduce the variance of the change in Shapiro delay, $\langle(\Delta t_{\text{sh}})^2\rangle$ (if the expectation value is zero). For simple models such as a Gaussian sphere, the equations for the distributions are well-known, therefore it is possible to determine the PDFs and $\langle(\Delta t_{\text{sh}})^2\rangle$ analytically.

In the numerical approach a model was created to determine the Shapiro delay. This approach uses a Monte-Carlo (MC) simulation to randomly generate the stars along with their initial positions and velocities. From this, it was possible to move each star and to determine the Shapiro delay for every star. The mean squared change in the Shapiro delay per star, $\langle(\Delta t_{\text{sh}})^2\rangle$, was then determined by averaging the square of the Shapiro delay of every star.

The two approaches are independent of one another in determining the value of $\langle(\Delta t_{\text{sh}})^2\rangle$, the analytical method approaching from the PDF, whilst the numerical method makes the determination without using PDFs, therefore, as long as the initial conditions for both approaches are the same, it is possible to compare the results. This serves as a useful tool when checking whether the numerical simulation is producing results as expected by the analytical prediction, or otherwise.

The following sections describe the two different approaches in detail, and a comparison is made between the two approaches on some models. All the analytical expressions (for the 1D, 2D and 3D cases) is original work.

3.1 Analytical approach

The analytical approach determines the variance of the change in Shapiro delay, $\langle(\Delta t)^2\rangle$, using probability distribution functions (PDFs).

For a star generated inside the globular cluster described by a Gaussian sphere, the PDF describing the phase space co-ordinates of this star can be written as the product of its position and velocity distribution functions,

$$p(x, y, z, v_x, v_y, v_z) = p(x, y, z) p(v_x, v_y, v_z) \quad (3.1)$$

$$= p(x) p(y) p(z) p(v_x) p(v_y) p(v_z). \quad (3.2)$$

Each component is generated separately, this means that velocity and position distributions are independent. This assumption was made to simplify the ana-

lytical (and numerical) approach.

The Shapiro delay equation in Section 2.7 and Section 2.8, uses cylindrical polar co-ordinates (ρ, ξ, θ) . Therefore, we need to transform the co-ordinate system of the star from Cartesian to cylindrical polar in order to determine its Shapiro delay. The change in co-ordinate system is achieved by computing the appropriate Jacobian (see Figure 3.1). The cylindrical polar PDF describing the star's position and velocity is now

$$p(\rho, \xi, \theta, v_\rho, v_\xi, v_\theta) = p(x, y, z) \left| \frac{\partial(x, y, z)}{\partial(\rho, \xi, \theta)} \right| p(v_\rho, v_\xi, v_\theta) \left| \frac{\partial(v_x, v_y, v_z)}{\partial(v_\rho, v_\xi, v_\theta)} \right|, \quad (3.3)$$

where the terms in the modulus signs represent Jacobians, one to transform position co-ordinates, and the other to transform velocity co-ordinates. Since the

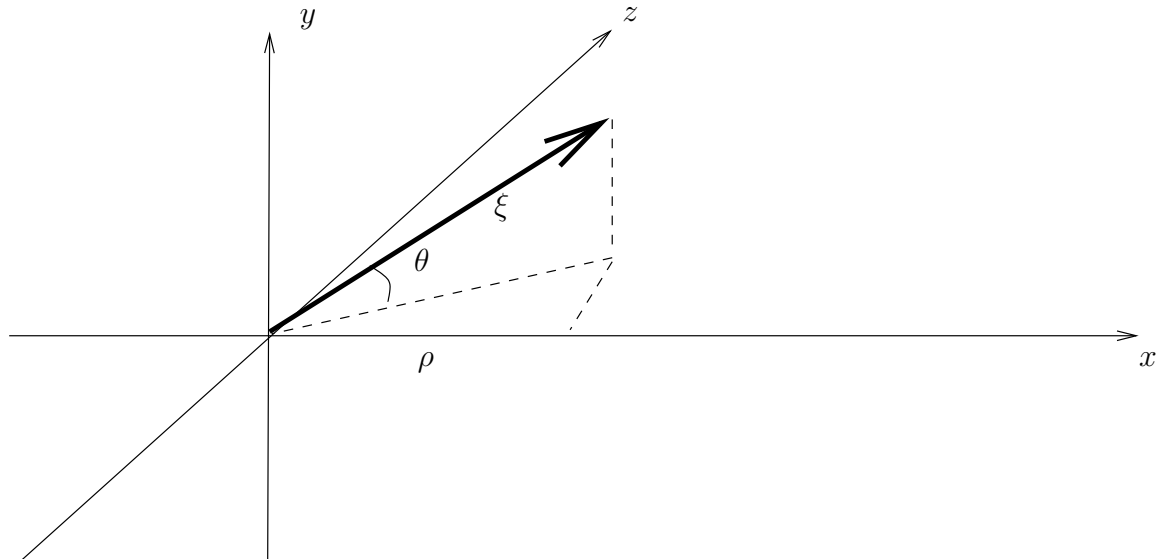


Figure 3.1: The relationship between the Cartesian co-ordinate system (x, y, z) and cylindrical polar co-ordinate system (ρ, ξ, θ) . The centre of the globular cluster (and pulsar position) is at the origin. The LOS is along the x-axis.

Shapiro delay is a function of (ρ, ξ, θ) , its change is dependent on the change in any of the three variables. The change in Shapiro delay is due to stellar motion affecting the position of the stars. The change, however, is not a large amount,

namely $\rho, \xi \gg vT$, where v is the stellar velocity in a particular direction, and T is the total time of the observation/simulation. From Section 2.9 the change in Shapiro delay can be approximated as a linear change in the variables,

$$\Delta t_{\text{sh}}(\xi, \rho, \theta) \simeq \frac{\partial t_{\text{sh}}}{\partial \xi} \Big|_{\xi_f} \Delta \xi + \frac{\partial t_{\text{sh}}}{\partial \rho} \Big|_{\rho_f} \Delta \rho + \rho \frac{\partial t_{\text{sh}}}{\partial \theta} \Big|_{\theta_f} \Delta \theta, \quad (3.4)$$

where the partial derivatives can be obtained from differentiating Equation 2.32. The third term, the dependence on θ can be ignored as the Shapiro delay equation is symmetrical around the LOS, and so only the dependence on ξ and ρ will be investigated. Also, from the linear approximation,

$$\Delta \xi = v_\xi T \quad \text{and} \quad \Delta \rho = v_\rho T, \quad (3.5)$$

as these variables describe the distance travelled by the star in a particular direction.

Equation 3.4 describes the relationship between the change in Shapiro delay, Δt_{sh} , with its co-ordinate system (ρ, ξ, θ) . It is possible to change one of the variables in Equation 3.1 to include the Δt_{sh} term, using another Jacobian. For example, if one uses the Jacobian,

$$J_{\Delta t_{\text{sh}}} = \left| \frac{\partial v_\rho}{\partial (\Delta t_{\text{sh}})} \right|, \quad (3.6)$$

the PDF can now be written as

$$\begin{aligned} p(\rho, \xi, \theta, \Delta t_{\text{sh}}, v_\xi, v_\theta) &= p(\rho, \xi, \theta, v_\rho, v_\xi, v_\theta) \left| \frac{\partial v_\rho}{\partial (\Delta t_{\text{sh}})} \right| \\ &= p(\rho, \xi, \theta, v_\rho, v_\xi, v_\theta) J_{\Delta t_{\text{sh}}}. \end{aligned} \quad (3.7)$$

To compute the probability density function for the change in Shapiro delay, Δt_{sh} , we require to marginalise over all other variables. After carrying out this marginalisation, $p(\Delta t_{\text{sh}})$ is then

$$p(\Delta t_{\text{sh}}) = \iiint \int p(\rho, \xi, \theta, \Delta t_{\text{sh}}, v_\xi, v_\theta) J_{\Delta t_{\text{sh}}} d\rho d\xi d\theta dv_\xi dv_\theta. \quad (3.8)$$

After integrating to obtain $p(\Delta t_{\text{sh}})$, $\langle (\Delta t_{\text{sh}})^2 \rangle$ is determined by

$$\langle (\Delta t_{\text{sh}})^2 \rangle = \int p(\Delta t_{\text{sh}}) (\Delta t_{\text{sh}})^2 d(\Delta t_{\text{sh}}). \quad (3.9)$$

Using the analytical approach, it is therefore possible to determine $\langle(\Delta t_{\text{sh}})^2\rangle$ from the position and velocity distributions used to generate a random star. Note that the analytical approach gives a $\langle(\Delta t_{\text{sh}})^2\rangle$ value for one star and one pulsar, situated at the centre of the globular cluster.

The assumption that the pulsar is positioned at the centre of the globular cluster and is stationary (i.e. no velocity components) may be a crude assumption, but by using this the problem is simplified by excluding additional constraints (and terms) from the analytical approach (Equation 3.8) and the numerical approach (additional initial conditions). To a first approximation, the assumption of a stationary pulsar at the centre of the globular cluster is valid to use for comparing the two different approaches.

3.2 Numerical approach

The analytical approach determines the variance of the change in Shapiro delay, $\langle(\Delta t_{\text{sh}})^2\rangle$, by using the position and velocity distributions. The numerical approach, on the other hand, will determine the variance by generating stars (position and velocity values) using these distributions, and then calculating the change in Shapiro delay of these stars.

For our simple model (distribution of stars in a globular cluster being approximated by a Gaussian sphere), the numerical approach will randomly generate a position value for a star using the Gaussian distribution. The stellar velocity is generated using a different Gaussian distribution. The Shapiro delay of this configuration is measured, then the star is ‘moved’ to its new position according to its velocity. Since the position of this star is different, a new value for the Shapiro delay is calculated at this configuration. The difference between the two Shapiro delay quantities is the change in Shapiro delay for that particular star. This simulation is repeated a large number of times, each time producing new position and velocity for the star, so that a large number (and range) of Δt_{sh} val-

3: GLOBULAR CLUSTER SIMULATION

ues is obtained. Using these values it was then possible to plot the distribution of Δt_{sh} for this one star-one pulsar configuration, which can be compared to the analytical approach for the same configuration.

The numerical approach simulated a globular cluster with the same dimensions as 47 Tucanae (5130 pc away, 38 pc across), with a stellar distribution described by a Gaussian sphere. The simulation was written using the programming software **MATLAB**. The distributions of the stellar position and motion were specified as Gaussian (`randn` function in **MATLAB**) for our simple model. The standard deviation, $\sigma = 5$ pc, for the stellar positions was determined such that the stars populate the entire 38 pc diameter of the globular cluster. This Gaussian sphere is not an accurate representation of the density profile of 47 Tucanae (see Chapter 6 for more details), however the analytical solution for the Gaussian sphere is less complex, and therefore more suitable for comparing the analytical and numerical approaches.

The σ for the velocity distribution was assumed to be 100 km s^{-1} as this was thought to be a sensible value. The observation time was chosen to be ten years noting the current longest pulsar timing observations, which is approximately 12 years. An observational cadence of 30 days was chosen to reduce computing time as simulating the TOA of every pulse for 3600 days would have taken too long. Six pulsars were also generated in a similar manner to the stars, but were originally at rest, so that in the simple model, the pulsar position does not change over time. Since pulsars are concentrated in the core of the globular cluster, the Gaussian distribution used to generate their position had a smaller σ than that of the stars. Table 3.1 shows the initial conditions used in the simulation.

For each star, a Gaussian distribution (using the conditions described above) was used to generate the positions (x, y, z) and the velocities (v_x, v_y, v_z). The pulsar positions were also generated using a different Gaussian distribution, however no velocity components were generated as the pulsars were assumed to be stationary throughout the simulation.

Variable	Quantity	GC variable	Quantity
Star mass	$1 M_{\odot}$	Distance to GC	5130 pc
$\sigma_{\text{star}} (x,y,z)$	5 pc	Diameter	38 pc
$\sigma_{\text{pulsar}} (x,y,z)$	1 pc	Number of Stars	100 000
$\sigma (v_x, v_y, v_z)$	$100 000 \text{ ms}^{-1}$	Number of Pulsars	6
Spacing Interval	30 days	Total observation time	3600 days

Table 3.1: Initial conditions for MC simulation

Once a star was created, its initial Shapiro delay was derived from Equation 2.32. Each star was then moved in increments of 30 days at its given speed, and a Shapiro delay of its new position was calculated. This was repeated for a total observation time of 3600 days, and then for 10^5 stars and six pulsars at the core of the globular cluster. The results of these calculations are shown in Figure 3.2.

Let us now repeat the definition of Shapiro noise (from Chapter 1): Shapiro noise is the Shapiro delay variation (from one or an ensemble of stars) over the whole observed period as a continuous function of time. This is the noise term that the Shapiro delay will add to the pulsar time of arrival equation, Equation 1.2. See Chapter 4 for further details.

Figure 3.2 shows that the Shapiro noise is different for every pulsar, as shown by different coloured lines. Due to the LOS being different for every pulsar, the stars contribute differently to the Shapiro delay for each one. In our simple model the magnitudes of the Shapiro noise appear to be similar for all six pulsars, suggesting that the number (and the separation) of stars along close to the LOS are similar. Figure 3.2 also shows that the Shapiro noise resembles that of a linear function. This result is not unexpected – positions of the stars do not change much, therefore the change in Shapiro delay (and hence the Shapiro noise) will be small (see Section 2.9). Figure 3.2 verifies that a linear approximation for the Shapiro noise use in the analytical approach is valid.

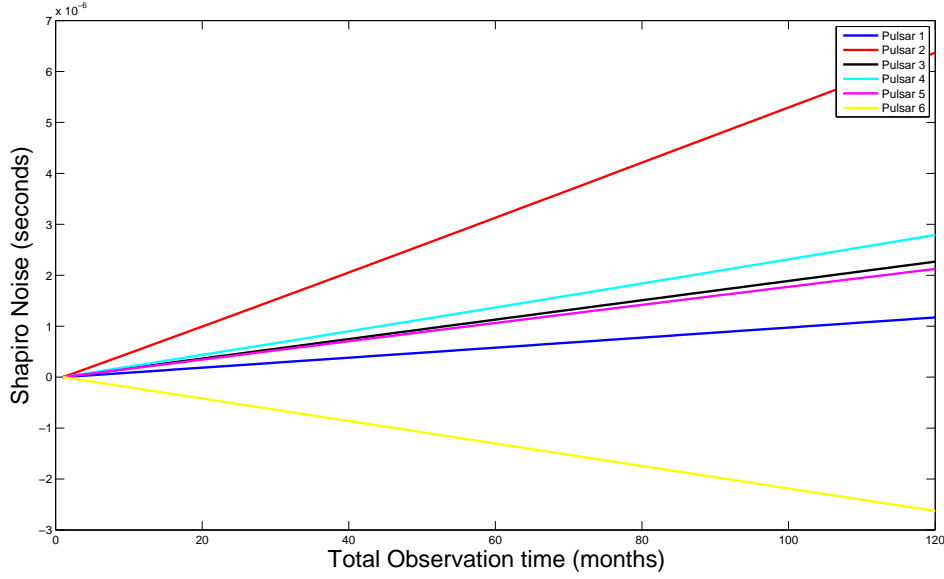


Figure 3.2: Shapiro noise for a mini globular cluster containing 6 pulsars in the core and 10^5 stars, over an observing period of 3600 days. The pulsars are randomly distributed near the center of the globular cluster, and the stars are distributed within the dimensions of the globular cluster. Note that in the simulation 1 month = 30 days.

The sign of the Shapiro noise is dependent on the motion of the star that has the largest contribution - if the star is moving away from the LOS the Shapiro delay decreases (hence negative Shapiro noise) and vice versa.

The magnitude of the Shapiro noise, Δt_{sh} , for 10^5 stars over a ten year observing period is $\sim 1 \times 10^{-6}$ s, dominated by a slope of $\sim 10^{-7}$ s yr $^{-1}$. Since the Shapiro noise increases with the number of stars, it is a sum of the change in Shapiro delay of every star, one can expect that the Shapiro noise scales as $N\langle(\Delta t_{\text{sh}})^2\rangle$, where N is the number of stars. For $N = 10^8$ the Shapiro noise is $\sim 1 \times 10^{-3}$ s, or $\sim 10^{-4}$ s yr $^{-1}$ (see Section 3.4.2). As stated in Chapter 1, pulsar timing arrays can accurately time pulsars to the order of 10 μ s (for the PPTA). This value may be as low as 10 ns for larger arrays, such as the Square Kilometer

Array (SKA). Shapiro noise is therefore large in terms of current pulsar timing precision, making investigation of this effect very important. As it will be seen in Chapter 4, the magnitude of the observed Shapiro noise has a potentially far smaller effect, as the linear and quadratic components are subtracted out in the fitting procedure.

3.3 Comparison of simulation results with analytical expression

Before investigating further the effect of Shapiro noise on pulsar timing, it is first necessary to verify that the numerical simulation is correct. This is done by comparing the results of the numerical approach with that of the analytical approach described previously.

The Shapiro delay due to a single star (Equation 2.32) is

$$t_{\text{Sh}} = \frac{2GM}{c^3} \left(\ln \left| \frac{\sqrt{D_L^2 + \xi^2}}{\xi} + \frac{D_L}{\xi} \right| + \kappa \ln \left| \frac{\sqrt{\rho^2 + \xi^2}}{\xi} + \kappa \frac{\rho}{\xi} \right| \right), \quad (3.10)$$

where $\kappa = \rho/|\rho|$. Assuming the small angle approximation, $D_L \gg \xi$ this can be re-written as

$$t_{\text{Sh}} = \frac{2GM}{c^3} \left(\ln \left| \frac{2D_L}{\xi} \right| + \kappa \ln \left| \frac{\sqrt{\rho^2 + \xi^2}}{\xi} + \kappa \frac{\rho}{\xi} \right| \right). \quad (3.11)$$

This equation is used to determine the delay inferred by the stars, and also used to determine the Shapiro noise of the globular cluster. As was shown previously, this equation is a function of ρ , the distance along the LOS, and ξ , the distance on a plane perpendicular to LOS, of a star.

Let us now compare the numerical and analytical approaches for 1D, 2D and 3D. This comparison is made to show that both approaches predict the same results in all three dimensions. In both approaches, the 1D case corresponds to the distribution (and the movement) of the star on a line perpendicular to the

LOS, i.e. $\rho = 0$, with ξ the distance along this line (i.e. 1D). In the 2D case, ξ is a distance on a plane perpendicular to the LOS (i.e. $\rho = 0$). The 3D case uses a non zero value of ρ with a 2D ξ . (See Figure 3.1). The case for each dimension is investigated below.

3.3.1 1D model

In the 1D case, the stars populate a line perpendicular to the LOS at $\rho = 0$. The Shapiro delay simplifies to

$$t_{\text{Sh}} = \frac{2GM}{c^3} \left(\ln \left| \frac{2D_L}{\xi} \right| \right), \quad (3.12)$$

as the second logarithm term at $\rho = 0$ is zero. The first order derivative of this equation is,

$$\frac{\partial t_{\text{Sh}}}{\partial \xi} = -\frac{2GM}{c^3} \frac{1}{\xi}. \quad (3.13)$$

From Equation 3.4 the change in Shapiro delay, Δt_{sh} , for the 1D case ($\rho = 0$) can be simplified to,

$$\Delta t_{\text{Sh}} = \frac{\partial t_{\text{Sh}}}{\partial \xi} \Delta \xi. \quad (3.14)$$

If one assumes the stellar velocity is constant along the line it is possible to re-write $\Delta \xi$ as $v_\xi \Delta T$, where ΔT is the total observed time, and so

$$\Delta t_{\text{Sh}} = \frac{\partial t_{\text{Sh}}}{\partial \xi} v_\xi \Delta T. \quad (3.15)$$

Rearranging this equation for the 1D velocity component,

$$v_\xi = \left(\frac{2GM}{c^3} \Delta T \right)^{-1} \xi \Delta t_{\text{sh}}. \quad (3.16)$$

This equation will be used later on in the Jacobian to introduce the Δt_{sh} term into the probability distribution function.

The probability of observing a change in time delay of Δt_{sh} can be written

$$p(\Delta t_{\text{sh}}) = \int p(\xi, \Delta t_{\text{sh}}) d\xi \quad (3.17)$$

3.3: COMPARISON OF SIMULATION RESULTS WITH ANALYTICAL EXPRESSION

where ξ is a 1D distance. Let us now replace Δt_{sh} in $p(\xi, \Delta t_{\text{sh}})$ with v_ξ using a Jacobian $J_{\Delta t_{\text{sh}}}$ so the probability now becomes

$$\begin{aligned} p(\Delta t_{\text{sh}}) &= \int p(\xi, v_\xi) J_{\Delta t_{\text{sh}}} d\xi \\ &= \int p(\xi) p(v_\xi) J_{\Delta t_{\text{sh}}} d\xi, \end{aligned} \quad (3.18)$$

since the probabilities of ξ and v_ξ are independent of one another they can be separated. The Jacobian is

$$J_{\Delta t_{\text{sh}}} = \left| \frac{\partial(v_\xi)}{\partial(\Delta t_{\text{sh}})} \right|. \quad (3.19)$$

From Equation 3.16 this Jacobian is

$$\left| \frac{\partial(v_\xi)}{\partial(\Delta t_{\text{sh}})} \right| = \left(\frac{2GM}{c^3} \Delta T \right)^{-1} \xi. \quad (3.20)$$

In the numerical approach, a Gaussian distribution was used to generate the position and velocity values for every star. For the 1D model, this corresponds to two Gaussian distributions, $G(\xi)$ for the position distribution given by

$$G(\xi) = \sqrt{\frac{2}{\pi\sigma_\xi^2}} \exp\left(-\frac{\xi^2}{2\sigma_\xi^2}\right) \quad \xi \geq 0, \quad (3.21)$$

and $G(v_\xi)$ for the velocity dispersion given by

$$G(v_\xi) = \frac{1}{\sqrt{2\pi\sigma_{v_\xi}^2}} \exp\left(-\frac{v_\xi^2}{2\sigma_{v_\xi}^2}\right), \quad (3.22)$$

with a different σ value for each distribution. For the 1D model, the probability distribution of the position and velocity is simply the Gaussian distributions used to generate the position and velocity. Equation 3.18 can then be re-written

$$\begin{aligned} p(\Delta t_{\text{sh}}) &= \int p(\xi) p(v_\xi) J_{\Delta t_{\text{sh}}} d\xi \\ &= \int G(\xi) G(v_\xi) \left| \frac{\partial(v_\xi)}{\partial(\Delta t_{\text{sh}})} \right| d\xi, \end{aligned} \quad (3.23)$$

3: GLOBULAR CLUSTER SIMULATION

where the Jacobian is given in Equation 3.20. Writing the full expressions for the distributions and replacing v_ξ the probability becomes

$$\begin{aligned} p(\Delta t_{\text{sh}}) &= \int_0^\infty \sqrt{\frac{2}{\pi\sigma_1^2}} \exp\left(-\frac{\xi^2}{2\sigma_1^2}\right) \sqrt{\frac{2}{\pi\sigma_2^2}} \exp\left(-\frac{v_\xi^2}{2\sigma_2^2}\right) \left(\frac{2GM}{c^3}\Delta T\right)^{-1} \xi d\xi \\ &= \int_0^\infty \frac{2\xi}{\pi\sigma_1\sigma_2} \exp\left[-\left(\frac{\xi^2}{2\sigma_1^2} + \frac{\left(\frac{2GM}{c^3}\Delta T\right)^{-2}(\Delta t_{\text{sh}})^2\xi^2}{2\sigma_2^2}\right)\right] \left(\frac{2GM}{c^3}\Delta T\right)^{-1} d\xi \\ &= \frac{2}{\pi\sigma_1\sigma_2} \left(\frac{2GM}{c^3}\Delta T\right)^{-1} \int_0^\infty \xi \exp\left[-\left(\frac{1}{2\sigma_1^2} + \frac{\left(\frac{2GM}{c^3}\Delta T\right)^{-2}(\Delta t_{\text{sh}})^2}{2\sigma_2^2}\right)\xi^2\right] d\xi, \end{aligned}$$

where σ_1 is the position variance and σ_2 is the velocity variance. Using the identity

$$\int_0^\infty x \exp(-ax^2) dx = \frac{1}{2a}, \quad (3.24)$$

the probability can be integrated out and becomes

$$p(\Delta t_{\text{sh}}) = \frac{1}{\pi\sigma_1\sigma_2} \left(\frac{2GM}{c^3}\Delta T\right)^{-1} \frac{1}{a}, \quad (3.25)$$

where,

$$a = \frac{1}{2\sigma_1^2} + \frac{\left(\frac{2GM}{c^3}\Delta T\right)^{-2}(\Delta t_{\text{sh}})^2}{2\sigma_2^2}. \quad (3.26)$$

The probability distribution is a Cauchy distribution, of the form $p(\Delta t_{\text{sh}}) \propto \frac{1}{1+(\Delta t_{\text{sh}})^2}$. The distribution indicates that there is a chance for a large Δt_{sh} value, but for most cases Δt_{sh} is a small number ($\pm 2 \times 10^{-8}$ s). This reflects reality, as the probability of obtaining a large time delay – caused by a star moving very close to the LOS – is very small, and for most stars the Shapiro noise is very small.

Figure 3.3 shows the plot of the (normalized) probability distribution function plotted over the simulation results for 1D stellar position and velocity. The analytical distribution of Δt_{sh} compares very well with the simulation output. The distribution is centered on $\Delta t_{\text{sh}} = 0$ and shows that, in most cases, the stellar dynamics do not contribute much to the change in Shapiro delay. This is certainly true for stars that are very far away. The cases where Δt_{sh} is large is when the stars are either positioned close to the LOS or have very large velocities.

3.3: COMPARISON OF SIMULATION RESULTS WITH ANALYTICAL EXPRESSION

The correlation between the analytical result and simulation gets worse at larger Δt_{sh} due to the linear approximation that was made when deriving the analytical expression (Equation 3.15) breaking down. This means that the analytical solution cannot accurately predict the simulation results at high Δt_{sh} . However the cases for high Δt_{sh} are very rare, in most situations it can be said that the analytical and numerical simulations agree well with one another.

3: GLOBULAR CLUSTER SIMULATION

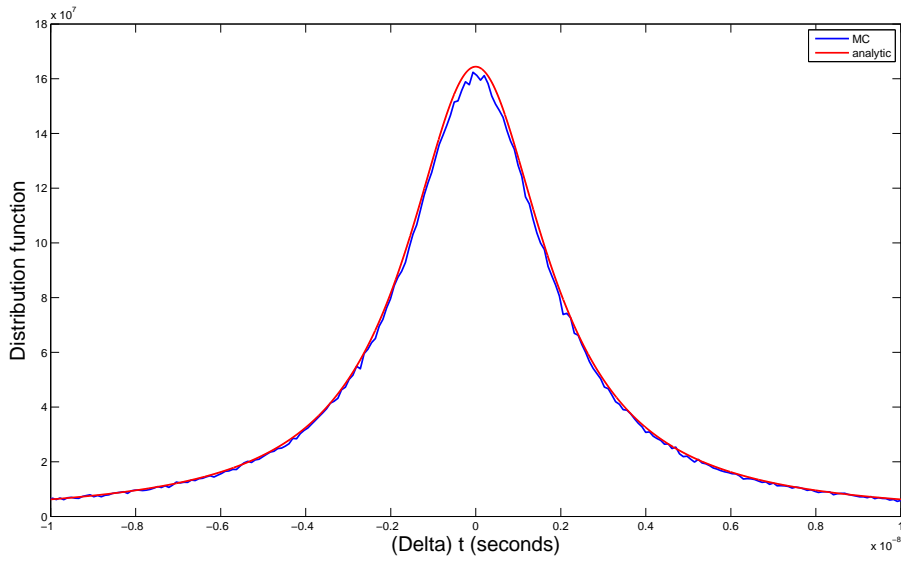


Figure 3.3: Comparison of the analytical and numerical results for the normalized 1D probability distribution function (PDF).

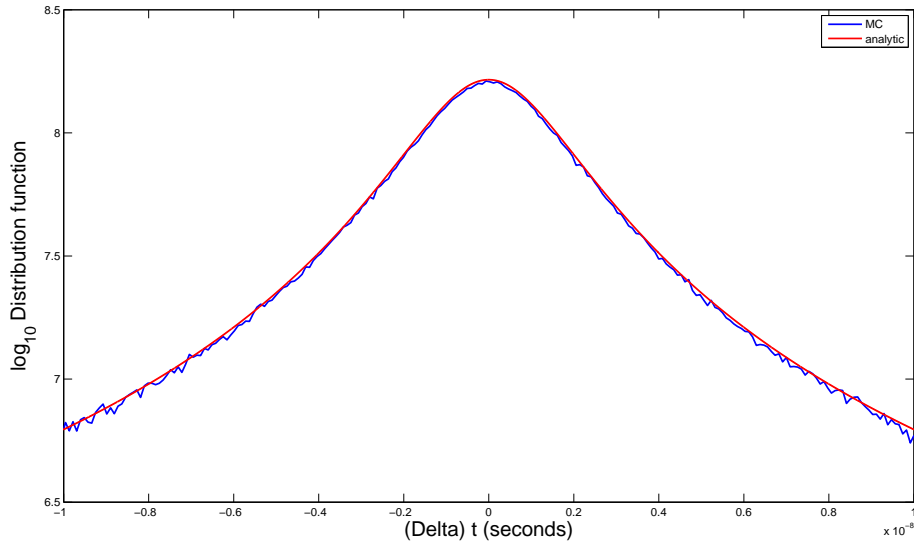


Figure 3.4: The PDF shown in Figure 3.3 in \log_{10} scale. The figure shows that the correlation between the analytical results (red line) and the numerical results (blue line) is very good.

3.3.2 2D model

Adding a second dimension changes the line perpendicular to the LOS into a plane perpendicular to the LOS. The position of the star on this plane can be described using polar co-ordinates (ξ, θ) , where θ describes the orientation of ξ in the plane perpendicular to the LOS (see Figure 3.5).

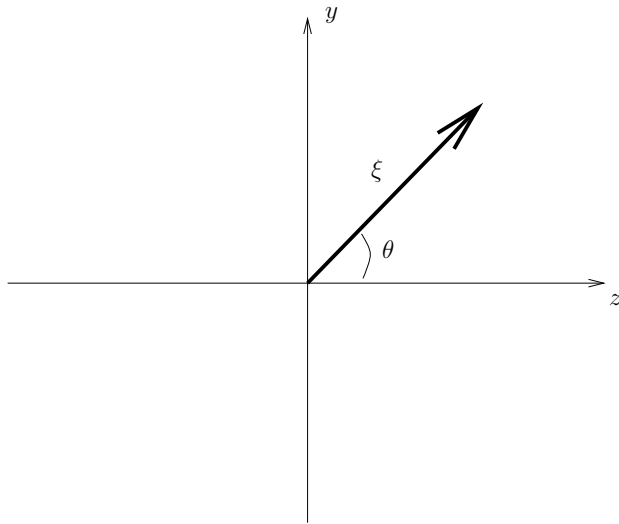


Figure 3.5: The relationship between the two-dimensional Cartesian co-ordinate system (y, z) and polar co-ordinate system (ξ, θ) . The centre of the globular cluster is at the origin, and the LOS to the observer (the x direction) is out of the page.

The probability $p(\Delta t_{\text{sh}})$ in this case is given by

$$p(\Delta t_{\text{sh}}) = \iiint p(\xi, \theta, v_\theta, \Delta t_{\text{sh}}) d\xi d\theta dv_\theta. \quad (3.27)$$

The position and velocity distribution in the polar co-ordinate system $(\xi, \theta, v_\theta, \Delta t_{\text{sh}})$ is not known, but the distributions are known in the Cartesian co-ordinate system of (y, z, v_y, v_z) . A Jacobian can be used to change the co-ordinate system from Cartesian to polar co-ordinates. The position parameters in the two co-ordinate systems are related by:

$$y = \xi \cos \theta$$

$$z = \xi \sin \theta.$$

3: GLOBULAR CLUSTER SIMULATION

From these relations, the velocities can be written as

$$\begin{aligned} v_y &= \frac{dy}{dt} = \frac{d\xi}{dt} \cos \theta - \xi \sin \frac{d\theta}{dt} \\ v_z &= \frac{dz}{dt} = \frac{d\xi}{dt} \sin \theta + \xi \cos \frac{d\theta}{dt}. \end{aligned}$$

It is possible to re-write $\frac{d\xi}{dt} = v_\xi$ the velocity of the impact parameter. The function $\frac{d\theta}{dt}$, the change of angle, can be ignored in the case of the Shapiro delay as this is symmetrical around the LOS. In other words, the change in Shapiro delay is due to a change in ξ by the speed v_ξ , and does not depend on θ or its change, $\frac{d\theta}{dt}$. As a result, the change in variable for the velocity can be expressed as

$$v_\xi^2 = v_x^2 + v_y^2. \quad (3.28)$$

A Jacobian for the position is

$$\begin{aligned} J_{y,z} &= \left| \frac{\partial(y, z)}{\partial(\xi, \theta)} \right| \\ &= \left| \begin{array}{cc} \frac{\partial y}{\partial \xi} & \frac{\partial y}{\partial \theta} \\ \frac{\partial z}{\partial \xi} & \frac{\partial z}{\partial \theta} \end{array} \right| \\ &= \left| \begin{array}{cc} \cos \theta & -\xi \sin \theta \\ \sin \theta & \xi \cos \theta \end{array} \right| \\ &= \xi. \end{aligned} \quad (3.29)$$

Changing the co-ordinate system from polar (ξ, θ) to Cartesian (y, z) using the Jacobian $J_{y,z}$, the PDF is

$$\begin{aligned} p(\Delta t_{sh}) &= \iiint p(\xi, \theta, v_\theta, \Delta t_{sh}) d\xi d\theta dv_\theta \\ &= \iiint p(y) p(z) J_{y,z} p(\Delta t_{sh}) p(v_z) dy dz dv_z \\ &= \iiint p(y) p(z) J_{y,z} p(v_y) p(v_z) J_{v_y, v_z} J_{\Delta t_{sh}} dy dz dv_z. \end{aligned} \quad (3.30)$$

The Jacobian $J_{\Delta t_{sh}}$ is shown in Equation 3.19. Since the distributions used in the simulation is Gaussian for each Cartesian co-ordinate and velocity, the PDF can

3.3: COMPARISON OF SIMULATION RESULTS WITH ANALYTICAL EXPRESSION

now be expressed as

$$\begin{aligned}
 p(\Delta t_{\text{sh}}) &= \iiint p(y) p(z) J_{y,z} p(v_y) p(v_z) J_{\Delta t_{\text{sh}}} dy dz dv_z \\
 &= \iiint \frac{1}{2\pi\sigma_1^2} \exp\left(-\frac{y^2+z^2}{2\sigma_1^2}\right) J_{y,z} \frac{1}{2\pi\sigma_2^2} \exp\left(-\frac{v_y^2+v_z^2}{2\sigma_2^2}\right) J_{\Delta t_{\text{sh}}} dy dz dv_z \\
 &= \iiint \frac{1}{2\pi\sigma_1^2} \exp\left(-\frac{\xi^2}{2\sigma_1^2}\right) J_{y,z} \frac{1}{2\pi\sigma_2^2} \exp\left(-\frac{v_\xi^2}{2\sigma_2^2}\right) J_{\Delta t_{\text{sh}}} d\xi d\theta dv_\theta. \quad (3.31)
 \end{aligned}$$

Due to symmetry around the LOS, θ and v_θ can be integrated out separately, therefore:

$$\begin{aligned}
 p(\Delta t_{\text{sh}}) &= \iiint \frac{1}{2\pi\sigma_1^2} \exp\left(-\frac{\xi^2}{2\sigma_1^2}\right) J_{y,z} \frac{1}{2\pi\sigma_2^2} \exp\left(-\frac{v_\xi^2}{2\sigma_2^2}\right) J_{\Delta t_{\text{sh}}} d\xi d\theta dv_\theta \\
 &= \frac{1}{(2\pi)^2\sigma_1^2\sigma_2^2} \left(\int_{-\infty}^{\infty} d\theta \right) \left(\int_0^{\infty} dv_\theta \right) \left[\int_0^{\infty} \exp\left(-\frac{\xi^2}{2\sigma_1^2}\right) J_{y,z} \exp\left(-\frac{v_\xi^2}{2\sigma_2^2}\right) \right] J_{\Delta t_{\text{sh}}} d\xi \\
 &= \frac{1}{\sigma_1^2\sigma_2^2} \left(\frac{2GM}{c^3} \Delta T \right)^{-1} \int_0^{\infty} \xi^2 \exp\left[-\left(\frac{1}{2\sigma_1^2} + \frac{\left(\frac{2GM}{c^3} \Delta T\right)^{-2} (\Delta t_{\text{sh}})^2}{2\sigma_2^2}\right) \xi^2\right] d\xi \quad (3.32)
 \end{aligned}$$

Using the identity

$$\int_0^{\infty} x^2 \exp(-ax^2) dx = \frac{1}{(2a)^{3/2}}, \quad (3.33)$$

the probability can be integrated and becomes

$$p(\Delta t_{\text{sh}}) = \frac{1}{\sigma_1^2\sigma_2^2} \left(\frac{2GM}{c^3} \Delta T \right)^{-1} \frac{2}{(2a)^{3/2}}. \quad (3.34)$$

where,

$$a = \frac{1}{2\sigma_1^2} + \frac{\left(\frac{2GM}{c^3} \Delta T\right)^{-2} (\Delta t_{\text{sh}})^2}{2\sigma_2^2}. \quad (3.35)$$

Compared to the 1D case, the resulting function is a steeper Cauchy distribution, suggesting that more stars are distributed around $\Delta t_{\text{sh}} = 0$.

Figure 3.6 shows the distribution of the analytical solution mapped onto the numerical result for two dimensions. Similar to the 1D case, the results agree well with one another.

3: GLOBULAR CLUSTER SIMULATION

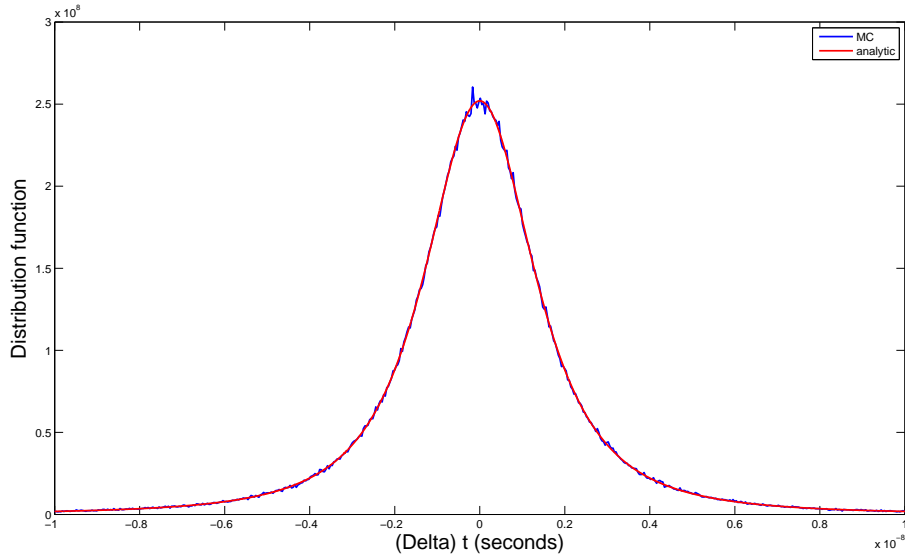


Figure 3.6: Comparison of the analytical and numerical results for the normalized two dimensional probability distribution function (PDF).

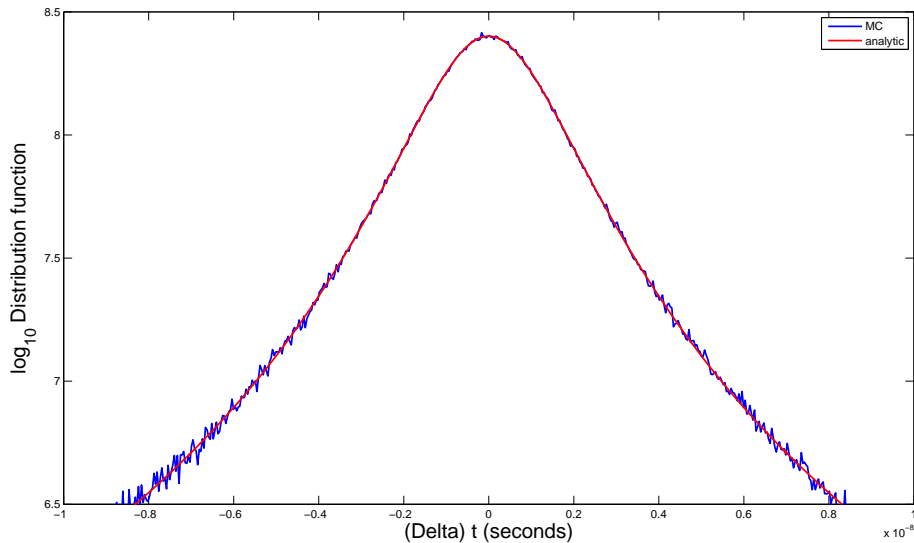


Figure 3.7: The PDF shown in Figure 3.6 in \log_{10} scale, showing good correlation between the analytical and numerical results.

3.3.3 3D model

For the 1D and 2D cases, the Shapiro delay is a function of the impact parameter ξ . For 3D, the Shapiro delay function is sensitive to ξ and also ρ , the stellar position along the LOS. From Figure 2.7 it was shown that the Shapiro delay is not symmetrical in ρ . This might indicate that the analytical solution is more complex than in the case of two dimensions.

Let us revisit Equation 2.32. In terms of ξ and ρ this equation is expressed as

$$\Delta t_{\text{sh}}(\xi, \rho) = \frac{\partial t_{\text{sh}}}{\partial \xi} \Big|_{\xi_f} \Delta \xi + \frac{\partial t_{\text{sh}}}{\partial \rho} \Big|_{\rho_f} \Delta \rho. \quad (3.36)$$

Due to symmetry along the LOS the θ term can be ignored. It is now necessary to include the second term in Δt_{Sh} . The two partial derivatives are obtained by differentiating Equation 2.32. The first term is then,

$$\frac{\partial t_{\text{Sh}}}{\partial \xi} = \frac{2GM}{c^3} \left[\frac{\kappa \left(-\frac{1}{\xi^2} \sqrt{\rho^2 + \xi^2} + \frac{1}{\sqrt{\rho^2 + \xi^2}} - \kappa \frac{\rho}{\xi^2} \right)}{\frac{1}{\xi} \sqrt{\rho^2 + \xi^2} + \kappa \frac{\rho}{\xi}} - \frac{1}{\xi} \right] \quad (3.37)$$

$$= \frac{2GM}{c^3} \left[\frac{\kappa \left(-\sqrt{\rho^2 + \xi^2} + \frac{\xi}{\sqrt{\rho^2 + \xi^2}} - \kappa \rho \right)}{\sqrt{\rho^2 + \xi^2} + \kappa \rho} - \frac{1}{\xi} \right] \quad (3.38)$$

$$= -\frac{2GM}{c^3} \left[\frac{\kappa \left(\sqrt{\rho^2 + \xi^2} + \kappa \rho \right)}{\xi} - \frac{\xi^2}{\sqrt{\rho^2 + \xi^2}} + \frac{1}{\xi} \right]. \quad (3.39)$$

The first term in the square brackets in Equation 3.39 is zero when $\rho = 0$, consistent with the one- and two-dimensional cases. For small ρ (i.e. $\xi \gg \rho$) the same term can be approximated as $\frac{1}{\xi} \frac{\rho}{\xi + \kappa \rho} \rightarrow 0$. For the case when $\rho \sim \xi$ the first term in the bracket is always smaller than the second term, and for the case $\rho \gg \xi$ the first term approximates to $\frac{\kappa}{\xi}$. In all three cases, the second term dominates in important areas of the parameter space (regions of space that contribute significantly to the Shapiro delay), meaning that the partial derivative

can be approximated as

$$\frac{\partial t_{\text{Sh}}}{\partial \xi} \sim -\frac{2GM}{c^3} \frac{1}{\xi}. \quad (3.40)$$

The second partial derivative is

$$\frac{\partial t_{\text{Sh}}}{\partial \rho} = \frac{2GM}{c^3} \kappa \left(\frac{\frac{\rho}{\xi \sqrt{\rho^2 + \xi^2}} + \frac{\kappa}{\xi}}{\frac{1}{\xi} \sqrt{\rho^2 + \xi^2} + \kappa \frac{\rho}{\xi}} \right) \quad (3.41)$$

$$= \frac{2GM}{c^3} \kappa \left(\frac{\frac{\rho}{\sqrt{\rho^2 + \xi^2}} + \kappa}{\sqrt{\rho^2 + \xi^2} + \kappa \rho} \right). \quad (3.42)$$

When $\xi = 0$, $\gg \rho^1$, or $\rho \sim \xi$ the partial derivative reduces to

$$\frac{\partial t_{\text{Sh}}}{\partial \rho} \sim \frac{2GM}{c^3} \frac{1}{\rho}. \quad (3.43)$$

Returning to Equation 3.36, since the partial derivative with respect to ξ is the same as the case for two dimensions, the results from the two dimensional case will be used for this component of Δt_{Sh} . The component with the partial derivative with respect to ρ is determined as follows.

Implementing Equation 3.43 into Equation 3.36, the second term becomes

$$\Delta t_{\text{Sh},\rho} = \frac{\partial t_{\text{Sh}}}{\partial \rho} \Delta \rho \quad (3.44)$$

$$= \frac{2GM}{c^3} \frac{1}{\rho} v_\rho \Delta T. \quad (3.45)$$

The linear approximation (stars travelling in a straight line at constant velocity) has been made for $\Delta \rho = v_\rho \Delta T$, and ΔT is the total observation time. Re-arranging for the velocity gives

$$v_\rho = \left(\frac{2GM}{c^3} \Delta T \right)^{-1} \rho \Delta t_{\text{Sh}}, \quad (3.46)$$

and the Jacobian that will be used to change the variable in the PDF to introduce the Δt_{Sh} is given by,

$$J_{\Delta t_{\text{sh}}} = \left| \frac{\partial(v_\rho)}{\partial(\Delta t_{\text{sh}})} \right| = \left(\frac{2GM}{c^3} \Delta T \right)^{-1} \rho. \quad (3.47)$$

¹In this case the second term in the brackets tends to zero.

3.3: COMPARISON OF SIMULATION RESULTS WITH ANALYTICAL EXPRESSION

Let us now determine the probability distribution function for the 3D case. For a globular cluster where the stellar position is generated using a Gaussian distribution (for each dimension), the PDF for the change in Shapiro delay is given by

$$\begin{aligned} p(\Delta t_{\text{sh}}) &= \iiint p(x, y, z, \Delta t_{\text{sh},\xi}, v_y, \Delta t_{\text{sh},\rho}) dx dy dz dv_y \\ &= \iiint p(x, y, z, v_x, v_y, v_z) J_{\Delta t_{\text{sh}},\xi} J_{\Delta t_{\text{sh}},\rho} dx dy dz dv_y \end{aligned}$$

where the Jacobian can be determined from Equation 3.19 and Equation 3.47. There are two Jacobians due to the Shapiro delay being a function of both ξ and ρ . The change in position from Cartesian to Cylindrical polar co-ordinates is achieved by using a Jacobian

$$\begin{aligned} J_{x,y,z} &= \left| \frac{\partial(x, y, z)}{\partial(\rho, \xi, \theta)} \right| \\ &= \left| \begin{array}{ccc} \frac{\partial x}{\partial \rho} & \frac{\partial x}{\partial \xi} & \frac{\partial x}{\partial \theta} \\ \frac{\partial y}{\partial \rho} & \frac{\partial y}{\partial \xi} & \frac{\partial y}{\partial \theta} \\ \frac{\partial z}{\partial \rho} & \frac{\partial z}{\partial \xi} & \frac{\partial z}{\partial \theta} \end{array} \right| \\ &= \left| \begin{array}{ccc} 1 & 0 & 0 \\ 0 & \cos \theta & -\xi \sin \theta \\ 0 & \sin \theta & \xi \cos \theta \end{array} \right| \\ &= \xi. \end{aligned} \tag{3.48}$$

The comparison of co-ordinate systems is shown in Figure 3.1.

As the 3D case has been shown to be just the 2D case with the extra dimension added, the PDF can be simplified to

$$p(\Delta t_{\text{sh}}) = p(\Delta t_{\text{sh}})_\xi \int p(\rho, \Delta t_{\text{sh},\rho}) d\rho, \tag{3.49}$$

where $p(\Delta t_{\text{sh}})_\xi$ is the PDF in ξ . As the PDF for ξ and ρ are independent of one another and therefore separable, let us define the integration in the above equation as $p(\Delta t_{\text{sh}})_\rho$, the PDF for ρ . Similar to the 1D case $p(\Delta t_{\text{sh}})_\rho$ can be

written as

$$\begin{aligned} p(\Delta t_{\text{sh}})_{\rho} &= \int p(\rho, v_{\rho}) J_{\Delta t_{\text{sh}}, \rho} d\rho \\ &= \int p(\rho) p(v_{\rho}) J_{\Delta t_{\text{sh}}, \rho} d\rho, \end{aligned} \quad (3.50)$$

where the Jacobian has been determined previously. Gaussian distributions were used to generate the values of x and v_x . x is in the same direction as ρ , however the origin of the two variables are different; $\rho = 0$ is at the centre of the globular cluster, whereas $x = 0$ is at the observer. The relation between the two is then $x = \rho - \mu$, where μ is the distance to the centre of the globular cluster from the observer. So the probability is

$$\begin{aligned} p(\Delta t_{\text{sh}}) &= \int p(\rho - \mu) p(v_{\rho}) J_{\Delta t_{\text{sh}}} d\rho \\ &= \int G(\rho - \mu) G(v_{\rho}) \left| \frac{\partial(v_{\rho})}{\partial(\Delta t_{\text{sh}})} \right| d\rho, \end{aligned} \quad (3.51)$$

where the Jacobian is given in Equation 3.47. Writing the full expressions for the distributions and replacing v_{ξ} the probability becomes

$$\begin{aligned} p(\Delta t_{\text{sh}})_{\rho} &= \int_0^{\infty} \sqrt{\frac{2}{\pi\sigma_1^2}} \exp\left(-\frac{(\rho - \mu)^2}{2\sigma_1^2}\right) \sqrt{\frac{2}{\pi\sigma_2^2}} \exp\left(-\frac{v_{\rho}^2}{2\sigma_2^2}\right) \left(\frac{2GM}{c^3}\Delta T\right)^{-1} \rho d\rho \\ &= \int_0^{\infty} \frac{2\rho}{\pi\sigma_1\sigma_2} \exp\left(-\frac{(\rho - \mu)^2}{2\sigma_1^2} - \frac{\left(\frac{2GM}{c^3}\Delta T\right)^{-2} (\Delta t_{\text{sh}})^2 \rho^2}{2\sigma^2}\right) \left(\frac{2GM}{c^3}\Delta T\right)^{-1} d\rho. \end{aligned}$$

The term in the first bracket can be re-written by completing the square,

$$\begin{aligned} -\frac{(\rho - \mu)^2}{2\sigma_1^2} - \frac{\left(\frac{2GM}{c^3}\Delta T\right)^{-2} (\Delta t_{\text{sh}})^2 \rho^2}{2\sigma^2} &= -\frac{1}{2\sigma_1^2} \left[\rho^2 - 2\mu\rho + \mu^2 + \left(\frac{2GM}{c^3}\Delta T\right)^{-2} (\Delta t_{\text{sh}})^2 \frac{\sigma_1^2}{\sigma_2^2} \rho^2 \right] \\ &= -\frac{1}{2\sigma_1^2} [E^2 \rho^2 - 2\mu\rho + \mu^2], \end{aligned} \quad (3.52)$$

where,

$$E = 1 + \left(\frac{2GM}{c^3}\Delta T\right)^{-2} (\Delta t_{\text{sh}})^2 \frac{\sigma_1^2}{\sigma_2^2}. \quad (3.53)$$

3.3: COMPARISON OF SIMULATION RESULTS WITH ANALYTICAL EXPRESSION

The terms in the square brackets can then be written as,

$$\begin{aligned}
 -\frac{1}{2\sigma_1^2} [E^2\rho^2 - 2\mu\rho + \mu^2] &= -\frac{E^2}{2\sigma_1^2} \left[\rho^2 - \frac{2\mu}{E^2}\rho + \frac{\mu^2}{E^2} \right] \\
 &= -\frac{E^2}{2\sigma_1^2} \left[\left(\rho - \frac{\mu}{E^2} \right)^2 + \frac{\mu^2}{E^2} - \frac{\mu^2}{E^4} \right] \\
 &= -\frac{E^2}{2\sigma_1^2} \left(\rho - \frac{\mu}{E^2} \right)^2 - \frac{\mu^2}{2\sigma_1^2} \left(1 - \frac{1}{E^2} \right).
 \end{aligned}$$

As a result

$$p(\Delta t_{sh})_\rho = \frac{2}{\pi\sigma_1\sigma_2} \left(\frac{2GM}{c^3} \Delta T \right)^{-1} \exp \left[-\frac{\mu}{2\sigma_1^2} \left(1 - \frac{1}{E^2} \right) \right] \int_0^\infty \rho \exp \left[-\frac{E^2}{2\sigma_1^2} \left(\rho - \frac{\mu}{E^2} \right)^2 \right] d\rho. \quad (3.54)$$

Using the identity,

$$\int_{-\infty}^\infty x \exp[-a(x-b)^2] dx = b \sqrt{\frac{\pi}{a}}, \quad (3.55)$$

the PDF becomes

$$p(\Delta t_{sh})_\rho = \frac{2}{\pi\sigma_1\sigma_2} \left(\frac{2GM}{c^3} \Delta T \right)^{-1} \exp \left[-\frac{\mu}{2\sigma_1^2} \left(1 - \frac{1}{E^2} \right) \right] \mu \sqrt{2\pi\sigma_1^2} \frac{1}{E^3}. \quad (3.56)$$

The PDF of the whole system is the product of the two probabilities shown in Equation 3.34 and Equation 3.56, so it is written as

$$p(\Delta t_{sh}) = \frac{2\mu\sqrt{2}}{\sigma_1^2\sigma_2^3\sqrt{\pi}} \left(\frac{2GM}{c^3} \Delta T \right)^{-2} \exp \left[-\frac{\mu}{2\sigma_1^2} \left(1 - \frac{1}{E^2} \right) \right] \frac{1}{E^3} \frac{1}{(2a)^{3/2}}, \quad (3.57)$$

where,

$$a = \frac{1}{2\sigma_1^2} + \frac{\left(\frac{2GM}{c^3} \Delta T \right)^{-2} (\Delta t_{sh})^2}{2\sigma_1^2} \quad (3.58)$$

$$E = 1 + \left(\frac{2GM}{c^3} \Delta T \right)^{-2} (\Delta t_{sh})^2 \frac{\sigma_1^2}{\sigma_2^2}. \quad (3.59)$$

The PDF is a steeper Cauchy distribution compared to the two dimension case, as $\frac{1}{E^2} \sim \frac{1}{1+(\Delta t_{sh})^6}$.

Figure 3.8 and 3.9 shows the distribution of the analytical solution mapped onto the numerical result for a 3D model. The agreement between the two approaches is good at the centre ($\Delta t_{sh} = 0$). However at the edges of the distribution

3: GLOBULAR CLUSTER SIMULATION

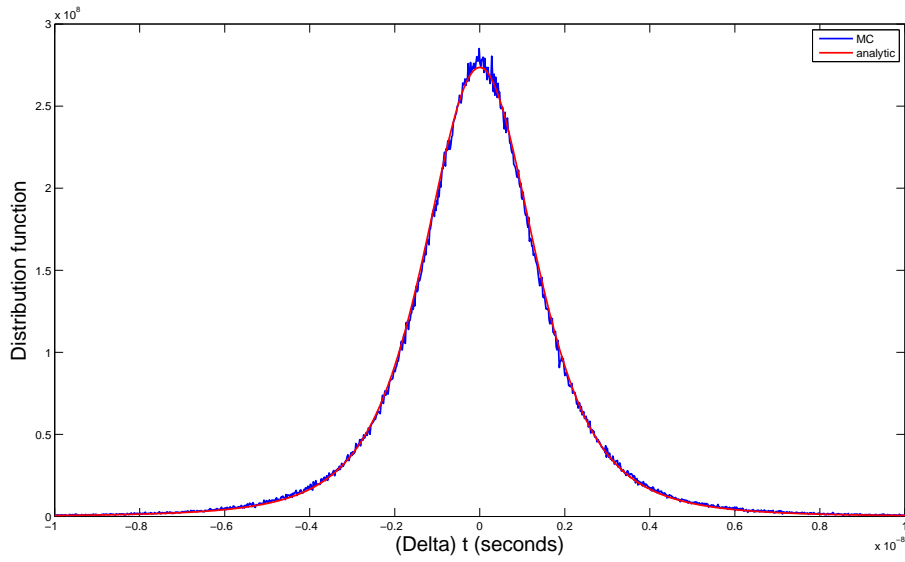


Figure 3.8: Comparison of the analytical and numerical results for the normalized 3D probability distribution function (PDF).

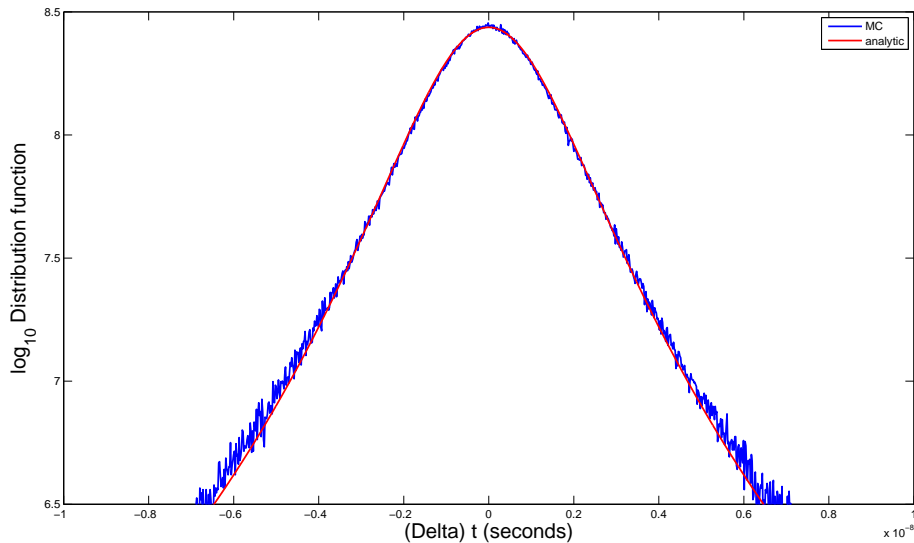


Figure 3.9: The PDF shown in Figure 3.8 in \log_{10} scale. The analytical and numerical results also correlate very well in the 3D case.

3.3: COMPARISON OF SIMULATION RESULTS WITH ANALYTICAL EXPRESSION

the analytical approach slightly underestimates the probabilities when compared to the numerical approach. The cause for this discrepancy arises from the linear approximation that was made when determining the change in Shapiro delay. The linear approximation will underestimate the change in Shapiro delay for stars approaching the LOS – the actual change in Shapiro delay is much greater than that predicted in the linear approximation, and will, similarly, overestimate the change in Shapiro delay for stars moving away from the LOS. This means that the normalised PDFs look very similar, but the analytical approach will over- and under-estimate the change in Shapiro delay dependent on whether the stars are approaching or moving away from the LOS. The MC simulation (numerical approach) does not use the linear approximation so its PDF is the actual distribution of the change in Shapiro delay.

The analytical approach indicates that the results of the numerical simulation agree well with predictions. Therefore, it can be said that the simulation is producing reliable results, and so it is possible to use this simulation to determine the Shapiro noise produced by the stellar motion around pulsars.

3.3.4 PDF overview

Before determining the Shapiro noise of a globular cluster to obtain the timing residual for the pulsar (Chapter 5), let us look at how the PDF varies with added dimensions.

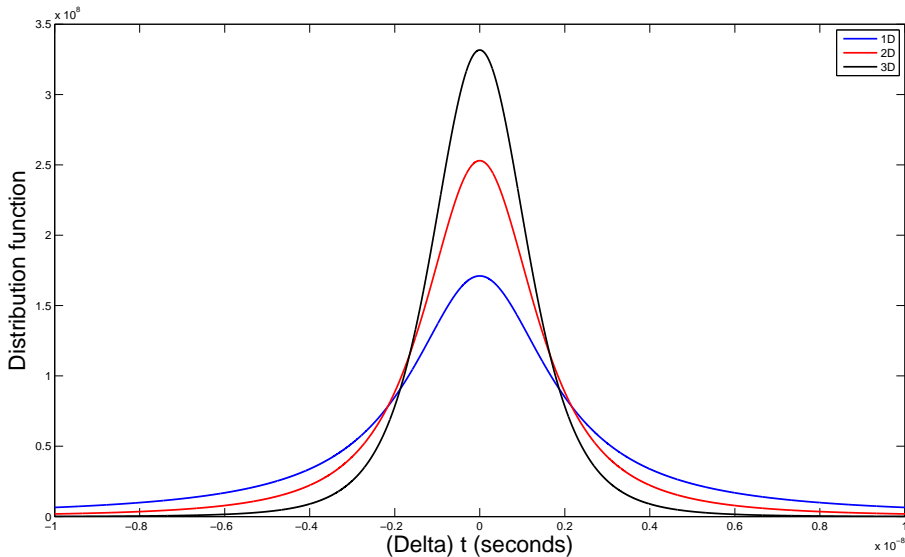


Figure 3.10: Comparisons of the normalized PDF for each dimension.

Figure 3.10 shows the difference in the PDF of analytical solutions for 1D, 2D and 3D. The addition of a dimension increases the peak around $\Delta t_{sh} = 0$. This indicates that the extra dimension affects the distribution of position and velocities of the stars. The added dimension reduces the effect a star has on the Shapiro delay, as the PDF peak becomes narrower and larger in amplitude.

This effect can be clearly seen for the positions. In 1D, for a variance of $\sigma = 5$ pc, a Gaussian distribution means that the majority of stars are situated within the region $-5\text{pc} \leq \xi \leq 5\text{pc}$. In two dimensions, the range of values possible for ξ is $\sqrt{5^2 + 5^2} \sim 7$ pc, meaning that the distribution of stars is wider than the 1D case. Therefore, increasing the number of dimensions of the Gaussian distribution increases the fraction of the distribution concentrated within a given fixed radius

from the centre. This wider distribution and increased fraction means that the effect of each star on the Shapiro noise is reduced, as it is less likely to be close to the LOS. On the other hand, the increased fraction means that the probability of a smaller change in Shapiro delay is increased. The same can be said when moving from 2D to 3D, and the resulting PDF has a much larger peak around $\Delta t_{\text{Sh}} = 0$.

3.4 Determining $\langle(\Delta t_{\text{Sh}})^2\rangle$

The primary reason for determining the analytical and numerical solutions for the change in Shapiro delay, Δt_{Sh} , is to have a ‘check’ for the MC simulations described in Section 3.2 and also predict the expected value of Δt_{Sh} for 10^8 stars, the total number of stars inside the globular cluster.

Analytically, $\langle(\Delta t_{\text{Sh}})\rangle$ is determined by

$$\langle(\Delta t_{\text{Sh}})\rangle = \int p(\Delta t_{\text{Sh}}) (\Delta t_{\text{Sh}})^2 d(\Delta t_{\text{Sh}}) \quad (3.60)$$

The root-mean-square (RMS) of Δt_{Sh} can be determined numerically from the MC simulations.

3.4.1 Number of dimensions

Let us now investigate the RMS of Δt_{Sh} . For this, the MC simulation of one star and one pulsar (positioned at the centre of the globular cluster and non-moving) was made. Initially the position and velocity were generated using a Gaussian distribution in 1D. The change in Shapiro delay of this star over an observed period of 3600 days was determined. Then a new star was generated (from the same distribution) for the same pulsar and its change in Shapiro delay was determined in the same manner as for the first star. This was repeated 10^7 times. The high number of realizations was done in order to obtain a smooth PDF from which the RMS could be determined.

This simulation was repeated for 2D and later on 3D. Table 3.2 shows how $(\Delta t_{\text{sh}})_{\text{rms}}$ varies with dimensions. Since the distribution becomes more concentrated around $\xi = 0$ as described in Section 2.7.1, the values of Δt_{sh} decreases with increasing number of dimensions. The values for the analytical and numerical simulations correlate well with one another. The discrepancy (as described earlier) stems from the linear approximation in the analytical approach.

Number of dimensions	Analytical ($\times 10^{-9}$ s)	Numerical ($\times 10^{-9}$ s)	Ratio
1	7.804768	8.539496	0.913961
2	2.320076	2.084895	1.112801
3	1.726819	1.411108	1.223732

Table 3.2: Comparison of the root-mean-square (RMS) value for the change in Shapiro delay, Δt_{Sh} for one star and one pulsar, observed for a period of 3600 days.

3.4.2 Number of stars

Since globular clusters contain more than one star, let us now populate a globular cluster with more than one star. For this, the MC simulation was altered so that it would generate more than one star and one pulsar stationary at the centre. The stars were allowed to move by generated velocities for a period of 3600 days. The change in Shapiro delay due to each star was determined, and then added together. The Shapiro noise for the system was then determined. This simulation was repeated 100 times (to get an average Δt_{Sh} value), and then repeated for different numbers of stars. Table 3.3 shows how the average Δt_{sh} varies with the number of stars. With increasing number of stars, the more likely it is for a star to be positioned close to the LOS, and results in a larger Shapiro noise. In addition, even if the stars are situated far from the LOS, the Shapiro delay is an additive term, so it accumulates to produce a large effect.

Number of Stars	$\langle\Delta t_{\text{Sh}}\rangle$ (seconds)
10^0	1.970047×10^{-9}
10^1	7.738209×10^{-9}
10^2	2.453314×10^{-8}
10^3	7.656143×10^{-8}
10^4	2.297258×10^{-7}
10^5	7.341568×10^{-7}
10^6	2.222465×10^{-6}

Table 3.3: The change in Shapiro delay, $\langle(\Delta t_{\text{Sh}})\rangle$ for different number of stars in a globular cluster, observed over a period of 3600 days.

3.4.3 Prediction for Δt for 10^8 stars

From Table 3.3 the $\langle(\Delta t_{\text{sh}})\rangle$ varies with the number of stars by a factor $\sim \sqrt{N}$, where N is the number of stars. For example, the Δt_{Sh} value for 10^6 stars, $\sim 2 \times 10^{-6}$ s, is similar to that of one star, $\sim 2 \times 10^{-9}$ s, multiplied by a factor of $\sqrt{10^6} = 10^3$.

The reasoning behind this relationship is rather simple: since every star is allocated a random direction and speed for successive short time intervals, the resulting trajectory is that of a random walk. For a random walk that varies with a Gaussian distribution with zero mean and a finite variance – such as the position and velocity components in the simulation – the expectation (or mean) value E for the Shapiro noise is the summation of the square of the Shapiro noise of every star, namely

$$\begin{aligned} E &= (\Delta t_{\text{Sh}})_1^2 + (\Delta t_{\text{Sh}})_2^2 + (\Delta t_{\text{Sh}})_3^2 + \dots + (\Delta t_{\text{Sh}})_N^2 \\ &= \sum_{i=1}^N (\Delta t_{\text{Sh}})_i^2, \\ &\sim N(\Delta t_{\text{Sh}})^2. \end{aligned} \tag{3.61}$$

The root mean square for the Shapiro noise is then the square root of E ,

$$\sqrt{E} = \sqrt{N} (\Delta t_{\text{Sh}}). \tag{3.62}$$

Therefore for 10^8 stars, the expected value for the change in Shapiro delay is $\sim \sqrt{10^8} \times 10^{-9}$ s $\sim 10^{-5}$ s, or 10 microseconds. This value – that was previously ignored – will be an observable noise term for the PPTA (see Chapter 1). For larger, more sensitive, arrays, such as the SKA, the Shapiro noise will become an important factor for pulsar timing.

3.5 Summary

In this section a simple globular cluster was created in order to determine the magnitude of the Shapiro noise. An analytical approach was taken to meticulously check the validity of the globular cluster. Once satisfied with the validity of this simulation the magnitude of the Shapiro noise was determined for a globular cluster containing 10^6 stars. The results from this simulation were then scaled up to determine the predicted magnitude of the Shapiro noise for a 10^8 star globular cluster, which was of the order of 10 microseconds.

It was also mentioned that the Shapiro delay is a term that cannot be directly observed, but is inferred from movement of stars within the globular cluster. Since the stars move around the globular cluster, this results in the change in Shapiro delay over time – the Shapiro noise – which is an observable quantity. Chapter 4 will investigate how pulsar timing residuals are affected by Shapiro noise alone.

Part IV

Timing Residuals

4

Pulsar timing residuals

In the previous chapter it was shown that the Shapiro noise is a potentially observable effect in pulsar timing, but no consideration was given to how the noise would appear in real pulsar timing residuals. From this Chapter to Chapter 7, this Shapiro noise is the **only** noise term added to pulsar timing.

The differentiations shown in Section 4.3.3, and the implementation of the polynomial fitting method to pulsar timing in Section 4.4 are all original work.

4.1 Timing residual

Before investigating the effects, let us determine (and define) the timing residual. For more information on timing residuals for pulsars in 47 Tucanae see Freire et al. (2001a).

The phase ϕ of a signal arriving at time t_{SSB} with apparent pulsar spin frequency f is given by (see Lorimer and Kramer 2004 for full details),

$$\phi(t_{\text{SSB}}) = \int 2\pi f dt_{\text{SSB}} \quad (4.1)$$

$$= 2\pi \left(f_0 t_{\text{SSB}} + \frac{1}{2} \dot{f}_0 t_{\text{SSB}}^2 \right) + 2\pi n(t_{\text{SSB}}), \quad (4.2)$$

where $n(t)$ is the additional (intrinsic) noise term, which accounts for higher orders, $\mathcal{O}(t^3)$, in the time dependence of the phase, f_0 is the pulsar spin frequency

at $t_{\text{SSB}} = 0$ and \dot{f}_0 is the rate of change of spin frequency at $t_{\text{SSB}} = 0$ (this term is usually negative). The term in brackets is simply the second order Taylor expansion of f . Converting the phase into a (arrival) pulse number $N = \frac{\phi}{2\pi}$, the above equation can be written as,

$$N = f_0 t_{\text{SSB}} + \frac{1}{2} \dot{f}_0 t_{\text{SSB}}^2 + n(t_{\text{SSB}}), \quad (4.3)$$

which has solutions for the time of arrival (or TOA) of the N^{th} pulse given by,

$$t_{\text{TOA}}(N) = -\frac{f_0}{\dot{f}_0} \pm \sqrt{\left(\frac{f_0}{\dot{f}_0}\right)^2 + \frac{2N}{\dot{f}_0}} \quad \text{for } n(t) = 0. \quad (4.4)$$

Figure 4.1 shows the relationship between pulse number N and the time of arrival t of that particular pulse, assuming no change in spin frequency of the pulsar ($\dot{f}_0 = 0$). When there is no change in spin frequency of the pulsar, i.e. $\dot{f}_0 = 0$, Equation 4.4 breaks down as Equation 4.3 becomes a linear function with one solution for the pulse number N ,

$$N = f_0 t_{\text{SSB}} \quad \text{for } \dot{f}_0 = 0 \text{ and } n(t) = 0. \quad (4.5)$$

Figure 4.1 also shows the difference between the linear solution and one (the plus-sign) of the solutions for Equation 4.4. The change in time of arrival of a particular pulse increases over observation time when an \dot{f}_0 term is introduced.

Figure 4.2 compares the two solutions given in Equation 4.4 with the linear relation. The introduction of \dot{f}_0 , which is nearly always a negative value (pulsar spin down), means that it takes longer for a particular pulse to arrive, as the frequency decreases (and spin period increases). This changes the function from linear into a quadratic, as shown in Equation 4.4. Although Equation 4.4 has two solutions, only the first (positive sign) solution is valid, as it is not possible for the TOA of a pulse to be shorter with decreasing spin frequency, meaning that the second (minus sign) solution can be ignored in this analysis.

Equation 4.4 can therefore be seen as expressing the predicted TOA of the N^{th} pulse. This predicted TOA can then be compared to the actual TOA obtained

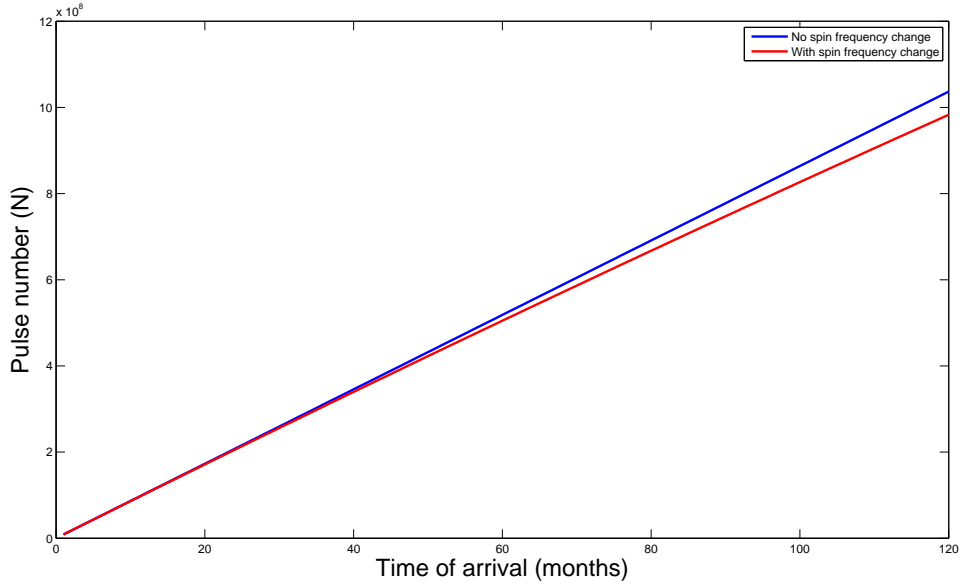


Figure 4.1: The arrival pulse number as a function of arrival time for the case of no change in spin frequency (blue line), and for the case where the change in spin frequency, \dot{f}_0 , is set to 1×10^{-7} Hz s $^{-1}$ (red line). The red line is the plus-sign solution in Equation 4.4.

from observations. The timing residual is the difference between these two TOA values, namely

$$\text{Residual} = t_{\text{TOA,Obs}} - t_{\text{TOA,Pred}}. \quad (4.6)$$

Since the predicted TOA is a quadratic function of the arrival time t_{SSB} , and this is subtracted from the observed TOA, the timing residual consists of cubic and higher order terms, i.e. $\mathcal{O}(t^3)$ and higher. The timing residual therefore contains elements such as $\ddot{f}t^3$.

The standard method of pulsar timing is to determine the frequency f and the change in frequency \dot{f} that minimize the timing residual. In other words, it tries to get a TOA model as close as possible to the observed TOA. The standard method is described in more detail below. Being able to determine the noise terms that are present in the higher order terms will allow for a better prediction

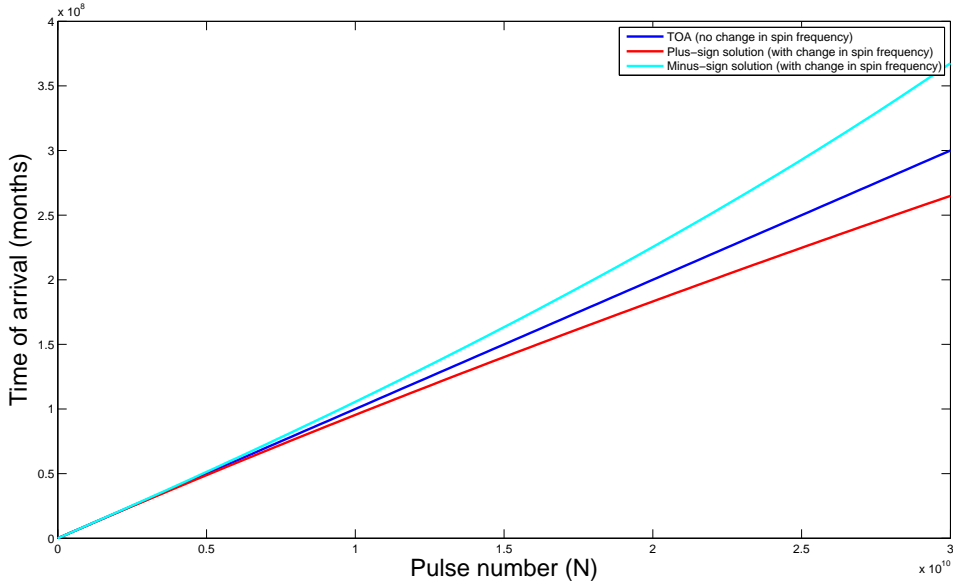


Figure 4.2: The change in time of arrival when a change in spin frequency is introduced. The red and cyan curves are solutions to Equation 4.4.

in TOA, and therefore will reduce timing noise.

4.2 Determining f_0 and \dot{f}_0

Least-Squares fit

To minimize timing residual, it is necessary for the predicted TOA to correlate very well with observed data. This is done by fitting the spin frequency f and the rate of change in frequency \dot{f} to the observed TOA, using a least squares fit. This fitting process determines the values for frequency and the rate of change in frequency, called f_0 and \dot{f}_0 , respectively, that best-fit the predicted TOA to the observed TOA.

The least-squares fit determines the values of f_0 and \dot{f}_0 that minimize the sum of squared errors. For the case of the spin frequency, the least-squares criterion

can be written as,

$$S = \sum_{i=1}^n (f_{0,i} - f_{0,\min})^2 \quad (4.7)$$

$$= \sum_{i=1}^n (f_{0,i}^2 + f_{0,\min}^2 - 2f_{0,i}f_{0,\min}) \quad (4.8)$$

$$= \sum_{i=1}^n f_{0,i}^2 + nf_{0,\min}^2 - 2f_{0,\min} \sum_{i=1}^n f_{0,i}, \quad (4.9)$$

where i is the i^{th} TOA out of a total of n TOAs, and $f_{0,i}$ is the f_0 value of the i^{th} TOA. It is necessary to determine S that minimizes $f_{0,\min}$, namely,

$$\frac{\partial S}{\partial f_{0,\min}} = 0 \quad (4.10)$$

$$= 2nf_{0,\min} - 2 \sum_{i=1}^n f_{0,i} \quad (4.11)$$

$$\Rightarrow f_{0,\min} = \frac{1}{n} \sum_{i=1}^n f_{0,i} \quad (4.12)$$

Also, to check for the minimum the 2nd order must be greater than zero,

$$\frac{\partial^2 S}{\partial f_{0,\min}^2} > 0 \quad (4.13)$$

$$= 2n > 0, \text{ i.e. minimum} \quad (4.14)$$

so the (unbiased) least-squared estimator (LSE) is then given by,

$$f_{0,\min} = \frac{1}{n} \sum_{i=1}^n f_{0,i} \quad (4.15)$$

Once the LSE has been determined it can be used to estimate the parameters of the distribution function.

Maximum-likelihood

The likelihood L is the probability of observing the data, given the value of a parameter $f_{0,\max}$ (which is exactly the same as $f_{0,\min}$, above). A more detailed definition is given as follows: When the joint probability density function (PDeF)

$Y_n(f_0|f_{0,\max})$ of the observations in a random sample is regarded as a function of a parameter $f_{0,\max}$ for given values $f_0 = (f_{0,1}, \dots, f_{0,n})$, it is called the likelihood function (DeGroot 1986). That is,

$$\mathcal{L}(f_{0,\max}; f_0) = Y_n(f_0|f_{0,\max}). \quad (4.16)$$

Since the spin frequency is independent at each TOA, it is possible to exploit the property that the PDF of the data is simply the product of the PDeFs specific to each observation, namely,

$$\mathcal{L}(f_{0,\max}; f_0) = \mathcal{L}(f_{0,\min}; f_{0,1}, \dots, f_{0,n}) = Y(f_{0,1}|f_{0,\max}) \dots Y(f_{0,n}|f_{0,\max}) = \prod_{i=1}^n Y(f_{0,i}|f_{0,\max}). \quad (4.17)$$

The maximum likelihood estimate of the parameter maximizes the probability of the observed data such that

$$\frac{\partial \mathcal{L}}{\partial f_{0,\max}} = 0, \quad \text{and} \quad (4.18)$$

$$\frac{\partial^2 \mathcal{L}}{\partial f_{0,\max}^2} < 0. \quad (4.19)$$

4.3 Maximum-likelihood method for the TOA

In order to maximize the probability of obtaining the observed TOAs, it is necessary to minimize the residual in Equation 4.6 using the least-squares fit, then use this value to maximise the likelihood of determining the most probable f_0 and \dot{f}_0 values for use within the predicted model, $t_{\text{TOA,Pred}}$.

The likelihood L , the probability of obtaining the observed TOA (which is a function of f_0 and \dot{f}_0), is expressed as,

$$L = \prod_{i=1}^n \frac{1}{\sqrt{2\pi}\sigma_i} \exp \left[-\frac{1}{2} \frac{(t_{\text{TOA,Obs,i}} - t_{\text{TOA,Pred,i}})^2}{\sigma_i^2} \right]. \quad (4.20)$$

Let us now define the log-likelihood l , which is $l = \ln L$, and is,

$$l = -\frac{n}{2} \ln(2\pi) - \ln \sum_{i=1}^n \sigma_i - \frac{1}{2} \sum_{i=1}^n \left(\frac{t_{\text{TOA,Obs,i}} - t_{\text{TOA,Pred,i}}}{\sigma_i} \right)^2. \quad (4.21)$$

When differentiating with respect to f_0 and \dot{f}_0 the σ_i term can be ignored (as it has no effect in determining the values of f_0 and \dot{f}_0) and so the log likelihood function can be simplified to

$$l = \text{constant} - \frac{1}{2} \sum_{i=1}^n (t_{\text{TOA,Obs},i} - t_{\text{TOA,Pred},i})^2. \quad (4.22)$$

For a particular pulse number $i = N$, and writing $t_{\text{TOA,Pred}}$ in full for that pulsar number,

$$l_N = -\frac{1}{2} \left(t_{\text{TOA,Obs}} + \frac{f_0}{\dot{f}_0} - \sqrt{\left(\frac{f_0}{\dot{f}_0}\right)^2 - \frac{2N}{\dot{f}_0}} \right)^2. \quad (4.23)$$

The standard method for reducing timing residuals tries to maximize this likelihood function.

4.3.1 Log-likelihood function

The log likelihood function l has a maximum at $(f_{0,\max}, \dot{f}_{0,\max})$ that meets the criteria

$$\left. \frac{\partial l}{\partial f_0} \right|_{f_{0,\max}} = 0 \quad (4.24)$$

$$\left. \frac{\partial l}{\partial \dot{f}_0} \right|_{\dot{f}_{0,\max}} = 0. \quad (4.25)$$

Taylor expanding l around $f_0 = f_{0,\max}$, $\dot{f}_0 = \dot{f}_{0,\max}$ the expression becomes

$$\begin{aligned} l(f_0, \dot{f}_0) &= l(f_{0,\max}, \dot{f}_{0,\max}) + \left. \frac{\partial l}{\partial f_0} \right|_{f_{0,\max}} \cdot (f_0 - f_{0,\max}) + \left. \frac{\partial l}{\partial \dot{f}_0} \right|_{\dot{f}_{0,\max}} \cdot (\dot{f}_0 - \dot{f}_{0,\max}) + \\ &+ \frac{1}{2} \left[\left. \frac{\partial^2 l}{\partial f_0^2} \right|_{f_{0,\max}} \cdot (f_0 - f_{0,\max})^2 + \left. \frac{\partial^2 l}{\partial \dot{f}_0^2} \right|_{\dot{f}_{0,\max}} \cdot (\dot{f}_0 - \dot{f}_{0,\max})^2 + \right. \\ &\left. + \left. \frac{\partial^2 l}{\partial f_0 \partial \dot{f}_0} \right|_{f_{0,\max}; \dot{f}_{0,\max}} \cdot (f_0 - f_{0,\max})(\dot{f}_0 - \dot{f}_{0,\max}) \right]. \end{aligned} \quad (4.26)$$

Substituting from Equation 4.24 and Equation 4.25 it is possible to eliminate the second and third terms of Equation 4.26. This is due to either f_0 or \dot{f}_0 being at

a maximum (so the first derivative is zero), thus the two terms in the top row are zero. The fourth and fifth terms are zero for the same reason. Therefore, the likelihood function simplifies to

$$l(f_0, \dot{f}_0) = l(f_{0,\max}, \dot{f}_{0,\max}) + \frac{1}{2} \left[\frac{\partial^2 l}{\partial f_0^2} \Big|_{f_{0,\max}} \cdot (f_0 - f_{0,\max})^2 + \frac{\partial^2 l}{\partial \dot{f}_0^2} \Big|_{\dot{f}_{0,\max}} \cdot (\dot{f}_0 - \dot{f}_{0,\max})^2 \right]. \quad (4.27)$$

Since the above equation is for a log-likelihood, the likelihood for f_0 and \dot{f}_0 , $p(f_0, \dot{f}_0)$, is the exponential of l . As a result, the probability can be approximated as a Gaussian,

$$p(f_0, \dot{f}_0) \propto \exp \left[l(f_0, \dot{f}_0) \right] \quad (4.28)$$

$$\propto \exp \left(-\frac{1}{2} Q \right), \quad (4.29)$$

where Q is the quadratic form of l

$$Q = (f_0 - f_{0,\max}, \dot{f}_0 - \dot{f}_{0,\max}) \begin{bmatrix} A & C \\ C & B \end{bmatrix} \begin{pmatrix} f_0 - f_{0,\max} \\ \dot{f}_0 - \dot{f}_{0,\max} \end{pmatrix}, \quad (4.30)$$

where the elements

$$A = \frac{\partial^2 l}{\partial f_0^2} \Big|_{f_{0,\max}} \quad (4.31)$$

$$B = \frac{\partial^2 l}{\partial \dot{f}_0^2} \Big|_{\dot{f}_{0,\max}} \quad (4.32)$$

$$C = \frac{\partial^2 l}{\partial f_0 \partial \dot{f}_0} \Big|_{f_{0,\max}; \dot{f}_{0,\max}}, \quad (4.33)$$

such that maximizing the likelihood Q will minimise the least-squares fit, or χ^2 .

4.3.2 Eigenvalues and eigenvectors

Let us now determine the eigenvalues and eigenvectors of the likelihood function l (and Q). There are analytical solutions for the eigenvalues and eigenvectors for the log-likelihood function, and so in a similar manner to Chapter 3, the eigenvalue and eigenvectors can be used as a check for the numerical (MC) simulation.

For a (co-ordinate) transformation represented by a matrix M , the eigenvalue equation can be expressed as

$$(M - \lambda I)\mathbf{x} = 0, \quad (4.34)$$

where I is the identity matrix, and \mathbf{x} is the eigenvector. The eigenvalues are obtained using the “characteristic equation”,

$$\det(M - \lambda I) = 0. \quad (4.35)$$

For the 2×2 matrix in Q in Equation 4.30 the characteristic equation is

$$\det \begin{vmatrix} A - \lambda & C \\ C & B - \lambda \end{vmatrix} = 0 \quad (4.36)$$

which has the solution

$$(A - \lambda)(B - \lambda) - C^2 = 0 \quad (4.37)$$

$$\Rightarrow \lambda^2 - (A + B)\lambda + AB - C^2 = 0. \quad (4.38)$$

Solving for λ , the eigenvalues are then

$$\lambda_+ = \frac{(A + B) + \sqrt{(A + B)^2 - 4(AB - C^2)}}{2} \quad (4.39)$$

$$\lambda_- = \frac{(A + B) - \sqrt{(A + B)^2 - 4(AB - C^2)}}{2}. \quad (4.40)$$

The magnitudes of the eigenvalues are related to the Fischer information matrix

$$F_{f_0, \dot{f}_0} = \frac{\partial^2 l}{\partial f_0 \partial \dot{f}_0} = \left[-\sigma_{f_0, \dot{f}_0}^2 \right]^{-1} \quad (4.41)$$

and the direction axes are the eigenvectors of F .

4.3.3 Determining eigenvalues and eigenvectors

In order to determine the elements A , B , C in the 2×2 matrix in Q let us differentiate the log-likelihood with respect to f_0 and \dot{f}_0 . The partial derivatives

are then,

$$\frac{\partial l}{\partial f_0} = 2 \left(\frac{1}{f_0} - \frac{f_0}{\dot{f}_0 \sqrt{\left(\frac{f_0}{\dot{f}_0}\right)^2 - \frac{2N}{\dot{f}_0}}} \right) \left(t_{\text{Obs}} + \frac{f_0}{\dot{f}_0} - \sqrt{\left(\frac{f_0}{\dot{f}_0}\right)^2 - \frac{2N}{\dot{f}_0}} \right) \quad (4.42)$$

$$\begin{aligned} \frac{\partial^2 l}{\partial f_0^2} &= 2 \left(\frac{f_0^2}{\dot{f}_0^4 \left[\left(\frac{f_0}{\dot{f}_0}\right)^2 - \frac{2N}{\dot{f}_0} \right]^{3/2}} - \frac{1}{\dot{f}_0^2 \sqrt{\left(\frac{f_0}{\dot{f}_0}\right)^2 - \frac{2N}{\dot{f}_0}}} \right) \left(t_{\text{Obs}} + \frac{f_0}{\dot{f}_0} - \sqrt{\left(\frac{f_0}{\dot{f}_0}\right)^2 - \frac{2N}{\dot{f}_0}} \right) \\ &\quad + 2 \left(\frac{1}{f_0} - \frac{f_0}{\dot{f}_0 \sqrt{\left(\frac{f_0}{\dot{f}_0}\right)^2 - \frac{2N}{\dot{f}_0}}} \right)^2 \end{aligned} \quad (4.43)$$

$$\frac{\partial l}{\partial \dot{f}_0} = 2 \left(-\frac{f_0}{\dot{f}_0} - \frac{\frac{2N}{\dot{f}_0^2} - \frac{2f_0^2}{\dot{f}_0^3}}{\dot{f}_0^2 \sqrt{\left(\frac{f_0}{\dot{f}_0}\right)^2 - \frac{2N}{\dot{f}_0}}} \right) \left(t_{\text{Obs}} + \frac{f_0}{\dot{f}_0} - \sqrt{\left(\frac{f_0}{\dot{f}_0}\right)^2 - \frac{2N}{\dot{f}_0}} \right) \quad (4.44)$$

$$\begin{aligned} \frac{\partial^2 l}{\partial \dot{f}_0^2} &= 2 \left(\frac{2f_0}{\dot{f}_0^3} - \frac{\frac{6f_0^2}{\dot{f}_0^4} - \frac{4N}{\dot{f}_0^3}}{2\sqrt{\left(\frac{f_0}{\dot{f}_0}\right)^2 - \frac{2N}{\dot{f}_0}}} + \frac{\left(\frac{2N}{\dot{f}_0^2} - \frac{2f_0^2}{\dot{f}_0^3}\right)^2}{4 \left[\left(\frac{f_0}{\dot{f}_0}\right)^2 - \frac{2N}{\dot{f}_0} \right]^{3/2}} \right) \left(t_{\text{Obs}} + \frac{f_0}{\dot{f}_0} - \sqrt{\left(\frac{f_0}{\dot{f}_0}\right)^2 - \frac{2N}{\dot{f}_0}} \right) \\ &\quad + 2 \left(-\frac{f_0}{\dot{f}_0} - \frac{\frac{2N}{\dot{f}_0^2} - \frac{2f_0^2}{\dot{f}_0^3}}{\dot{f}_0^2 \sqrt{\left(\frac{f_0}{\dot{f}_0}\right)^2 - \frac{2N}{\dot{f}_0}}} \right)^2 \end{aligned} \quad (4.45)$$

$$\begin{aligned} \frac{\partial^2 l}{\partial f_0 \partial \dot{f}_0} &= 2 \left(\frac{2f_0}{\dot{f}_0^3 \sqrt{\left(\frac{f_0}{\dot{f}_0}\right)^2 - \frac{2N}{\dot{f}_0}}} + \frac{f_0 \left(\frac{2N}{\dot{f}_0^2} - \frac{2f_0^2}{\dot{f}_0^3} \right)}{2\dot{f}_0^2 \left[\left(\frac{f_0}{\dot{f}_0}\right)^2 - \frac{2N}{\dot{f}_0} \right]^{3/2}} - \frac{1}{\dot{f}_0^2} \right) \left(t_{\text{Obs}} + \frac{f_0}{\dot{f}_0} - \sqrt{\left(\frac{f_0}{\dot{f}_0}\right)^2 - \frac{2N}{\dot{f}_0}} \right) \\ &\quad + 2 \left(\frac{1}{f_0} - \frac{f_0}{\dot{f}_0 \sqrt{\left(\frac{f_0}{\dot{f}_0}\right)^2 - \frac{2N}{\dot{f}_0}}} \right) \left(-\frac{f_0}{\dot{f}_0} - \frac{\frac{2N}{\dot{f}_0^2} - \frac{2f_0^2}{\dot{f}_0^3}}{\dot{f}_0^2 \sqrt{\left(\frac{f_0}{\dot{f}_0}\right)^2 - \frac{2N}{\dot{f}_0}}} \right). \end{aligned} \quad (4.46)$$

The second order derivatives of f_0 and \dot{f}_0 are the elements A and B , respectively, and the final equation is for the element C in Equation 4.30, which is also a second order derivative. These are then substituted into Equation 4.39 and 4.40

to obtain the eigenvalues. The C coefficient can also be used to determine the Fisher matrix eigenvectors.

The analytical approach will now be compared to the MC simulation and the effect the Shapiro noise will have on the timing residual is investigated.

4.3.4 Application to MC simulation

A new MC simulation was run to predict the timing residuals using the techniques described above. For this MC simulation, a pulsar of spin frequency $f = 100$ Hz and a spin decay $\dot{f} = -2 \times 10^{-15}$ Hz s $^{-1}$ was generated to determine the pulse time of arrival ($t_{\text{TOA,Obs}}$) for all the pulses over a 3600-day period. This new simulation used the same method described in Section 3.2 to determine the Shapiro noise for a 10^5 star globular cluster with one pulsar at the centre. The Shapiro noise term was then added to $t_{\text{TOA,Obs}}$ as the only noise term. The standard method determines a χ^2 -fit for every pulse N to determine the most likely f_0 and \dot{f}_0 values for the model, using estimated ('best guess') values of $f_{0,\text{max}}$ and $\dot{f}_{0,\text{max}}$ (see below). In our MC simulation the f_0 and \dot{f}_0 were determined for observations of one pulse every 30 days. Figure 4.3 shows a χ^2 plot over the f_0 - \dot{f}_0 plane for a random pulse number. Due to the characteristics of f_0 and \dot{f}_0 the contour lines are not circles, but sheared ellipticals. A negative \dot{f}_0 is equivalent to pulsar slowing down in its rotation, and as a result the pulse period increases and the frequency f_0 decreases. The opposite is also true for a positive \dot{f}_0 . This relationship between f_0 and \dot{f}_0 results in the shearing of the χ^2 slightly to the left in Figure 4.3.

The eigenvectors have been plotted over the χ^2 contour lines in Figure 4.4 to compare the analytical prediction with the results of the simulation. While it may not be apparent in Figure 4.4, the two eigenvectors are perpendicular to one another – the scaling of the axes does not properly display this property. The eigenvectors correlate well with the direction of the shearing of the ellipses.

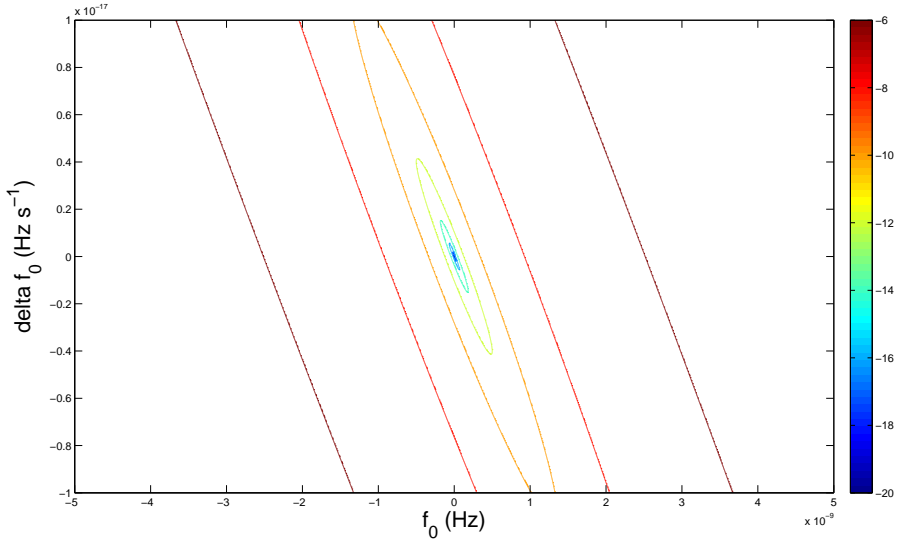


Figure 4.3: χ^2 -fit to determine the best fit values for f_0 and \dot{f}_0 .

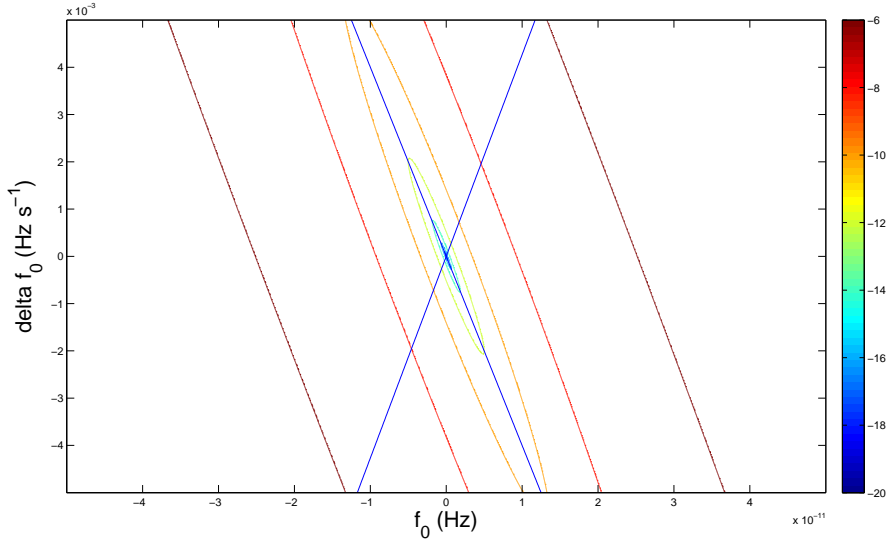


Figure 4.4: Comparison between the analytical estimation (eigenvectors, blue) and the contour lines from the χ^2 -fit obtained from the numerical simulation. The eigenvectors are perpendicular to one another, the cross hairs at the same location as the minimum of the χ^2 contour levels.

4.3.5 Note on χ^2 -fitting

The accuracy of the best-fit values obtained using the χ^2 -fit depends on the resolution – i.e. number of points on the grid – of the f - \dot{f} plane. The greater the number of points, the finer the resolution of the grid, and a more accurate best fit value for f_0 and \dot{f}_0 can be obtained.

In addition to a fine grid to determine the likelihood, two additional constraints are necessary – an initial estimate of the values for f_0 and \dot{f}_0 , hereafter defined as $f_{0,g}$ and $\dot{f}_{0,g}$, respectively. These constraints will limit the range of values for which the χ^2 fitting is valid, as it is less likely for the best fit values to be outside this region. The estimated values $f_{0,g}$ and $\dot{f}_{0,g}$ are determined from previous pulsar timing observations. As the estimated values of $f_{0,g}$ and $\dot{f}_{0,g}$ determine the range in f and \dot{f} it is necessary to accurately define these values.

Once the best-fit values of f_0 and \dot{f}_0 are determined by χ^2 -fitting using a set of estimated values $f_{0,g}$ and $\dot{f}_{0,g}$, respectively, these are used to determine the model pulsar TOA, $t_{\text{TOA,Pred}}$. This is then subtracted from our simulated pulsar TOA, $t_{\text{TOA,Obs}}$, to produce the timing residuals. As the TOA is a function of pulse number N , this process (determining f_0 and \dot{f}_0 and updating $f_{0,g}$ and $\dot{f}_{0,g}$ values after every N) has to be repeated for every pulse – a very intensive task computationally for millisecond pulsar observations over ten years. This, in addition to requiring a high resolution grid in order to accurately determine the best-fit values for f_0 and \dot{f}_0 using χ^2 , results in a very time consuming simulation.

The Shapiro noise is a function of the position and velocities of the stars around the pulsar over observation time, and independent of f_0 and \dot{f}_0 . As a result, it may not be necessary to obtain a model for the TOA by calculating for the maximum f_0 and \dot{f}_0 values using the maximum likelihood method. In the next section an alternative method will be introduced to produce a model for the TOA which can be used to determine the timing residuals from the Shapiro noise.

4.4 Polynomial fitting

As stated previously, the Shapiro noise is a function of the stellar positions and velocities and the evolution of these parameters over the observation time. The Shapiro noise is therefore independent on the evolution of the spin frequency f_0 and also the evolution of the change in spin frequency \dot{f}_0 of the pulsar. As a consequence, it may not be necessary to produce a TOA model for the pulsar by using the maximum likelihood method to obtain the most likely f_0 and \dot{f}_0 values for the pulsar.

The standard method to determine the timing residual produces a TOA model by subtracting the first two orders (f_0 and \dot{f}_0) from the observed TOA. In this section an alternative method to subtract the first two orders from the observed TOA will be introduced. The derivation and implementation of this alternative method is all original work.

Let us suppose that the *observed* TOA can be Taylor expanded to form the polynomial

$$t_{\text{Obs}} = a + bt + \frac{1}{2!}ct^2 + \frac{1}{3!}dt^3 + \frac{1}{4!}et^4 + \dots, \quad (4.47)$$

where (a, b, c, d, e) contain timing noise elements, such as the Shapiro noise. The “standard” f_0 and \dot{f}_0 fitting procedure described above will produce a model

$$t_{\text{TOA}} = f_0 t + \frac{1}{2}\dot{f}_0 t^2, \quad (4.48)$$

which then means that the timing residual is

$$t_{\text{residual}} = t_{\text{Obs}} - t_{\text{TOA}} \quad (4.49)$$

$$= a + (b - f_0) \cdot t + \frac{1}{2!}(c - \dot{f}_0) \cdot t^2 + \frac{1}{3!}dt^3 + \frac{1}{4!}et^4 + \dots \quad (4.50)$$

This is analogous to fitting a second order polynomial to the observed TOA to determine the most precise values of f_0 and \dot{f}_0 . Such a fit will remove the first three terms in the above equation completely, as a is an offset and $(b - f_0)$, $(c - \dot{f}_0)$ become zero – they are fitted out. The resulting timing residual is then a function

of the third and higher orders

$$t_{\text{residual}} = \frac{1}{3!} dt^3 + \frac{1}{4!} et^4 + \dots \quad (4.51)$$

If the noise term in the observed TOA consists solely of the Shapiro noise, the timing residual can be obtained by subtracting the second order polynomial fit of the Shapiro noise from the observed TOA. Using this method it is possible to obtain the timing residual without the need to determine f_0 and \dot{f}_0 explicitly, and requires much less computational power compared to gridding for χ^2 -fit.

The risk of using a second-order polynomial fit to obtain a timing residual is that any real (observed) information contained in the first two orders are lost and cannot be recovered. However, this risk is similar to that of using the least-squares fit method to determine the timing residual.

4.4.1 Polynomial fitting for Δt_{Sh}

Let us now investigate whether it is possible to implement this polynomial fitting for the Shapiro noise to obtain the timing residual. The MC simulation (in Section 3.2) that produced Δt_{Sh} for one pulsar (at the centre of the globular cluster) and one star was used to test this method. The command `polyval` (polynomial evaluation) in MATLAB was used to determine an n -degree polynomial (in this case, $n = 1, 2$) of the form:

$$p(t) = p_1 t^n + p_2 t^{n-1} + p_3 \quad (4.52)$$

where the coefficients p_1 , p_2 and p_3 are such that the polynomial $p(t)$ matches closely to the Shapiro noise. Then the command `polyfit` (polynomial curve fitting) utilises these coefficients to create the timing model, t_{TOA} , which was then subtracted from the Shapiro noise to produce the timing residual.

Three different variations of the MC simulation were created, each with different stellar position ($\xi = 5 \times 10^{-4}$ pc, 1 pc, and 50 pc) to generate the Shapiro noise (Figure 4.5). This was done to investigate how the timing residual changes

over a range of ξ . Each star was positioned at $\rho = 0$ pc. The pulsar is positioned at the centre of the globular cluster for this simulation. The timing residuals produced after fitting for the first and second order are shown below.

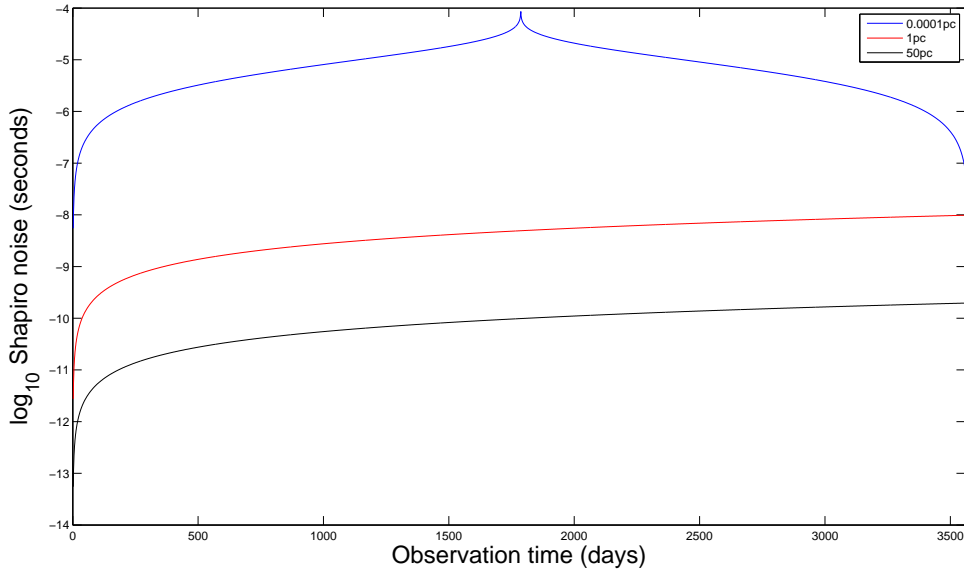


Figure 4.5: Logarithm of Shapiro noise as a function of observation time.

A single star at $\xi = 5 \times 10^{-4}$ pc

This star is the closest (of the three) to the LOS. Due to this position its absolute time delay is the largest of the three, and the change in Shapiro delay is the also the largest as shown in Figure 4.5. When the star moves during the 3600-day observation period it passes across the LOS, creating a ‘spike’ in the Shapiro noise. The Shapiro noise function has two distinct components – the spike from the star crossing the LOS, and the slope. When subtracting out the first order (linear term), the most dominant component of the timing residual is the spike. The first order fit removes the slope. The magnitude of the other components are much smaller. One can then assume that subtracting the second order does not significantly change the shape or the magnitude of the timing residual. From Fig-

ure 4.6 the timing residual after the combined first and second order subtraction also has a similar shape, with the same magnitude.

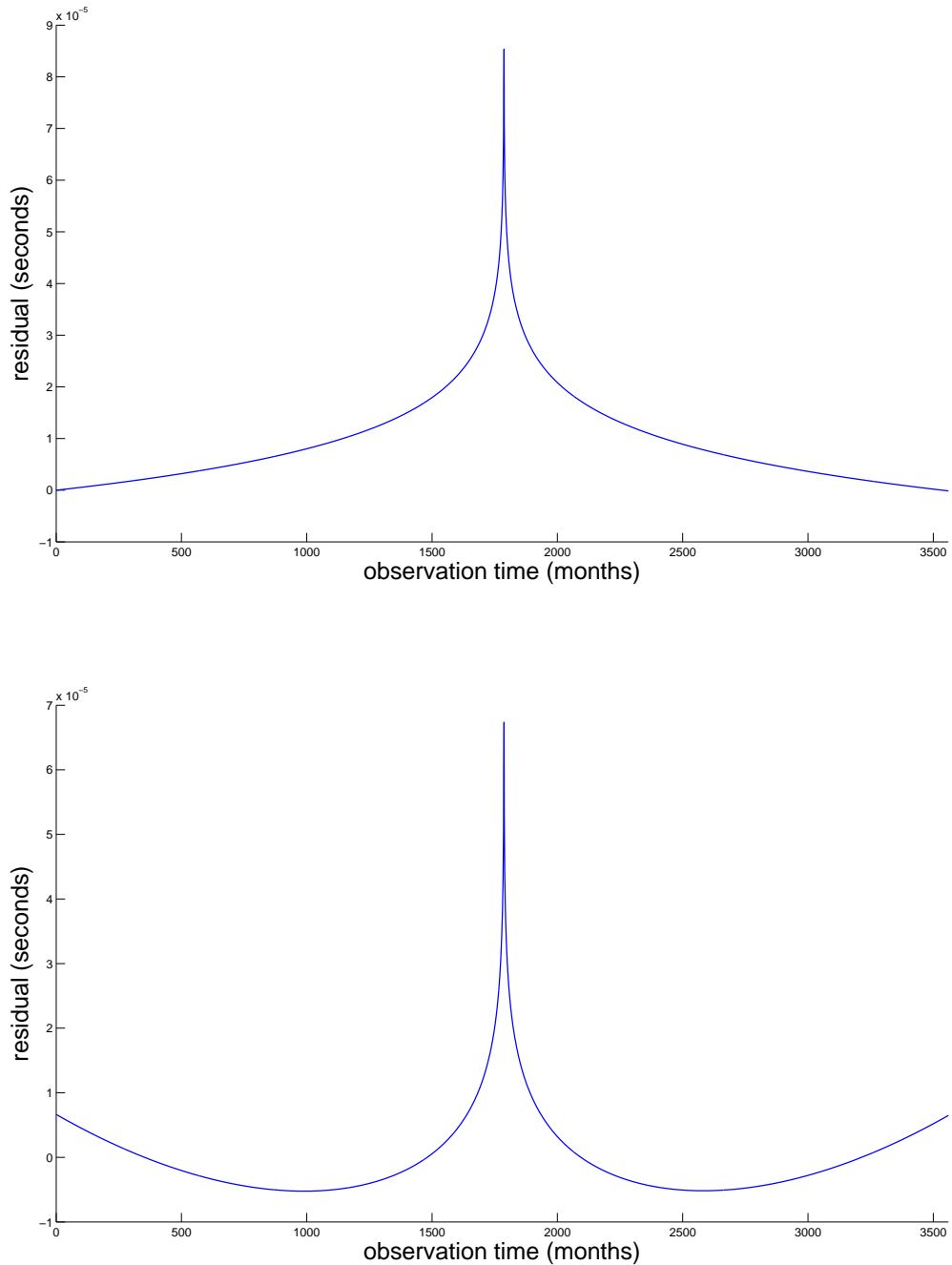


Figure 4.6: *Top*: Timing residual after first order subtracted. *Bottom*: Timing residual after first and second order subtracted.

A single star at $\xi = 1 \text{ pc}$

This star is positioned further away from the pulsar LOS than the previous case. As a result, the magnitude of the Shapiro noise is far smaller. In addition, from its position it is not possible for this star to get near (or across) the LOS, so there is no ‘spike’ in the Shapiro noise. When subtracting out the first order, the timing residual does not look similar to the Shapiro noise function. From Figure 4.7 subtracting a linear term from the Shapiro noise results in a quadratic timing residual. This suggests that the largest remaining coefficient is that of the second order, and that the higher orders in the Shapiro noise are far too small to have an effect over the (simulated) ten-year observation. When fitting out the second order, the timing residual has a cubic shape, with a smaller magnitude by a factor of $\sim 10^4$.

4: PULSAR TIMING RESIDUALS

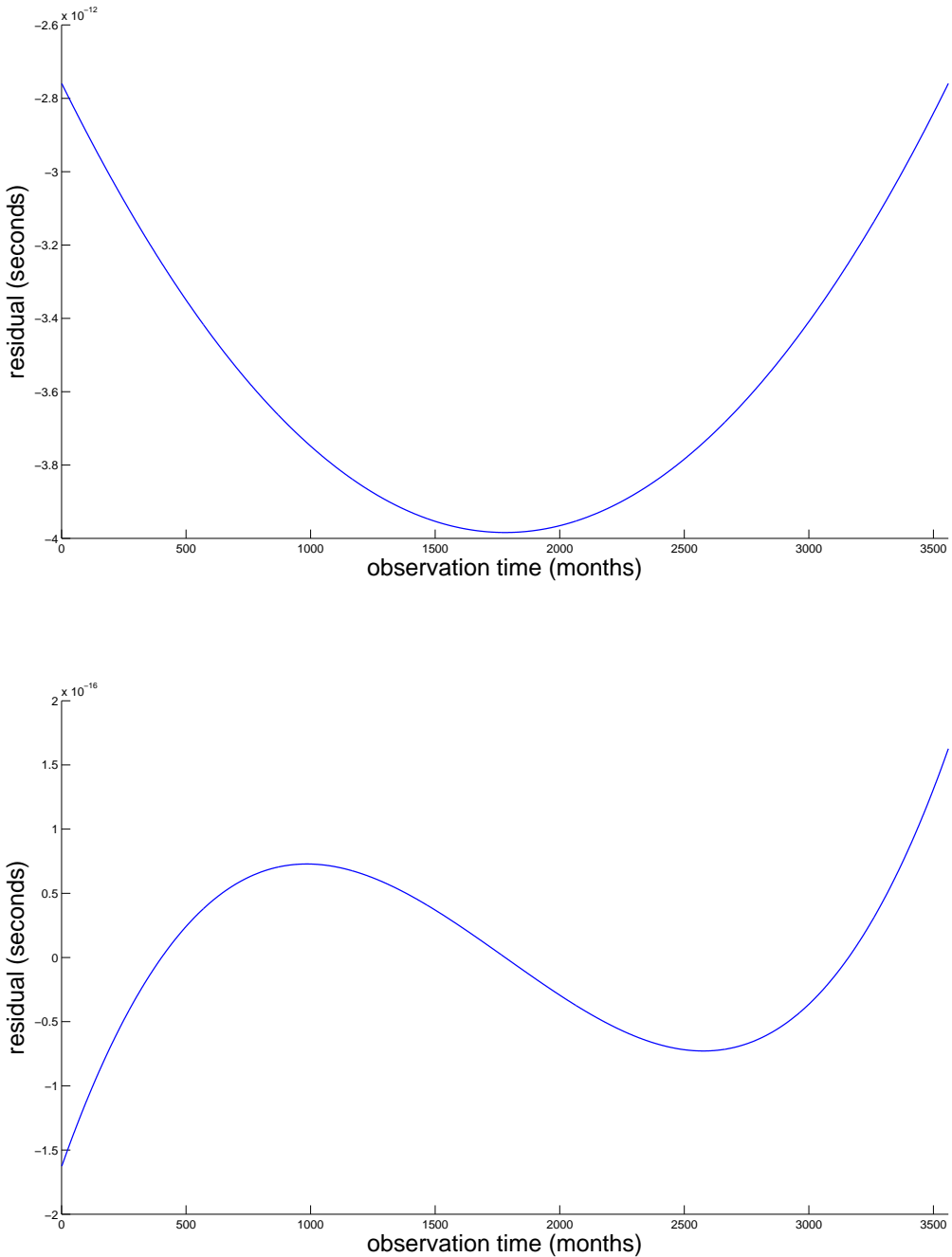


Figure 4.7: *Top*: Timing residual after first order subtracted. *Bottom*: Timing residual after first and second order subtracted.

A single star at $\xi = 50$ pc

This star is positioned furthest away from the central core of the globular cluster (the furthest of the three cases). The magnitude of the absolute time delay and the change in the time delay are so small that the effect of this star on the timing residual is negligible. This is apparent when fitting out the first two orders (Figure 4.8) the resulting timing residual is similar to white noise with a very small ($\sim 10^{-20}$ s) amplitude.

The timing residual is sensitive to the pulsar position. This is due to the nature of the stellar position in the time delay function.

The results from polynomial fitting – that the timing residual must be dominated by a cubic (and higher order) function – is consistent with Hobbs (2003) and Freire et al. (2001a).

This study suggests that subtracting using a polynomial fit as a model can produce the timing residuals for pulsars without the need for determining f_0 and \dot{f}_0 explicitly.

4: PULSAR TIMING RESIDUALS

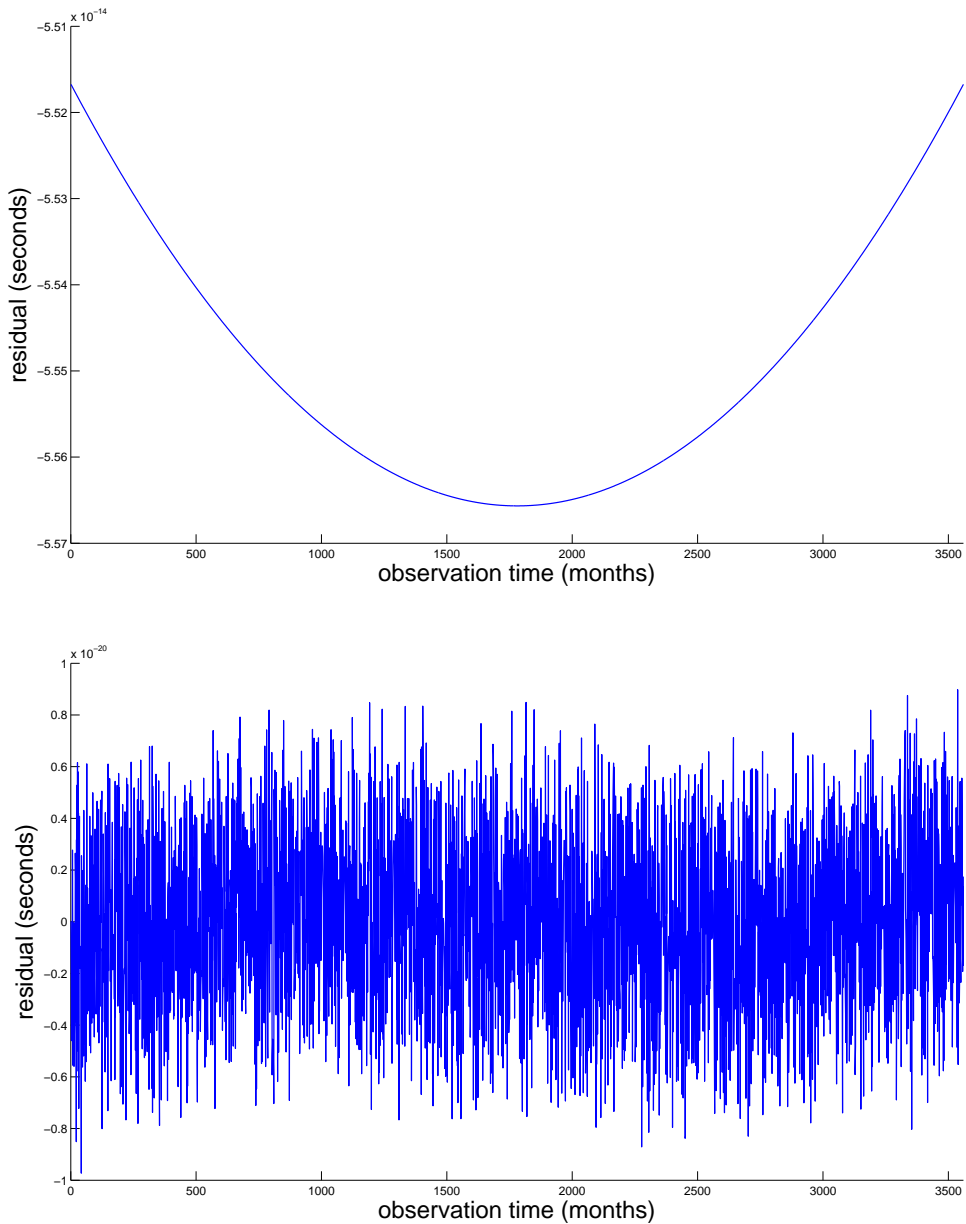


Figure 4.8: *Top:* Timing residual after first order subtracted. *Bottom:* Timing residual after first and second order subtracted. Note the scale, the fluctuations in the bottom figure are very small compared to the other figures – this would be a straight line when plotted over Figures 4.6 and 4.7.

4.5 Summary

In this chapter the method to measure the effect of Shapiro delay on pulsar timing is described. The standard method determines the timing residuals by comparing the observed time of arrival (TOA) with a modeled TOA, created from the likely values of the frequency f_0 and the change in frequency \dot{f}_0 .

Since the Shapiro noise is independent of f_0 and \dot{f}_0 , a new method which uses a polynomial to subtract the first and second order of the observed TOA, is used to determine the timing residuals. This new method is computationally more efficient - as described in the chapter - than the standard method to determine timing residuals over long observation periods.

The simulations described in this chapter suggest that polynomial fitting produces timing residuals that have similar properties to those obtained using the standard method. From here onwards, polynomial fitting will be used to determine the timing residuals from the Shapiro noise.

5

Determining timing residuals from MC simulation

Chapter 4 has described a method to obtain timing residuals from the Shapiro noise, let us now determine the timing residuals of the pulsars for a simple globular cluster.

In order to get a more accurate representation of the timing residuals let us use the MC simulation, with initial conditions shown in Table 3.1, for 10^6 stars (1% of total number of stars in the globular cluster), but using the *actual* pulsar positions. The pulsar positions are given in Freire et al. (2001a) (for RA and DEC – z and y in Cartesian), and Freire et al. (2001b) (for x in Cartesian). The Cartesian (x, y, z) is defined in Section 3.1. The units for RA and DEC – in units of (h:m:s) and ($^\circ$ ‘ ’), respectively – have been converted from angular into a linear distance (pc). The LOS distance R for each pulsar has been estimated by comparing the period derivatives \dot{P} with the dispersion measure (DM) (see Freire et al. 2001b for full derivation). The model dispersion measure (\mathcal{DM}) for a pulsar is given by

$$\mathcal{DM}_i = DM_c + n_e R_i \left[(\dot{P}/P)_{\text{obs},i} - \langle (\dot{P}/P)_{\text{int}} \rangle \right], \quad (5.1)$$

where DM_c is the dispersion measure at the core of the globular cluster, n_e is

the number density of the plasma, $(\dot{P}/P)_{\text{obs},i}$ is the acceleration along the LOS (Freire et al. 2001a), and $\langle(\dot{P}/P)_{\text{int},i}\rangle$ is the average intrinsic acceleration for all pulsars. To determine the distance Freire et al. (2001b) uses a model to predict the dispersion measure \mathcal{DM} closest to the observed value of the dispersion velocity, DM , that minimises the function

$$\mu \equiv \sum_{i=1}^{15} (DM_i - \mathcal{DM}_i)^2. \quad (5.2)$$

In order to obtain uncertainty estimates in the parameters derived from the model, Freire et al. (2001b) made an MC simulation using observed pulsar DM 's and relevant pulsar parameters consistent with uncertainties from observations of the globular cluster. The resulting distance along the LOS and the uncertainties obtained in Freire et al. (2001b) are shown in Table 5.1.

The proper motions of the pulsars are also given in Freire et al. (2003) so these values were used to compute velocities in the simulation (instead of randomly generating these values). Table 5.1 shows the Cartesian co-ordinates and velocity components for each pulsar in 47 Tucanae, and Figure 5.1, Figure 5.2 plot the positions.

Each pulsar will have a unique stellar distribution around its LOS, so the timing residuals due to the Shapiro noise for each pulsar should be different, although pulsars which are close together will have similar timing residuals. Additionally, one can expect the pulsars at the centre of the globular cluster – where there is a larger number of stars and therefore a smaller impact parameter between the star and the LOS – to have larger timing residuals than the pulsars that are further away.

Other than the pulsar positions, the initial condition for every realisation of the MC simulation was the same as in Table 5.1. The resulting timing residuals for three such realisations are shown in Figure 5.3 to Figure 5.5.

Pulsar	RA (pc)	DEC (pc)	LOS (pc)	PM RA (10^5 m s^{-1})	PM DEC (10^5 m s^{-1})
J0023-7204C	1.758	0.525	2.60 ± 0.6	1.382	-0.770
J0024-7204D	-0.942	0.218	$5.20^{+2.2}_{-1.2}$	1.047	-0.699
J0024-7205E	-0.623	-0.685	-1.50 ± 0.4	1.580	-0.616
J0024-7204F	0.209	0.244	$-0.15^{+0.04}_{-0.08}$	1.374	-0.865
J0024-7204G	-0.263	0.321	$0.12^{+0.08}_{-0.03}$	1.133	-0.301
J0024-7204H	-0.118	1.139	0.04 ± 0.02	1.138	-0.798
J0024-7204I	-0.260	0.322	$0.15^{+0.15}_{-0.05}$	1.100	-0.938
J0023-7203J	0.719	1.339	$3.40^{+0.9}_{-0.7}$	1.285	-0.858
J0023-7205M	1.284	-0.948	$0.12^{+0.06}_{-0.04}$	1.333	-0.790
J0024-7204N	-0.403	0.590	$2.90^{+0.7}_{-0.6}$	1.347	-0.790
J0024-7204O	0.117	-0.029	-0.04 ± 0.02	1.253	-0.513
J0024-7204Q	-1.241	0.683	$-0.02^{+0.01}_{-0.03}$	1.347	-0.790
J0024-7204S	0.194	0.255	-0.02*	0.824	-1.561
J0024-7204T	-0.330	0.340	-0.40 ± 0.2	1.347	-0.790
J0024-7203U	-0.478	1.316	$-1.20^{+0.3}_{-0.2}$	1.324	-1.006

Table 5.1: The position and velocity of each pulsar, given in <http://www.naic.edu/~pfreire/47Tuc/>. The distance along the LOS and the uncertainty are taken from Freire et al. (2003). *The LOS position of the S-pulsar is an estimation, as the actual distance is not included in Freire et al. (2003).

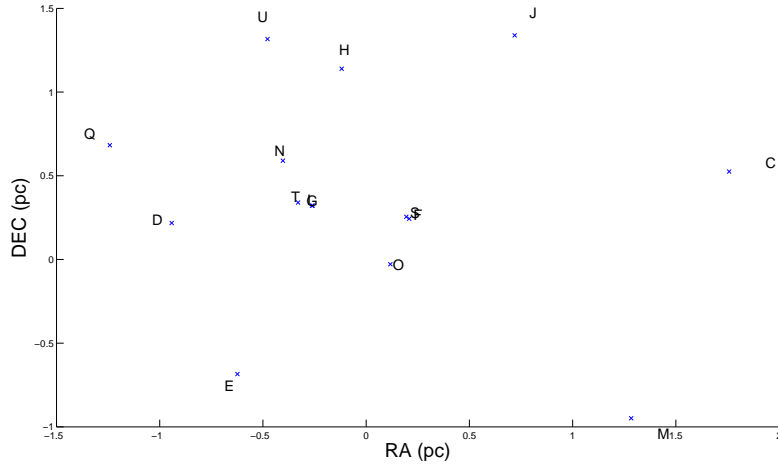


Figure 5.1: RA and DEC of each pulsar. The RA and DEC values are given in <http://www.naic.edu/~pfreire//47Tuc/> and the units have been converted into parsecs.

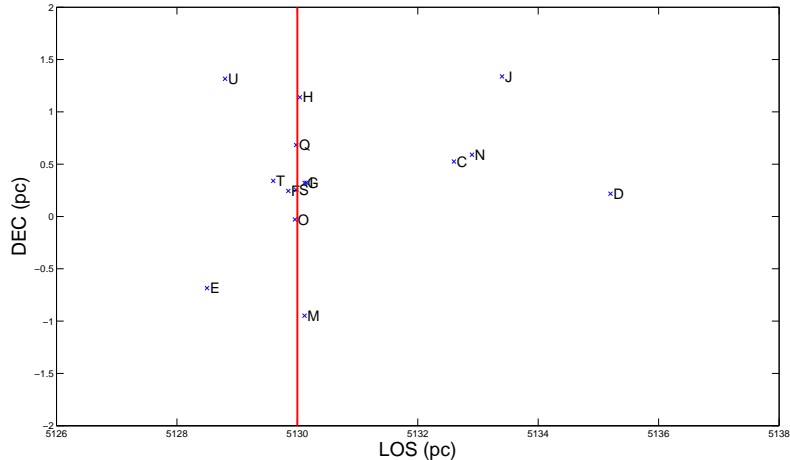


Figure 5.2: DEC and the distance along the LOS for each pulsar. See Freire et al. (2003) and Table 5.1 for errors in pulsar position along the LOS (not drawn in figure). The red line shows the distance from the observer to the centre of 47 Tucanae (5130 pc).

5.1 Sample realisations

The initial conditions for each realisation are given in Table 3.1. The globular cluster is 5130 pc away from Earth, containing 10^6 stars (instead of 10^5 stated in Table 3.1). The position of each star was generated using a Gaussian distribution with a $\sigma_{\text{star}} = 5$ pc, and the velocity for each star was generated using a Gaussian distribution with $\sigma = 13200 \text{ m s}^{-1}$ (Webbink 1985). The total observation time is 3600 days, at intervals of 30 days. The 15 observed pulsar positions and velocities are given in Table 5.1 instead of generating these two parameters using a Gaussian distribution.

For each realisation (including simulations A1 to A3) a different value for the position and velocity of the stars is generated. This change in the configuration of the stars leads a different value of the Shapiro noise along the LOS of the pulsar, leading to a different value for the timing residuals.

5.1.1 Simulation A1

Figure 5.3 shows that the structure – cubic, or dominated by the third order – of the timing residual is very similar for every pulsar. This is similar to the case described in Section 4.4.1, indicating that the closest star is approximately a parsec away in the plane perpendicular to the LOS. The differences in timing residuals for each pulsar are the magnitudes, ranging from 10^{-8} to 10^{-11} seconds. This is affected by the position of the star with respect to the pulsar, as well as the velocities of both star and pulsar.

The timing residuals for the D-pulsar look similar to the case described in Section 4.4.1. For this case, the separation between the star and the pulsar is much greater than the other pulsars. This results in a smaller Shapiro noise, and hence smaller timing residuals. The minimum separation between a star and the C, F, N and Q-pulsars are inbetween the cases described in Section 4.4.1, and as a result the cubic structure is not as smooth as the other cases.

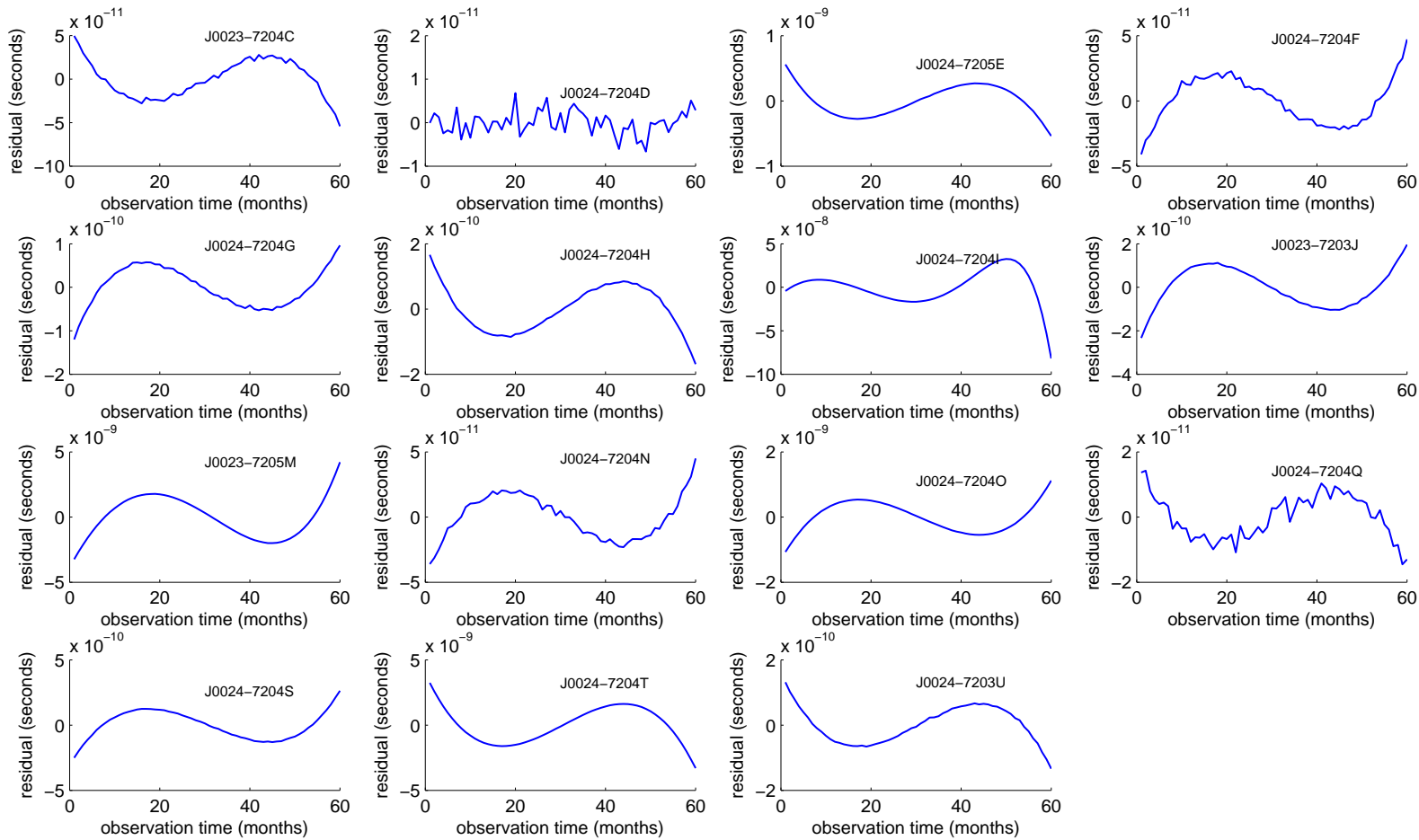


Figure 5.3: Simulation A1: Timing residuals from a sample run of a globular cluster containing 10^6 stars.

5.1.2 Simulation A2

For most pulsars the second realisation (Figure 5.4) produces timing residuals that were similar to the first realisation, as the timing residuals are dominated by the cubic (third order) term. This, again, means that the perpendicular distance between the closest star and the LOS to the pulsar is approximately a parsec away.

This realisation however produces an interesting timing residual for the N-pulsar. The timing residuals is not a cubic for this pulsar but of higher order. The ‘spike’ at 30 months may be a result of a transiting star, as described in Section 4.4.1 Curiously, the Q-pulsar has a similar timing residual – the peak is offset slightly. From Figure 5.1 and Figure 5.2 the N and Q pulsars are far apart from one another, and therefore it is highly unlikely that the same star transitted across the LOS for each pulsar and affected the timing residual. The most likely explanation for the similarity is that two different stars transitted across two different LOS at approximately the same time. Since there are 10^6 stars in the simulation, the probability for this happening is small, but non-zero (see Section 2.8).

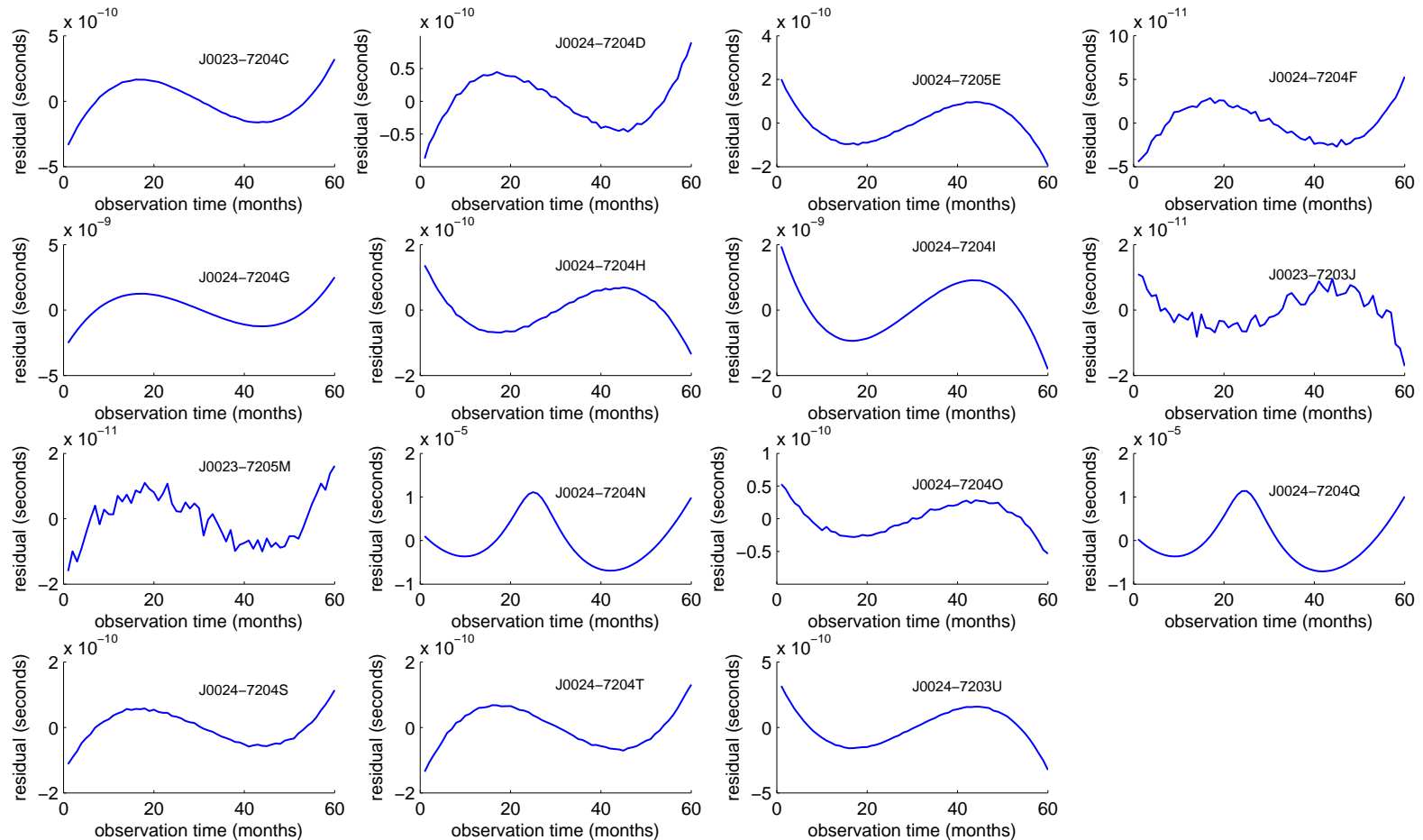


Figure 5.4: Simulation A2: Timing residuals from a sample run of a globular cluster containing 10^6 stars.

5.1.3 Simulation A3

The third realisation shows that for a large portion of the pulsars the minimum separation is large (> 1 pc). The timing residuals for the majority of the pulsars look similar to the case shown in Section 4.4.1. The timing residuals for the C, G, M and T pulsars are similar to that of random noise. Only two pulsars (D and S) have timing residuals of the order of nanoseconds, the other pulsars all have timing residuals that are much smaller.

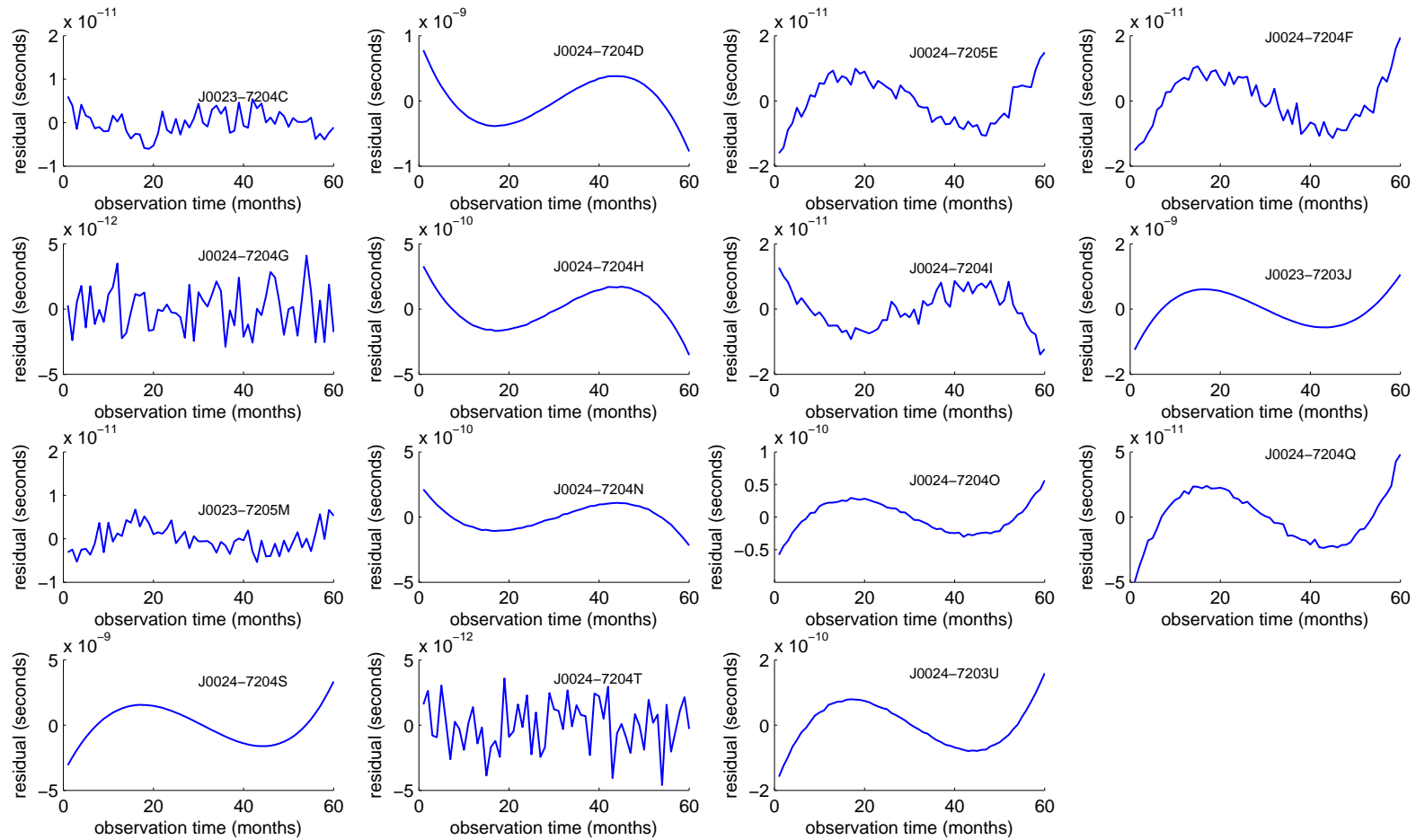


Figure 5.5: Simulation A3: Timing residuals from a sample run of a globular cluster containing 10^6 stars.

5.1.4 Summary of realisations

The realisations show that the timing residual for each pulsar is dependent on the generated positions and velocities of the stars. As a result the magnitude and RMS of the timing residuals (as well as the function of timing residuals over observation time) can vary significantly with each realisation. Therefore a lot (~ 100) of realisations were done in order to determine the average RMS timing residuals and also the spread, or σ of the RMS timing residuals for each pulsar. If the average RMS timing residuals for each pulsar is the same after 100 realisations, this may indicate that either (i) the Shapiro noise affects the timing residuals for each pulsar in the same way, or (ii) the globular cluster used in the MC simulation was made so big causing the core of the cluster to envelop all the pulsars.

Pulsar	$\langle t_{\text{RMS}} \rangle (10^{-9}\text{s})$	$\sigma (10^{-9}\text{s})$
J0023-7204C	147.009240	982.738571
J0024-7204D	3.537374	12.531174
J0024-7205E	53.258640	293.158848
J0024-7204F	4.891511	13.950917
J0024-7204G	1.595120	3.501558
J0024-7204H	5.031296	19.895663
J0024-7204I	39.940922	263.464447
J0023-7203J	5.520901	12.464959
J0023-7205M	12.965606	73.150190
J0024-7204N	384.411153	1785.343614
J0024-7204O	4.230011	16.808911
J0024-7204Q	188.637896	1150.045422
J0024-7204S	72.202016	465.668874
J0024-7204T	4.079968	13.392077
J0024-7203U	1.034556	3.318412

Table 5.2: The average and variance RMS value for the timing residual for each pulsar in a 10^6 star 47 Tucanae.

Table 5.2 shows the RMS timing residual for each pulsar in the MC simulation. The magnitudes of the timing residuals, considering the Shapiro noise was the

only noise term in pulsar timing, are of the order of nanoseconds. The Shapiro noise will be a significant effect in actual observations.

The variance σ of the timing residuals is much larger than the average values. This indicates that, for some realisations of the MC simulation, there is a star positioned close to the LOS that produces a high timing residual for that pulsar. The average values however suggest that such an event is rare, and that for most realisations the nearest stars are positioned further away, of the order of a parsec. However, there are a few realisations where the configuration of the stars produces a large timing residual. Figure 5.6 shows the distribution of the RMS timing residual values for the I-pulsar, for 100 realisations. For 90 realisations, the RMS timing residual is of the order of 10^{-8} to 10^{-9} s, however there are ten realisations producing larger (order of 10^{-6} to 10^{-7} s) RMS timing residuals. These latter realisations are the reason why σ is much larger than the average RMS timing residual for the I-pulsar. If more (~ 1000) realisations were done, it will most likely result in a small number of realisations filling the gap between 10^{-6} to 10^{-7} s in Figure 5.6, but most of the realisations will be in the 10^{-8} to 10^{-9} s region.

The large σ values show that, while lensing events are rare, they do happen in the simulations. Therefore, σ gives an indication on how likely it is for a star to be close to the LOS of a particular pulsar. The larger σ is compared to the average RMS timing residual, the more likely it is for a star to be close to the LOS, and it is more likely for a real lensing event to be present in the observed data. The variance does however come with one drawback: if there is one realisation where the timing residual is sufficiently large (say, 100 times larger than the average RMS timing residual), this will result in a σ -value that is not a true reflection of observed data. The difference between one realisation and another is the random generation of the position and velocity of the stars, and in the confines (i.e. dimensions) of the globular cluster, the probability of a star randomly generated close to the LOS is non-zero. Therefore, it should be

stressed that such an event is very rare (non zero probability), and as a result determining the average and the variance of the RMS timing residual is a good indicator of the magnitude and fluctuation of the timing residual for each pulsar.

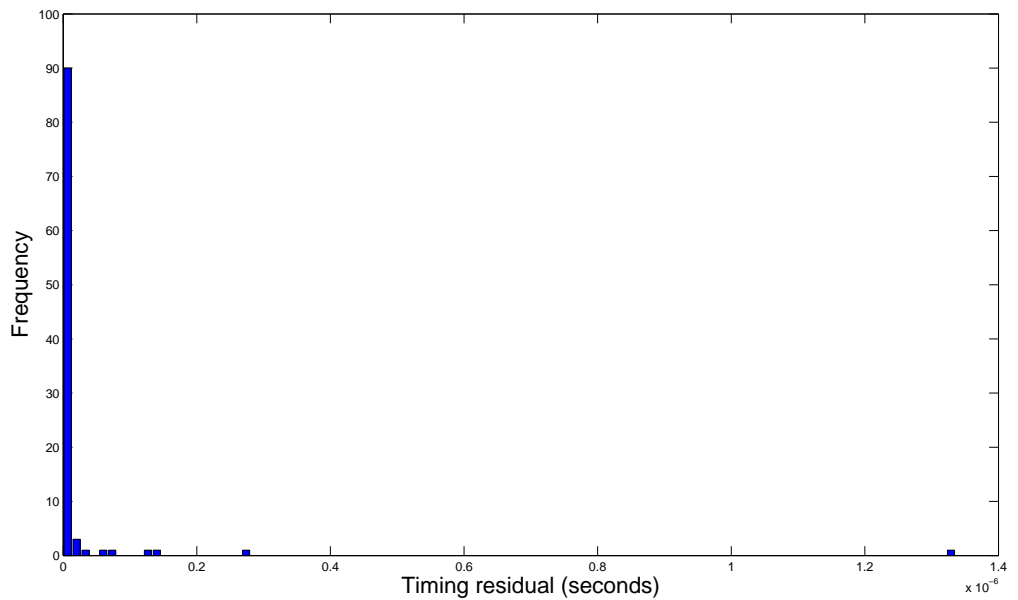


Figure 5.6: Histogram of the RMS timing residuals for 100 realisations for the I-pulsar.

The largest RMS timing residual value is for the N-pulsar, followed by the C- and Q-pulsars. From above, this may be the result of a star being very close to the LOS for one of the realisations.

Apart from these three pulsars, the timing residuals of the other pulsars are of the order of 10^{-9} s, for a globular cluster containing 10^6 stars. This is a curious result, as observations have shown that the timing residuals of the pulsars (in 47 Tucanae) are very different from one another (see Section 7.2). This uniformity in the timing residuals suggest that the stellar distribution is uniform for all pulsar LOS, with the occasional close star causing large deviations in the timing residuals. This uniform characteristic of the timing residuals may originate from the fact that the distributions used to generate the stars used a large variance σ .

This value was chosen when the analytical prediction and the numerical simulation were being compared, and was not estimated from observations. Therefore this mass distribution may not reflect the actual mass distribution of 47 Tucanae.

5.2 Optimizing the MC Simulation

Let us for a moment assume that the Gaussian sphere used in the simulations is an adequate reflection of the actual stellar distribution. In Section 4.4.1 it was shown that stars close to the LOS produce the largest change in the Shapiro delay, and therefore the largest effect in timing residual. Since stars far away from the pulsar contribute the least to the timing residual one can ask the question “how close to the pulsar does a star have to be in order to significantly contribute to its timing residual?”. If the contribution is small, for example $< 0.001\%$, then, as long as every (10^8) star does not contribute in this manner it is possible to neglect the star.

From the time delay function, it is clear that the contributions get smaller with increasing distance from the LOS. So a “cut-off” radius – a radius where the stellar contribution becomes negligible – can be implemented into the MC simulation to filter out stars that are not within this region. This optimises the MC simulation as it does not require all the stars (10^8) but only a fraction of them to obtain, to an adequate approximation (for example over 95%), the timing residual of the entire globular cluster.

To determine this cut-off radius, let us revert to the MC simulation of one pulsar at the centre of the globular cluster. Using the MATLAB command `sortarray` it is possible to sort the stars in order of distance from the pulsar. Using the sorted stars, the cut-off radius was determined in the following manner.

5.2.1 Cumulative Distribution Function

At first, the Shapiro noise for the closest star was determined by the MC simulation. From this, its timing residual and t_{RMS} (the RMS of the timing residual) were determined. Then, the second closest star was introduced, and the Shapiro noise, timing residual, and t_{RMS} were determined for this two-star system. This process of adding one star at a time was repeated until all the stars were included. The t_{RMS} values from each iterative simulation were then divided by the total t_{RMS} , obtained from the final (all stars) simulation. This procedure indicates how much each iteration contributes to the final timing residual. The cumulative distribution function (CDF) of the timing residual can then be used to determine how many stars – and what radii – should be included in order to obtain a significant fraction of the total timing residual. This MC simulation was repeated 100 times to estimate the average cut-off radius.

Figure 5.7 shows the CDF for different total numbers of stars in a globular cluster. The CDF varies with the total stellar number from the globular cluster. For the case of 10^5 stars, the CDF is around 0.98, or 98% of the total timing residual, when determining the Shapiro noise using the nearest 1000 stars to the pulsar. This means that only the nearest 1000 stars are necessary to accurately (98%) predict the total timing residual for the entire globular cluster containing 10^5 stars. More nearby stars are needed to achieve such CDF values for higher total stellar numbers. Curiously, the CDF for 5×10^5 and 2×10^6 stars seem very similar to one another. It was predicted that the CDF for 2×10^6 stars would have been flatter than that of 1×10^6 stars, as more stars should be required in order to accurately determine the timing residual.

Let us now plot the CDF as a function of the fraction of the number of stars. The fraction is defined as the nearest number of stars to the pulsar divided by the total number of stars inside the globular cluster. The results are shown in Figure 5.8. This shows that the CDF for 2×10^6 stars is the steepest, and the

5: DETERMINING TIMING RESIDUALS FROM MC SIMULATION

CDF for 10^5 stars to be the flattest. All four CDF's converge at a stellar fraction of ~ 0.1 .

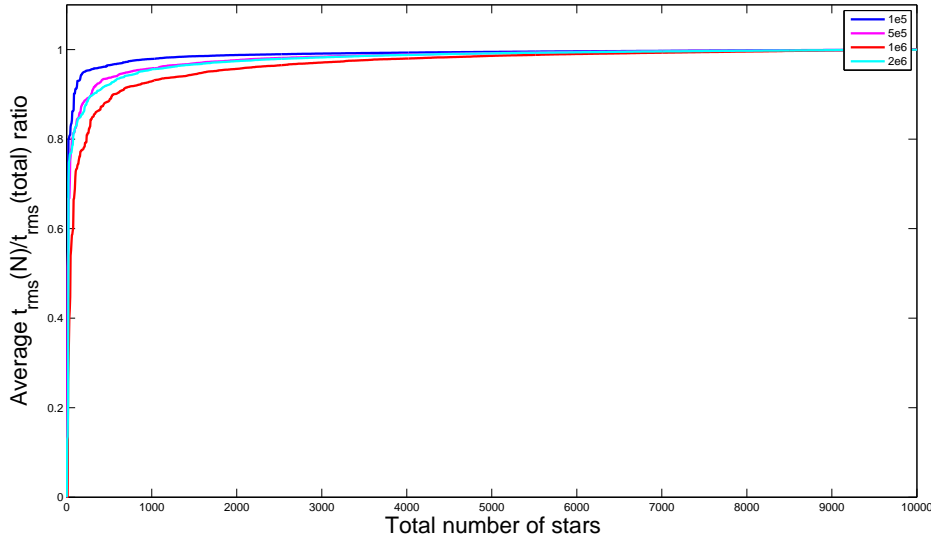


Figure 5.7: Comparison of the cumulative distribution function (CDF) for different number of stars in a globular cluster.

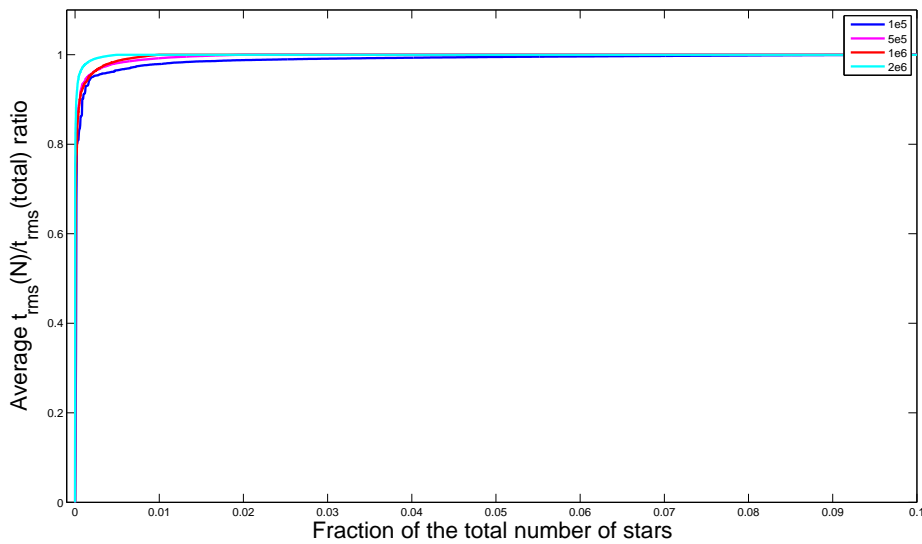


Figure 5.8: Comparison of the cumulative distribution function (CDF) for different number of stars in a globular cluster.

What is interesting to note is that the CDFs do not lie on top of each other. This most likely stems from nature of the Shapiro noise. While some stars may be closer to the pulsar, the configuration with respect to the LOS may result in these stars not producing the largest Shapiro noise. For example, a closest star at distance r away from the pulsar but between the pulsar and an observer will produce a larger Shapiro noise than a star at the same distance r but behind the pulsar with respect to the observer. In addition, since the velocities of the stars were generated at random, some stars further away from the pulsar (i.e. not the closest) that have a faster velocity (along the plane perpendicular to the LOS) may produce a larger timing residual compared to the closest pulsar. This is because the faster velocity of the star the greater the change in the configuration of the star with respect to the LOS, which produces a large Shapiro noise. These may be the reasons why the CDF's do not align with one another when plotted as a function of the fraction of stars.

This result suggests that, while it is necessary to include more stars (for the larger globular clusters), the total fraction needed in order to achieve an accurate value of the timing residual for the globular cluster is very similar. From the different stellar counts modeled, the fraction necessary to achieve 0.95 of the total timing residual for the globular cluster is ~ 0.05 of the total stars.

5.2.2 Cylinder approximation

From above it was noted that it was necessary to only model a fraction of the total number of stars (closest to the LOS) to produce an accurate value of the timing residual for the entire globular cluster. Let us now determine a cut-off radius – this is the distance (from the LOS) necessary for a star to have an effect on the timing residuals. Using this distance it is possible to approximate the stars occupying a volume around the LOS which has a cylindrical shape (circular area in the plane perpendicular to the LOS, stretched along the LOS). This cut-off is

5: DETERMINING TIMING RESIDUALS FROM MC SIMULATION

not to be confused with the detection radius (Section 2.8.1). The detection radius is the minimum distance between a star and the LOS for a given distribution (to determine whether a lensing event happens), whereas this cut-off radius is the distance between a star and the LOS necessary for a star to have an effect on the timing residuals. Therefore, $\xi_{\text{cut-off}} \gg r_{\text{det}}$.

Figure 5.9 shows the two-dimensional (plane perpendicular to LOS) distribution of the stars from the centre of the globular cluster in our simulations. Let us assume that the pulsar is at the centre of this globular cluster, at $r = 0$. The stars that will greatly affect the timing residual would be in the region shown in the black box in Figure 5.9. These are analogous to the 5% of total stars discussed previously. In this box the Gaussian distribution can be assumed to be flat. This assumption is necessary when determining the cut-off radius, and hence the cylinder.

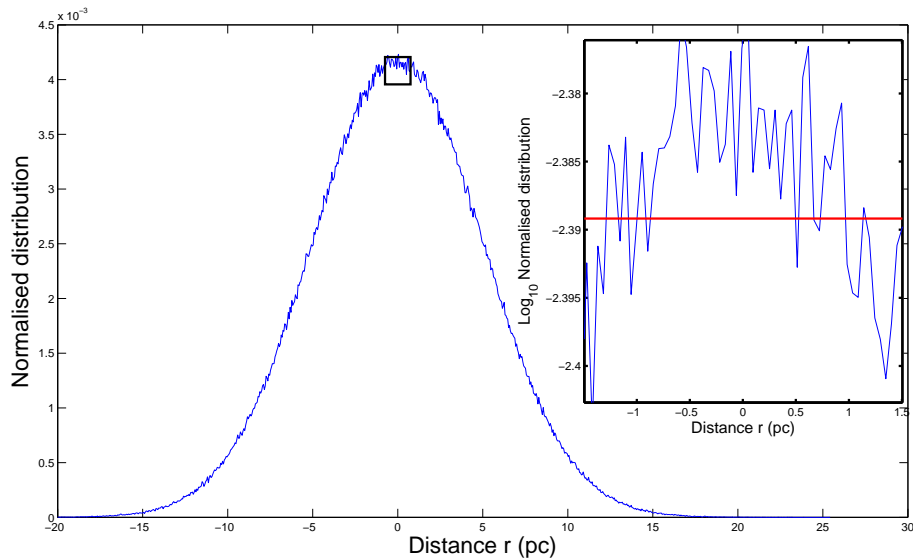


Figure 5.9: The cylinder approximation for a Gaussian distribution.

Let us now calculate how many stars (out of the original number) are present

inside this cylinder. This value is determined by:

$$\text{Number of stars in cylinder} = \int_{\text{cylinder}} \rho \, d(Vol) \quad (5.3)$$

where ρ is the density within the cylinder. The density is determined by the distribution used in the MC simulation, hence:

$$N = \frac{N_0}{(2\pi\sigma^2)^{\frac{3}{2}}} \int \exp\left[-\frac{x^2 + y^2 + z^2}{2\sigma^2}\right] dx \, dy \, dz \quad (5.4)$$

where N_0 is the total number of stars. Since the distribution around the LOS can be approximated as being uniform, it is possible to simplify the distributions in y and z so that:

$$N \approx \frac{N_0}{(2\pi\sigma^2)^{\frac{3}{2}}} A \int_{-\infty}^{\infty} \exp\left[-\frac{x^2}{2\sigma^2}\right] dx \quad (5.5)$$

where $A = \pi\xi_0^2$, the area around the LOS, with ξ_0 being the radius of this circle. The integration has the solution $\sqrt{2\pi\sigma^2}$, and hence:

$$\begin{aligned} N &= \frac{N_0}{2\pi\sigma^2} \pi \xi_0^2 \\ &= \frac{N_0}{2} \left(\frac{\xi_0}{\sigma}\right)^2 \end{aligned} \quad (5.6)$$

From the CDF the number of stars required was determined to be 5% (see Section 5.2.1), so the cut-off radius can be derived by rearranging this equation:

$$N(\xi_{\text{cut-off}}) = \frac{N_0}{2} \left(\frac{\xi_{\text{cut-off}}}{\sigma}\right)^2 \quad (5.7)$$

$$\Rightarrow \xi_{\text{cut-off}} = \left(\frac{2N(\xi_{\text{cut-off}})}{N_0}\sigma^2\right)^{\frac{1}{2}} \quad (5.8)$$

which results in $\xi_{\text{cut-off}} = 1.58$ pc.

5.2.3 Comparison of the cut-off distance derived from the cylindrical approximation with the simulation prediction

Let us now compare the cut-off distance derived from the analytical solution with the MC simulation used to determine the CDF.

Figure 5.10 shows how ξ_0 varies as a function of the number of stars (starting from the nearest one to the pulsar). The lower the number, the nearer the star is to the pulsar. Figure 5.11 shows how ξ_0 varies as a function of the fraction of total stars. The fraction is defined as the number of stars nearest to the pulsar divided by the total stellar count in the globular cluster. The two figures indicate that the radii enclosed by 5% of the total star count is approximately 1.52 pc, which is consistent with the analytical prediction.

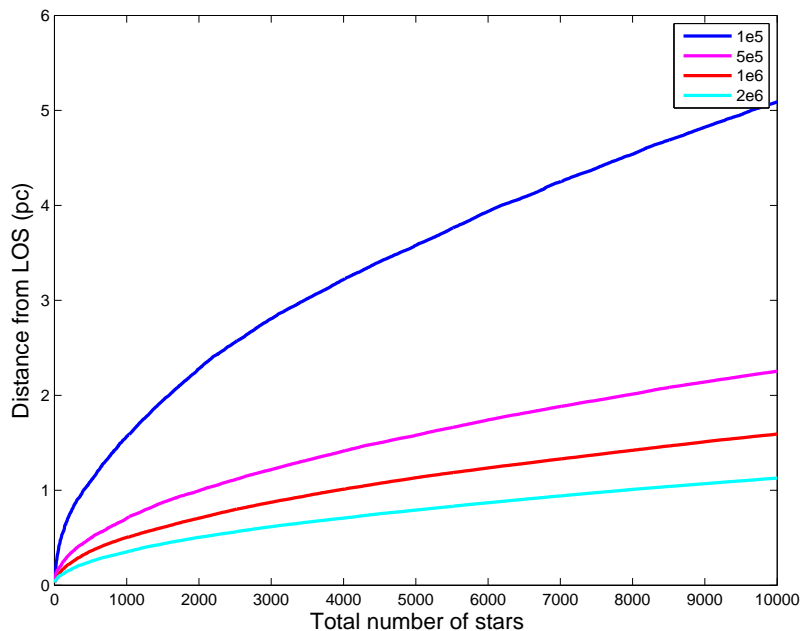


Figure 5.10: Comparison of ξ_0 as a function of the number of stars for varying total number of stars in a globular cluster.

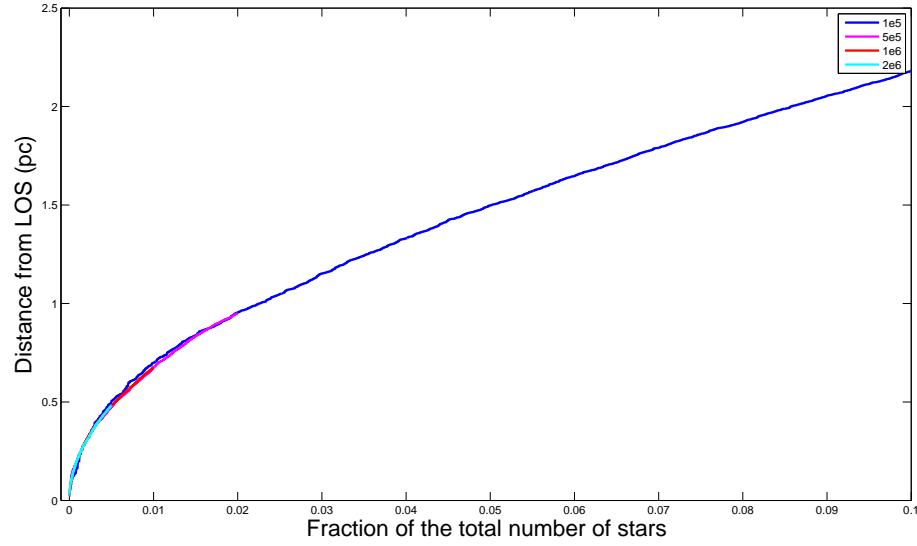


Figure 5.11: Comparison of ξ_0 as a function of the number of stars for varying total number of stars in a globular cluster.

5.2.4 Comparison of the timing residual of the optimised simulation with the MC simulation

It is now important to confirm that the optimised simulation does give the desired result, i.e. it is necessary to compare the root mean square of the timing residual, $\langle t_{\text{RMS}} \rangle$, between the optimised and the full MC simulation for a varying number of total stars. The MC simulation was done for multiple realisations, and an average $\langle t_{\text{RMS}} \rangle$ was determined, shown in Table 5.3. Table 5.3 shows there is minimal difference in the timing residuals between the optimised and the full simulation.

Number of stars	Optimised simulation $\langle t_{\text{RMS}} \rangle$	Full simulation $\langle t_{\text{RMS}} \rangle$	Ratio
	(10^{-10} s)	(10^{-10} s)	
1×10^5	1.009231	1.009182	1.000048
5×10^5	4.418820	4.419067	0.999944
1×10^6	16.058432	16.059773	0.999916
2×10^6	12.086644	12.086546	1.000008

Table 5.3: Comparison of $\langle t_{\text{RMS}} \rangle$ values of the optimised simulation with the full simulation, for a different number of total stars in the globular cluster.

5.3 Summary

In this chapter the timing residual for a pulsar in a globular cluster containing 10^6 stars is predicted using MC simulation. The actual positions of the pulsars in 47 Tucanae were used in order to determine the timing residual for each pulsar. From the MC simulation the majority of the timing residuals are the order of 10^{-8} to 10^{-9} seconds. The variance for the timing residuals suggest that while for most realisations the RMS timing residual is small (of the order of 10^{-9} s), there are a few realisations where a star does get sufficiently close to the LOS, resulting in a large RMS timing residual. This also showed that, while the probability of a lensing event is low, it is non-zero.

Since the majority of the pulsars had timing residuals of similar magnitude an investigation was done to determine whether the MC simulation could be optimised in order to speed up the process of calculating these residuals. It was shown that, for a stellar distribution that can be represented as a Gaussian sphere, it was only necessary to simulate the nearest 5% of the stars along the LOS of the pulsar in order to obtain timing residuals that are an accurate (95%) representation of the timing residual obtained when modeling all the stars in the globular cluster.

6

Stellar distribution

Until this moment the assumption was made that the stellar mass distribution in 47 Tucanae could be modeled using a Gaussian distribution in all three Cartesian (x, y, z) co-ordinates. The core of 47 Tucanae is undergoing dynamical evolution, which results in a centre of gravity of the globular cluster being offset from the luminosity centre (Calzetti et al. 1993). This results in a more concentrated core inside a core. From Calzetti et al. (1993) this distribution is described as a double King profile (King 1966) projected on the plane perpendicular to LOS (y, z in our co-ordinate system) shown by,

$$\rho(\xi) = \rho_0 \left[\frac{1}{1 + a^2 \xi^2} + \frac{1}{1 + b^2 \xi^2} \right], \quad (6.1)$$

where $a = \frac{1}{r_{cc}}$ is the canonical core radius (25 arcseconds, Djorgovski and King 1984) and $b = \frac{1}{r_c}$ is the core radius in the region < 13 arcseconds (8 arcseconds, Calzetti et al. 1993). Since this is a mass distribution that is *projected* onto the plane, an inverse Abel transform is made in order to change this into a 3D distribution. The inverse Abel transform is given by

$$f(r) = -\frac{1}{\pi} \int_r^\infty \frac{dF(\xi)}{d\xi} \frac{d\xi}{\sqrt{\xi^2 - r^2}}, \quad (6.2)$$

where ξ and r are the 2D and 3D radius, respectively, $F(\xi)$ and $f(r)$ are the 2D and 3D mass distributions, respectively. Implementing Equation 6.1 the inverse

Abel transform shows that the three dimensional mass distribution is

$$\rho(r) = -\frac{1}{\pi} \int_r^\infty \frac{d\rho(\xi)}{d\xi} \frac{d\xi}{\sqrt{\xi^2 - r^2}} \quad (6.3)$$

$$= \frac{2\rho_0}{\pi} \left[\int_r^\infty \frac{a^2\xi}{(1+a^2\xi^2)^2} \frac{d\xi}{\sqrt{\xi^2 - r^2}} + \int_r^\infty \frac{b^2\xi}{(1+b^2\xi^2)^2} \frac{d\xi}{\sqrt{\xi^2 - r^2}} \right] \quad (6.4)$$

$$= \frac{\rho_0\pi}{2} \left[\frac{1}{a} \frac{1}{(a^2r^2+1)^{3/2}} + \frac{1}{b} \frac{1}{(b^2r^2+1)^{3/2}} \right], \quad (6.5)$$

where the identity ,

$$\int_r^\infty \frac{\xi}{(1+a^2\xi^2)^2} \frac{d\xi}{\sqrt{\xi^2 - r^2}} = \frac{\pi}{4a} \frac{1}{(a^2r^2+1)^{3/2}}, \quad (6.6)$$

was used. From the three dimensional distribution it is possible to generate the Cartesian (x, y, z) co-ordinates by having first generated the spherical polar co-ordinates (r, θ, ϕ). It is assumed that the distribution of θ and ϕ is isotropic. The distance r is generated from the cumulative distribution function of $\rho(r)$, and the values of θ and ϕ are generated as shown in Figure 6.1.

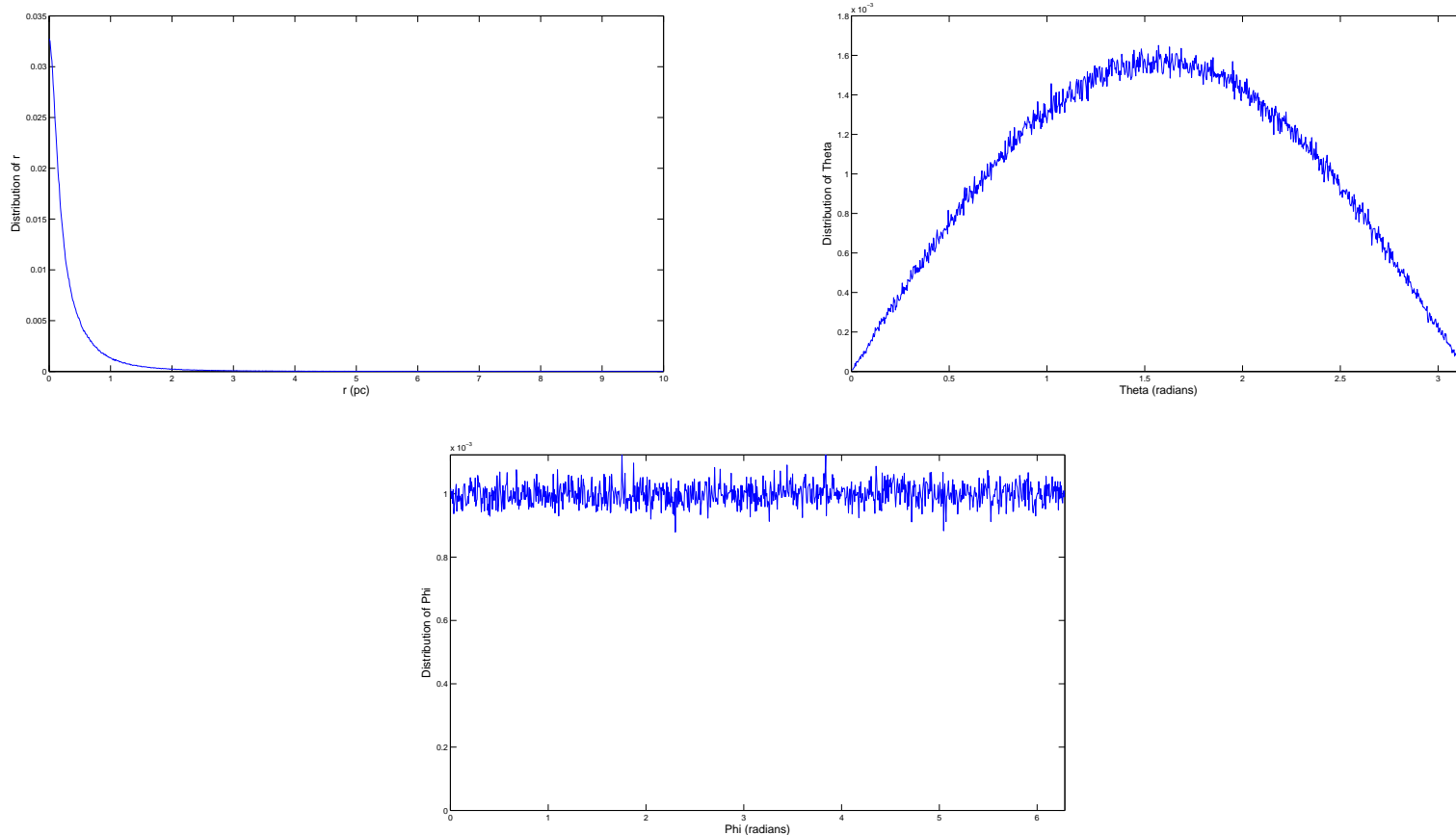


Figure 6.1: Distribution of r , θ , and ϕ to change the distances from spherical to Cartesian (x,y,z) co-ordinates.

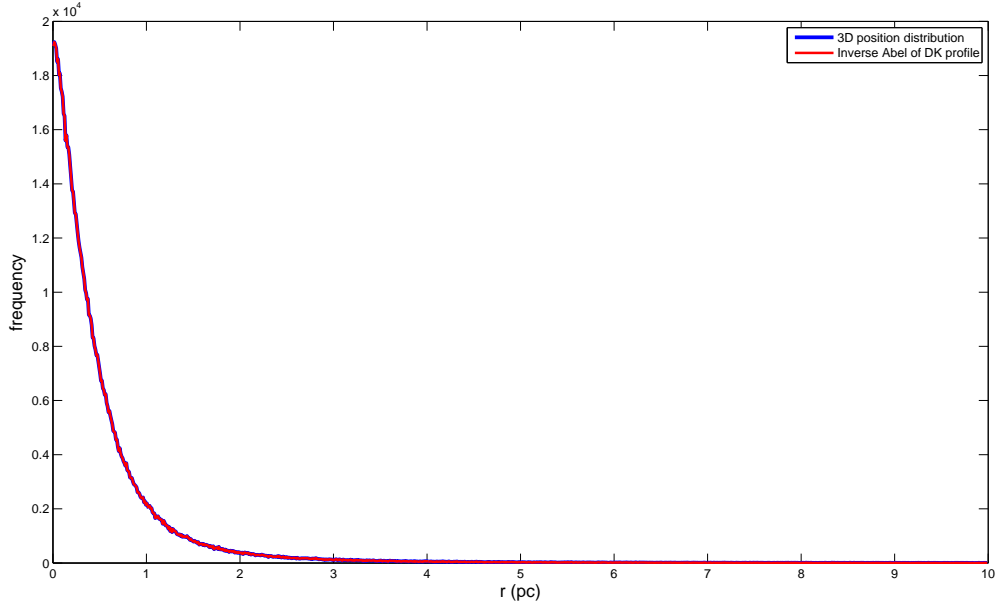


Figure 6.2: Comparison with the three dimensional position distribution in the simulation and the double king profile.

Figure 6.2 shows the comparison between the inverse Abel transformed double King profile, and the generated r that is used in the simulations. The agreement between the two is very good in the three dimensional case. In order to verify whether the co-ordinates were properly generated, let us project the distribution of the generated radii (to the plane perpendicular to the LOS) with the radial distribution of distance using the double King profile. Figure 6.3 shows that the agreement between the analytical and numerical simulation is also very good in the two dimensional case. This implies that the initial condition, generation of stellar position, is correct for both 2D and 3D. The stellar distribution is more concentrated in the centre of the globular cluster than the Gaussian sphere. This suggests that pulsars close to the centre of globular clusters will be affected the greatest – and will also have the largest magnitude – compared with those pulsars further away. Therefore, this updated mass distribution is expected to have a larger effect on the pulsars at the centre, and (almost) negligible effect on

pulsars further away. In addition, since the distribution is more concentrated than the triple-Gaussian distribution, the “cylinder approximation” may no longer be valid, as the majority of stars may have to be included in order to determine Δt_{Sh} .

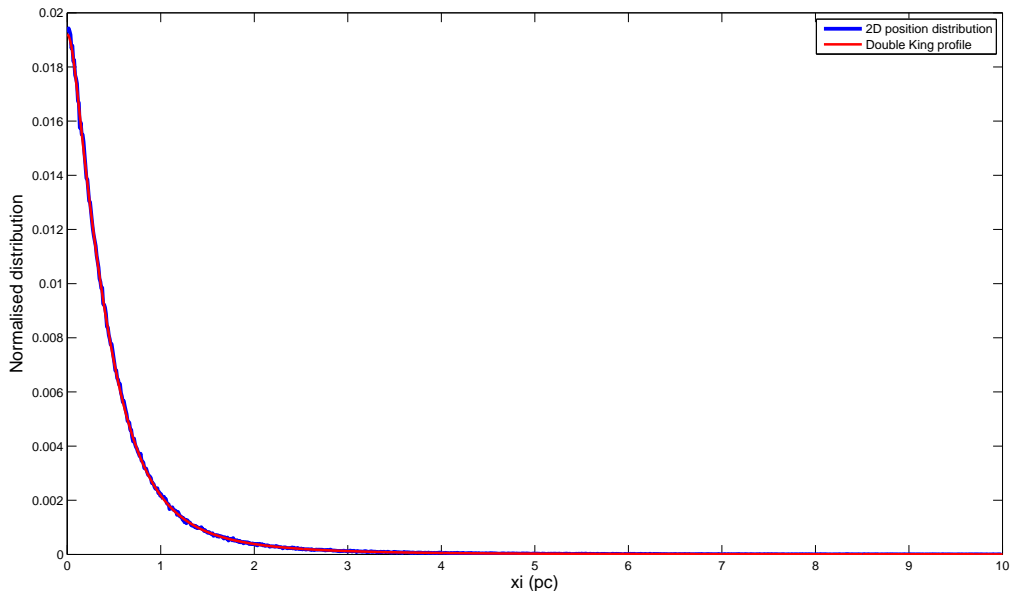


Figure 6.3: Comparison with the two dimensional position distribution in the simulation and the double king profile.

6.1 Timing residuals

Figures 6.4 to 6.6 shows three realisations of the simulations to determine timing residuals taking into account the new stellar distribution, obtained from the inverse Abel transform. Other than using the double King profile used to distribute the stars in the globular cluster, the initial conditions for the simulations are the same as Section 5.

6.1.1 Simulation B1

In this realisation the timing residual with the largest magnitude is the O-pulsar. This pulsar is also the closest to the centre of the globular cluster. The G-pulsar, also very close to the centre, has the second largest timing residual value. As there is a very dense region of stars at the centre of the globular cluster, there is a greater probability of stars being adequately close to the LOS of the pulsars which produce a large Shapiro noise. As a result the pulsars in the central regions of the globular cluster – the two above and the J, N, and S-pulsars – have large timing residuals.

The pulsar with the lowest timing residual is the U-pulsar. This pulsar is very far from the centre of the globular cluster, in terms of both the plane perpendicular to LOS and radial distance. As a result, there may not have been many stars present in the vicinity of its LOS in order to produce a large Shapiro noise, and hence the Shapiro noise had little effect on the timing residual. The same can be said about the M-pulsar, which has the second smallest timing residual value.

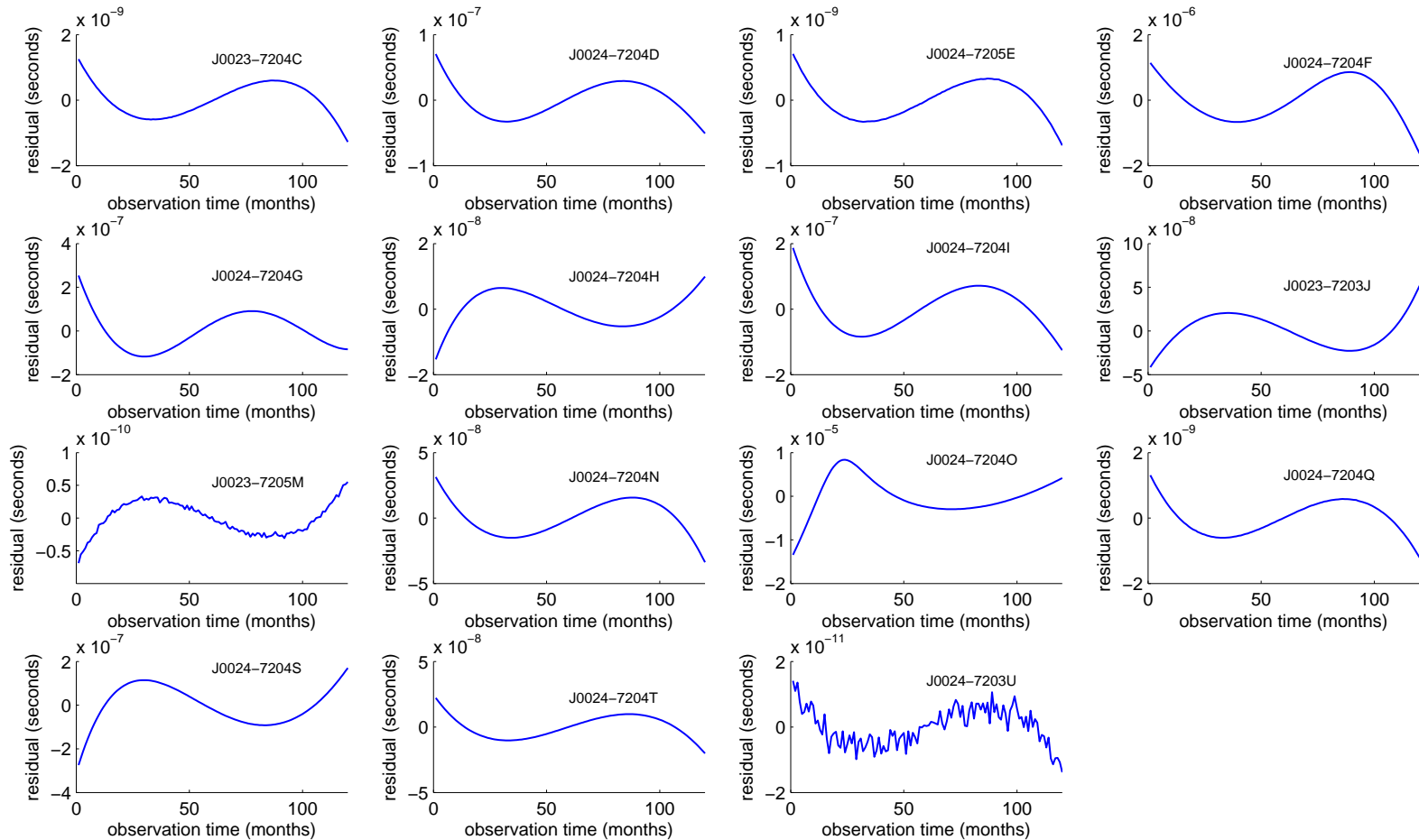


Figure 6.4: Simulation B1: Timing residuals from a sample run of a globular cluster containing 10^6 stars using a double King profile to generate the stars within the globular cluster.

6.1.2 Simulation B2

This realisation is different from the first realisation as the pulsar with the smallest timing residual seems to be the E-pulsar. This suggests thats, for this particular realisation, there were very few stars close to its LOS.

The timing residual for the I-pulsar for this realisation shows an interesting structure. The timing residual seems to be dominated not by the third order (as is the case for the other pulsars) but by effects of a higher order, possibly fourth or higher order. This may be an indication that towards the end of the simulation a star was getting very close to this pulsar's LOS in order to have a large effect. Upon investigating the simulated data it turns out that this indication is incorrect – there are no stars that were getting very close to the pulsars LOS. There was however one star close to the pulsar that moved past the pulsar in the direction parallel to the LOS. This resulted in a sudden change in the Shapiro noise.

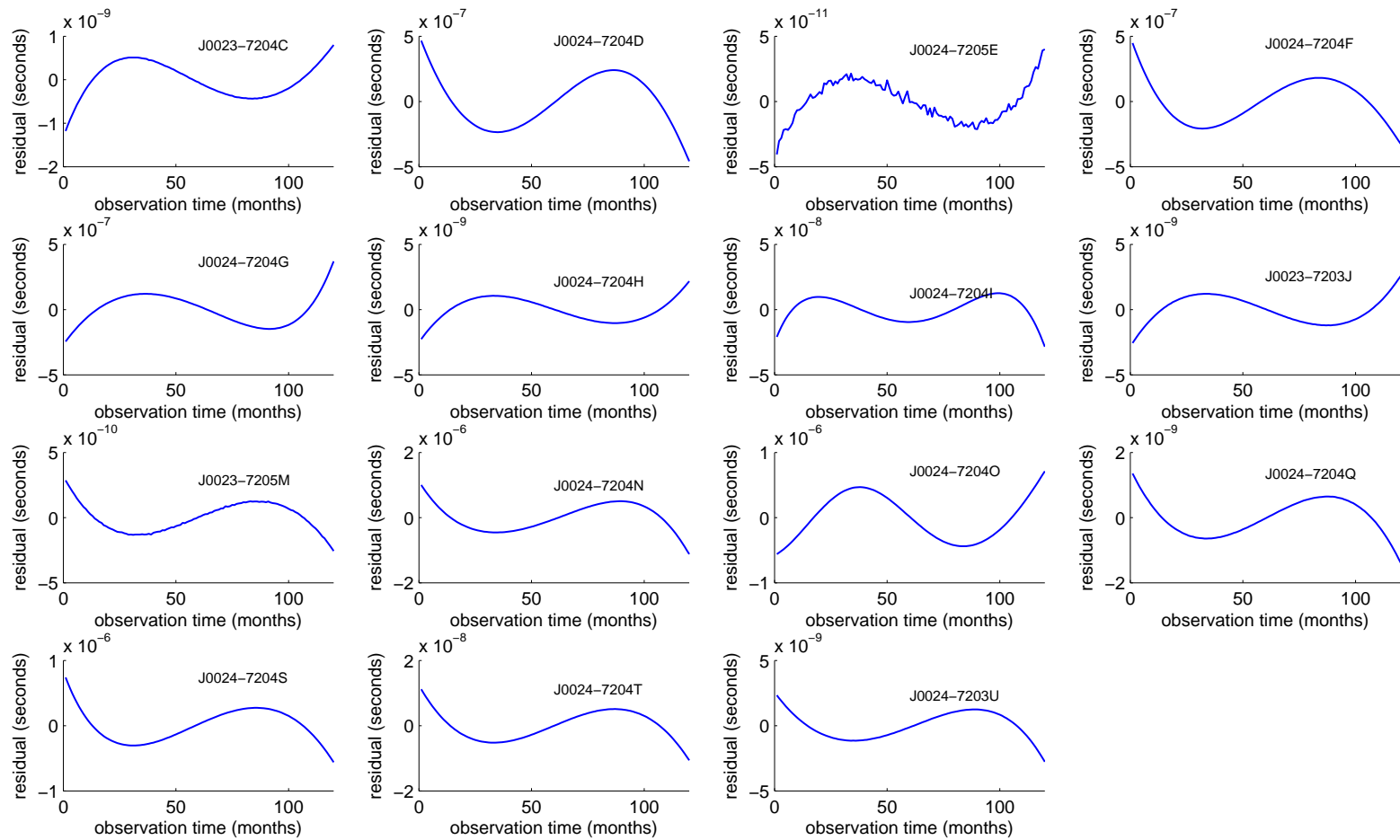


Figure 6.5: Simulation B2: Timing residuals from a sample run of a globular cluster containing 10^6 stars using a double King profile to generate the stars within the globular cluster.

6.1.3 Simulation B3

In this realisation the timing residuals for a lot of pulsars were dominated by the fourth or fifth order. In particular, the timing residuals of the S, I, and O-pulsars have a distinct peak, and the timing residual of the M-pulsar seems to have similar properties to that of the I-pulsar in Simulation B2. The peaks in the S, I, and O-pulsars may be attributed to a star approaching fairly closely to the LOS. The star along the LOS of the S-pulsar was most likely the closest of the three.

While it was initially thought that the timing residuals for all three pulsars were affected by the same star – as the three pulsars are in close proximity to one another and the peaks for the I- and O-pulsar happened almost at the same time – it is most likely that three different stars affected the three pulsar timings. First of all, the distances between the three pulsars are so large that a 1 M_\odot star could not have had such a large effect on each pulsar. Secondly, such an effect would also be present on the timing residuals of other nearby pulsars, such as the G-pulsar. However, as the G-pulsar does not feature such a peak, therefore it is more likely, for this particular realisation, that three different stars affected the timing residuals of the three different pulsars. Upon investigating the simulated data the timing residuals of the three pulsars were indeed affected by three different stars. The star that caused the peak in the timing residual of the S-pulsar was the closest of the three, at $\sim 8 \times 10^{-4}$ pc traveling at the fastest velocity (in a plane perpendicular to the LOS) of the three at $\sim 12\,000\text{ m s}^{-1}$. The star that caused the peak in the timing residual for the I-pulsar is the second closest, at $\sim 4 \times 10^{-3}$ pc traveling at $\sim 10\,000\text{ m s}^{-1}$. The star that produced the peak for the O-pulsar was the furthest away and the slowest, at $\sim 9 \times 10^{-3}$ pc away and $\sim 9\,000\text{ m s}^{-1}$, respectively.

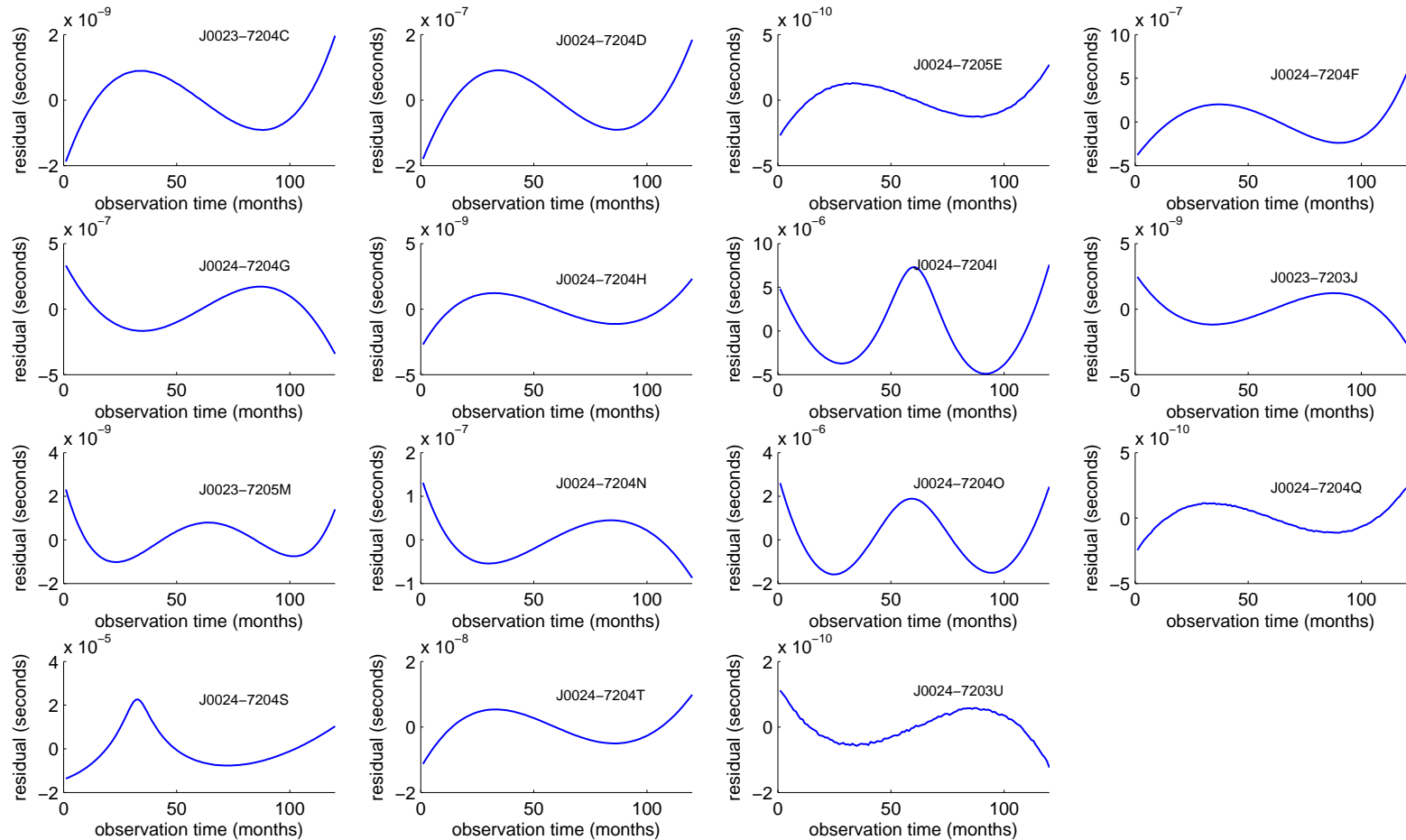


Figure 6.6: Simulation B3: Timing residuals from a sample run of a globular cluster containing 10^6 stars using a double King profile to generate the stars within the globular cluster.

6.2 Determining $\langle t_{\text{RMS}} \rangle$ and summary

Table 6.1 shows the average RMS timing residual for every pulsar during the 100 realisations of the MC simulation. Comparison with Table 5.2 shows that changing the stellar distribution from a Gaussian sphere to a (inverse Abel transformed) double King profile has a large effect on the timing residuals.

Pulsar	$\langle t_{\text{RMS}} \rangle (10^{-9}\text{s})$	$\sigma (10^{-9}\text{s})$
J0023-7204C	10.169289	53.908989
J0024-7204D	815.050708	2601.047265
J0024-7205E	0.877800	2.417444
J0024-7204F	853.238381	1469.989580
J0024-7204G	546.831905	1434.215547
J0024-7204H	156.868397	740.976187
J0024-7204I	1245.101079	2757.024012
J0023-7203J	12.373827	38.405547
J0023-7205M	0.809550	1.871215
J0024-7204N	604.299182	1568.128637
J0024-7204O	3993.142184	5416.650578
J0024-7204Q	9.781752	50.881473
J0024-7204S	2070.230086	4147.219307
J0024-7204T	66.756956	193.680121
J0024-7203U	1.784514	5.704576

Table 6.1: The average and variance of the RMS value for the timing residual for each pulsar in a 10^6 star 47 Tucanae. The stellar distribution of this globular cluster was modelled using a double King profile.

Table 6.1 shows the O-pulsar has the largest timing residuals, followed by the S- and I-pulsars. All three pulsars are very close to the central regions of the globular cluster. This increases the chance of stars being close to the pulsars' LOS, producing a large Shapiro noise, and hence a large timing residual. The pulsars far away from the centre of the globular cluster, such as the E-, M- and U-pulsars have very small timing residuals.

The variance (of the RMS timing residual) for each pulsar is larger than the average RMS timing residual. This means that while there is the possibility for

stars to be very close to the LOS, there are also some realisations where the stars are further away from the LOS.

The simulation suggests that, for a 10^6 star globular cluster, the Shapiro delay will have a significant effect, the order of microseconds, on the pulsars close to the globular cluster centre. Increasing the stellar count (see following chapter) will most likely increase the magnitude – by a factor of \sqrt{N} (see Section 3.4.3) – of the timing residuals for each pulsar. This is, and will be, a very significant, and observable, effect that has been ignored previously.

7

Full globular cluster simulation

The full globular cluster simulation is carried out by increasing the number of stars in the globular cluster, from 10^6 to 10^8 stars in the MC simulation. This is a more accurate reflection of the total number of stars in 47 Tucanae.

Pulsar	MC Simulation $\langle t_{\text{RMS}} \rangle (10^{-6}\text{s})$	$\sigma (10^{-6}\text{s})$	Observation $\langle t_{\text{RMS}} \rangle (10^{-6}\text{s})$
J0023-7204C	0.375506	0.454231	10.73
J0024-7204D	5.900098	16.102202	6.25
J0024-7205E	0.107463	0.830789	4.53
J0024-7204F	17.368777	70.086333	9.04
J0024-7204G	18.267667	95.110043	7.73
J0024-7204H	1.137560	4.909109	19.62
J0024-7204I	22.099014	24.347777	13.66
J0023-7203J	2.906875	15.672934	3.10
J0023-7205M	1.434300	11.264297	16.68
J0024-7204N	15.054943	51.945913	11.62
J0024-7204O	33.330008	127.936930	8.20
J0024-7204Q	2.794278	13.934424	18.88
J0024-7204S	29.080082	58.762029	10.46
J0024-7204T	9.684987	37.070401	50.26
J0024-7203U	0.147104	0.170945	8.48

Table 7.1: Comparison between the observational and simulated RMS timing residual values.

Table 7.1 shows that the timing residuals are now of the order of microseconds.

The magnitude of the largest timing residual is that of the O-pulsar at $33.33 \pm 127.94 \mu\text{s}$. This pulsar is the closest pulsar to the centre of the globular cluster. The smallest magnitude is that of the E-pulsar, one of the furthest pulsars from the globular cluster centre, at $0.11 \pm 0.83 \mu\text{s}$. As was shown in Chapter 6, the variance of the timing residuals is much greater than the average values of the RMS timing residuals. This strongly indicates that the timing residuals are very sensitive to the stellar configuration of the globular cluster, and therefore, the stellar distribution around the LOS of the pulsar. Actual RMS values for the pulsars in 47 Tucanae are also shown in Table 7.1 obtained from Freire et al. (2003).

When comparing the simulated and observed values of the timing residuals, the observed timing residuals for pulsars far away from the globular cluster core are much greater than the simulated timing residuals. However, pulsars in the core - the F, G, I, N, O and S-pulsars - have a larger simulated (predicted) timing residual than what is observed. This may indicate that the current accepted knowledge of the stellar mass distribution (the double King profile) and the dispersion velocity – $\sigma = 13200 \text{ m s}^{-1}$ (Webbink 1985, see Section 5.1) – used in the simulation may not be an accurate representation of the actual stellar configuration for 47 Tucanae. The Shapiro noise is only affected by both these parameters, the stellar distribution (see Section 7.4), and the velocity dispersion.

The value of the dispersion velocity used in this thesis, $\sigma = 13.2 \text{ km s}^{-1}$ (Webbink 1985), was a higher value compared to the dispersion velocity values determined through more recent observations. The observed values range from $10.9 \pm 1.3 \text{ km s}^{-1}$ (Meylan and Mayor 1986) to $11.8 \pm 0.8 \text{ km s}^{-1}$ (McLaughlin et al. 2006). In addition, Meylan and Mayor (1986) and McLaughlin et al. (2006) both show that the dispersion velocity is not the same throughout the entire globular cluster – the dispersion velocity profile decreases as a function of R (the distance between the star and the centre of the globular cluster) from $\sim 12 \text{ km s}^{-1}$ at $\sim 0.04 \text{ pc}$ (McLaughlin et al. 2006, Figure 24) to $\sim 6 \text{ km s}^{-1}$ at ~ 3.5

pc (Meylan and Mayor 1986, Figure 6b). This range of values of the dispersion velocity could suggest that the simulations may have predicted a higher value of the RMS timing residuals for the nearby pulsars (F, G, I, N, O and S-pulsars) as the dispersion values used were larger by $\sim 1 \text{ km s}^{-1}$. As the discrepancy is small, it may not be the only reason why the predicted RMS timing residuals are higher than what is observed for the nearby pulsars.

For pulsars further away from the core (pulsars with $r > 1 \text{ pc}$), the simulations shows that the Shapiro noise is not the dominant term in the timing residuals. This suggest that some other effect is present in these timing residuals.

7.1 Simulated timing residual map

Figure 7.1 shows the timing residual maps for each pulsar from the full GC simulation. While some pulsars (the E, M, and U-pulsars for example) still exhibit a predominantly cubic function, the other pulsars have more complex functions. For example, the O-pulsar contains lots of peaks and does not exhibit a cubic structure as shown by the E-pulsar. From Section 4.4, each peak may represent a star approaching close to the LOS of the O-pulsar. Similar structure can be found on the D, F, S and T-pulsars. In the case of the T-pulsar, the function suggests that there was one star close to the LOS after approximately 58 months, and the timing residual has the form of a transit event. For the O and S-pulsars there were many stars that approached and receded from the LOS.

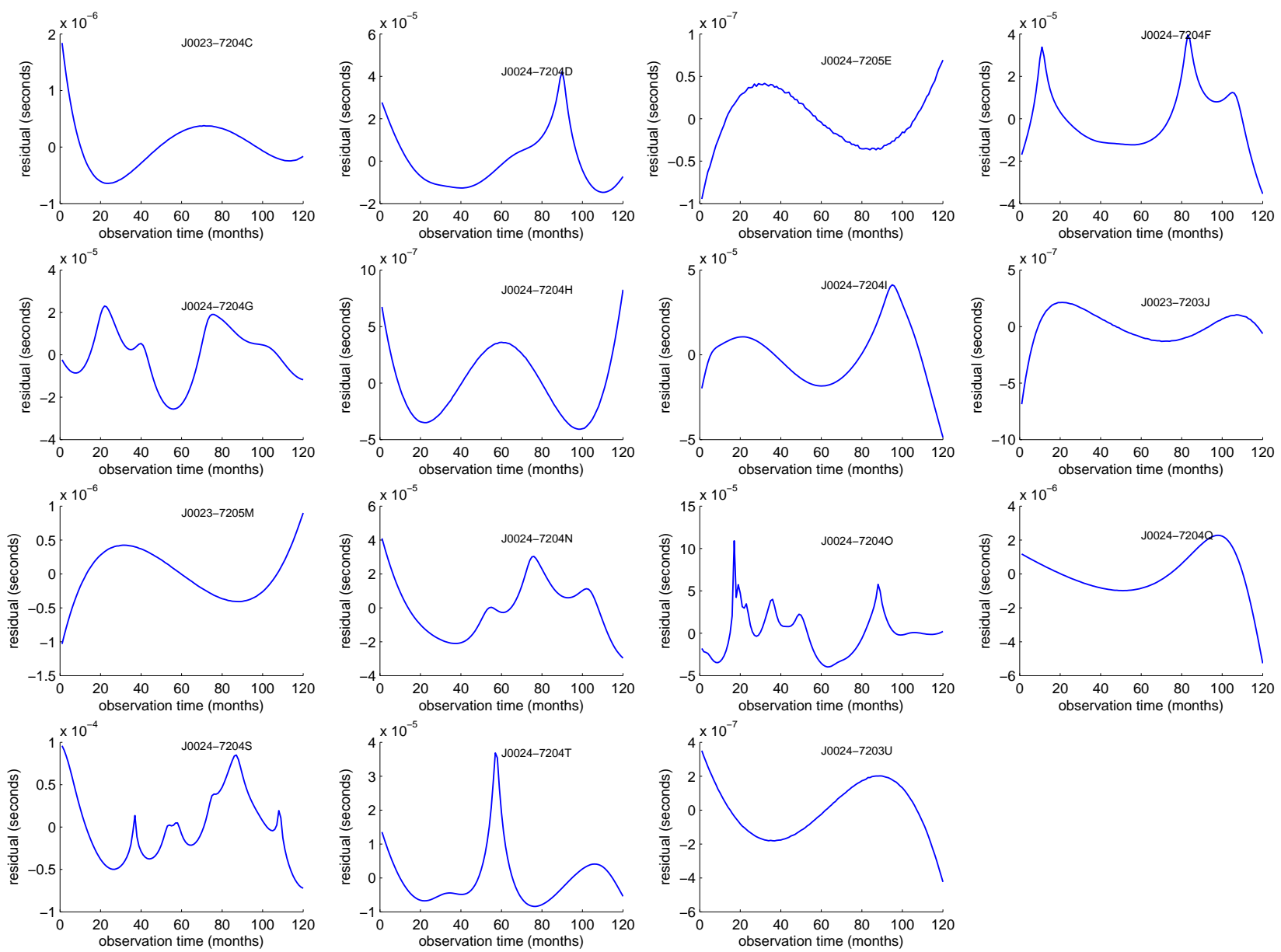


Figure 7.1: Timing residuals from a sample run of a globular cluster containing 10^8 stars.

7.2 Observed timing residuals

Figures 7.2 to Figure 7.16 show the observed timing residuals for every pulsar in 47 Tucanae. Images taken from the “The 23 millisecond radio pulsars in 47 Tucanae” webpage,

<http://www.naic.edu/~pfreire//47Tuc/>

The observed timing residuals are of the order to 10^{-4} to 10^{-6} s. This is larger than predictions from previous simulations, which were of the order of 10^{-9} seconds. However, the 100 realisations were for 10^6 stars, not 10^8 stars, the actual number of stars in the globular cluster. From the predictions described in Section 3.4.3, the timing residuals are expected to be larger for greater stellar number (i.e. scales as a function of \sqrt{N} – see Section 3.4.2). In addition, the Shapiro noise for 10^8 stars is predicted to be of the order of 10^{-5} seconds, and one can therefore assume the timing residuals will be smaller, perhaps of the order of 10^{-8} seconds.

For all the plots (Figure 7.2 to Figure 7.16), “the 430-MHz residuals are coloured red, the 660-MHz residuals are coloured magenta, the low-resolution L-band residuals (centered at 1374 MHz) are coloured yellow and the high-resolution L-band residuals (centered at 1390 MHz) are coloured green” (citation taken from website listed above).

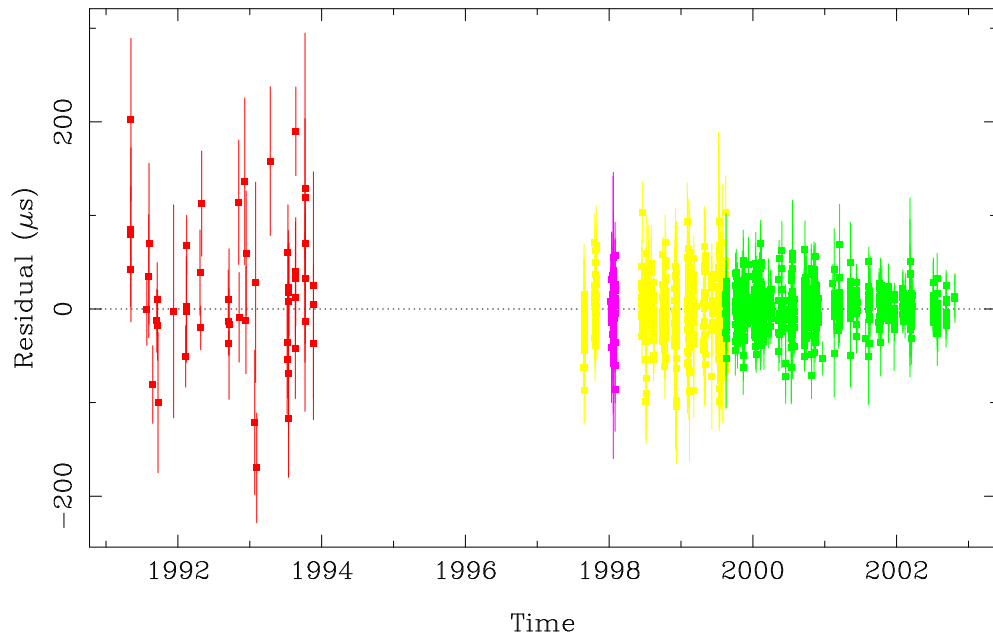


Figure 7.2: Timing residuals for the C-pulsar. From the simulations, the average RMS timing residual, $\langle t_{\text{RMS}} \rangle = 0.38 \pm 0.45 \mu\text{s}$.

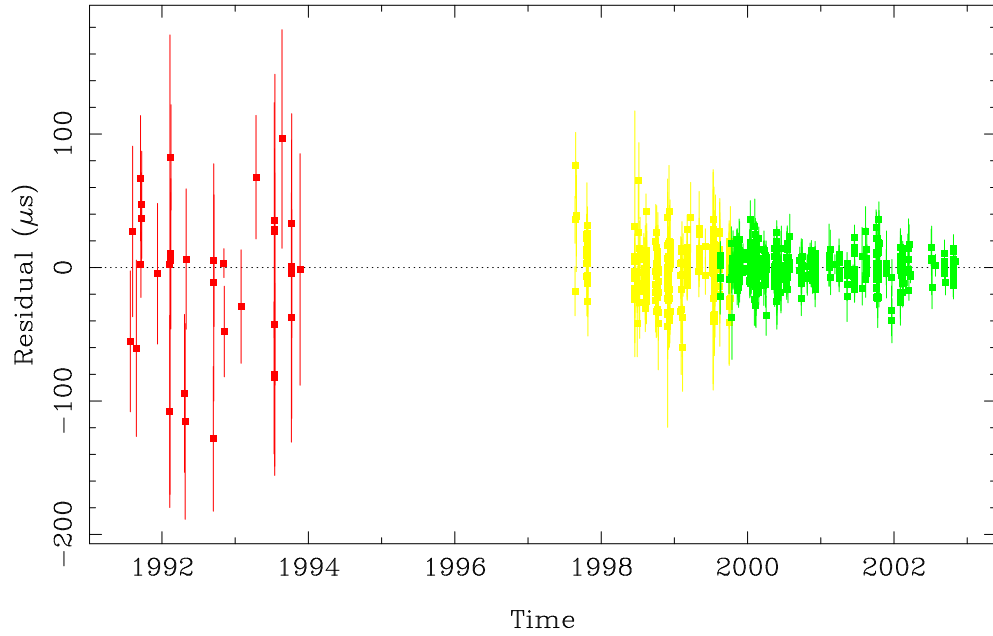


Figure 7.3: Timing residuals for the D-pulsar. From the simulations, the average RMS timing residual, $\langle t_{\text{RMS}} \rangle = 5.90 \pm 16.10 \mu\text{s}$.

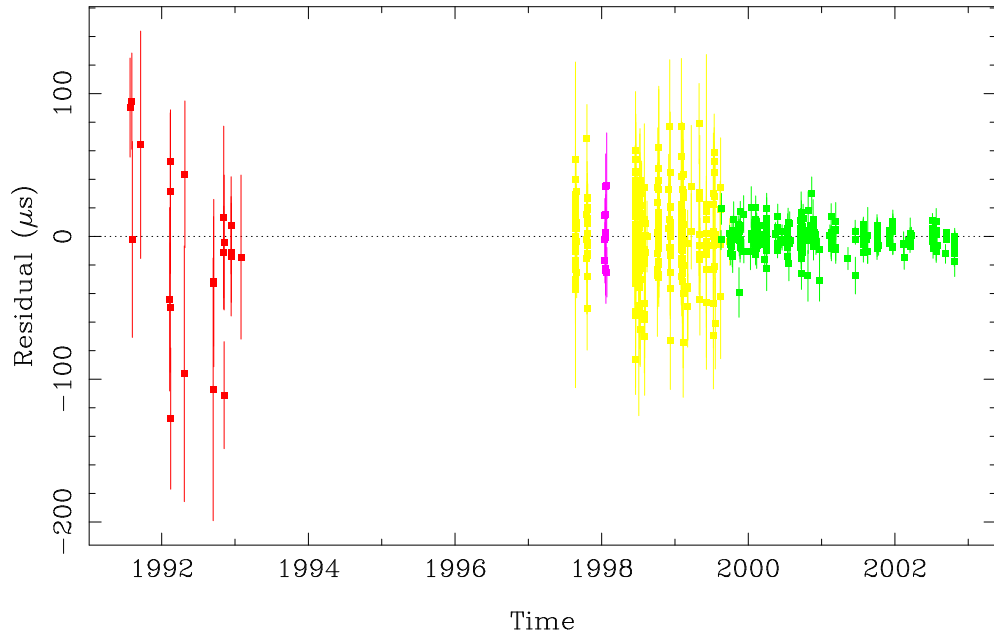


Figure 7.4: Timing residuals for the E-pulsar. From the simulations, the average RMS timing residual, $\langle t_{\text{RMS}} \rangle = 0.11 \pm 0.83 \mu\text{s}$.

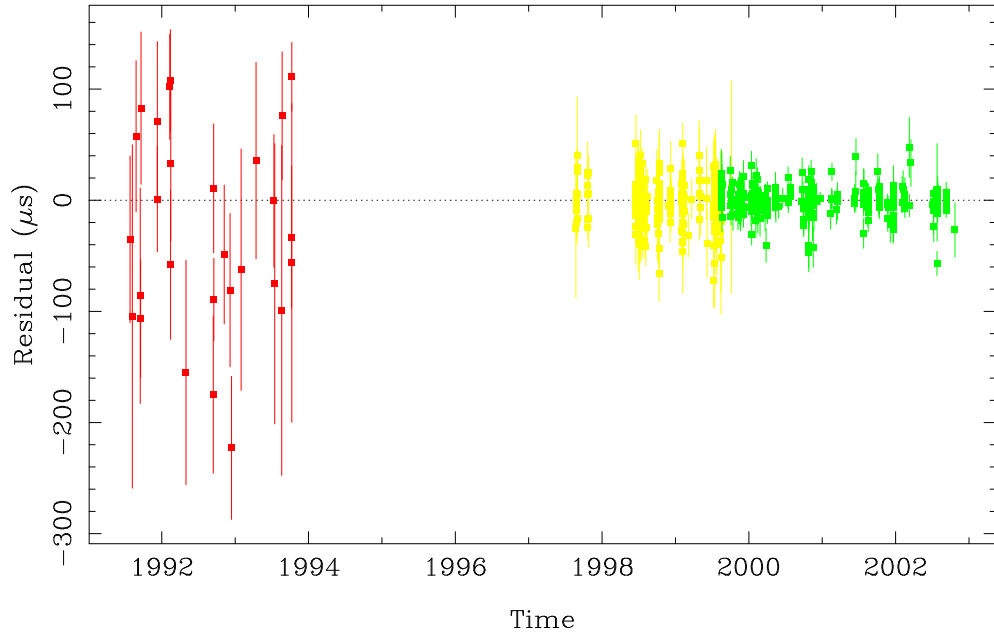


Figure 7.5: Timing residuals for the F-pulsar. From the simulations, the average RMS timing residual, $\langle t_{\text{RMS}} \rangle = 17.37 \pm 70.09 \mu\text{s}$.

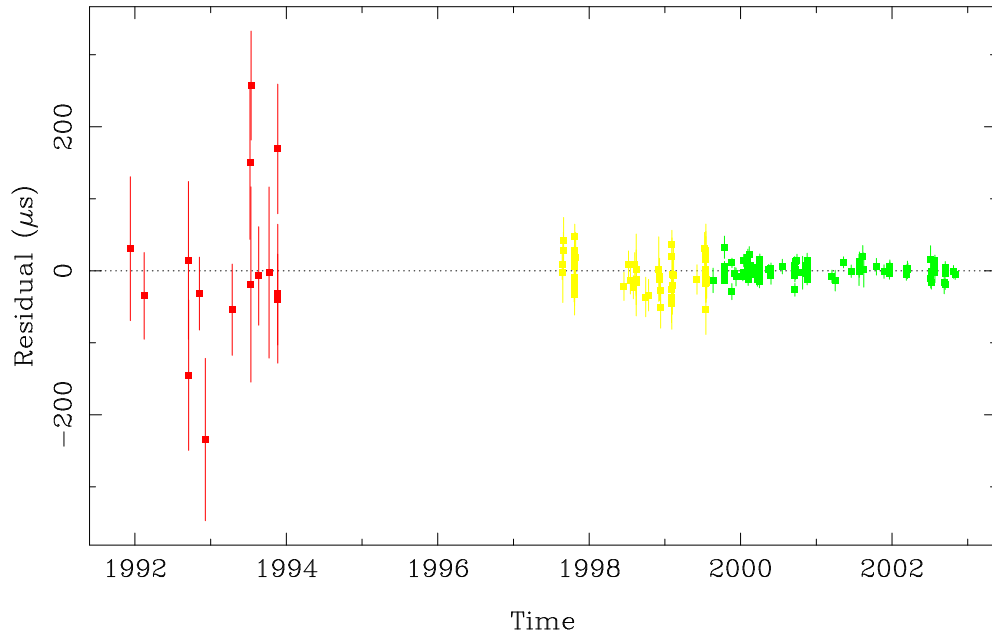


Figure 7.6: Timing residuals for the G-pulsar. From the simulations, the average RMS timing residual, $\langle t_{\text{RMS}} \rangle = 18.27 \pm 95.11 \mu\text{s}$.

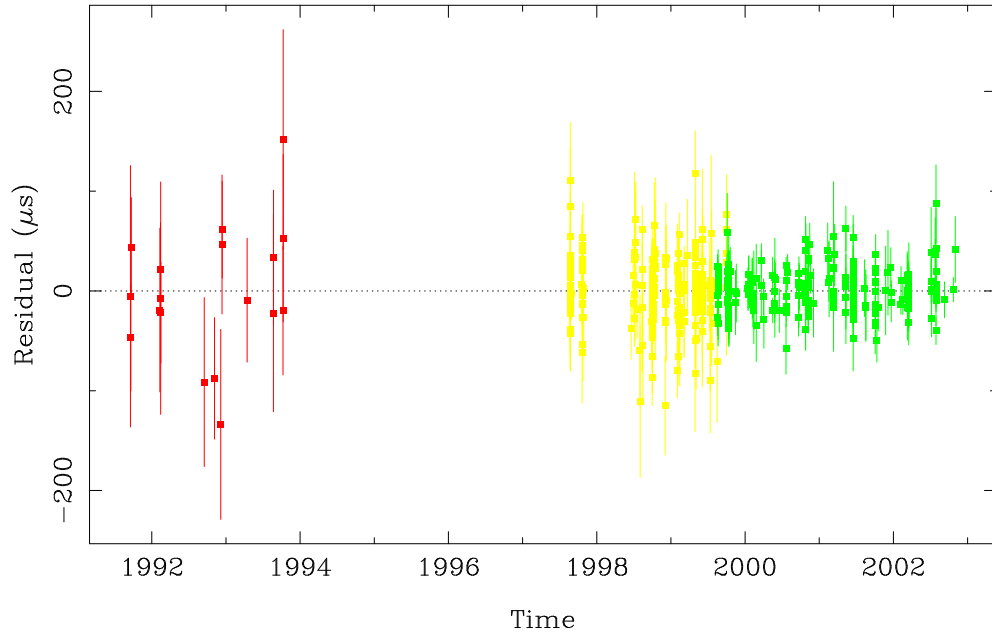


Figure 7.7: Timing residuals for the H-pulsar. From the simulations, the average RMS timing residual, $\langle t_{\text{RMS}} \rangle = 1.14 \pm 4.91 \mu\text{s}$.

7.2: OBSERVED TIMING RESIDUALS

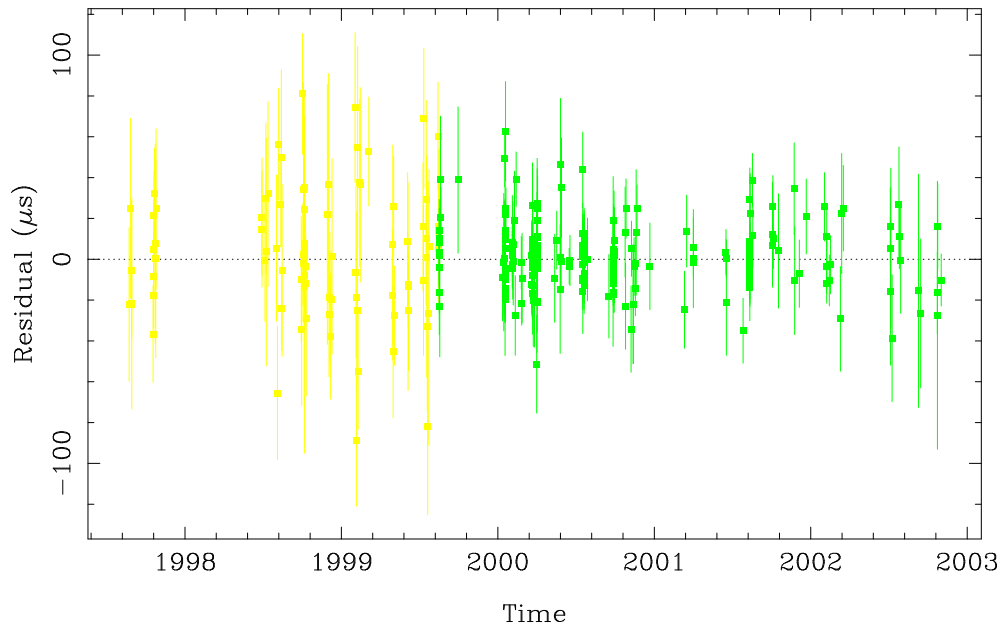


Figure 7.8: Timing residuals for the I-pulsar. From the simulations, the average RMS timing residual, $\langle t_{\text{RMS}} \rangle = 22.10 \pm 24.35 \mu\text{s}$.

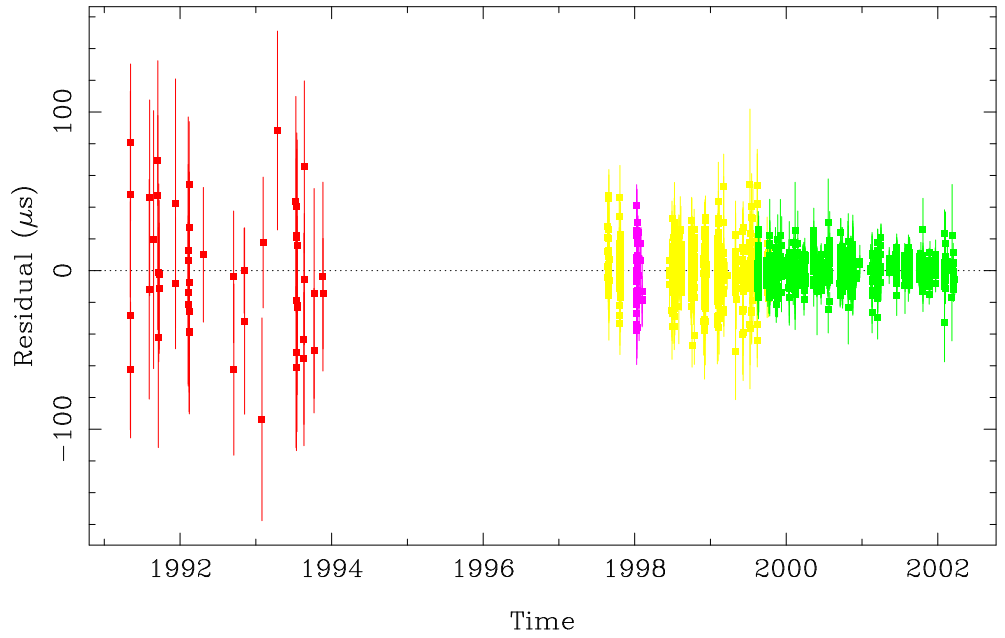


Figure 7.9: Timing residuals for the J-pulsar. From the simulations, the average RMS timing residual, $\langle t_{\text{RMS}} \rangle = 2.91 \pm 15.67 \mu\text{s}$.

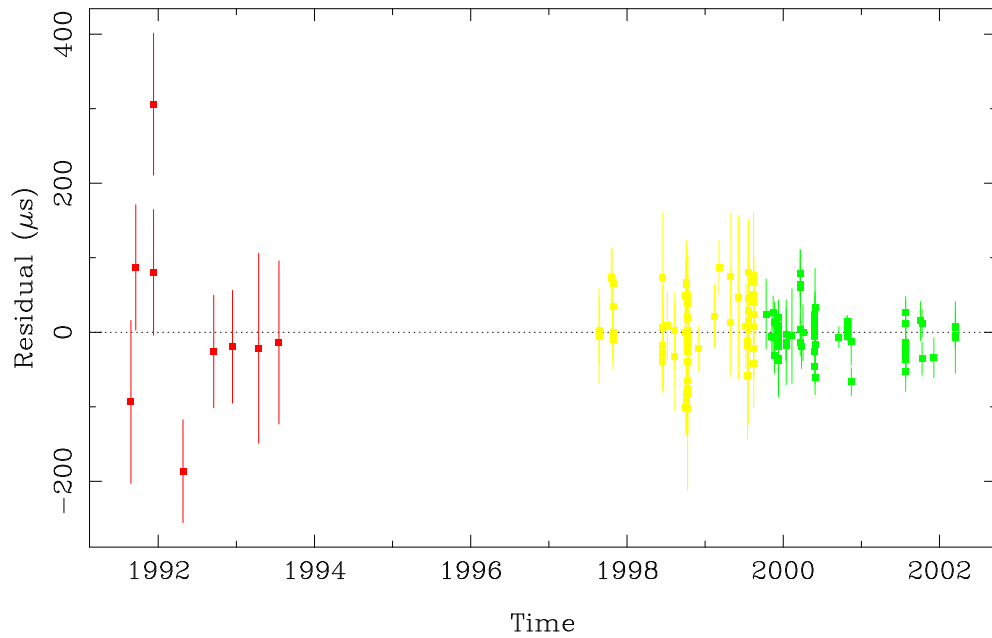


Figure 7.10: Timing residuals for the M-pulsar. From the simulations, the average RMS timing residual, $\langle t_{\text{RMS}} \rangle = 1.43 \pm 11.26 \mu\text{s}$.

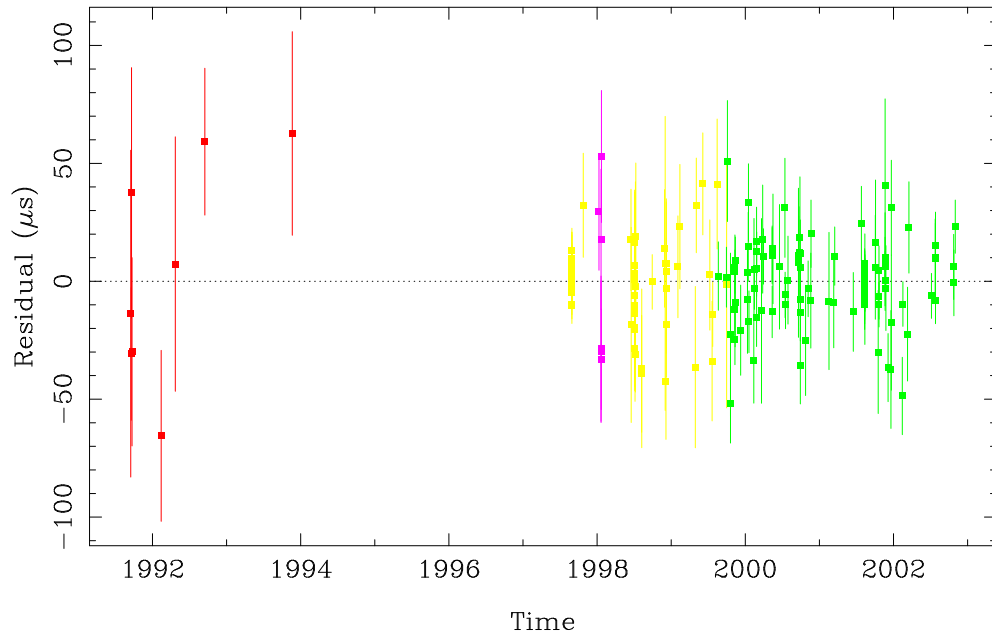


Figure 7.11: Timing residuals for the N-pulsar. From the simulations, the average RMS timing residual, $\langle t_{\text{RMS}} \rangle = 15.05 \pm 51.95 \mu\text{s}$.

7.2: OBSERVED TIMING RESIDUALS

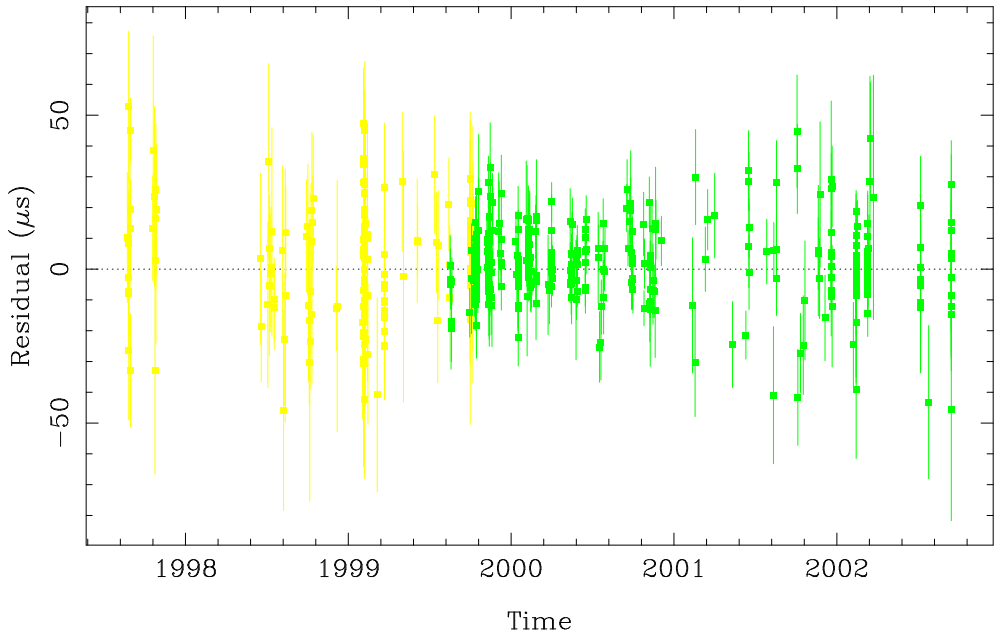


Figure 7.12: Timing residuals for the O-pulsar. From the simulations, the average RMS timing residual, $\langle t_{\text{RMS}} \rangle = 33.33 \pm 127.94 \mu\text{s}$.

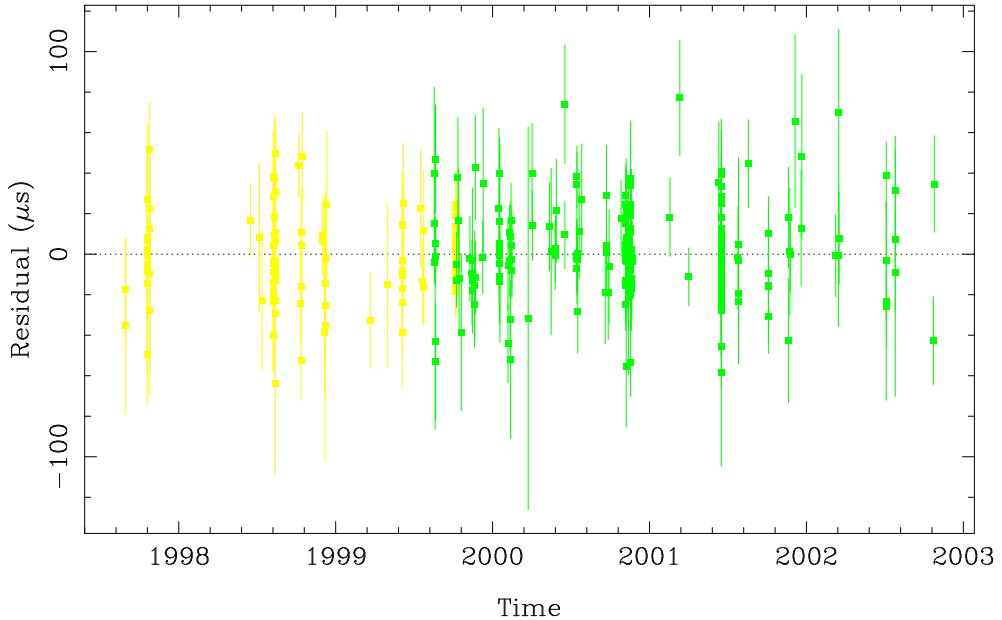


Figure 7.13: Timing residuals for the Q-pulsar. From the simulations, the average RMS timing residual, $\langle t_{\text{RMS}} \rangle = 2.76 \pm 13.93 \mu\text{s}$.

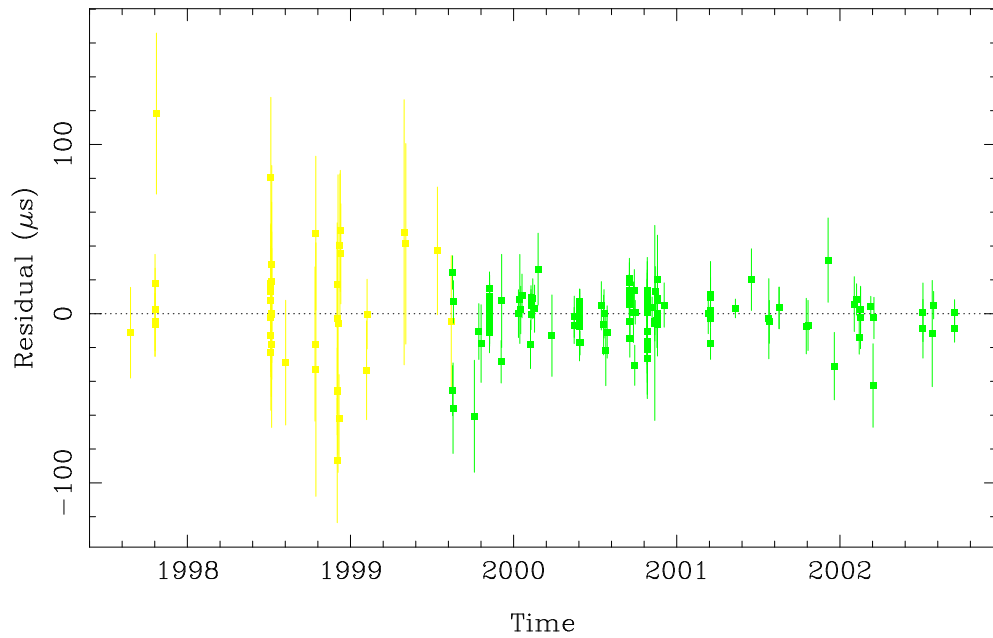


Figure 7.14: Timing residuals for the S-pulsar. From the simulations, the average RMS timing residual, $\langle t_{\text{RMS}} \rangle = 29.08 \pm 58.76 \mu\text{s}$.

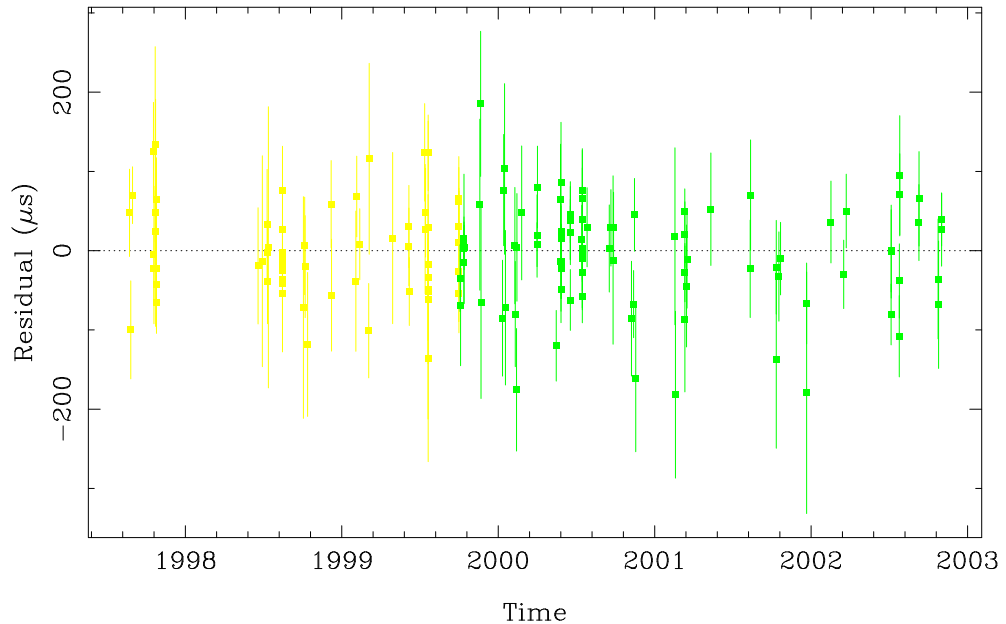


Figure 7.15: Timing residuals for the T-pulsar. From the simulations, the average RMS timing residual, $\langle t_{\text{RMS}} \rangle = 9.68 \pm 37.07 \mu\text{s}$.

7.2: OBSERVED TIMING RESIDUALS

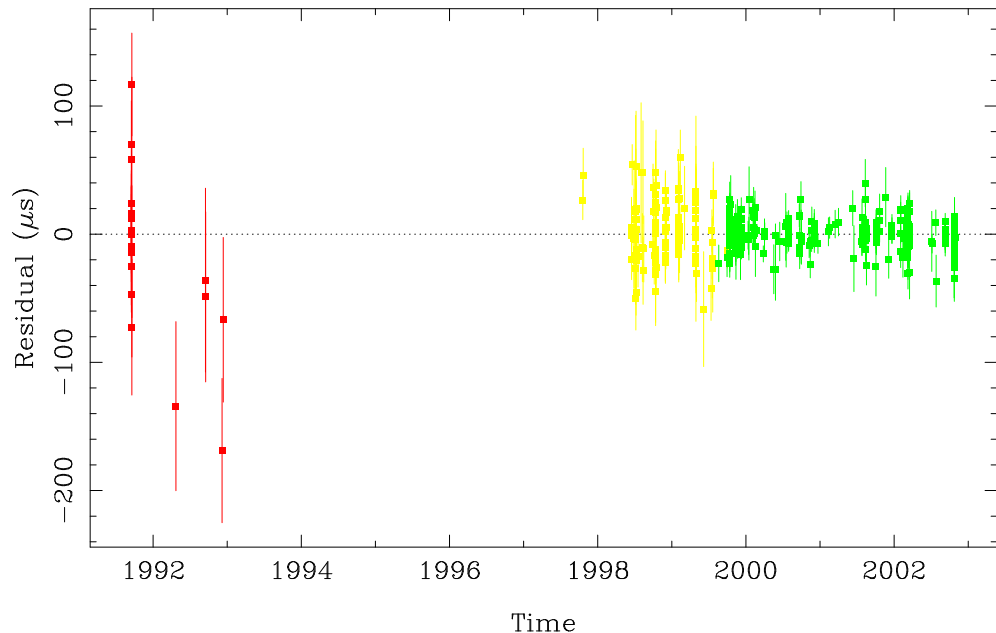


Figure 7.16: Timing residuals for the U-pulsar. From the simulations, the average RMS timing residual, $\langle t_{\text{RMS}} \rangle = 0.15 \pm 0.17 \mu\text{s}$.

7.3 Overplotting the simulated and observed timing residuals for the J-pulsar

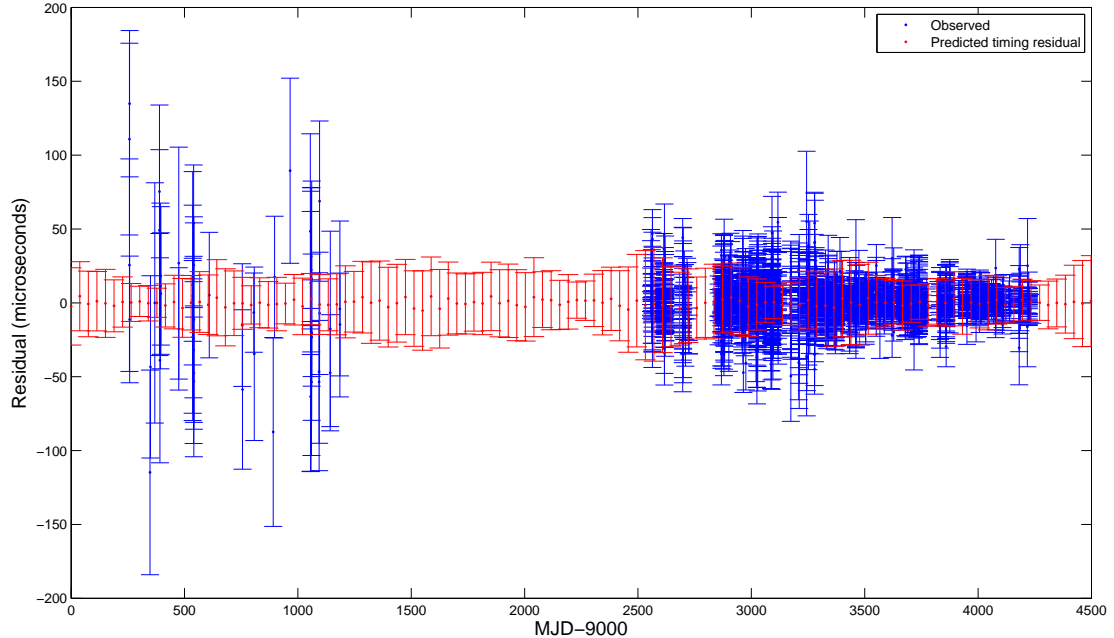


Figure 7.17: Comparison of observed and predicted timing residual for the J-pulsar.

Table 7.1 shows there is good agreement between the predicted (by the MC simulations) and the observed timing residuals. Let us now compare the timing residual plot. Figure 7.17 exhibits the comparison of the two timing residuals (the observed and simulated/predicted) for the J-pulsar in 47 Tucanae. The observed timing residuals were obtained from Paulo Freire (private communication). The average and variance of the simulated timing residuals were obtained from the MC simulation that was used to determine the RMS timing residuals for the J-pulsar (Table 7.1). From Table 5.1 it can be seen that the J-pulsar is one of the pulsars situated away from the core of the globular cluster, and therefore has one of the smaller RMS timing residual magnitudes.

Figure 7.17 shows that the variance in the observed timing residual decreases over observation time. This is due to the improvements in instrumentation. This characteristic is not visible for the simulated timing residuals. The magnitude of the predicted average timing residual and the variance is smaller than the observed timing residuals. This indicates that, while the Shapiro noise is a small factor in the timing residuals (it would be buried in the noise), it can be used to reduce timing noise.

7.4 $\langle t_{\text{RMS}} \rangle$ and pulsar position

In the previous section it was predicted that the further a pulsar is from the centre of a globular cluster, the smaller the magnitude of its Shapiro noise, resulting in a smaller magnitude of the timing residual for that pulsar. This was due to fewer stars being close to its LOS, and therefore a smaller portion of the stars in the globular cluster will have a significant contribution to the Shapiro noise.

Let us now investigate how much the pulsar position affects the observed t_{RMS} and the simulated $\langle t_{\text{RMS}} \rangle$ values. Figure 7.18 shows t_{RMS} and $\langle t_{\text{RMS}} \rangle$ as a function of r , the (three-dimensional) distance between the pulsar and the centre of the globular cluster. The error in r (shown as error bars in Figure 7.18) arises from the error in the pulsar position along the LOS, as discussed in Section 5. The error bars for the simulated RMS timing residuals, $\langle t_{\text{RMS}} \rangle$, in both Figure 7.18 and Figure 7.19 have been reduced in size (by a factor of 10) so that the error bars fit into the figures. The actual error bars from the simulated timing residuals for all pulsars do intersect the observed timing residuals for that particular pulsar. The observed error bars (red error bars in both figures) is the error in the position of the pulsars, as shown in Freire et al. (2003). This error in position will result in a different (although same magnitude) RMS timing residual, as described in Section 2.7.1.

In Figure 7.18, there seems to be no correlation between r and the observed

timing residual, t_{RMS} . There is a correlation between r and the average simulated timing residual, $\langle t_{\text{RMS}} \rangle$, as the $\langle t_{\text{RMS}} \rangle$ values get smaller as r increases. For pulsars with $r < 1$ pc, the simulated $\langle t_{\text{RMS}} \rangle$ values are greater than the observed t_{RMS} values. For pulsars in the range of $1 < r < 2$ pc the observed values are larger than the simulated value. For pulsars at $r > 3$ pc, the t_{RMS} and $\langle t_{\text{RMS}} \rangle$ values become very similar – for pulsars such as the F- and G-pulsars, the two timing residual values are almost identical.

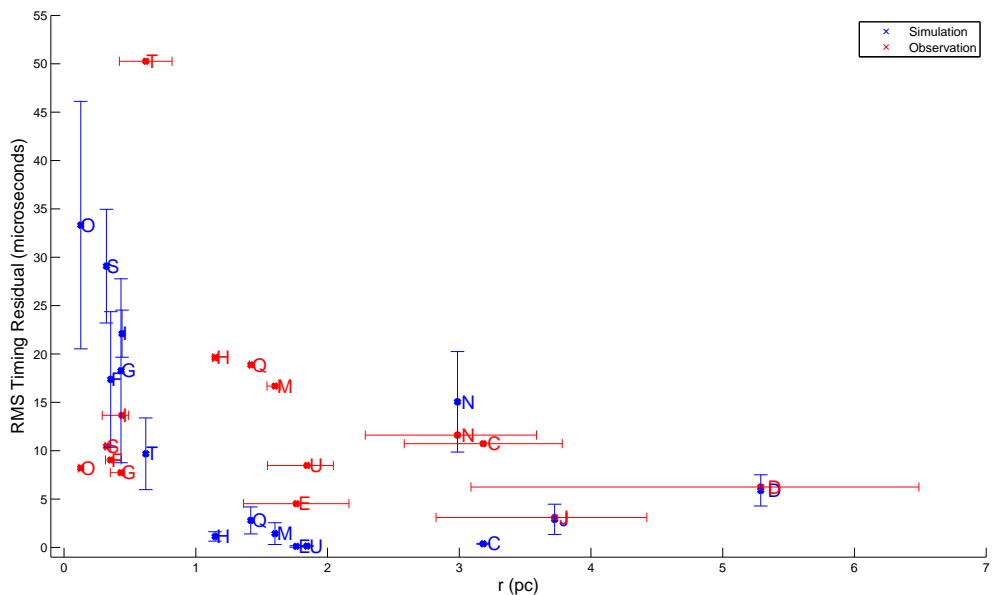


Figure 7.18: $\langle t_{\text{RMS}} \rangle$ as a function of r , the distance from the centre of the globular cluster. Error bars obtained from Freire et al. (2003) are shown in red. The blue error bars, showing the error in simulated timing residual, has been reduced by a factor of 10.

Figure 7.19 shows the relation between the timing residual and the perpendicular distance of the pulsar from the LOS, from the centre of the globular cluster.

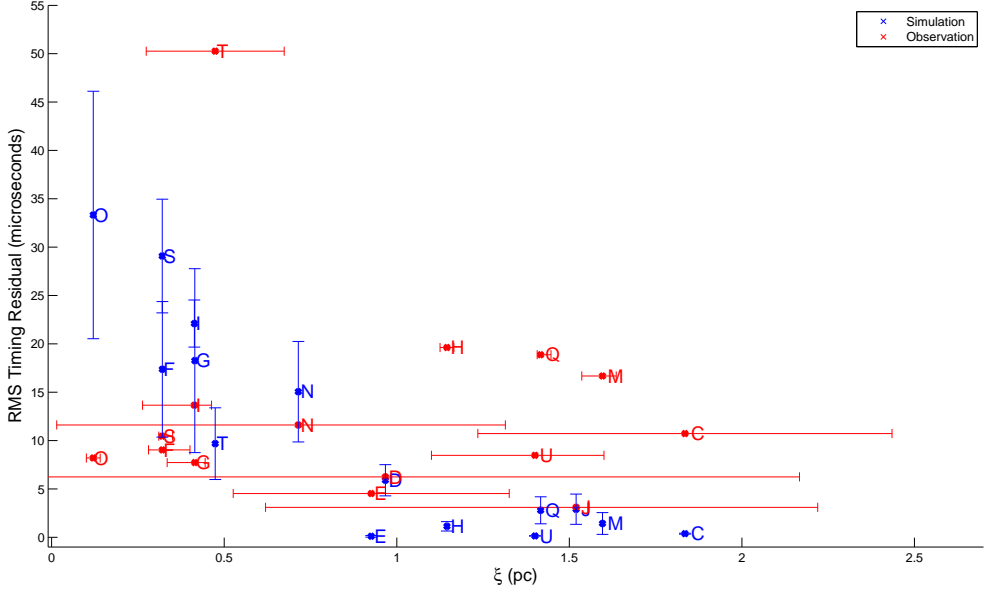


Figure 7.19: $\langle t_{\text{RMS}} \rangle$ as a function of ξ , the perpendicular distance between the pulsar and the globular cluster centre, along the LOS. Error bars obtained from Freire et al. (2003) are shown in red. The blue error bars, showing the error in simulated timing residual, has been reduced by a factor of 10.

It can be seen that the simulated timing residuals for pulsars with $\xi < 1$ pc, where ξ here is the distance between the pulsar and the centre of the globular cluster (in the plane perpendicular to the LOS from the globular cluster centre to the observer), are much greater than the observed RMS timing residuals, with the exception of the T-pulsar. The discrepancy gets larger the closer the pulsar is to the core. The opposite is also true for pulsars further away from the core where the discrepancy between the simulated and observed RMS timing residuals gets smaller. Table 7.2 shows the ξ distances and the ratios of the simulated and observed average timing residuals for each pulsar. From the table it can be seen that there is a trend of decreasing ratio with increasing ξ .

While Figure 7.19 shows a clear and visible relationship of the predicted RMS timing residual as a function of ξ , it is difficult to determine an analytical equation

describing this relation. The reason is because (i) there is a large variance σ for the timing residual, and (ii) it is not possible to (accurately) analytically predict the components of the Shapiro noise that will be subtracted by polynomial fitting. The large variance in the predicted RMS timing residuals means that the ‘best fit’ curve to show such a relationship will not be accurately defined (and as a result, may not mean much). While Chapter 3 (Section 3.3.1 to 3.3.3) showed analytical predictions for the change in Shapiro delay, Δt_{Sh} , and the probability of having such a change, $p(\Delta t_{\text{Sh}})$, for a given simulation of the globular cluster. The polynomial fit in Section 4.4 subtracted the first and second order terms of the pulsar TOA, t_{TOA} , from the Shapiro noise. Therefore, these two analytical models use a completely different base unit. A large Δt_{Sh} might infer a large change in Δt_{TOA} , but such a relation has to be investigated in more detail. As a result, it is difficult to integrate the two methods to produce one analytical solution that fully describes the relation shown in Figure 7.19.

Table 7.2 suggests that stellar density in the outer ($\xi > 1 \text{ pc}$) regions of the core modeled by the double King profile may be too low¹. Table 7.2 also suggests that the stellar density in the inner ($\xi < 1 \text{ pc}$) regions of the core modeled by the double King profile may be too high. This has resulted in the simulated timing residuals being far greater than those observed. Since the Shapiro noise is the only noise term in these simulated timing residuals, the simulated values should be lower than the observed timing residuals (as these residuals contain more noise terms in addition to the Shapiro noise). The simulated timing residual is very sensitive to the stellar density, suggesting that there may be more stars in the core than currently observed suggest.

Let us now investigate the stellar distribution in the globular cluster. The double King profile that was used in the simulations seems to overestimate (com-

¹This is not (strictly) true. The observed timing residuals contain other parameters (such as intrinsic timing noise) as well as the Shapiro noise. These other parameters may be the more dominant effect in these ($\xi > 1 \text{ pc}$) regions, and not the Shapiro noise.

pared to the actual density distribution of 47 Tucanae) the stellar density around the core, up to a radius of ~ 1 pc, and also seems to underestimate¹ the stellar density further away (> 1 pc) from the centre of the globular cluster. The double King profile, as described in Chapter 6, concentrated the stellar distribution more towards the centre compared to the Gaussian distribution used in Chapter 5. While the Gaussian distribution used in Chapter 5 may have had a large σ , a Gaussian distribution with a smaller σ , such as $\sigma = 2$ pc, could be used to describe the stellar distribution in 47 Tucanae.

Figure 7.20 shows the different distribution functions over a range of ξ . The double King profile (shown in blue) has the highest stellar density in the core compared to the three Gaussian distributions. The double King profile decreases with increasing radius a lot more quickly than the Gaussian distributions, and with this profile there are hardly any stars with $\xi > 2$ pc. The Gaussian distributions all decrease more gradually than the double King profile.

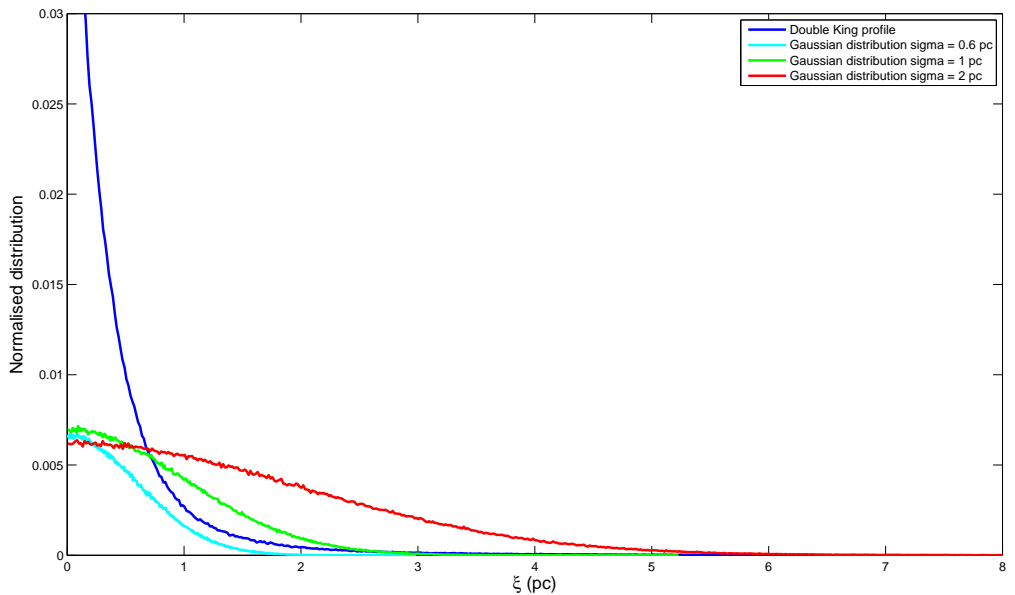


Figure 7.20: Comparison of the stellar distributions functions.

To determine which distribution produces a timing residual that correlates

the best with the observed timing residual, let us determine the ratio of the simulated timing residual and the observed timing residual, $\frac{TR}{TR_{\text{Obs}}}$. Four separate simulations were done; one where the stellar distribution was described by the double King profile, and three simulations that used the Gaussian sphere as a model for the stellar distribution. Each Gaussian sphere simulation used a different σ value (0.6 pc, 1 pc and 2 pc) to generate the position of the stars. These three values of σ were chosen to determine whether it has a significant effect on the timing residuals. The three Gaussian distributions and the double King profile, as a function of ξ , are shown in Figure 7.20. None of the Gaussian distributions exhibit good correlation with the double King profile. From Figure 7.20 it can be seen that the stellar distribution from the double King profile concentrates a great proportion of the stars within $\xi < 1$ pc. The three Gaussian distributions have a less concentrated centre, but are much wider, which may have an effect on the pulsars with $\xi > 1$ pc – as the double King distribution seems to underestimate¹ the timing residuals of pulsars in this region.

The timing residuals obtained for each Gaussian distribution is shown in Table 7.2. The table shows that the Gaussian distribution produces ratios that are less correlated than the double King profile, as the ratios seem to be independent of the distance of the pulsar to the centre of the globular cluster (ξ). However, for the H, U, Q, J, M and C-pulsars the obtained ratios are larger than those for the double King profile. This suggests that, while there may be more stars in the $\xi > 1$ pc region, it has minimal effect on the timing residuals. The larger number of stars means that there is an increased likelihood that a star will be situated close to the LOS (see J-pulsar for $\sigma = 0.6$ pc), however the density around the LOS is not large enough to have a significant effect on the timing residuals.

From the simple comparisons it can be shown that that a Gaussian sphere is not a good approximation to the stellar distribution of 47 Tucanae. The timing residuals produced by the Gaussian distribution are dependent on the generated position of the stars more than the pulsar position. The best correlation between

ξ and the timing residuals is produced by the double King profile. However, this distribution overestimates the timing residuals for pulsars with $\xi < 1\text{pc}$ compared to the observed timing residuals for the pulsars, and underestimates¹ the timing residuals for pulsars with $\xi > 1\text{pc}$ when compared with observed values. Being able to accurately determine the most likely ratios of the timing residuals may allow for an improvement in (i) determining the mass distribution of the globular cluster, and (ii) determining the pulsar position along the LOS.

Pulsar	ξ (pc)	$\frac{TR_{\text{sim,DK}}}{TR_{\text{obs}}}$	Ratio	Timing residuals from Gaussian distribution			$\frac{TR_{\text{sim,GD}}}{TR_{\text{obs}}}$ ratio		
				$\sigma = 0.6$ pc (10^{-6} s)	$\sigma = 1$ pc (10^{-6} s)	$\sigma = 2$ pc (10^{-6} s)	$\sigma = 0.6$ pc	$\sigma = 1$ pc	$\sigma = 2$ pc
J0024-7204O	0.120601	4.064635		1.132861	11.743929	9.819551	0.138154	1.432186	1.197506
J0024-7204S	0.320586	2.780122		18.663832	11.508706	9.154114	1.784304	1.100259	0.875154
J0024-7204F	0.320835	1.921324		0.175635	0.202008	7.524504	0.019429	0.022346	0.832356
J0024-7204I	0.413430	1.617790		33.381608	10.201391	0.829482	2.443748	0.746808	0.060723
J0024-7204G	0.414742	2.363216		11.098854	13.724752	0.965193	1.435815	1.775518	0.124863
J0024-7204T	0.473938	0.192697		11.532071	5.080871	1.034931	0.229448	0.101092	0.020591
J0024-7204N	0.714794	1.295606		19.205354	16.302036	6.397150	1.652784	1.402929	0.550529
J0024-7205E	0.926041	0.023722		12.011699	7.807675	5.847536	2.651583	1.723549	1.290847
J0024-7204D	0.966979	0.944015		3.044703	5.779910	1.643527	0.487152	0.924786	0.262964
J0024-7204H	1.145296	0.057979		44.135380	8.546390	4.862897	2.249509	0.435596	0.247854
J0024-7203U	1.400475	0.017347		23.152604	26.544730	8.983178	2.730260	3.130275	1.059337
J0024-7204Q	1.416953	0.148002		2.927281	5.867396	5.510195	0.155047	0.310773	0.291854
J0023-7203J	1.519679	0.937701		32.342307	8.873774	8.958854	10.433002	2.862508	2.889952
J0023-7205M	1.596002	0.085989		29.088778	9.397996	6.357220	1.743932	0.563429	0.381128
J0023-7204C	1.835028	0.034995		0.057311	3.443763	2.835975	0.005341	0.320947	0.264303

Table 7.2: Comparison of the stellar distribution ratio of a Gaussian distribution (with varying values of σ) and the double King profile.

7.5 Summary

A polynomial fit was carried out on the Shapiro noise to determine the timing residuals. This approach was adopted instead of the standard method, which uses the least-squares fitting method to determine the most likely values of the spin frequency f_0 and the change in spin frequency \dot{f}_0 , from which a model of the TOA is created. This model TOA is then subtracted from the observed TOA to obtain a timing residual. Since the Shapiro noise is independent from f_0 and \dot{f}_0 it was possible to use the polynomial fit method as an alternative to this standard model. In the polynomial fit the first two orders (equivalent to subtracting f_0 and \dot{f}_0) of the Shapiro noise was subtracted (assuming the Shapiro noise is the only noise component in the observed TOA) to obtain a timing residual.

The pulsar timing residuals for a 10^6 star globular cluster (Gaussian sphere) were of the order of nanoseconds, a result that is larger than indicated by previous literature. Using 10^8 stars (total number of stars in 47 Tucanae) and a double King profile, the timing residuals were of the order of microseconds. This result would be an observable effect, with a magnitude that is much larger than previously expected. In addition, it was shown that the pulsar position, relative to the centre of the globular cluster (in a plane perpendicular to the LOS), has an effect on the magnitude of the timing residual for a particular pulsar. The closer the pulsar is to the centre of the globular cluster, the larger the timing residuals, and vice versa.

It was also found that the timing residuals predicted for the pulsars in the central region of the globular cluster are much greater than their observed values, suggesting the possibility that the double King profile may not be an accurate reflection of the actual stellar distribution in 47 Tucanae.

8

Gravitational Acceleration

So far, we have only considered that stars move with constant velocity. However, stars positioned very close (< 0.1 pc) to pulsars also interact with the pulsars due to the gravitational attraction between the two objects, causing the star and the pulsar to deviate from their respective linear trajectories.

In this section we investigate how pulsar motion is affected by the gravitational force from nearby stars. The change in pulsar position along the LOS will change the TOA of a pulse, as the pulse may have to travel further/shorter depending on the pulsar position. This delay in the TOA will contain constant (linear) velocity and acceleration (quadratic) terms, which will be included in the timing residuals. As a result, the timing residuals will consist of higher order terms.

It is important to note that this effect is independent of the Shapiro noise. The Shapiro noise is affected by stars close to the LOS whereas the gravitational acceleration effects on the pulsar are from the stars in the immediate surroundings of the pulsar.

Let us determine the minimum separation r necessary (between a pulsar and a star, both at rest) for the two bodies to collide with each other over a time period t , the time period over which the acceleration changes significantly. It is necessary to determine whether this distance is comparable to the minimum separation between the pulsar and a star in the simulations. From Newtonian

gravitation, the acceleration of the pulsar a can be written as

$$F = ma = m\ddot{r} = -\frac{GMm}{r^2} \quad (8.1)$$

$$\Rightarrow \ddot{r} = -\frac{GM}{r^2}, \quad (8.2)$$

where M is the mass of the star, m is the pulsar mass, and r is the distance between the two objects. In this model we assume the star is fixed and only the pulsar moves. The acceleration is simply,

$$\ddot{r} = \frac{dv}{dt} = \frac{dv}{dr} \cdot \frac{dr}{dt} = v \frac{dv}{dr}, \quad (8.3)$$

where v is the velocity of the pulsar. Substituting into the above equation, both sides can be integrated, namely

$$\begin{aligned} - \int_0^r \frac{GM}{r'^2} dr' &= \int_0^v v' dv' \\ \frac{GM}{r} &= \frac{1}{2} v^2 \\ \frac{2GM}{r} &= v^2. \end{aligned}$$

Since the velocity v also represents a change in distance between the two bodies,

$$\begin{aligned} v = \dot{r} &= \left(\frac{2GM}{r} \right)^{1/2} \\ \frac{dr}{dt} &= (2GM)^{1/2} r^{-1/2} \\ \Rightarrow \int_{r_0}^0 r^{1/2} dr &= (2GM)^{1/2} \int_0^t dt \\ \frac{2}{3} r_0^{3/2} &= (2GM)^{1/2} t \\ \Rightarrow r_0 &= \left(\frac{3}{2} \right)^{2/3} (2GM)^{1/3} t^{2/3}. \end{aligned} \quad (8.4)$$

This r_0 is the separation distance between star and pulsar at time t during a collision event when both bodies start at rest. For an observation period of 10 years,

$$r_0 \sim 10^{-4} \text{ pc.} \quad (8.5)$$

This distance will be different if the stars were allowed to move and not assumed to be at rest (as was done here). Some stars in the MC simulation (double King profile) will have separations of this magnitude, therefore it is necessary to determine how much the gravitational acceleration affects the timing residuals.

8.1 Simulations: Initial Conditions

Two simulations were pursued – one where all bodies started at rest, and another where the stars and pulsars were given random velocities. It should be stated that the first simulation is a physically unrealistic model, and that it was only made to determine the magnitudes of the effect (the results were used to compare with the second simulation).

In both simulations a pulsar was placed in the middle of a cube of width D . The cube is an approximation of the high density core region of a globular cluster. A total of 10^6 stars were then generated and positioned inside this cube. The value chosen for D will affect the separation r between the pulsar and the stars, and so will affect the gravitational acceleration between the two bodies. As described in Section 5.2.2 the assumption is that the effects by stars further away from the pulsars cancel each other out, and therefore only the stars closest to the pulsar will be included. The simulation ignores the stars furthest from the line of sight – at the edges of the cube.

There were variations done for the two simulations mentioned above. In one variant the parameter D was changed to determine how the timing residuals are affected by the number density around the pulsar.

The simulation ran for a period of 3600 days, at timesteps (Δt) of 30 days. The movement of the pulsars were dictated solely by the gravitational acceleration. For all simulations, the stars were assumed to be fixed in position with no initial velocity (unless otherwise stated).

The following section will show how the gravitational acceleration affects the

velocity and position of the pulsars for simple systems.

8.2 Determining the change in pulsar time of arrival

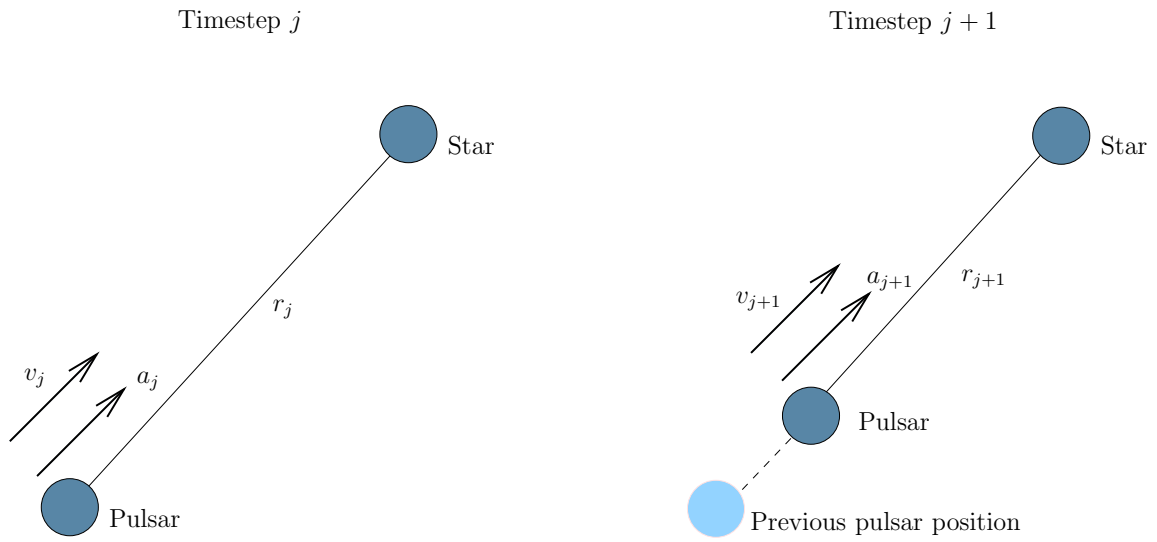


Figure 8.1: The effect of gravitational acceleration between one pulsar and one star. The acceleration a and velocity v are both along the distance r for both timesteps.

Let us investigate the configuration of one pulsar and one star, both at rest so the pulsar initial conditions are $t = 0$ and $v_0 = 0$. In addition, we will assume that the star does not move from its position throughout the simulation, i.e. the star will not have any acceleration or velocity components.

At timestep j (Figure 8.1 left), the acceleration of a pulsar at a distance r_j from the star is given from Equation 8.1,

$$\vec{a}_j = -\frac{GM}{r_j^2} \hat{r}_j, \quad (8.6)$$

where M is the mass of the star, equal to $1 M_\odot$. The pulsar will travel at acceleration \vec{a}_j between timestep j and $j+1$, the following timestep. The velocity

of the pulsar traveling in the next timestep is given by,

$$\vec{v}_j = \vec{v}_0 + \vec{a}_j \Delta t, \quad (8.7)$$

where Δt is the time interval between the two timesteps. The pulsar then moves from its position r_j with velocity v_j to its new position in the next timestep. At the following timestep, $j + 1$ (Figure 8.1 right), the pulsar is now at a new distance from the star, r_{j+1} which is given by,

$$\vec{r}_{j+1} = \vec{r}_j + \vec{v}_j \Delta t. \quad (8.8)$$

In this timestep, the acceleration term becomes,

$$\vec{a}_{j+1} = -\frac{GM}{r_{j+1}^2} \hat{r}_{j+1}, \quad (8.9)$$

and the velocity term (during this timestep) is then given by,

$$\vec{v}_{j+1} = \vec{v}_j + \vec{a}_{j+1} \Delta t. \quad (8.10)$$

In the following timestep, $j + 2$, the pulsar moves from r_{j+1} to its new position traveling at velocity v_{j+1} ,

$$\vec{r}_{j+2} = \vec{r}_{j+1} + \vec{v}_{j+1} \Delta t, \quad (8.11)$$

from which the acceleration and velocity terms during this timestep, a_{j+1} and v_{j+2} , respectively, can be determined. This process is repeated until the final timestep (full observation period t).

Multiple stars

The above equations describe the case for one star and one pulsar. For multiple stars, let us re-write the acceleration term given in Equation 8.6 as,

$$\vec{a}_j = GM \frac{(\vec{r}_{\text{pul},j} - \vec{r}_{\text{star},j})}{|\vec{r}_{\text{pul},j} - \vec{r}_{\text{star},j}|^3}, \quad (8.12)$$

where \vec{a}_j is the acceleration at timestep j and $(\vec{r}_{\text{pul},j} - \vec{r}_{\text{star},j})$ is the distance between the pulsar and star at timestep j . For N stars this term can be written as,

$$\vec{a}_j = GM \sum_{k=1}^N \frac{(\vec{r}_{\text{pul},j} - \vec{r}_{k,j})}{|\vec{r}_{\text{pul},j} - \vec{r}_{k,j}|^3}. \quad (8.13)$$

The velocity at this timestep (j) is given by Equation 8.7,

$$\vec{v}_j = \vec{v}_0 + \vec{a}_j \Delta t, \quad (8.14)$$

This net velocity results in a net change in the pulsar position

$$\vec{r}_j = \vec{r}_0 + \vec{v}_j \Delta t. \quad (8.15)$$

The change in the pulsar distance between the timesteps is then

$$\Delta \vec{r} = \vec{r}_{j+1} - \vec{r}_j. \quad (8.16)$$

Since this change in the pulsar distance, $\Delta \vec{r}_N$ (where the subscript N denotes the total number of stars), is a three dimensional vector, it can be decomposed into Cartesian co-ordinates such that

$$\Delta x = (\Delta r_N) \sin \theta \quad (8.17)$$

$$\Delta y = (\Delta r_N) \cos \theta \sin \phi \quad (8.18)$$

$$\Delta z = (\Delta r_N) \cos \theta \cos \phi. \quad (8.19)$$

The x -direction is along the LOS, and therefore Δx is the variable that changes the pulsar TOA. This change in pulsar arrival time can then be represented by

$$\Delta \tau = \frac{\Delta x}{c}, \quad (8.20)$$

where c is the speed of light.

The simulation determined $\Delta \tau$ from the stars inside the globular cluster (with a pulsar at the centre), and produced a timing residual using polynomial fitting (see Section 4.4).

8.3 Simulation 1: No initial velocity

This simulation was made to determine the magnitude of the effect of gravitational acceleration before the inclusion of initial velocities, in order to have a comparison with the more complicated situation that includes initial velocities.

In this simulation, there were no initial velocities assigned to the pulsars so their motions would be determined purely by the gravitational acceleration of the stars which were considered to remain static for the duration of the simulation.

As the gravitational acceleration is a function of r , which is the distance between the pulsar and a star, the number density of the core of a globular cluster may have an affect on the change in TOA. Stars are more likely to be closer to a pulsar (having, therefore, a smaller r) for a dense globular cluster core than for one that is diffuse. A smaller r separation between the pulsar and a star will result in a larger acceleration term, which may lead to a greater change in the TOA $\Delta\tau$.

The simulation was as follows. A globular cluster was constructed where the core was modelled as a cube of width D pc containing 10^6 stars, with a pulsar at the centre. The inferred gravitational acceleration on the pulsar from the surrounding stars is then calculated, and the pulsar is moved by the velocity generated from the accelerations to its new position. This process was modelled for a 3600 days using 30 days timesteps of 30 days. Many (~ 100) realisations were done to determine $\langle t_{\text{rms}} \rangle$ for the pulsar for every box/cube width D .

Figure 8.2 shows how $\langle t_{\text{rms}} \rangle$ varies with D , the width of the box representing the core of a globular cluster. The form is rather complex. For box sizes $D \sim 0.15$ pc there is a very sharp reduction in the timing residual to 10^{-5} s. Thereafter it decreases slowly with increasing D and increasing scatter until at $D \sim 2$ pc. This is because at these larger cluster volumes the minimum separation between a pulsar and its nearest star is so large that the gravitational acceleration does not produce significant velocities. Only in a very few realisations was the

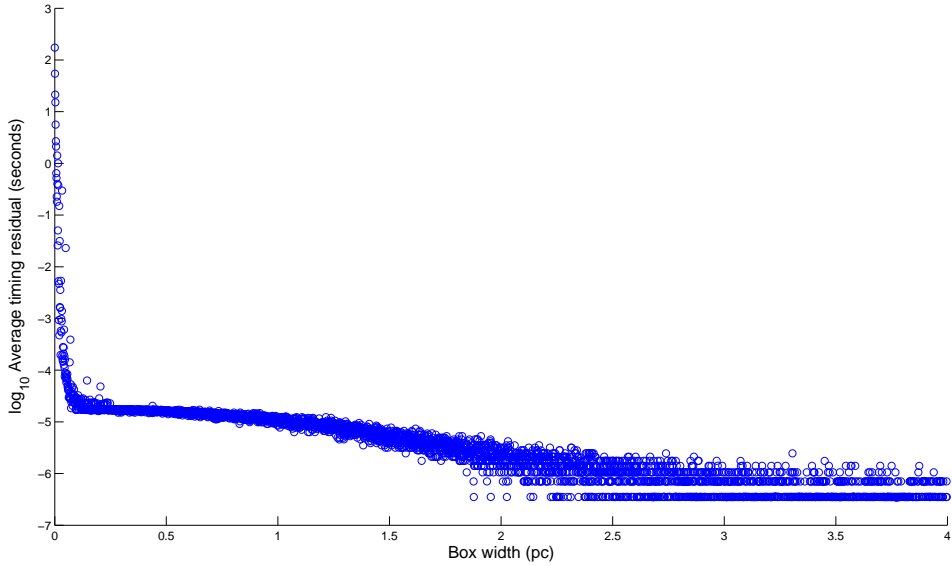


Figure 8.2: Variations in timing residual as a function of D , the core box width, for a 10^6 star globular cluster.

configuration suitable for a timing residual to be generated. Due to the number density decreasing with increasing box width D , the probability of generating a star close to the pulsar becomes lower with increasing D .

How the average RMS timing residual varies with stellar density is shown in Figure 8.3. The function is of similar complexity to that determined in Figure 8.2. The red line shows the (logarithm of the) core stellar density of 47 Tucanae (Pryor and Meylan 1993) of $1.5 \times 10^5 M_\odot \text{ pc}^{-3}$. At this particular density, the timing residuals are, at most, of the order of 10^{-5} s. This is a significant conclusion as these are the results from the physically unrealistic case where the stars and pulsars have no initial velocity, and therefore warrants further study. It is most likely that when adding initial velocities to the stars and pulsars (i.e. a more realistic model – see Section 8.4) to the simulations it will greatly increase the effect of gravitational acceleration on the timing residuals.

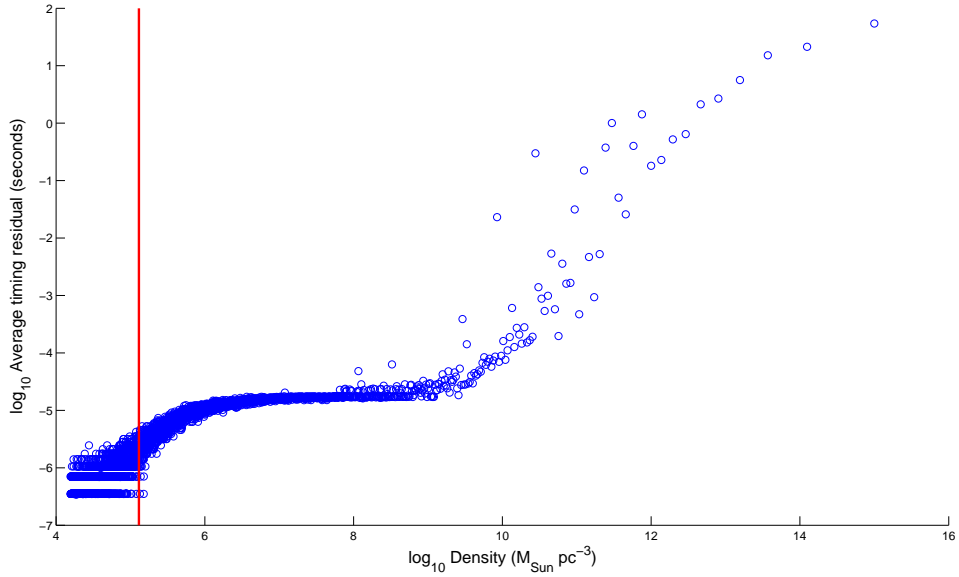


Figure 8.3: Variations in timing residual as a function of stellar density in the core ρ , for a 10^6 star globular cluster. The red line denotes the core stellar density of 47 Tucanae as described in Pryor and Meylan (1993).

8.4 Simulation 2: With initial velocity

Let us now investigate how the above result is affected by the inclusion of velocities to stars and pulsars. The velocities for both stars and pulsars were generated using a Gaussian distribution with σ shown in Table 3.1. The simulation method used here is similar to Simulation 1 but with the inclusion of the velocity parameters.

Figure 8.4 shows how $\langle t_{\text{rms}} \rangle$ varies with D . As was the case in Simulation 1, the average rms timing residual decreases with the box width D , although not as rapidly. The magnitudes of the residuals are larger than the residuals produced in Simulation 1, suggesting that the inclusion of the initial velocity parameters does have an effect on the timing residuals. The densest distributions ($D < 0.1$ pc) have the largest variation (spread) in the timing residual values. This is most likely due to the star closest to the pulsar – the location r of this star will affect

the acceleration, and hence will have an effect on the timing residual.

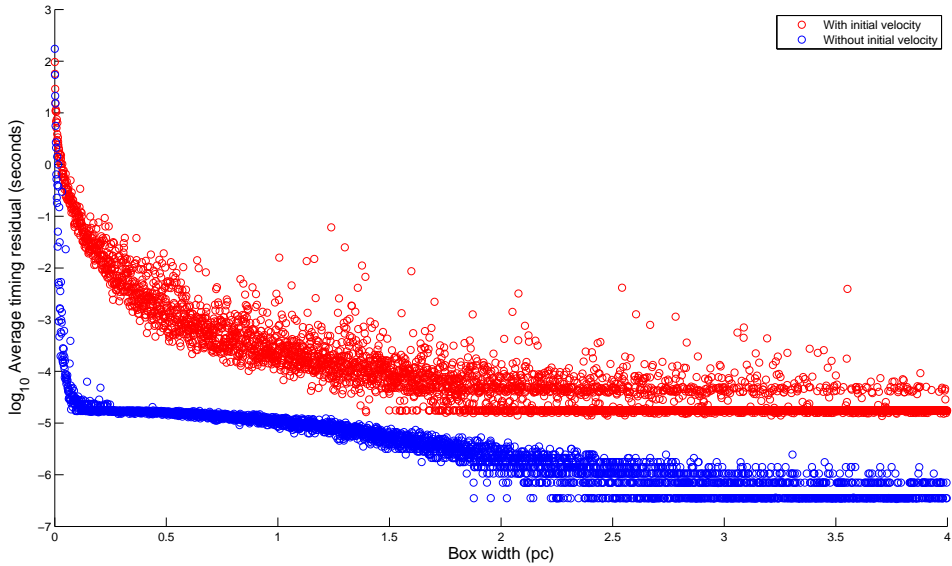


Figure 8.4: Variations in timing residual as a function of D , the core box width, for a 10^6 star globular cluster.

Figure 8.5 (below) shows how the timing residuals vary with stellar density. The timing residuals for the simulation with initial velocity are greater than those found for the simulation without initial velocities and both are shown in the figure. The structure of the two functions is also different – the initial velocity (red line) does not contain the ‘plateau’ that the no initial velocity (blue line) has at $\rho \sim 10^9 M_{\odot} \text{ pc}^{-3}$. In the case of the simulation with initial velocity, the timing residual one expects from a core stellar density similar to that of 47 Tucanae to be of the order of 10^{-4} to 10^{-5} seconds.

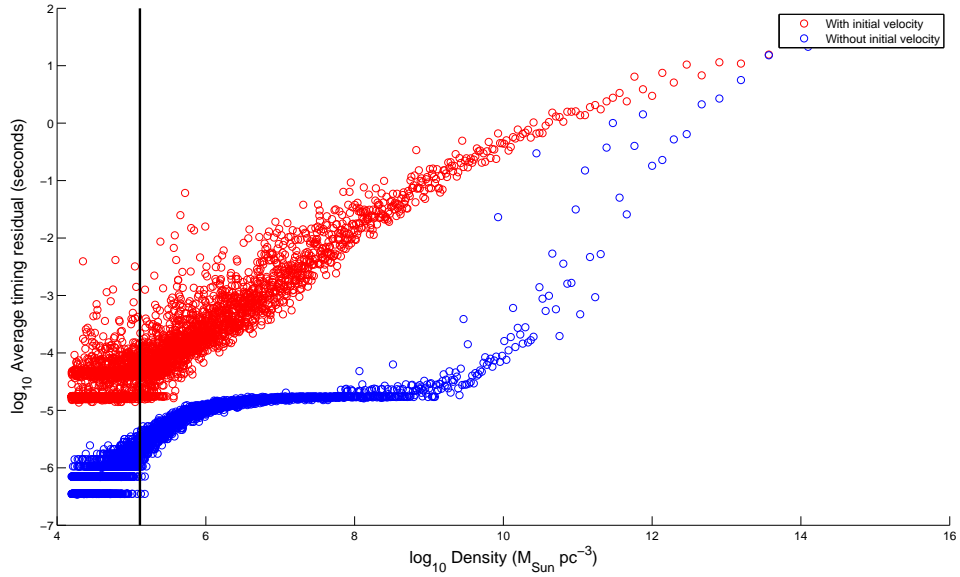


Figure 8.5: Variations in timing residual as a function of ρ , the stellar density, for a 10^6 star globular cluster. The red line denotes the core stellar density of 47 Tucanae as described in Pryor and Meylan (1993).

8.5 Combining with Shapiro noise

Let us now combine two effects – the Shapiro noise and the gravitational acceleration (Simulation 2, see Section 8.4) – into the simulation and determine the resulting timing residual. In this simulation, 10^6 stars were generated using the double King profile and the actual pulsar positions and velocities. The remaining initial conditions are the same as previous simulations. Table 8.1 shows how the timing residuals are affected if gravitational acceleration is included in the calculations.

From Table 8.1 it can be seen that for pulsars that are furthest away from the core the gravitational acceleration has a negligible affect on the timing residual when compared to that of the Shapiro noise. However, for stars in the core, such as the O-pulsar in 47 Tucanae the gravitational acceleration does have a large effect on the timing residuals. The exception to this is the F-pulsar, where the

timing residual is significantly affected by the inclusion of gravitational acceleration effects. This may be due to a star being generated (in one of the realisations) sufficiently close to the pulsar that it infers a large change in the pulsar distance along the LOS, resulting in a σ -bias.

Pulsar	Shapiro noise		Shapiro noise & gravitational acceleration	
	(10^{-9} s)	σ (10^{-9} s)	(10^{-9} s)	σ (10^{-9} s)
J0023-7204C	0.17181	0.27602	0.17203	0.27567
J0024-7204D	77.33208	213.63506	77.33188	213.63519
J0024-7205E	0.02397	0.03442	0.06252	0.19311
J0024-7204F	68.77878	107.24345	292.56550	485.51931
J0024-7204G	327.36862	597.95265	332.65878	599.81249
J0024-7204H	0.53428	0.85025	0.51309	1.60628
J0024-7204I	586.80975	1784.49970	617.00326	1787.36029
J0023-7203J	21.35217	50.52859	21.37556	50.53270
J0023-7205M	0.16816	0.29948	0.21933	0.30473
J0024-7204N	14.90031	21.97074	14.90201	21.97107
J0024-7204O	1053.78123	2053.93642	2980.95575	3883.33519
J0024-7204Q	0.16935	0.27971	0.16256	0.50678
J0024-7204S	756.57148	2040.93763	898.15895	1871.13700
J0024-7204T	24.32024	35.26797	48.80774	69.95056
J0024-7203U	0.03988	0.08677	0.05520	0.15871

Table 8.1: Comparison of the timing residual with and without gravitational acceleration for a 10^6 star globular cluster.

There are more stars present around pulsars which are situated in the core of the globular cluster. Table 8.1 shows that for these pulsars the gravitational acceleration (from the stars surrounding this pulsar) has a greater effect than the Shapiro noise (stars surrounding the LOS to the pulsar). The timing residual for the O-pulsar increases by a factor of ~ 3 with the inclusion of gravitational acceleration.

The gravitational acceleration becomes less dominant as one moves away from the core. The timing residual for the G-pulsar (which is at a distance of $r \sim 0.5$ pc from the core) shows that it is dominated more by the Shapiro noise than by the gravitational acceleration. Therefore, to an approximation, the gravitational

acceleration will have an effect on the timing residuals of the pulsars that are situated < 0.5 pc from the core of the globular cluster.

8.6 Summary

In this chapter a new concept, gravitational acceleration between the stars and the pulsars, was investigated to determine how it will affect pulsar timing residuals. The investigation was made by generating stars (at a certain volume) around a pulsar, and allowing the stars and pulsars to interact gravitationally over a 3600-day period. The gravitational interaction between the stars themselves was ignored in the simulations. The change in the pulsar position along the LOS due to gravitational acceleration was made to this new delay term. A second order polynomial fit (as described in Section 4.4) was done to this new delay term to obtain the timing residuals. The timing residuals indicate that gravitational acceleration does have an effect on the timing residuals, provided that there is a sufficiently large stellar density surrounding the pulsar.

When combined with the Shapiro noise, the gravitational acceleration affects only the pulsars close (< 0.5 pc) to the centre of the globular clusters – for all other pulsars the effect from the Shapiro noise is much greater.

Part V

Stellar Mass Density

9

Stellar Mass Density

In the previous chapters, it was shown that stars in globular clusters have an effect on the timing residual of a pulsar. This effect is in the region of microseconds to milliseconds, depending on the pulsar position with respect to the centre of the globular cluster. This new result is important, as for some pulsars, such as the O-pulsar, the magnitude of timing residuals predicted solely from the Shapiro noise is similar to the magnitudes that are obtained from pulsar timing observations. For pulsars further away from the centre of the globular cluster the effect of the Shapiro noise on the timing residuals is far smaller than that observed.

Chapter 8 also investigated how gravitational acceleration affects pulsar timings. For dense cores such as 47 Tucanae, it was (initially) thought that the acceleration will influence the timing residual, however the extent of this effect was not known. Chapter 8 showed that while the effect from acceleration is present in the timing residuals, the effect from the Shapiro noise is far greater for most GC pulsars. This result suggest that stars along the LOS will have a greater effect on the timing residuals than stars around the pulsars – unless the pulsar is situated close to, or at, the core of the globular cluster.

For the case of 47 Tucanae, the line of sight (LOS) is approximately 5 kpc. This is a vast distance, one which may be filled with ISM. Since the Shapiro delay is very sensitive around the LOS (see Figure 2.6) than (radially) along it

9: STELLAR MASS DENSITY

(see Figure 2.7), any foreground star close to the LOS will have an impact on the timing residuals. This poses an important question for pulsar timing: how much do foreground stars affect timing residuals? If the influence is significant, then the Shapiro delay will have an effect on timing residuals of pulsars not only in globular clusters but also in the galactic plane.

Let us assume there is a single pulsar located as shown in Figure 9.1. The LOS contains a lot of foreground stars. Any star close enough to the LOS, e.g. in a ‘window’ region around the LOS, will produce a Shapiro delay, as shown in Figure 9.2. The density of this ‘window’, along with the stellar velocities, will affect the Shapiro delay and pulsar timing.

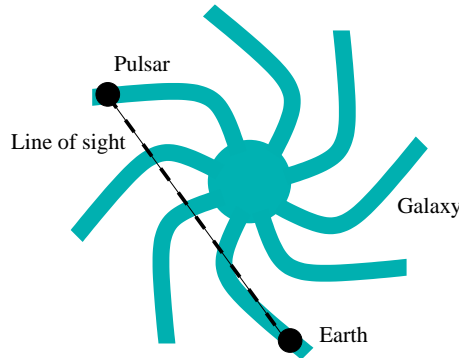


Figure 9.1: LOS to a pulsar in the spiral arms of a galaxy.

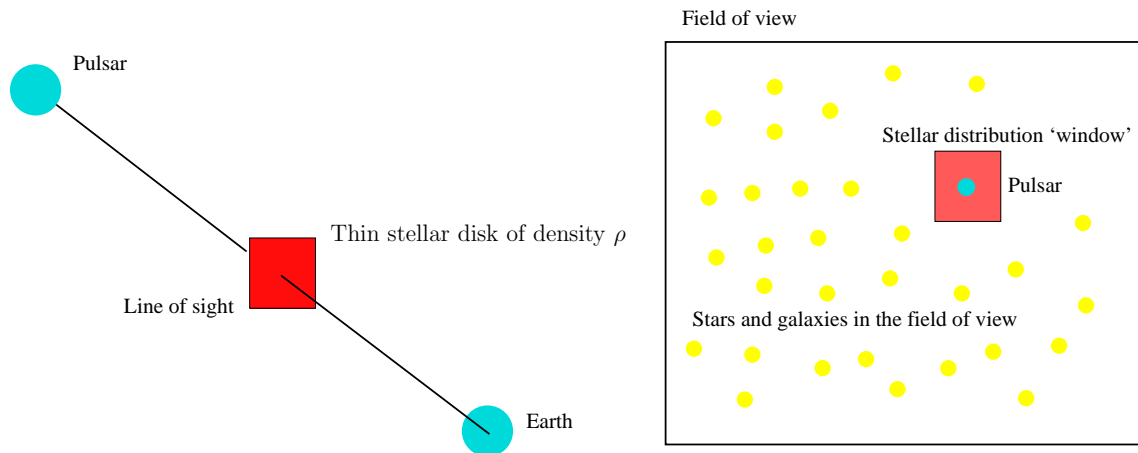


Figure 9.2: *Left:* The thin stellar disk along the LOS between pulsar and Earth.

Right: The ‘window’ of stellar distribution around the LOS to the pulsar.

In order to determine the timing residuals, a simulation of one isolated pulsar (no stars surround it) was created. Stars were then distributed into a window (i.e. a thin disk), 1 pc^2 in size, all at the same distance along the LOS to the pulsar. Stars were then given velocities and were allowed to move for 3600 days. The timing residual for the pulsar was determined using polynomial fitting as described in Chapter 4. This simulation was then repeated 50 times to determine the average RMS timing residual. This whole process was realised for (i) different thin disk (surface) density, and (ii) different distances along the LOS.

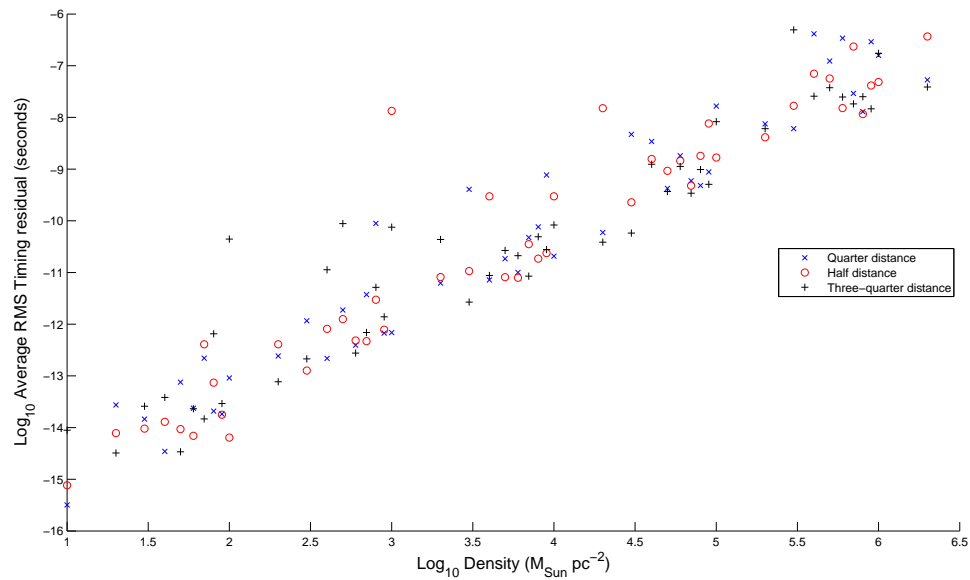


Figure 9.3: The average RMS timing residual as a function of stellar surface density in a thin disk at varying distances along the LOS.

Figure 9.3 shows how the average RMS timing residuals vary with respect to the density of the thin disk and distance along the LOS. As described before, the variation of the timing residual along the LOS does not change the result significantly. The trend for all three separation distances is very similar. The density of the disk does have an effect on the timing residuals. The greater the stellar density, the larger the timing residual. This is expected, as a larger den-

sity of stars means that the probability of one being close to the LOS increases, and therefore more likely to produce a large Shapiro noise. The foreground stellar surface density, Σ_{\min} , necessary to produce an observable ($> 10^{-7}$ s) timing residual is

$$\Sigma_{\min} \approx 10^6 \text{ M}_\odot \text{ pc}^{-2} \quad \text{up to } R \leq 0.71 \text{ pc}, \quad (9.1)$$

where R is the region (perpendicular distance) around the LOS. This is similar to the initial conditions (and the results obtained) for the MC simulation of the globular cluster modelled using a Gaussian sphere (Section 3.2), which in turn means, that in order for the foreground stars to have an effect on the timing residuals, there must be at least a large cluster of stars along the LOS to the pulsar. This means that any diffuse ($\rho < 10^3 \text{ M}_\odot \text{ pc}^{-2}$) matter between the pulsar and the Earth can be ignored, as it is less likely that a star in such regions will approach close enough to the LOS in order to produce an effect on the timing residual.

Let us now return to stars positioned around pulsars. It was shown previously in Chapter 3 (and Chapter 5) that an increase in the number of stars inside the globular cluster did have an effect on the timing residuals. No previous literature has determined the minimum stellar density required in order for the cluster to have an effect on the timing residual.

Therefore, let us simulate a box of stars, with dimensions 1 pc^3 , with a pulsar at the centre. Stars were generated in this box and were allowed to move for 3600 days (see above), and the timing residual was determined from the Shapiro noise (see above). This was then repeated 50 times, and this whole simulation was realised for different total numbers. Figure 9.4 shows how the average RMS timing residual varies with the stellar (box) density. Similar to above, increasing the stellar density increases the magnitude of the timing residuals. From Figure 9.4, the minimum density ρ_{\min} required in order to have an observable effect ($> 10^{-7}$

s) on the timing residual is

$$\rho_{\min} \approx 10^5 \text{ M}_\odot \text{ pc}^{-3} \quad \text{up to } R \leq 0.87 \text{ pc}, \quad (9.2)$$

where R is the distance around the pulsar.

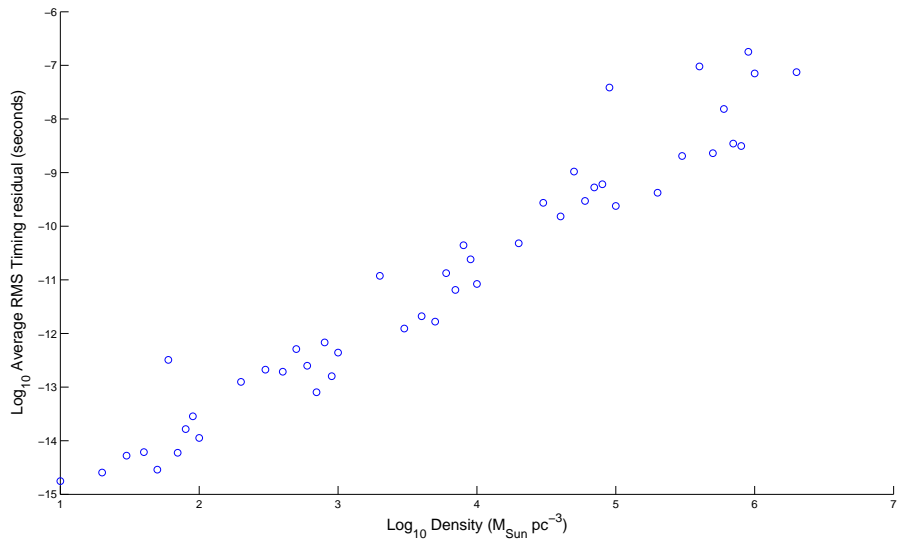


Figure 9.4: The Average RMS timing residual as a function of stellar density around the pulsar.

Let us now compare this value with the density of globular cluster that contains pulsars. Table 9.1 shows the stellar core density of the globular cluster that contains milli-second pulsars. It was possible to obtain the values (or a range of value) for the core stellar density for all but three globular clusters (NGC 6517, NGC 6656, NGC 6838).

Let us now plot the distribution of stellar core densities of the globular cluster. The distribution is shown in Figure 9.5. For globular clusters that have a range of density values, the middle of the range is taken to be the stellar core density for the globular cluster. From Figure 9.5 it can be seen that many (15 out of 22) of the globular clusters have core stellar densities larger than ρ_{\min} . This result indicates that pulsars within these globular clusters will be affected by Shapiro noise (and gravitational acceleration).

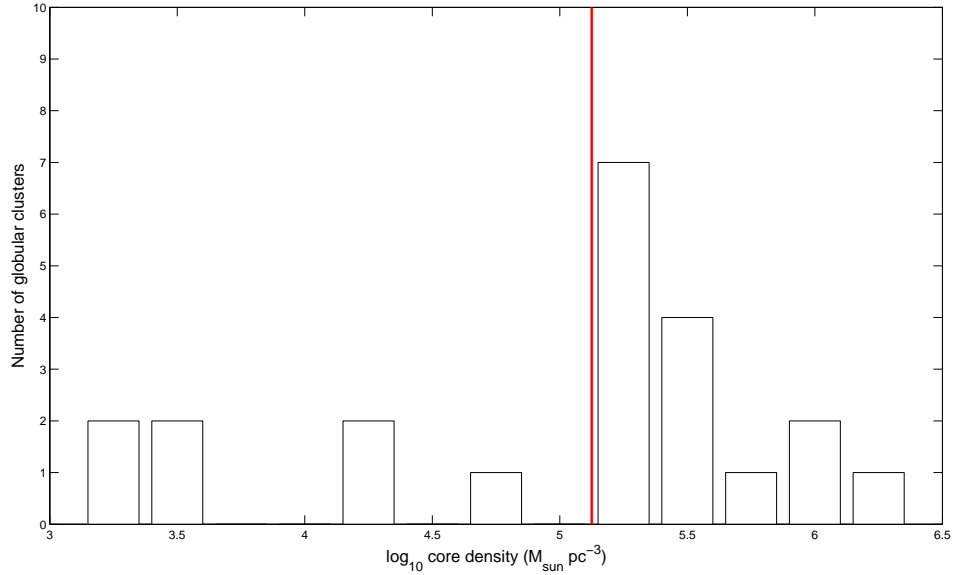


Figure 9.5: The distribution of core stellar density for 22 globular clusters containing MSPs. The red line is ρ_{\min} , the minimum core stellar density.

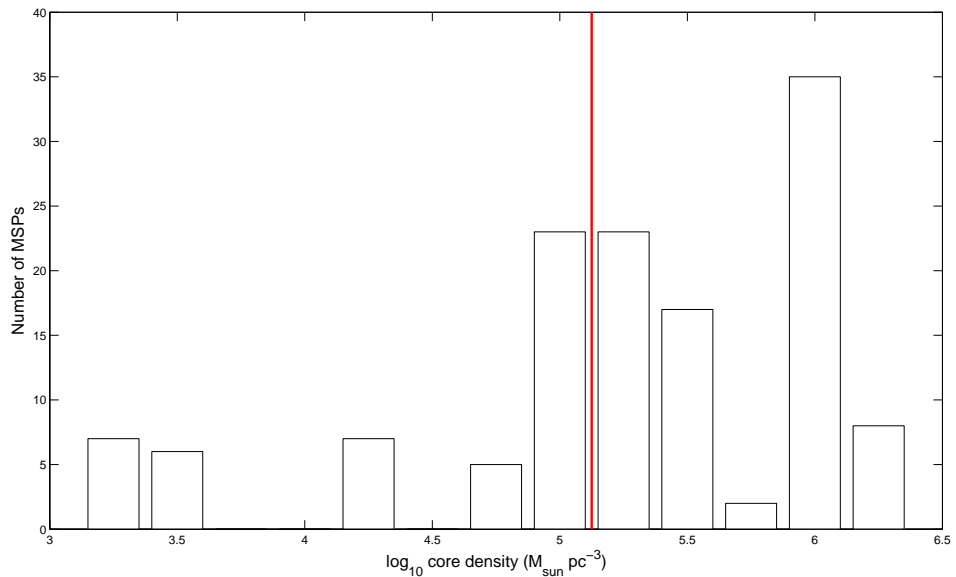


Figure 9.6: The distribution of pulsars according to the core stellar density of the globular cluster containing the pulsar. The red line is ρ_{\min} , the minimum core stellar density.

Figure 9.6 shows the distribution of pulsars as a function of the core stellar density of the globular cluster. Again, there are a large number of pulsars situated in globular clusters of core stellar density greater than ρ_{\min} . Figure 9.6 suggests that the timing residuals of 82 (out of 139) pulsars¹, or $\sim 60\%$ of the total number of MSPs observed to date, will be affected by Shapiro noise and gravitational acceleration. This is a significant result.

This thesis has determined the RMS timing residuals for 15 of the 82 pulsars. From these 15 pulsars it was shown that the pulsar position (relative to the centre of the globular cluster) does have an affect on the timing residuals. This is because the Shapiro noise and the gravitational acceleration are sensitive to the perpendicular distance between a star and the LOS (Shapiro noise) and the distance between a star and the pulsar (gravitational acceleration).

If the majority of the remaining pulsars are far from the globular cluster centre, the RMS timing residuals for such pulsars will have smaller magnitudes. In this situation, the Shapiro noise and gravitational acceleration will be too small to be observed in the timing residuals, such as the case for the J-pulsar. As a result, the Shapiro noise and gravitational acceleration will have minimal effect on reducing the timing noise.

However, if the majority of the remaining pulsars are situated close to the globular cluster centre, the RMS timing residuals will be higher in magnitude, and almost comparable to the magnitude of the observed timing residuals. In such case, the effects of Shapiro noise and gravitational acceleration will have a significant effect on reducing the timing noise.

From Figure 7.18, in the case of 47 Tucanae there are fewer pulsars positioned close to the globular cluster centre compared to the number of pulsars situated further away. If one assumes a similar pulsar distribution pattern in other globular clusters, the RMS timing residuals for most MSPs will of the order of $\sim 10^{-7}$

¹There are in fact 146 pulsars, however 7 of them are contained in the three globular clusters for which the core stellar density could not be found.

seconds, suggesting that, while these effects affect $\sim 60\%$ of MSPs in globular clusters, they may not be large enough to be observed in the timing residuals.

Table 9.1: Comparison of the core stellar density of globular clusters containing millisecond pulsars (MSPs).

Cluster	Other names	Number of MSPs	$\log_{10} \rho_c (\text{M}_\odot \text{ pc}^{-3})$	Reference
NGC 104	47 Tucanae	23	5.18	Pryor and Meylan (1993)
NGC 1851		1	≥ 5.48	Bahcall et al. (1977)
NGC 5024	M53	1	3.34	Beccari et al. (2008)
NGC 5272	M3	4	3.51	Guhathakurta et al. (1994)
NGC 5904	M5	5	$3.8 \sim 4.6$	Ivanova et al. (2008)
NGC 5986		1	3.40	Lynch and Ransom (2011)
NGC 6121	M4	5	4.63	Peterson et al. (1995)
NGC 6205	M13	5	3.40	Cohen et al. (1997)
NGC 6266	M62	6	5.32	Possenti et al. (2003)
NGC 6342		1	> 5.35	Ivanova et al. (2008)
NGC 6397		1	> 5.35	Ivanova et al. (2008)
Terzan 5		33	~ 6.00	Cohn et al. (2002)
NGC 6440		6	5.66	Williams and Bahcall (1979)
NGC 6441		4	≥ 4.95	Ivanova et al. (2008)
NGC 6517		4	-	<i>no references found</i>
NGC 6522		3	> 5.35	Ivanova et al. (2008)
NGC 6539		1	$2.8 \sim 3.8$	Ivanova et al. (2008)
NGC 6544		2	> 5.75	Possenti et al. (2001)
NGC 6624		6	> 5.60	Ivanova et al. (2005)
NGC 6626	M28	12	$4.6 \sim 5.05$	Ivanova et al. (2008)
NGC 6656	M22	2	-	<i>no references found</i>
NGC 6749		2	$2.8 \sim 3.8$	Ivanova et al. (2008)
NGC 6752		5	$4.6 \sim 5.05$	Ivanova et al. (2008)
NGC 6760		2	$3.8 \sim 4.6$	Ivanova et al. (2008)
NGC 6838	M71	1	-	<i>no references found</i>
NGC 7078	M15	8	6.20	Guhathakurta et al. (1996)
NGC 7099	M30	2	5.90	Yanny et al. (1994)

Part VI

Conclusion

The motivation for this thesis was to determine how much the stars travelling close to the LOS and around the pulsar contribute to pulsar timing residuals. This contribution was introduced as an additional term in the pulsar TOA Equation 1.2, called the Shapiro noise, derived from the time delay. As described in Chapter 1, this effect had been previously assumed to be small, and therefore an unobservable effect in pulsar timing residuals.

There are two components to the time delay, the geometric and gravitational time delay. As shown in Figure 2.3, the geometric time delay has a large effect for stars positioned less than 10^{-5} pc from the LOS; for all other distances the gravitational time delay is the more dominant effect. It was then estimated that the probability of detecting a star less than 10^{-5} pc from the LOS was sufficiently small that the geometric term associated with this situation may be ignored and only the gravitational (Shapiro) time delay component was used in the investigation. In order to determine this effect for the globular cluster 47 Tucanae, the full expression for the Shapiro delay for one star and a pulsar was derived in Chapter 2 using gravitational lensing.

In Chapter 3 a simple globular cluster with the same dimensions as 47 Tucanae containing 10^6 stars was simulated. Using a Monte-Carlo (MC) simulation the stars were moved for a period of 3600 days (the current longest pulsar observation time) to determine the effects of the Shapiro delay. The changes in stellar position result in the change of the Shapiro delay called the Shapiro noise. The Shapiro noise is an observable effect, whilst the Shapiro delay is not. The simulations predicted the Shapiro noise to be of the order of 10^{-6} seconds for a 10^6 star globular cluster, and from the \sqrt{N} described in Section 3.4.2 it was estimated

that the Shapiro noise would be of the order of 10^{-5} seconds for a 10^8 star globular cluster. This effect is large, and will be observable in pulsar timing. In order to check that the simulations were producing correct results analytical expressions were produced and compared with the numerical predictions. The results, shown in Chapter 3, suggest that both approaches predict similar values for the Shapiro noise. It was therefore determined that the MC simulation produced accurate results.

Chapter 4 investigated the timing residuals that result from the Shapiro noise. The standard model uses least-squares fitting process that produces a TOA model with the most likely values for the spin frequency f and the change in spin \dot{f} . Timing residuals are determined by subtraction of the TOAs predicted by the model from actual observed TOAs. As the Shapiro noise is independent of f and \dot{f} , it was postulated that a second order polynomial fitting procedure to produce a model would give the same timing residual as the least-squares fitting, without the need to obtain values of f and \dot{f} .

Also in Chapter 4 the actual pulsar positions and a more accurate stellar distribution (a double King profile) was used in order to get timing residuals that compared with observations. The simulations predict that not only is the Shapiro noise a significant factor in the timing residuals but also that these timing residuals correlate well with actual pulsar observations. However, the timing residuals also suggest that the core regions of the globular cluster may not be as dense as predicted by the double King profile.

In Chapter 8 the gravitational acceleration has been added to the pulsar time of arrival to determine its effects on pulsar timing residuals. All the previous simulations assumed that stars and pulsars move at a constant velocity. The simulations suggest that the inclusion of gravitational acceleration does not have a significant effect on the timing residuals when compared to the effect of the Shapiro noise.

The effect generated by the combination of Shapiro noise and gravitational

acceleration on timing residuals is so significant that it will be observable in pulsar timing.

To see how many pulsars will be affected by these two effects, Chapter 9 determined the minimum stellar core density (both in two- and three dimensions) necessary for a globular cluster in order for the stars inside the cluster to have an affect on pulsar timing. The minimum density, ρ_{\min} , required in order to observe an effect from both Shapiro noise and gravitational acceleration on the timing residual is given as,

$$\rho_{\min} \approx 10^5 M_{\odot} \text{ pc}^{-3} \quad \text{up to } R \leq 0.87 \text{ pc}, \quad (9.3)$$

where R is the distance around the pulsar. This core density can be found for 15 of the 22 globular clusters that are currently known to contain milli-second pulsars (MSPs). The result is that 82 of the 139 pulsars in these globular clusters will be affected by Shapiro noise and gravitational acceleration. However, due to the position of the pulsar within the globular cluster, for the majority of pulsars the effect from either will most likely be unobservable in the pulsar timing residuals with current observation techniques. However, for improved observation facilities such as the SKA, these effects will have to be taken into consideration for reducing timing noise.

Part VII

Appendices

Appendix A

A.1 Change in Römer delay

The Römer delay across the Solar System for a pulsar at Ecliptic co-ordinates λ (longitude) and β (latitude),

$$\Delta_{R\odot} \simeq 500 \cos \beta \cos(\theta(t) + \lambda) \text{ s} \quad (\text{A.1})$$

where $\theta(t)$ is the orbital phase of the Earth with respect to the vernal equinox, arises from the assumption that the Earth's orbit is circular. An error in position, $\Delta\lambda$ and $\Delta\beta$ causes a differential Römer delay to be present in the timing residuals,

$$\Delta(\Delta_{R\odot}) \simeq 500 [\cos(\beta + \Delta\beta) \cos(\theta(t) + \lambda + \Delta\lambda) - \cos \beta \cos(\theta(t) + \lambda)]. \quad (\text{A.2})$$

For small position errors, using the small angle approximation, $\Delta\beta\Delta\lambda \sim 0$ the above equation reduces to (see Section A.2) ,

$$\Delta(\Delta_{R\odot}) \simeq 500 [\Delta\lambda \cos \beta \sin(\theta(t) + \lambda) + \Delta\beta \sin \beta \cos(\theta(t) + \lambda)] \quad (\text{A.3})$$

From the trigonometric identity,

$$A \sin([\theta(t) + \lambda] + \phi) = A \cos \phi \sin(\theta(t) + \lambda) + A \sin \theta \cos(\theta(t) + \lambda) \quad (\text{A.4})$$

it is possible to simplify the above equation to

$$A \cos \phi = -500 \Delta\lambda \cos \beta \quad (\text{A.5})$$

$$A \sin \phi = -500 \Delta\beta \sin \beta, \quad (\text{A.6})$$

A:

resulting in

$$\Delta\lambda = -\frac{A \cos \phi}{500 \cos \beta} \quad (\text{A.7})$$

$$\Delta\beta = -\frac{A \sin \phi}{500 \sin \beta}, \quad (\text{A.8})$$

where A and ϕ are amplitude and phase error in the timing residuals. When a pulsar is located close to the ecliptic ($\beta \sim 0$) means that $\cos \beta \rightarrow 1$, maximising the error ($\Delta\lambda$) in longitude determination, similarly at the ecliptic ($\sin \beta \sim 0$) maximising the error ($\Delta\beta$) in latitude.

A timing fit and the amplitude of A (in units of light travel time) will determine A to a precision of ΔA that is approximately equal to the uncertainty in the TOA. For very small timing uncertainty, e.g. $10 \mu\text{seconds}$ for a milli-second pulsar (MSP) and $N = 12$ measurements (once a month) over the course of a year (or $N = 120$ for a decade) the average phase errors is $\sim 10\mu\text{s}/\sqrt{120} \sim 9.129 \times 10^{-7}$ seconds. For a MSP at ecliptic latitude 30 degrees ,

$$\Delta\lambda \sim \frac{9.129 \times 10^{-7}}{500 \cos 30} = 2.108 \times 10^{-9}\text{rad} \quad (\text{A.9})$$

$$\Delta\beta \sim \frac{9.129 \times 10^{-7}}{500 \sin 30} = 3.652 \times 10^{-9}\text{rad} \quad (\text{A.10})$$

which results in a change in Römer delay due to changes in Earth position to be ,

$$\Delta(\Delta_{R\odot}) \sim 1.967 \times 10^{-6}\text{s} \quad (\text{A.11})$$

A.2 Small angle approximation

$$\Delta(\Delta_{R\odot}) \simeq 500 [\cos(\beta + \Delta\beta) \cos(\theta(t) + \lambda + \Delta\lambda) - \cos(\beta) \cos(\theta(t) + \lambda)] \quad (\text{A.12})$$

Let us expand the terms inside the square brackets

$$\cos(\beta + \Delta\beta) = \cos(\beta) \cos(\Delta\beta) - \sin(\beta) \sin(\Delta\beta) \quad (\text{A.13})$$

$$= \cos(\beta) - \sin(\beta)\Delta\beta \quad (\text{A.14})$$

from small angle approximation, $\cos(\Delta\beta) \rightarrow 1$, $\sin(\Delta\beta) \approx \Delta\beta$. The second term in the square brackets can be simplified to,

$$\cos(\theta(t) + \lambda) \cos(\Delta\lambda) - \sin(\theta(t) + \lambda) \sin(\Delta\lambda) = \cos(\theta(t) + \lambda) - \Delta\lambda \sin(\theta(t) + \lambda), \quad (\text{A.15})$$

since $\cos(\Delta\lambda) \rightarrow 1$, $\sin(\Delta\lambda) \approx \Delta\lambda$. The product of these two is then given by

$$\begin{aligned} \cos(\beta + \Delta\beta) \cos(\theta(t) + \lambda + \Delta\lambda) &= [\cos(\beta) - \sin(\beta)\Delta\beta] [\cos(\theta(t) + \lambda) - \Delta\lambda \sin(\theta(t) + \lambda)] \\ &= \cos(\beta) \cos(\theta(t) + \lambda) - \Delta\lambda \cos(\beta) \sin(\theta(t) + \lambda) \\ &\quad - \Delta\beta \sin(\beta) \cos(\theta(t) + \lambda) + \Delta\beta \Delta\lambda \sin(\beta) \sin(\theta(t) + \lambda) \\ &= -[\Delta\lambda \cos(\beta) \sin(\theta(t) + \lambda) + \Delta\beta \sin(\beta) \cos(\theta(t) + \lambda)] \end{aligned}$$

The first term is canceled by the last term in square brackets, and the last term is removed by the small angle approximation, $\Delta\beta\Delta\lambda \rightarrow 0$. The resulting equation is then:

$$\Delta(\Delta_{R\odot}) \simeq 500 [\Delta\lambda \cos(\beta) \sin(\theta(t) + \lambda) + \Delta\beta \sin(\beta) \cos(\theta(t) + \lambda)] \quad (\text{A.16})$$

A:

References

- M. A. Alpar, A. F. Cheng, M. A. Ruderman, and J. Shaham. A new class of radio pulsars. *Nature*, 300:728–730, December 1982. doi: 10.1038/300728a0.
- W. Baade and F. Zwicky. On Super-novae. *Proceedings of the National Academy of Science*, 20:254–259, May 1934.
- D. C. Backer and R. W. Hellings. Pulsar timing and general relativity. *ARA&A*, 24:537–575, 1986. doi: 10.1146/annurev.aa.24.090186.002541.
- D. C. Backer, S. R. Kulkarni, C. Heiles, M. M. Davis, and W. M. Goss. A millisecond pulsar. *Nature*, 300:615–618, December 1982. doi: 10.1038/300615a0.
- N. A. Bahcall, B. M. Lasker, and W. Wamsteker. The central region of the X-ray globular cluster NGC 1851. *ApJL*, 213:L105–L107, May 1977. doi: 10.1086/182419.
- G. Beccari, B. Lanzoni, F. R. Ferraro, L. Pulone, M. Bellazzini, F. Fusi Pecci, R. T. Rood, E. Giallongo, R. Ragazzoni, A. Grazian, A. Baruffolo, N. Bouche, P. Buschkamp, C. De Santis, E. Diolaiti, A. Di Paola, J. Farinato, A. Fontana, S. Gallozzi, F. Gasparo, G. Gentile, F. Pasian, F. Pedichini, R. Smareglia, R. Speziali, V. Testa, and E. Vernet. The Blue Straggler Population in the Globular Cluster M53 (NGC 5024): A Combined HST, LBT, and CFHT Study. *ApJ*, 679:712–719, May 2008. doi: 10.1086/587689.
- G. S. Bisnovatyi-Kogan and B. V. Komberg. Pulsars and close binary systems. *Soviet Ast.*, 18:217–+, October 1974.
- A. Blaauw. On the origin of the O- and B-type stars with high velocities (the “run-away” stars), and some related problems. *Bull. Astron. Inst. Netherlands*, 15:265–+, May 1961.
- W. L. Burke. Multiple Gravitational Imaging by Distributed Masses. *ApJL*, 244:L1+, February 1981. doi: 10.1086/183466.

REFERENCES

- D. Calzetti, G. de Marchi, F. Paresce, and M. Shara. The center of gravity and density profile of 47 Tucanae. *ApJL*, 402:L1–L4, January 1993. doi: 10.1086/186685.
- R. L. Cohen, P. Guhathakurta, B. Yanny, D. P. Schneider, and J. N. Bahcall. Globular Cluster Photometry with the Hubble Space Telescope.VI.WF/PC-I Observations of the Stellar Populations in the Core of M13 (NGC 6205). *AJ*, 113:669–681, February 1997. doi: 10.1086/118285.
- H. N. Cohn, P. M. Lugger, J. E. Grindlay, and P. D. Edmonds. Hubble Space Telescope/NICMOS Observations of Terzan 5: Stellar Content and Structure of the Core. *ApJ*, 571:818–829, June 2002. doi: 10.1086/339874.
- N. L. de Lacaille. *Astronomiae fundamenta, novissimis SOLIS et Stellarum Observationibus*. Memoirs Roy. Astr. Society, 1757.
- G. de Marchi and F. Paresce. Low-mass stars in globular clusters. III. The mass function of 47 Tucanae. *A&A*, 304:211–+, December 1995.
- Morris H. DeGroot. *Probability and Statistics*. Massachusetts: Addison-Wesley, second ed. reading edition, 1986.
- S. Deguchi and W. D. Watson. Diffraction in gravitational lensing for compact objects of low mass. *ApJ*, 307:30–37, August 1986. doi: 10.1086/164389.
- S. Detweiler. Pulsar timing measurements and the search for gravitational waves. *ApJ*, 234:1100–1104, December 1979. doi: 10.1086/157593.
- S. Djorgovski and I. R. King. Surface photometry in cores of globular clusters. *ApJL*, 277:L49–L52, February 1984. doi: 10.1086/184200.
- A. S. Eddington. *Space, time and gravitation. an outline of the general relativity theory*. ESO, 1920.
- R. T. Edwards, G. B. Hobbs, and R. N. Manchester. TEMPO2, a new pulsar timing package - II. The timing model and precision estimates. *MNRAS*, 372: 1549–1574, November 2006. doi: 10.1111/j.1365-2966.2006.10870.x.
- A. Einstein. Erklarung der Perihelionbewegung der Merkur aus der allgemeinen Relativitatstheorie. *Sitzungsber. preuss.Akad. Wiss.*, vol. 47, No.2, pp. 831–839, 1915, 47:831–839, 1915.
- A. Einstein. Lens-Like Action of a Star by the Deviation of Light in the Gravitational Field. *Science*, 84:506–507, December 1936.
- A. C. Fabian, J. E. Pringle, and M. J. Rees. Tidal capture formation of binary

- systems and X-ray sources in globular clusters. *MNRAS*, 172:15P–+, August 1975.
- P. C. Freire, F. Camilo, D. R. Lorimer, A. G. Lyne, R. N. Manchester, and N. D’Amico. Timing the millisecond pulsars in 47 Tucanae. *MNRAS*, 326: 901–915, September 2001a. doi: 10.1046/j.1365-8711.2001.04493.x.
- P. C. Freire, M. Kramer, A. G. Lyne, F. Camilo, R. N. Manchester, and N. D’Amico. Detection of Ionized Gas in the Globular Cluster 47 Tucanae. *ApJL*, 557:L105–L108, August 2001b. doi: 10.1086/323248.
- P. C. Freire, F. Camilo, M. Kramer, D. R. Lorimer, A. G. Lyne, R. N. Manchester, and N. D’Amico. Further results from the timing of the millisecond pulsars in 47 Tucanae. *MNRAS*, 340:1359–1374, April 2003. doi: 10.1046/j.1365-8711.2003.06392.x.
- P. Guhathakurta, B. Yanny, J. N. Bahcall, and D. P. Schneider. Globular cluster photometry with the Hubble Space Telescope. 3: Blue stragglers and variable stars in the core of M3. *AJ*, 108:1786–1809, November 1994. doi: 10.1086/117193.
- P. Guhathakurta, B. Yanny, D. P. Schneider, and J. N. Bahcall. Globular Cluster Photometry With the Hubble Space Telescope. V. WFPC Study of M15’s Central density Cusp. *AJ*, 111:267–+, January 1996. doi: 10.1086/117779.
- J. G. Hills. The effects of sudden mass loss and a random kick velocity produced in a supernova explosion on the dynamics of a binary star of arbitrary orbital eccentricity - Applications to X-ray binaries and to the binary pulsars. *ApJ*, 267:322–333, April 1983. doi: 10.1086/160871.
- G. Hobbs. *The Discovery and Timing of Radio Pulsars*. PhD thesis, University of Manchester, 2003.
- G. Hobbs, F. Jenet, K. J. Lee, J. P. W. Verbiest, D. Yardley, R. Manchester, A. Lommen, W. Coles, R. Edwards, and C. Shettigara. TEMPO2: a new pulsar timing package - III. Gravitational wave simulation. *MNRAS*, 394:1945–1955, April 2009. doi: 10.1111/j.1365-2966.2009.14391.x.
- M. Hosokawa, K. Ohnishi, and T. Fukushima. Uncertainty of pulsar time scale due to the gravitational time delay of intervening stars and MACHOs. *A&A*, 351:393–397, November 1999.
- N. Ivanova, F. A. Rasio, J. C. Lombardi, Jr., K. L. Dooley, and Z. F. Proulx.

REFERENCES

- Formation of Ultracompact X-Ray Binaries in Dense Star Clusters. *ApJL*, 621: L109–L112, March 2005. doi: 10.1086/429220.
- N. Ivanova, C. O. Heinke, F. A. Rasio, K. Belczynski, and J. M. Fregeau. Formation and evolution of compact binaries in globular clusters - II. Binaries with neutron stars. *MNRAS*, 386:553–576, May 2008. doi: 10.1111/j.1365-2966.2008.13064.x.
- F. A. Jenet, G. B. Hobbs, K. J. Lee, and R. N. Manchester. Detecting the Stochastic Gravitational Wave Background Using Pulsar Timing. *ApJL*, 625: L123–L126, June 2005. doi: 10.1086/431220.
- P. Jetzer, M. Straessle, and U. Wandeler. Gravitational microlensing by globular clusters. *A&A*, 336:411–424, August 1998.
- I. R. King. The structure of star clusters. III. Some simple dynamical models. *AJ*, 71:64–+, February 1966. doi: 10.1086/109857.
- I. Kovner. Fermat principle in arbitrary gravitational fields. *ApJ*, 351:114–120, March 1990. doi: 10.1086/168450.
- L. M. Krauss and T. A. Small. A new approach to gravitational microlensing - Time delays and the galactic mass distribution. *ApJ*, 378:22–29, September 1991. doi: 10.1086/170403.
- T. I. Larchenkova and O. V. Doroshenko. Pulsars as a tool for detection of dark matter in the Galaxy. *A&A*, 297:607–+, May 1995.
- T. I. Larchenkova and S. M. Kopeikin. The relativistic time delay of pulsar radiation in the gravitational field of the globular cluster stars. *Neutron Stars and Black Holes in Star Clusters, 26th meeting of the IAU, Joint Discussion 6, 17-18 August 2006, Prague, Czech Republic, JD06, #13*, 6, August 2006.
- T. I. Larchenkova and A. A. Lutovinov. On the possibility of observing the Shapiro effect for pulsars in globular clusters. *Astronomy Letters*, 33:455–467, July 2007. doi: 10.1134/S1063773707070031.
- O. J. Lodge. Gravitation and Light. *Nature*, 104:354–+, December 1919. doi: 10.1038/104354a0.
- D. R. Lorimer and M. Kramer. *Handbook of Pulsar Astronomy*. ESO, CUP, December 2004.
- Duncan R. Lorimer. Binary and millisecond pulsars. *Living Reviews in Relativity*, 8(7), 2005. URL <http://www.livingreviews.org/lrr-2005-7>.

- R. S. Lynch and S. M. Ransom. A New Pulsar in Green Bank Telescope Searches of 10 Globular Clusters. *ApJL*, 730:L11+, March 2011. doi: 10.1088/2041-8205/730/1/L11.
- A. G. Lyne. Millisecond pulsars in globular clusters. In *X-Ray Binaries and the Formation of Binary and Millisecond Radio Pulsars*, pages 79–86, 1992.
- A. G. Lyne, A. Brinklow, J. Middleditch, S. R. Kulkarni, and D. C. Backer. The discovery of a millisecond pulsar in the globular cluster M28. *Nature*, 328: 399–401, July 1987. doi: 10.1038/328399a0.
- A. G. Lyne, M. Burgay, M. Kramer, A. Possenti, R. N. Manchester, F. Camilo, M. A. McLaughlin, D. R. Lorimer, N. D’Amico, B. C. Joshi, J. Reynolds, and P. C. C. Freire. A Double-Pulsar System: A Rare Laboratory for Relativistic Gravity and Plasma Physics. *Science*, 303:1153–1157, February 2004. doi: 10.1126/science.1094645.
- R. N. Manchester. Globular clusters and pulsars. In S. S. Holt & F. Verter, editor, *Back to the Galaxy*, volume 278 of *American Institute of Physics Conference Series*, pages 514–523, 1993. doi: 10.1063/1.43928.
- R. N. Manchester, A. G. Lyne, S. Johnston, N. D’Amico, J. Lim, and D. A. Kniffen. A 5.75-millisecond pulsar in the globular cluster 47 Tucanae. *Nature*, 345:598–600, June 1990. doi: 10.1038/345598a0.
- R. N. Manchester, A. G. Lyne, C. Robinson, M. Bailes, and N. D’Amico. Discovery of ten millisecond pulsars in the globular cluster 47 Tucanae. *Nature*, 352:219–221, July 1991. doi: 10.1038/352219a0.
- R. D. McClure, D. A. Vandenberg, G. H. Smith, G. G. Fahlman, H. B. Richer, J. E. Hesser, W. E. Harris, P. B. Stetson, and R. A. Bell. Mass functions for globular cluster main sequences based on CCD photometry and stellar models. *ApJL*, 307:L49–L53, August 1986. doi: 10.1086/184726.
- D. E. McLaughlin, J. Anderson, G. Meylan, K. Gebhardt, C. Pryor, D. Minniti, and S. Phinney. Hubble Space Telescope Proper Motions and Stellar Dynamics in the Core of the Globular Cluster 47 Tucanae. *ApJS*, 166:249–297, September 2006. doi: 10.1086/505692.
- G. Meylan and M. Mayor. Studies of dynamical properties of globular clusters. II - The rotation, velocity dispersion and mass of Omega Centauri and 47 Tucanae. *A&A*, 166:122–142, September 1986.

REFERENCES

- J. Michell. On the Means of Discovering the Distance, Magnitude, &c. of the Fixed Stars, in Consequence of the Diminution of the Velocity of Their Light, in Case Such a Diminution Should be Found to Take Place in any of Them, and Such Other Data Should be Procured from Observations, as Would be Farther Necessary for That Purpose. by the Rev. John Michell, B. D. F. R. S. In a Letter to Henry Cavendish, Esq. F. R. S. and a. S. *Royal Society of London Philosophical Transactions Series I*, 74:35–57, 1784.
- T. T. Nakamura and S. Deguchi. Wave Optics in Gravitational Lensing. *Progress of Theoretical Physics Supplement*, 133:137–153, 1999. doi: 10.1143/PTPS.133.137.
- R. Narayan and M. Bartelmann. Lectures on Gravitational Lensing. *ArXiv Astrophysics e-prints*, June 1996.
- V. Perlick. On Fermat's principle in general relativity. I. The general case. *Classical and Quantum Gravity*, 7:1319–1331, August 1990. doi: 10.1088/0264-9381/7/8/011.
- R. C. Peterson, R. F. Rees, and K. M. Cudworth. Radial velocities of stars in the globular cluster M4 and the cluster distance. *ApJ*, 443:124–135, April 1995. doi: 10.1086/175508.
- A. Possenti, N. D'Amico, R. N. Manchester, J. Sarkissian, A. G. Lyne, and F. Camilo. Searching for Millisecond Pulsars in Globular Clusters at Parkes: Further Results. *ArXiv Astrophysics e-prints*, August 2001.
- A. Possenti, N. D'Amico, R. N. Manchester, F. Camilo, A. G. Lyne, J. Sarkissian, and A. Corongiu. Three Binary Millisecond Pulsars in NGC 6266. *ApJ*, 599: 475–484, December 2003. doi: 10.1086/379190.
- C. Pryor and G. Meylan. Velocity Dispersions for Galactic Globular Clusters. In S. G. Djorgovski & G. Meylan, editor, *Structure and Dynamics of Globular Clusters*, volume 50 of *Astronomical Society of the Pacific Conference Series*, pages 357–+, January 1993.
- R. D. Reasenberg, I. I. Shapiro, P. E. MacNeil, R. B. Goldstein, J. C. Breidenthal, J. P. Brenkle, D. L. Cain, T. M. Kaufman, T. A. Komarek, and A. I. Zygielbaum. Viking relativity experiment - Verification of signal retardation by solar gravity. *ApJL*, 234:L219–L221, December 1979. doi: 10.1086/183144.
- S. Refsdal. The gravitational lens effect. *MNRAS*, 128:295–+, 1964.

- B. J. Rickett. Interstellar scattering and scintillation of radio waves. *ARA&A*, 15:479–504, 1977. doi: 10.1146/annurev.aa.15.090177.002403.
- M. Roos. *Introduction to cosmology*. Information and Computation, 2003.
- P. Schneider. A new formulation of gravitational lens theory, time-delay, and Fermat’s principle. *A&A*, 143:413–420, February 1985.
- P. Schneider. Gravitational Lensing: An Overview. In *KITP: Blackboard Lunch Series*, October 2006.
- P. Schneider, J. Ehlers, and E. E. Falco. *Gravitational Lenses*, page 560. ESO, SPRN, 1992.
- I. I. Shapiro. Fourth Test of General Relativity. *Physical Review Letters*, 13: 789–791, December 1964. doi: 10.1103/PhysRevLett.13.789.
- E. R. Siegel. What Millisecond Pulsars Can Tell Us About Matter In The Galaxy. *ArXiv e-prints*, 801, January 2008.
- E. R. Siegel, M. P. Hertzberg, and J. N. Fry. Probing dark matter substructure with pulsar timing. *MNRAS*, 382:879–885, December 2007. doi: 10.1111/j.1365-2966.2007.12435.x.
- J. Soldner. Über die ablenkung eines lichtstrahls von seiner geradlinigen bewegung durch die attraktion eines weltkörpers, an welchem er nahe vorbeigeht. *Berliner Astronomisches Jahrbuch*, 1804:161–172, 1801.
- K. S. Thorne. *Gravitational radiation.*, pages 330–458. Three hundred years of gravitation, p. 330 - 458, 1987.
- M. A. Walker. Gravitational lensing of millisecond pulsars. *Publications of the Astronomical Society of Australia*, 13:236–242, November 1996.
- D. Walsh, R. F. Carswell, and R. J. Weymann. 0957 + 561 A, B - Twin quasistar objects or gravitational lens. *Nature*, 279:381–384, May 1979.
- R. F. Webbink. Structure parameters of galactic globular clusters. In J. Goodman & P. Hut, editor, *Dynamics of Star Clusters*, volume 113 of *IAU Symposium*, pages 541–577, 1985.
- S. Weinberg. *Gravitation and Cosmology: Principles and Applications of the General Theory of Relativity*. Wiley, July 1972.
- N. Wex, J. Gil, and M. Sendyk. Microlensing of pulsar radiation in the Galactic Center. *A&A*, 311:746–757, July 1996.

REFERENCES

- T. B. Williams and N. A. Bahcall. Brightness, density, and color profiles of three globular clusters - NGC 6440, 6541, and 7099. *ApJ*, 232:754–760, September 1979. doi: 10.1086/157336.
- B. Yanny, P. Guhathakurta, D. P. Schneider, and J. N. Bahcall. WFPC2 observations of the globular cluster M30. *ApJL*, 435:L59–L62, November 1994. doi: 10.1086/187594.
- K. Zarb Adami, A. Gauci, and J. Abela. Gravitational wave detection and cosmic string detection with current radio interferometers. *ArXiv e-prints*, November 2010.
- F. Zwicky. On the Masses of Nebulae and of Clusters of Nebulae. *ApJ*, 86:217–+, October 1937.
- F. Zwicky. Nebulae as gravitational lenses. *Phys. Rev. Lett.*, 51:290, 1937a.
- F. Zwicky. On the probability of detecting nebulae which act as gravitational lenses. *Phys. Rev. Lett.*, 51:679, 1937b.